



Theoretical Analysis of a Fractal Ultrasonic
Transducer Using Renormalisation

Ebrahim Ateatullah Algehyne

Department of Mathematics and Statistics

University of Strathclyde

Glasgow, UK

June 2018

This thesis is submitted to the University of Strathclyde for the degree of Doctor of Philosophy in the Faculty of Science. The copyright of this thesis belongs to the author under the terms of the United Kingdom Copyright Acts as qualified by University of Strathclyde Regulation 3.50. Due acknowledgement must always be made of the use of any material in, or derived from, this thesis.

Dedications

To the beating heart of forgiveness that always pleases God, my darling mother and my wife's mother.

To the witness of my journey of truth and knowledge. My pillar of faith forever, my father.

To the voice of encouragement and love within towards the future and success personifying beauty, my wife.

To my angels sent by God, my children, allowing me to teach and to be taught.

To the wings of power, assurance and happiness, my loving siblings, my loyal and caring brothers and sisters for the words uttered with truthfulness and meaning forever and always.

To you all

Ebrahem Algehyne, June 2018.

Acknowledgements

I would like to express my deepest gratitude to my supervisor, Prof. Anthony J. Mulholland for his help, encouragement and valuable time during the preparation of this thesis and for his excellent guidance. He was far more than a supervisor, both mathematically and personally, and a constant source of inspiration. I would also like to thank the secretaries in the department for their assistance and kind cooperation.

I gratefully acknowledge the support given by the University of Tabuk, the Ministry of Education in Saudi Arabia, the Cultural Bureau and Royal Embassy of Saudi Arabia in UK.

I would like to extend my gratitude and special thanks to my brothers, sisters, brother-in-law, sisters-in-law and friends for their love and support.

I will be forever indebted to the patience, support, love and understanding of my mother, Fatemah, my father, Ateatullah, and my wife's mother, Hamedah. I will never ever forget their tears each time we left home and travelled to achieve this goal.

Finally, from the bottom of my heart, a very special thank you to my beloved wife Zainab and my children, Almoqdad, Alyas, Jihad and a little princess Albylsan who joined us later as I was preparing this thesis. Since October 2009 they followed me, convinced that I could complete this adventure. They have always trusted me, and their support and love have made this time the best of my life.

Last, but not the least, and above all, I would like to give grateful thanks and praise to Allah, for answering my prayers for giving me the strength to endure despite all the difficulties encountered and for giving me more than I asked for.

Ebrahim Ateatullah Algehyne, Glasgow, UK, June 2018.

Abstract

To ensure the safe operation of many safety critical structures such as nuclear plants, aircraft and oil pipelines, non-destructive imaging is employed using piezoelectric ultrasonic transducers. These sensors typically operate at a single frequency due to the restrictions imposed on their resonant behaviour by the use of a single length scale in the design. To allow these transducers to transmit and receive more complex signals it would seem logical to use a range of length scales in the design so that a wide range of resonating frequencies will result. In this thesis we derive a mathematical model to predict the operating characteristics of an ultrasound transducer that achieves this range of length scales by adopting a fractal architecture; the fractal in this case being the Sierpinski gasket. Expressions for the electrical and mechanical fields that are contained within this structure are expressed in terms of a finite element basis. A renormalisation approach is then used to calculate the key components from the discrete matrices that arise. The propagation of an ultrasonic wave in this transducer is then analyzed and used to derive expressions for the non-dimensionalised electrical impedance and the transmission and reception sensitivities as a function of the driving frequency. Comparing these key performance measures of the fractal transducer to an equivalent standard (Euclidean) design shows that the fractal devices have a significantly higher reception sensitivity and a significantly wider bandwidth.

Contents

1	Introduction	4
1.1	Motivation and background	4
1.2	Literature review	5
1.2.1	Ultrasound	5
1.2.2	Ultrasound applications	6
1.2.3	Fractals	8
1.2.4	Fractal applications	9
1.2.5	Fractal graphs	10
1.2.6	Wave propagation in fractal domains	11
1.2.7	Fractal ultrasonic transducers	12
1.3	Outline of Thesis	12
2	A fractal ultrasonic transducer based on the Sierpinski gasket	15
2.1	Introduction	15
2.2	Model derivation	17
2.3	Galerkin discretisation	22
2.3.1	Application of the mechanical boundary conditions	37
2.4	Renormalisation	45
2.4.1	Derivation of the pivotal recursion relationships	49

2.5	Electrical impedance and transmission sensitivity	55
2.6	Reception sensitivity	60
2.7	Steady state solutions	62
2.8	Results	67
2.8.1	Electrical impedance and transmission/reception sensitivities	68
2.8.2	Convergence	77
2.9	Conclusions	79
3	A fractal ultrasonic transducer based on the Sierpinski gasket with both piezoelectric and polymer phases	81
3.1	Introduction	81
3.2	Galerkin discretisation	84
3.2.1	Transformations of the fundamental basis functions	86
3.3	A Homogenised model of the transducer	143
3.4	Renormalisation model of the transducer operating characteristics .	153
3.5	Electrical impedance and transmission and reception sensitivities . .	156
3.6	Steady state solutions	157
3.7	Results	162
3.7.1	Electrical impedance and transmission/reception sensitivities	163
3.7.2	Homogeneous Euclidean transducers	173
3.7.3	Convergence	175
3.8	Conclusions	176
4	A fractal ultrasonic transducer based on the complement of the Sierpinski gasket	178
4.1	Introduction	178
4.2	Galerkin discretisation	181

4.3	Derivation of the matrix recursions	188
4.3.1	Application of the mechanical boundary conditions	199
4.4	Renormalisation	200
4.4.1	Derivation of the pivotal recursion relationships	202
4.5	Electrical impedance and transmission and reception sensitivities . .	207
4.6	Results	208
4.6.1	Convergence	214
4.7	Conclusions	217
5	Conclusion	219
5.1	Aim	219
5.2	Motivation	219
5.3	Results	220
5.4	Further work	223
A	Appendix	224
A.1	Geometrical and basis function details for fractal generation levels of the SG(3) graph	224
A.2	Geometrical and basis function details for fractal generation levels of the SG(3,4) graph	226
A.3	Geometrical and basis function details for fractal generation levels of the $\overline{\text{SG}}(3)$ graph	229
A.4	The material properties of PZT-5H and polymer HY1300/CY1301 hardset	230
A.5	Parameter values for the front and back mechanical loads and the electrical load	232
A.6	Nomenclature	233

Chapter 1

Introduction

1.1 Motivation and background

Ultrasonic transducers are devices that convert electrical energy into mechanical vibration and conversely can convert mechanical energy into an electrical signal [1–3]. These devices can be used to interrogate a medium by emitting a wave (electrical to mechanical energy) and then listening to the same wave after it has traversed the medium (mechanical to electrical energy). Piezoelectric ultrasonic transducers typically employ composite structures to improve their transmission and reception sensitivities [4–8]. Many biological species produce and receive ultrasound such as moths, bats, dolphins and cockroaches. The man-made transducers tend to have very regular geometry on a single length scale whereas the natural systems exhibit a wide variety of intricate geometries often with resonators over a range of length scales [9–18]. Due to this characteristic, man-made transducers are unable to operate over a wide range of frequencies and hence result in transmission and reception sensitivities with narrow bandwidths. The resolution of ultrasonic imaging is intimately linked to the bandwidth of the transducer, with wide bandwidth devices

corresponding to the best resolution. One approach to designing a new transducer is to experimentally assess its operating ability, however this is very time consuming. Each device requires materials to be sought, cut to the desired shape, bonded to other components such as matching and backing layers, and is expensive and time consuming. In addition, to determine its transmission sensitivity the device has to be immersed in a water tank, input voltages of different frequencies applied, and a hydrophone placed at some distance from the transducer to monitor the output. An assessment can also be made by connecting the transducer to an electrical circuit and measuring its electrical impedance over a range of frequencies. Given the large number of variables present in any design then the use of mathematical models to assess radically new concepts such as that proposed in this thesis is fully justified. Hence, to assess the benefits of having transducers with a wider range of length scales it would be useful to build mathematical models of them. That still leaves the question as to what particular design we should choose for this wideband transducer. One structure whose geometrical components consist of a range of length scales is a fractal [19–21]. Another motivating factor for focusing on a fractal design is that there have been a number of mathematical approaches which describe wave propagation in fractal media in other applications [22–31].

1.2 Literature review

1.2.1 Ultrasound

Ultrasound is an oscillating sound pressure wave with a frequency greater than the upper limit of the human hearing range (20 Hz - 20 KHz). current ultrasound technology ranges from 20 KHz to 10 MHz which is then subdivided into three main regions: low frequency, often used for high power ultrasound (20 - 100 KHz);

intermediate frequency, where medium power ultrasound is often used (100 KHz - 1 MHz); and high frequency, for low power ultrasound applications (1 - 10 MHz) [32–34].

1.2.2 Ultrasound applications

Low frequency, high power ultrasound is used in sonar (SOund Navigation And Ranging) systems [35]. Such systems operate over a very large spatial range in a fluid and mimic the sensor configuration of echo locating bats. Such systems have recently been applied in sensor-based robotics [36]. Specific sonar applications require many space-time processing procedures and associated tradeoffs. To optimize acoustic performance, system analysis and design should reflect the dynamics of the medium, sonar and target [37–41]. The examination of welds is of particular interest to the Non-Destructive Testing (NDT) community, given their role in safety critical structures in nuclear power plants, aero engines, pipelines, etc. They are subject to cyclic loads and, as with any type of bond, constitute the weak point of the structure [42]. Ultrasonic testing is the most commonly used method in NDT and is one which greatly benefits from modelling throughout the design of the ultrasound transducer and the signal processing algorithms in an inspection process [43–45]. Ultrasound techniques are relatively cheap, simple and energy efficient, and have also been used in non-imaging applications and, for example, have become an emerging technology in food processing. Ultrasound technology used in food systems are divided as low and high intensity ultrasound applications. The changes to the physical properties of ultrasound, such as scattering, attenuation and acoustic velocity caused by food materials have also been used in food quality assurance applications [46–50]. Ultrasound has been used in wastewater sludge pretreatment [51,52]. Municipal wastewater sludge, particularly

waste activated sludge (WAS), is more difficult to digest than primary solids due to a rate-limiting cell lysis step. The cell wall and the membrane of prokaryotes are composed of complex organic materials, which are not readily biodegradable. The exposure of the microbial cells to ultrasound energy ruptures the cell wall and membrane and releases the intracellular organics in the bulk solution, which enhances the overall digestibility. Therapeutic ultrasound is defined as the use of ultrasound for the treatment of diseased or injured organs or bodily structures [53,54]. There were many early attempts in the past to use ultrasound for therapy for a variety of applications and these have led to clinical applications which are now used routinely. Such progress has been made possible by a number of factors including advances in transducer design, more accurate measurement and calibration of acoustic power and careful experiments to determine the precise nature of the chemical processes taking place during and following the exposure of tissue to ultrasound [55,56]. Applications of ultrasound in medicine for therapeutic purposes are now well established. Low-power ultrasound of about 1 MHz has been widely applied since the 1950s for physical therapy in conditions such as tendinitis and bursitis [57–59]. In the 1980s, high-pressure-amplitude shock waves came into use for mechanically resolving kidney stones, and lithotripsy rapidly replaced surgery as the most frequent treatment choice [60–62]. The use of ultrasonic energy for therapy continues to expand, and approved applications now include cataract removal [63–65], surgical tissue cutting and hemostasis, transdermal drug delivery [66,67], bone fracture healing [68,69] and prostate cancer [70,71]. There are of course many uses of ultrasound imaging in medicine including the screening in pregnancy and detection of abnormalities in early pregnancy [72–76]. Therapeutic ultrasound typically has well-defined benefits and risks; undesirable bioeffects can occur, including burns from thermal-based therapies and severe hemorrhage

from mechanical-based therapies (eg, lithotripsy) [55,77]. High intensity focused ultrasound (HIFU) offers a promising method for hemorrhage control [78]. An important advantage of HIFU is that it can deliver energy to deep regions of tissue or in difficult to access anatomical regions where hemorrhage is occurring, allowing cauterization at depth of parenchymal tissues [79]. Ultrasound has been used to evaluate musculoskeletal injuries in athletes [80–84]; however, ultrasound applications extend well beyond musculoskeletal conditions, many of which are pertinent to athletes. Ultrasound can potentially be used to assist athletes with monitoring their muscle glycogen stores and the diagnosis of multiple nonmusculoskeletal conditions within sports medicine [85–87]. The first ultrasound scoring system of tendon damage in Rheumatoid Arthritis (RA) has also been developed [88–90]. Currently, there are researchers focusing on using microbubbles as a transportation mechanism for localized drug delivery, specifically in the treatment of various cancers, where high power ultrasound is used to burst the microbubbles and release their contents [91–100]. In many industrial processes high power ultrasound is used to noninvasively agitate a liquid using ultrasonication [101]. Sound waves propagate into the liquid media resulting in alternating high-pressure (compression) and low-pressure (rarefaction) cycles. During rarefaction, high-intensity sonic waves create small vacuum bubbles or voids in the liquid, which then collapse violently (cavitation) during compression, creating very high local temperatures [102–104].

1.2.3 Fractals

For the explanation of a fractal, we will give the following as a working definition. Lets think about a ball of string which can be observed as a three-dimensional ball, at one level of enlargement, or, upon closer examination, as a one-dimensional string. The string tries to fill a three-dimensional space, but cannot complete this

action because of the gaps in the ball of string. As we expand the string, we can define a dimension (fractal dimension) to the object which captures its space-filling capacity at the level of enlargement. In our example, this is going to be a real number that decreases from three to one. Normally it is going to be non-integer that provides a description of how well the object fills the topological dimension with which it is surrounded. The idea of non-integer dimension is one feature of fractals that provides a useful categorization of the geometry. At the core of these objects is the concept of self-similarity.

1.2.4 Fractal applications

In certain circumstances these structures are self-similar. This means that when we zoom in to a subset of the object the resultant image is indistinguishable from the original. This idea can be described by fractal mathematics and the fractal dimension of a structure [105–111]. This quantity conveys the usual meaning of dimension but is regularly not an integer. These concepts have been successfully used in a variety of applications such as brain image analysis and fracture patterns, brain tumour segmentation and detection [112,113], digital imaging [114,115] and image compression [116–118]. The fractals that are observed in nature are known as random or statistical fractals. In these cases, self-similarity relates to an approximate measure, and it only applies over a range of length scales. However, there is a possibility to create a mathematical object identified as a deterministic fractal. The common idea behind this method is to shrink and duplicate an object. However, this process is repeated an unlimited number of times. It is interesting to realise that self-similarity can happen on all scales. These mathematical fractals are essential since they can provide valuable insight into some principles pertaining to their naturally occurring counterparts [19,23]. Computer

simulations deliver a productive way into the study of the interaction of fractal geometry and physical models to test any theoretical results. One area of intensive research is in growth models [119–121]. These simulations follow some basic rules that try to capture some particular physical mechanisms. In the deposition of particles modelling these rules dictate how the particle arrives at the surface, and the fate of the particle afterwards. This model can be advanced by permitting surface diffusion where the particle can move to a local minimum inside a certain radius from its surface impact point [122,123]. The heights of the columns are therefore connected, and the resultant interface is more smooth. Another model that has been extensively examined is Diffusion Limited Aggregation (DLA) [124–127]. In this model, the particles go through a random walk before they come to rest when they come into contact with a substrate. In the simplest model, the particle remains in the same position once it hits the substrate and does not undergo any surface diffusion. The initial configuration (substrate) is typically a single seed and the structure that develops is a fractal.

1.2.5 Fractal graphs

By viewing components in a fractal structure as vertices and then describing the connectivity between these components as edges, a fractal graph can be created. This has certain advantages which includes their amenability to describing wave propagation in these fractal structures by discretising the associated field equation. Researchers have used a Green functions approach for the study of the discrete Schrodinger equation on two families of fractal graphs [128–130]. These are used to study eigenstate localization. More generally they present a method for constructing orbits in closed form for the dynamics of certain rational, planar maps. The mappings arise from renormalisation recursion relations for the Green func-

tions. Renormalisation has certain advantages in that it can be quickly calculate the key elements of the inverse matrices for any fractal generation level. It also, allows analytic insight and allows us to consider steady state solutions (infinite fractal generation level). Its disadvantages are that it only applies to a certain class of fractals (finitely ramified), and one can only get information on the dynamics of the fractal at the boundary vertices. In some cases it is possible to solve analytically the full recursion equations using methods which one uses to solves systems of nonlinear difference equations. This permits a detailed analysis of the scaling properties of the physical processes. Artificial as they may be, regular fractal graphs are attractive for several reasons. One is that statistical or dynamical models defined on such graphs often renormalise exactly [131–135]. Thus model properties on one length scale are connected by exact recursion relations to the same properties on another length scale. The scaling laws are extracted by linearizing the recursions relationships about a fixed point.

1.2.6 Wave propagation in fractal domains

There is of course extensive literature regarding wave propagation in Euclidean media. Therefore, researchers are interested in the effects that fractal geometry can have on the nature of the waveforms. An extensive literature now exists which uses a range of techniques to develop a sound mathematical basis [136–138]. It can be shown that the geometrical properties of the transporting medium has a marked effect upon the propagating wave [139]. The fractal geometries can be classified as one of two types [140]. The first type is where there is a fractal boundary to a Euclidean domain [141]. This interface can act as an impenetrable boundary to some homogeneous transporting medium or as the interface between two different homogeneous phases. Another type is where the transporting medium

itself is fractal, for example, a fractal lattice or a mass fractal [142]. Researchers have investigated a nonlinear diffusion equation on certain unbounded fractal domains [26], and others have discussed reaction-diffusion wave propagation in fractal lattices of infinite generation level [23].

1.2.7 Fractal ultrasonic transducers

There are a few researchers who have modelled a piezoelectric ultrasound transducer with a fractal geometry and compared its operational qualities with that of a homogeneous (Euclidean) design [19–21,143]. Here the fractal that was used to simulate this self-similar transducer was the Sierpinski gasket [19–21,143]. The graph counterpart of the Sierpinski gasket was used to express the electrical and mechanical fields in terms of a *finite difference* methodology. A fractal medium was used as this contains a wide range of length scales and yields to a renormalisation approach. The propagation of an ultrasonic wave in this heterogeneous medium was then analyzed and used to construct expressions for the electrical impedance, and the transmission and reception sensitivities of this device as a function of the driving frequency. The resulting comparison between the fractal transducer and Euclidean transducer showed a marked increase in the reception sensitivity of the fractal device [19,20]. It is worth noting that the use of finite elements as the basis for a study of fractal ultrasound transducers has not been attempted before in the literature.

1.3 Outline of Thesis

The aim of this PhD thesis is to use finite elements to model fractal ultrasonic transducers and to use renormalisation to compare these transducers with tradi-

tional designs. Chapters 2, 3 and 4 constitute the original work in this thesis.

Chapter 2 constructs the first finite element model of a fractal ultrasound transducer consisting of a piezoelectric material and then uses this model to compare its operational qualities with that of a standard (Euclidean) design. The fractal that is used to simulate this self-similar transducer is the Sierpinski gasket. The piezoelectric equations are described and then embedded in this modelling framework via a finite element formulation. The resulting discrete algebraic system then yields to a renormalisation approach. This then facilitates the analytical study of the performance of these fractal devices.

Chapter 3 builds a model of a fractal ultrasound transducer consisting of a piezoelectric-polymer composite and compares this model's operational qualities with that of a standard (simple) design. The governing equations are derived from the general tensor equations. This framework enables the deployment of different parameterisations and a scenario where the displacement acts out of the plane of the graph, with the electric field operating within the plane of the graph, will be examined. We will use a finite element methodology and introduce new basis functions to express the wave fields within the graph. This Galerkin approach leads to a discrete formulation that lends itself to a renormalisation approach. The Sierpinski gasket will be used for the simulation of a self-similar transducer. Such an ultrasonic transducer would start with an equilateral triangle of piezoelectric crystal. This equilateral triangle is composed of four identical equilateral sub-triangles whose side length is half of the original. The first generation ($n = 1$) would be obtained by replacing the central sub-triangle by a polymer material. This process is then repeated for several generations with the removed sub-triangles from the smallest

triangles being filled with a polymer. As in Chapter 2 a comparison between this device and an equivalent standard composite design is undertaken.

Chapter 4 studies the complement (or dual) of the standard Sierpinski gasket. Using the complement is vital as it has a range of triangle sizes whereas the Sierpinski gasket is composed of triangles of the same size for a given fractal generation level. It therefore has a much stronger coupling to a wide range of length scales and resonators. This appears to be the first time this dual graph has been constructed and hence the first time that any form of wave propagation in this structure has been considered. The dual graph is introduced and constructed by a process which starts from the order $n = 1$ design (which consists of four piezoelectric triangles). As in Chapter 2 the finite element model of a fractal ultrasound transducer consisting of a piezoelectric material is used to compare the fractal design (using the renormalisation derivation) with a conventional standard (Euclidean) design.

Chapter 2

A fractal ultrasonic transducer based on the Sierpinski gasket

2.1 Introduction

This chapter constructs a model of a fractal ultrasound transducer and then uses this model to compare its operational qualities with that of a standard (Euclidean) design. The fractal that will be used in this chapter to simulate this self-similar transducer is the Sierpinski gasket [144]. Such an ultrasonic transducer would start with an equilateral triangle of piezoelectric crystal, and the next generation ($n = 1$) would be obtained by replacing this by three copies of itself, each of which being half the size of the original triangle. This process is then repeated for several generations (see Figure 2.1). The degree of a vertex is the number of edges incident to it, so the Sierpinski gasket graph of degree 3, SG(3), is the graph counterpart of the Sierpinski gasket [145] (see Figure 2.2). The graph is constructed by a process which starts from the Sierpinski gasket of order $n = 1$ (which consists of three piezoelectric triangles), assigns a vertex to the centre of

each of these triangles and, by connecting these vertices together with edges, the SG(3) graph at generation level $n = 1$ is constructed. The graph has side length L units which remains constant as the generation level n increases. Therefore, as n increases, the length of the edge between adjacent vertices tends to zero and in this limit the graph will perfectly match the space filling properties of the original Sierpinski gasket [7]. The total number of vertices is $N = 3^n$ and $h^{(n)} = L/(2^n - 1)$ is the edge length of the fractal graph. The vertex degree is 3 apart from the boundary vertices (input/output vertices) which have degree 2 and $M = 3(3^n - 1)/2$ denotes the total number of edges. These boundary vertices will be used to interact with external loads (both electrical and mechanical) and so we introduce fictitious vertices A, B and C to accommodate these interfacial boundary conditions (see Figures 2.4 and 2.5). Let us denote by Ω the set of points lying on the edges or vertices of SG(3) and denote the region's boundary by $\partial\Omega$.

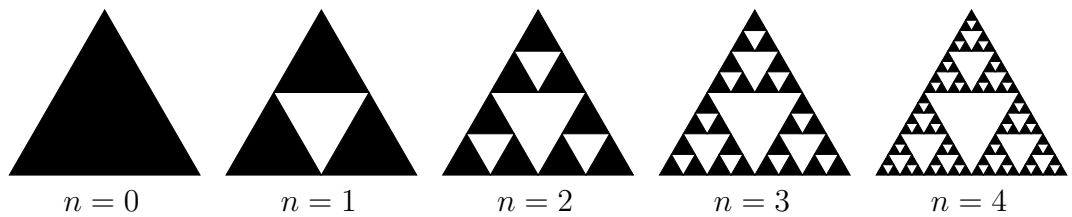


Figure 2.1: The first few generations of the Sierpinski gasket.

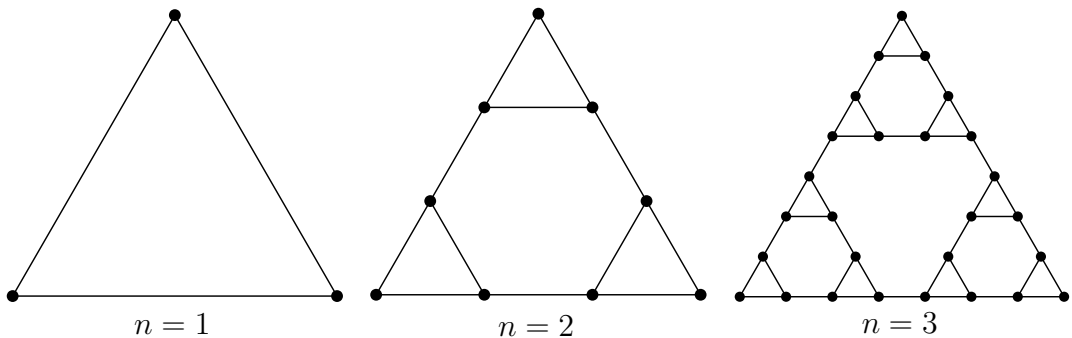


Figure 2.2: The first few generations of the Sierpinski gasket graph SG(3).

2.2 Model derivation

It will be useful to develop a more general model consisting of two phases for the work in Chapter 3 as this model reduces to the single phase (piezoelectric material only) to be studied first in this chapter. The graph represents the vibrations of piezoelectric and polymer materials (here the focus will be on PZT-5H and HY1300/CY1301 hardset respectively [2,146]) that have been manufactured to form a Sierpinski gasket. The interplay between the electrical and mechanical behaviour of the graph vertices is described by the piezoelectric constitutive equations [2,3]

$$T_{ij} = c_{ijkl}S_{kl} - e_{kij}E_k, \quad (2.2.1)$$

$$D_i = e_{ikl}S_{kl} + \varepsilon_{ik}E_k, \quad (2.2.2)$$

where T_{ij} is the stress tensor, c_{ijkl} is the stiffness tensor, S_{kl} is the strain tensor, e_{kij} is the piezoelectric tensor, E_k is the electric field vector, D_i is the electrical displacement tensor and ε_{ik} is the permittivity tensor (where the Einstein summation convention is adopted). The strain tensor is related to the displacement gradients $u_{i,j}$ by

$$S_{ij} = \frac{u_{i,j} + u_{j,i}}{2}, \quad (2.2.3)$$

and the electric field vector is related to the electric potential ϕ via

$$E_i = -\phi_{,i}.$$

The dynamics of the piezoelectric material is then governed by

$$\rho_T \ddot{u}_i = T_{ji,j}, \quad (2.2.4)$$

subject to Gauss' law

$$D_{i,i} = 0 \quad (2.2.5)$$

where ρ_T is the density and u_i is the component of displacement in the direction of the i^{th} basis vector. So, combining equations (2.2.4) and (2.2.1) gives

$$\rho_T \ddot{u}_i = c_{jikl} S_{kl,j} - e_{kji} E_{k,j}. \quad (2.2.6)$$

Combining equations (2.2.5) and (2.2.2) gives

$$D_{i,i} = e_{ikl} S_{kl,i} + \varepsilon_{ik} E_{k,i} = 0. \quad (2.2.7)$$

We will restrict attention to the out of plane displacement only (a horizontal shear wave) by stipulating that

$$\underline{u} = (0, 0, u_3(x_1, x_2, t)). \quad (2.2.8)$$

This choice of parameterisation will simplify the algebra significantly and will lead to a scalar dynamical equation. It also will allow us to consider the transverse vibrations of the device which is the primary engineering interest in its application. There are of course other parameterisations that could be chosen and a suitable choice would also afford the study of the vector elastodynamical equations. So, since only $u_{3,1}$ and $u_{3,2}$ are nonzero, then equation (2.2.6) gives

$$\rho_T \ddot{u}_3 = c_{13kl} S_{kl,1} + c_{23kl} S_{kl,2} - e_{kj3} E_{k,j}. \quad (2.2.9)$$

From equation (2.2.3) we get

$$S_{ij} = \begin{cases} \frac{1}{2}u_{3,1} & i = 1, j = 3 \text{ or } i = 3, j = 1 \\ \frac{1}{2}u_{3,2} & i = 2, j = 3 \text{ or } i = 3, j = 2 \\ 0 & \text{otherwise,} \end{cases}$$

so that equation (2.2.9) gives

$$\rho_T \ddot{u}_3 = c_{1331}u_{3,11} + c_{1332}u_{3,21} + c_{2331}u_{3,12} + c_{2332}u_{3,22} - e_{kj3}E_{k,j}.$$

The piezoelectric material is polarised in the x_3 direction and so, from the properties of PZT-5H (see Appendix A.4), then

$$\rho_T \ddot{u}_3 = c_{44}^T(u_{3,11} + u_{3,22}) - e_{kj3}E_{k,j}$$

since $c_{55}^T = c_{44}^T$ and the Voigt notation has been used. Now if $\underline{E} = (E_1(x_1, x_2), E_2(x_1, x_2), 0)$ then

$$\rho_T \ddot{u}_3 = c_{44}^T(u_{3,11} + u_{3,22}) - e_{113}E_{1,1} - e_{123}E_{1,2} - e_{213}E_{2,1} - e_{223}E_{2,2}.$$

That is

$$\rho_T \ddot{u}_3 = c_{44}^T(u_{3,11} + u_{3,22}) - e_{15}E_{1,1} - e_{14}E_{1,2} - e_{25}E_{2,1} - e_{24}E_{2,2}.$$

Then

$$\rho_T \ddot{u}_3 = c_{44}^T(u_{3,11} + u_{3,22}) - e_{24}(E_{1,1} + E_{2,2}), \quad (2.2.10)$$

since $e_{15} = e_{24}$ and $e_{14} = e_{25} = 0$. From equation (2.2.7) we get, for PZT-5H,

$$e_{113}S_{13,1} + e_{131}S_{31,1} + e_{223}S_{23,2} + e_{232}S_{32,2} + \varepsilon_{11}^T E_{1,1} + \varepsilon_{22}^T E_{2,2} = 0.$$

That is

$$e_{15}u_{3,11} + e_{24}u_{3,22} + \varepsilon_{11}^T E_{1,1} + \varepsilon_{22}^T E_{2,2} = 0.$$

Therefore

$$e_{24}(u_{3,11} + u_{3,22}) + \varepsilon_{11}^T (E_{1,1} + E_{2,2}) = 0$$

since $\varepsilon_{11}^T = \varepsilon_{22}^T$ for PZT-5H. So we get

$$E_{1,1} + E_{2,2} = -\frac{e_{24}}{\varepsilon_{11}^T}(u_{3,11} + u_{3,22}).$$

Substituting this into equation (2.2.10) gives

$$\rho_T \ddot{u}_3 = c_{44}^T (u_{3,11} + u_{3,22}) + \frac{e_{24}^2}{\varepsilon_{11}^T} (u_{3,11} + u_{3,22}).$$

That is

$$\rho_T \ddot{u}_3 = \mu_T (u_{3,11} + u_{3,22}).$$

A similar analysis can be conducted for the polymer phase. The dynamical equation in each phase can be written as

$$\ddot{u}_3 = c^2 \nabla^2 u_3$$

subject to continuity of displacement and force at the boundary with the mechanical loads, where c is the shear wave velocity defined as

$$c = \begin{cases} c_T = \sqrt{\mu_T/\rho_T}, & \text{PZT-5H} \\ c_P = \sqrt{\mu_P/\rho_P}, & \text{polymer} \end{cases} \quad (2.2.11)$$

$\nabla^2 = \partial^2/\partial x_1^2 + \partial^2/\partial x_2^2$, $\mu_T = c_{44}^T + e_{24}^2/\varepsilon_{11}^T$ is the piezoelectrically stiffened shear modulus in the ceramic phase, $\mu_P = c_{44}^P$ is the shear modulus of the polymer, $\rho_{T/P}$ is the density in the T -piezoelectric / P -polymer phase, e_{24} is an element of the piezoelectric tensor and ε_{11}^T is an element of the permittivity tensor of PZT-5H. The polymer's material tensors are given in the Appendix A.4 and the derivation c_P follows similar lines to these for the piezoelectric material. Note that in this chapter we will study a single phase transducer (piezoelectric material only) and hence $c = c_T$. We impose the initial conditions $u_3(\underline{x}, 0) = \dot{u}_3(\underline{x}, 0) = 0$ and the boundary conditions of continuity of displacement and force on $\partial\Omega$.

By introducing the non-dimensionalised variable $\theta = c_T t/h$ then (dropping the subscript on u)

$$\frac{\partial^2 u}{\partial \theta^2} = h^2 \nabla^2 u. \quad (2.2.12)$$

Applying the Laplace transform $\mathcal{L} : \theta \rightarrow q$ then gives

$$q^2 \bar{u} = h^2 \nabla^2 \bar{u}. \quad (2.2.13)$$

We will seek a weak solution $\bar{u} \in H^1(\Omega)$ where on the boundary $\bar{u} = \bar{u}_{\partial\Omega} \in H^1(\partial\Omega)$. Now multiplying by a test function $w \in H_B^1(\Omega)$, where $H_B^1(\Omega) := \{w \in H^1(\Omega) : w = 0 \text{ on } \partial\Omega\}$, integrating over the region Ω , and using Green's first identity $\int_{\Omega} \psi \nabla^2 \phi \, dv = \oint_{\partial\Omega} \psi (\nabla \phi \cdot \underline{n}) \, dr - \int_{\Omega} \nabla \phi \cdot \nabla \psi \, dv$, where \underline{n} is the outward pointing

unit normal of surface element dr , gives

$$\int_{\Omega} q^2 \bar{u} w d\underline{x} = h^2 \oint_{\partial\Omega} w(\nabla\bar{u} \cdot \underline{n}) dr - h^2 \int_{\Omega} \nabla\bar{u} \cdot \nabla w d\underline{x}.$$

Now $h^2 \oint_{\partial\Omega} w(\nabla\bar{u} \cdot \underline{n}) dr$ is zero since $w = 0$ on $\partial\Omega$ and so, we seek $\bar{u} \in H^1(\Omega)$ such that

$$q^2 \int_{\Omega} \bar{u} w d\underline{x} = -h^2 \int_{\Omega} \nabla\bar{u} \cdot \nabla w d\underline{x}$$

where $w \in H_B^1(\Omega)$.

2.3 Galerkin discretisation

Using a standard Galerkin method we replace $H^1(\Omega)$ and $H_B^1(\Omega)$ by the finite dimensional subspaces S_S and $S_B = S_S \cap H_B^1(\Omega)$. Let $U_B \in S_S$ be a function that approximates $\bar{u}_{\partial\Omega}$ on $\partial\Omega$, then the discretised problem involves finding $\bar{U} \in S_S$ such that

$$q^2 \int_{\Omega} \bar{U} W d\underline{x} = -h^2 \int_{\Omega} \nabla\bar{U} \cdot \nabla W d\underline{x},$$

where W is the test function expressed in this finite dimensional space. Let $\{\phi_1, \phi_2, \dots, \phi_N\}$ form a basis of S_B and set $W = \phi_j$, then

$$q^2 \int_{\Omega} \bar{U} \phi_j d\underline{x} = -h^2 \int_{\Omega} \nabla\bar{U} \cdot \nabla\phi_j d\underline{x}, \quad j = 1, \dots, N. \quad (2.3.1)$$

Furthermore, let ϕ_I , $I = \{N + 1, N + 2, N + 3\}$ form a basis for the boundary vertices and let

$$\bar{U} = \sum_{i=1}^N U_i \phi_i + \sum_{i \in I} U_{B_i} \phi_i. \quad (2.3.2)$$

Hence, equation (2.3.1) becomes

$$\begin{aligned} & \sum_{i=1}^N \left(\int_{\Omega} (q^2 \phi_i \phi_j + h^2 \nabla \phi_i \cdot \nabla \phi_j) d\underline{x} \right) U_i = \\ & - \sum_{i \in I} \left(\int_{\Omega} (q^2 \phi_i \phi_j + h^2 \nabla \phi_i \cdot \nabla \phi_j) d\underline{x} \right) U_{B_i} \end{aligned} \quad (2.3.3)$$

where $j \in \{1, 2, \dots, N\}$. That is

$$A_{ji} U_i = b_j \quad (2.3.4)$$

where

$$A_{ji} = q^2 \int_{\Omega} \phi_i \phi_j d\underline{x} + h^2 \int_{\Omega} \nabla \phi_i \cdot \nabla \phi_j d\underline{x}, \quad (2.3.5)$$

and

$$b_j = - \sum_{i \in I} \left(\int_{\Omega} (q^2 \phi_i \phi_j + h^2 \nabla \phi_i \cdot \nabla \phi_j) d\underline{x} \right) U_{B_i}. \quad (2.3.6)$$

It is important to now explicitly record the fractal generation level n and so equation (2.3.5) can be written

$$A_{ji}^{(n)} = q^2 H_{ji}^{(n)} + h^2 K_{ji}^{(n)}, \quad (2.3.7)$$

where

$$H_{ji}^{(n)} = \int_{\Omega} (\phi_j \phi_i) d\underline{x} \quad (2.3.8)$$

and

$$K_{ji}^{(n)} = \int_{\Omega} (\nabla \phi_j \cdot \nabla \phi_i) d\underline{x}. \quad (2.3.9)$$

The graph basis function at vertex \underline{x}_j is chosen to be (see Figure 2.3)

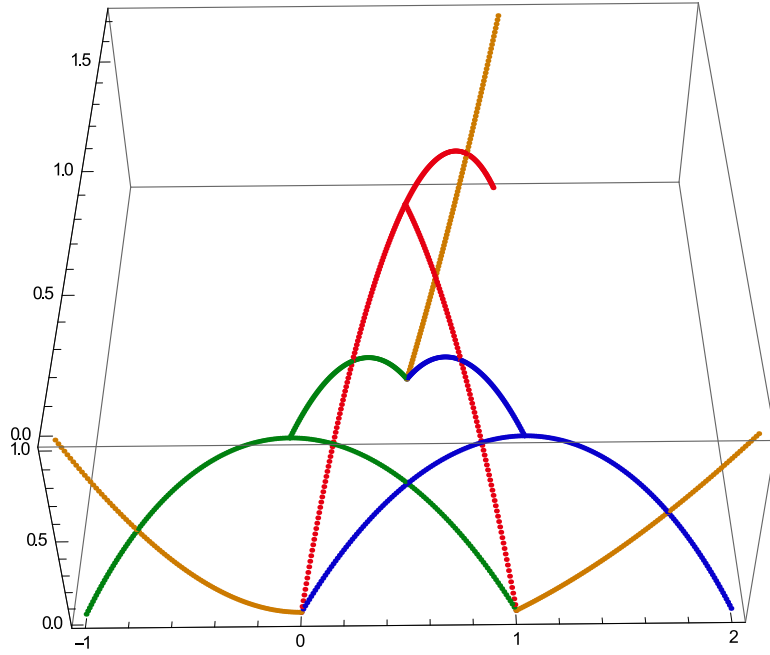


Figure 2.3: The graph basis function ϕ_j at vertex $\underline{x}_j = (x_j, y_j)$.

$$\phi_j(x, y) = \begin{cases} a + bx + cy + d(x^2 + y^2) & j \in \{1, \dots, N\} \\ a + d(x^2 + y^2) & j \in I, \end{cases} \quad (2.3.10)$$

where $(x, y) \in \Omega$ and $a, b, c, d \in \mathbb{R}$ are coefficients to be determined. Hence

$$\nabla \phi_j(x, y) = \begin{cases} (b + 2dx, c + 2dy) & j \in \{1, \dots, N\} \\ (2dx, 2dy) & j \in I. \end{cases} \quad (2.3.11)$$

Futhermore, the ϕ_j are defined as localised basis functions such that

$$\phi_j(x, y) = \begin{cases} 1 & \text{if } (x, y) = (x_j, y_j) \\ 0 & \text{if } (x, y) = \text{coordinates of vertices adjacent to vertex } j, \end{cases} \quad (2.3.12)$$

and $\phi_j(x, y) = 0$ at all points which do not lie in the edges adjacent to vertex j . For each generation level of the SG(3) graph the coordinates of the vertices

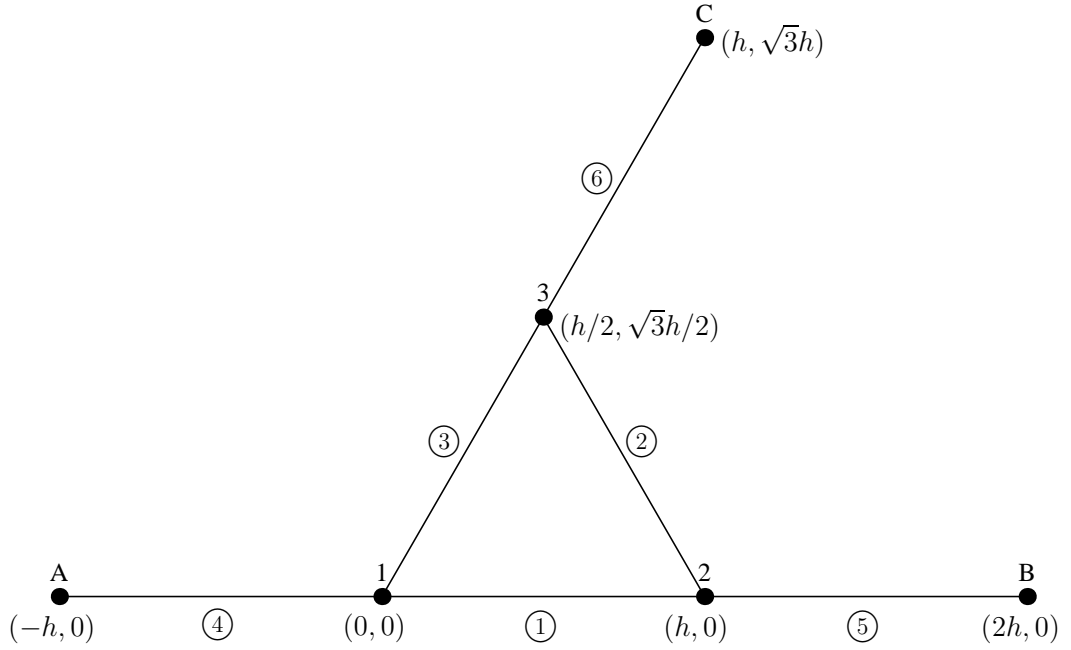


Figure 2.4: The Sierpinski Gasket graph $SG(3)$ at generation level $n = 1$. Vertices 1, 2 and 3 are the input/output vertices, and vertices A (or 4), B (or 5) and C (or 6) are fictitious vertices used to accommodate the boundary conditions. The graph has 6 elements (circled numbers), with two vertices adjacent to each element.

are known (see the Appendix A.1 for a detailed description for $n = 1$ and $n = 2$). Using equation (2.3.12) the coefficients in equation (2.3.10) can be determined (see the Appendix A.1 for the values of these coefficients for $n = 1$ and $n = 2$). From equation (2.3.10) the equation (2.3.8) can be written as, for $e \in \{1, \dots, M\}$,

$$\begin{aligned}
{}^e H_{ji}^{(n)} &= \int_e (a_j + b_j x + c_j y + d_j (x^2 + y^2)) (a_i + b_i x + c_i y + d_i (x^2 + y^2)) d\underline{x} \\
&= \int_e \left(a_j a_i + (a_j b_i + a_i b_j) x + (a_j c_i + a_i c_j) y + (c_j b_i + c_i b_j) x y + b_j b_i x^2 \right. \\
&\quad \left. + c_j c_i y^2 + (a_j d_i + a_i d_j) (x^2 + y^2) + (b_j d_i + b_i d_j) x (x^2 + y^2) \right. \\
&\quad \left. + (c_j d_i + c_i d_j) y (x^2 + y^2) + d_j d_i (x^2 + y^2)^2 \right) d\underline{x}. \tag{2.3.13}
\end{aligned}$$

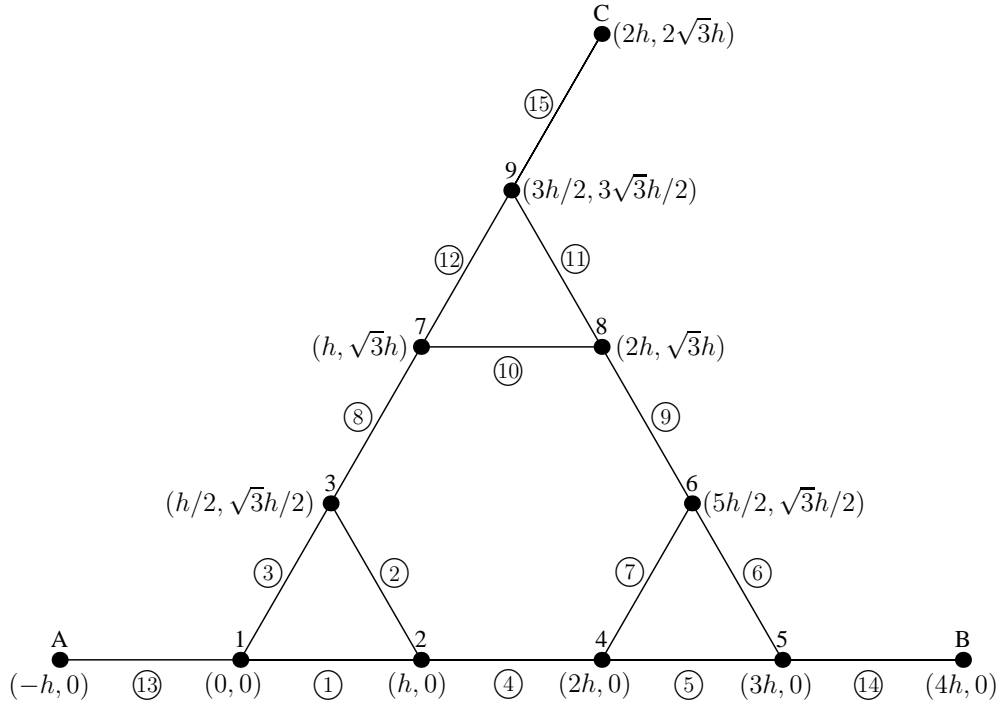


Figure 2.5: The Sierpinski Gasket graph $SG(3)$ at generation level $n = 2$. Vertices A (or 10), B (or 11) and C (or 12) are fictitious vertices used to accommodate the boundary conditions. The graph has 15 elements (circled numbers), with two vertices adjacent to each element.

For a particular element lying between vertex i and vertex j the isoparametric representation, given by

$$(x(s), y(s)) = ((x_j - x_i)s + x_i, (y_j - y_i)s + y_i) \quad (2.3.14)$$

is employed (see Figure 2.6), where $s_1 = 0$ and $s_2 = 1$ and $d\mathbf{x} = h ds$. Substituting

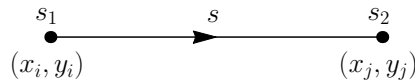


Figure 2.6: An isoparametric element (edge) between vertex (x_i, y_i) and vertex (x_j, y_j) .

this equation into equation (2.3.13) gives, for $e \in \{1, \dots, M\}$,

$${}^e H_{ji}^{(n)} = h \begin{cases} \int_0^1 (s^2 - 1)^2 ds & = \frac{8}{15} & \text{if } j = i = p \\ \int_0^1 (s^2 - 1)(s - 2)s ds & = \frac{11}{30} & \text{if } j, i \in \{p, q\}, j \neq i \\ \int_0^1 (s - 2)^2 s^2 ds & = \frac{8}{15} & \text{if } j = i = q \\ 0 & & \text{otherwise} \end{cases}$$

where element e connects vertex p to vertex q . For the boundary elements $e \in \{M + 1, M + 2, M + 3\}$,

$${}^e H_{ji}^{(n)} = h \begin{cases} \int_0^1 (s^2 - 1)^2 ds & = \frac{8}{15} & \text{if } j = i = q \\ 0 & & \text{otherwise} \end{cases}$$

where q is the corner vertex of the SG(3) graph connected to element e . Assembling the full matrix in equation (2.3.8) gives, for generation level $n = 1$

$$H_{ji}^{(1)} = h \begin{bmatrix} \frac{8}{5} & \frac{11}{30} & \frac{11}{30} \\ \frac{11}{30} & \frac{8}{5} & \frac{11}{30} \\ \frac{11}{30} & \frac{11}{30} & \frac{8}{5} \end{bmatrix} = h \hat{H}_{ji}^{(1)}, \quad (2.3.15)$$

and at generation level $n = 2$,

$$H_{ji}^{(2)} = h \begin{bmatrix} \frac{8}{5} & \frac{11}{30} & \frac{11}{30} & 0 & 0 & 0 & 0 & 0 & 0 \\ \frac{11}{30} & \frac{8}{5} & \frac{11}{30} & \frac{11}{30} & 0 & 0 & 0 & 0 & 0 \\ \frac{11}{30} & \frac{11}{30} & \frac{8}{5} & 0 & 0 & 0 & \frac{11}{30} & 0 & 0 \\ 0 & \frac{11}{30} & 0 & \frac{8}{5} & \frac{11}{30} & \frac{11}{30} & 0 & 0 & 0 \\ 0 & 0 & 0 & \frac{11}{30} & \frac{8}{5} & \frac{11}{30} & 0 & 0 & 0 \\ 0 & 0 & 0 & \frac{11}{30} & \frac{11}{30} & \frac{8}{5} & 0 & \frac{11}{30} & 0 \\ 0 & 0 & \frac{11}{30} & 0 & 0 & 0 & \frac{8}{5} & \frac{11}{30} & \frac{11}{30} \\ 0 & 0 & 0 & 0 & 0 & \frac{11}{30} & \frac{11}{30} & \frac{8}{5} & \frac{11}{30} \\ 0 & 0 & 0 & 0 & 0 & 0 & \frac{11}{30} & \frac{11}{30} & \frac{8}{5} \end{bmatrix}. \quad (2.3.16)$$

So, from equations (2.3.15) and (2.3.16), we can write matrix H , for $n \geq 2$ as

$$H_{ji}^{(n)} = h \begin{bmatrix} \hat{H}_{ji}^{(n-1)} & \frac{11}{30}V_{ji}^{(n)} & \frac{11}{30}V_{ji}^{(n)} \\ \frac{11}{30}V_{ji}^{(n)} & \hat{H}_{ji}^{(n-1)} & \frac{11}{30}V_{ji}^{(n)} \\ \frac{11}{30}V_{ji}^{(n)} & \frac{11}{30}V_{ji}^{(n)} & \hat{H}_{ji}^{(n-1)} \end{bmatrix},$$

where $\hat{H}_{ji}^{(n-1)} = H_{ji}^{(n-1)}/h$ and $V_{ji}^{(n)} = \mathbb{1}_{D^{(n)}}(ji)$ is the adjacency matrix for the subgraph of $\text{SG}^{(n)}(3)$ consisting of the edges $D^{(n)}$ that connect each of the three $\text{SG}^{(n-1)}(3)$ graphs (for $n = 2$, $D^{(2)} = \{\{2, 4\}, \{3, 7\}, \{6, 8\}\}$ and for $n = 3$, $D^{(3)} = \{\{5, 10\}, \{9, 19\}, \{18, 23\}\}$ (see Figures 2.4 and 2.5)). (where $\mathbb{1}_{\{A\}}(a)$ is

the indicator function which equals 1 if $a \in A$, and 0 otherwise). That is,

$$H_{ji}^{(n)} = h \left(\bar{H}_{ji}^{(n-1)} + \frac{11}{30} V_{ji}^{(n)} \right),$$

where $\bar{H}_{ji}^{(n-1)}$ is a block diagonal matrix consisting of three blocks of matrix $\hat{H}_{ji}^{(n-1)}$.

Similarly, from equation (2.3.11) the equation (2.3.9) can be written as

$$\begin{aligned} {}^e K_{ji}^{(n)} &= \int_e (b_j + 2d_j x, c_j + 2d_j y) \cdot (b_i + 2d_i x, c_i + 2d_i y) d\underline{x}, \\ &= \int_e \left(b_i b_j + 2(d_j b_i + d_i b_j) x + 4d_i d_j x^2 + c_i c_j + 2(d_i c_j + d_j c_i) y \right. \\ &\quad \left. + 4d_i d_j y^2 \right) d\underline{x}. \end{aligned} \quad (2.3.17)$$

Substituting equation (2.3.14) into equation (2.3.17) gives, for $e = 1, \dots, M$

$${}^e K_{ji}^{(n)} = \frac{4}{h} \begin{cases} \int_0^1 s^2 ds & = \frac{1}{3} & \text{if } j = i = p \\ \int_0^1 s(s-1) ds & = \frac{-1}{6} & \text{if } j, i \in \{p, q\}, j \neq i \\ \int_0^1 (s-1)^2 ds & = \frac{1}{3} & \text{if } j = i = q \\ 0 & & \text{otherwise} \end{cases} \quad (2.3.18)$$

where element e connects vertex p to vertex q . For the boundary elements $e \in \{M+1, M+2, M+3\}$ then equation (2.3.17) becomes

$${}^e K_{ji}^{(n)} = \frac{4}{h} \begin{cases} \int_0^1 s^2 ds & = \frac{1}{3} & \text{if } j = i = q \\ 0 & & \text{otherwise} \end{cases}, \quad (2.3.19)$$

where q is the corner vertex of the SG(3) graph connected to element e (for $n = 1$, $q \in \{1, 2, 3\}$, and for $n = 2$, $q \in \{1, 5, 9\}$). Note that there is only one combination of basis functions in these exterior piezoelectric elements since the left hand side of equation (2.3.3) does not involve the basis functions at boundary vertices I

denoted by ϕ_I . Combining equations (2.3.18) and (2.3.19) to assemble the full matrix in equation (2.3.9) gives, for generation level $n = 1$,

$$K_{ji}^{(1)} = \frac{1}{h} \begin{bmatrix} 4 & \frac{-2}{3} & \frac{-2}{3} \\ \frac{-2}{3} & 4 & \frac{-2}{3} \\ \frac{-2}{3} & \frac{-2}{3} & 4 \end{bmatrix} = \frac{1}{h} \hat{K}_{ji}^{(1)}, \quad (2.3.20)$$

and at generation level $n = 2$,

$$K_{ji}^{(2)} = \frac{1}{h} \begin{bmatrix} 4 & \frac{-2}{3} & \frac{-2}{3} & 0 & 0 & 0 & 0 & 0 & 0 \\ \frac{-2}{3} & 4 & \frac{-2}{3} & \frac{-2}{3} & 0 & 0 & 0 & 0 & 0 \\ \frac{-2}{3} & \frac{-2}{3} & 4 & 0 & 0 & 0 & \frac{-2}{3} & 0 & 0 \\ \hline 0 & \frac{-2}{3} & 0 & 4 & \frac{-2}{3} & \frac{-2}{3} & 0 & 0 & 0 \\ 0 & 0 & 0 & \frac{-2}{3} & 4 & \frac{-2}{3} & 0 & 0 & 0 \\ 0 & 0 & 0 & \frac{-2}{3} & \frac{-2}{3} & 4 & 0 & \frac{-2}{3} & 0 \\ \hline 0 & 0 & \frac{-2}{3} & 0 & 0 & 0 & 4 & \frac{-2}{3} & \frac{-2}{3} \\ 0 & 0 & 0 & 0 & 0 & \frac{-2}{3} & \frac{-2}{3} & 4 & \frac{-2}{3} \\ 0 & 0 & 0 & 0 & 0 & 0 & \frac{-2}{3} & \frac{-2}{3} & 4 \end{bmatrix}. \quad (2.3.21)$$

So, from equations (2.3.20) and (2.3.21), we can write matrix K , for $n \geq 2$ as

$$K_{ji}^{(n)} = \frac{1}{h} \begin{bmatrix} \hat{K}_{ji}^{(n-1)} & \frac{-2}{3}V_{ji}^{(n)} & \frac{-2}{3}V_{ji}^{(n)} \\ \frac{-2}{3}V_{ji}^{(n)} & \hat{K}_{ji}^{(n-1)} & \frac{-2}{3}V_{ji}^{(n)} \\ \frac{-2}{3}V_{ji}^{(n)} & \frac{-2}{3}V_{ji}^{(n)} & \hat{K}_{ji}^{(n-1)} \end{bmatrix},$$

where $\hat{K}_{ji}^{(n-1)} = h K_{ji}^{(n-1)}$. That is,

$$K_{ji}^{(n)} = \frac{1}{h} \left(\tilde{K}_{ji}^{(n-1)} - \frac{2}{3}V_{ji}^{(n)} \right),$$

where $\tilde{K}_{ji}^{(n-1)}$ is a block diagonal matrix consisting of three blocks of matrix $\hat{K}_{ji}^{(n-1)}$.

Combining equations (2.3.20) and (2.3.15) gives equation (2.3.7) as

$$A_{ji}^{(1)} = h \begin{bmatrix} \alpha & \beta & \beta \\ \beta & \alpha & \beta \\ \beta & \beta & \alpha \end{bmatrix} = h \hat{A}_{ji}^{(1)}, \quad (2.3.22)$$

where $\alpha = (8/5)q^2 + 4$ and $\beta = (11/30)q^2 - 2/3$. Similarly, for generation level $n = 2$,

$$A_{ji}^{(2)} = h \begin{bmatrix} \alpha & \beta & \beta & 0 & 0 & 0 & 0 & 0 & 0 \\ \beta & \alpha & \beta & \beta & 0 & 0 & 0 & 0 & 0 \\ \beta & \beta & \alpha & 0 & 0 & 0 & \beta & 0 & 0 \\ \hline 0 & \beta & 0 & \alpha & \beta & \beta & 0 & 0 & 0 \\ 0 & 0 & 0 & \beta & \alpha & \beta & 0 & 0 & 0 \\ 0 & 0 & 0 & \beta & \beta & \alpha & 0 & \beta & 0 \\ \hline 0 & 0 & \beta & 0 & 0 & 0 & \alpha & \beta & \beta \\ 0 & 0 & 0 & 0 & 0 & \beta & \beta & \alpha & \beta \\ 0 & 0 & 0 & 0 & 0 & 0 & \beta & \beta & \alpha \end{bmatrix}. \quad (2.3.23)$$

So, from equations (2.3.22) and (2.3.23), we can write matrix A , for $n \geq 2$ as

$$A_{ji}^{(n)} = h \begin{bmatrix} \hat{A}_{ji}^{(n-1)} & \beta V_{ji}^{(n)} & \beta V_{ji}^{(n)} \\ \hline \beta V_{ji}^{(n)} & \hat{A}_{ji}^{(n-1)} & \beta V_{ji}^{(n)} \\ \hline \beta V_{ji}^{(n)} & \beta V_{ji}^{(n)} & \hat{A}_{ji}^{(n-1)} \end{bmatrix},$$

where $\hat{A}_{ji}^{(n-1)} = A_{ji}^{(n-1)}/h$. That is,

$$A_{ji}^{(n)} = h \left(\bar{A}_{ji}^{(n-1)} + \beta V_{ji}^{(n)} \right), \quad (2.3.24)$$

where $\tilde{A}_{ji}^{(n-1)}$ is a block diagonal matrix consisting of three blocks of matrix $\hat{A}_{ji}^{(n-1)}$.

A similar treatment can be given to equation (2.3.6) to give (where $m = (N+1)/2$)

$$b_j^{(n)} = \begin{cases} - \left(\int_{\epsilon_{M+1}} (q^2 \phi_{N+1} \phi_j + h^2 \nabla \phi_{N+1} \cdot \nabla \phi_j) d\mathbf{x} \right) U_A, & j = 1 \\ - \left(\int_{\epsilon_{M+2}} (q^2 \phi_{N+2} \phi_j + h^2 \nabla \phi_{N+2} \cdot \nabla \phi_j) d\mathbf{x} \right) U_B, & j = m \\ - \left(\int_{\epsilon_{M+3}} (q^2 \phi_{N+3} \phi_j + h^2 \nabla \phi_{N+3} \cdot \nabla \phi_j) d\mathbf{x} \right) U_C, & j = N \\ 0 & \text{otherwise,} \end{cases} \quad (2.3.25)$$

where $M+1, M+2$ and $M+3$ are the set of edges M_I , U_A, U_B and U_C are the mechanical displacements at the fictitious vertices A, B and C respectively.

From equation (2.3.25) let us start to find $b_1^{(n)}$ at element $e = M+1$ (see Fig-

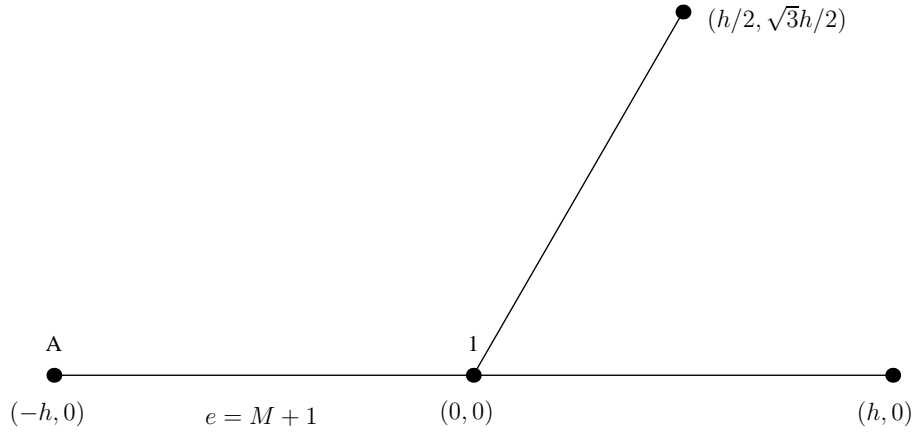


Figure 2.7: The boundary element for $e = M+1$

ure 2.7), which is connected between vertex A at $(x_A, y_A) = (-h, 0)$ and vertex 1 at $(x_1, y_1) = (0, 0)$. From equation (2.3.14) we get $(x(s), y(s)) = ((x_1 - x_A)s + x_A, (y_1 - y_A)s + y_A) = (h(s-1), 0)$ and $d\mathbf{x} = h ds$, gives

$$b_1^{(n)} = -h \left(\int_{M+1} (q^2 \phi_A \phi_1 + h^2 \nabla \phi_A \cdot \nabla \phi_1) ds \right) U_A. \quad (2.3.26)$$

From equation (2.3.10) the basis functions at vertex A in element $e = M + 1$ is

$$\phi_A(x, y) = \frac{x^2 + y^2}{h^2} \quad (2.3.27)$$

and at vertex 1 is

$$\phi_1(x, y) = 1 - \frac{x^2 + y^2}{h^2}. \quad (2.3.28)$$

Substituting equation (2.3.14) into equations (2.3.27) and (2.3.28) gives

$$\phi_A(x(s), y(s)) = \phi_A(h(s-1), 0) = (s-1)^2 \quad (2.3.29)$$

and

$$\phi_1(x(s), y(s)) = \phi_1(h(s-1), 0) = (2-s)s. \quad (2.3.30)$$

From equation (2.3.11), equations (2.3.27) and (2.3.28) gives

$$\nabla\phi_A(x, y) = \left(\frac{2x}{h^2}, \frac{2y}{h^2} \right) \quad (2.3.31)$$

and

$$\nabla\phi_1(x, y) = \left(\frac{-2x}{h^2}, \frac{-2y}{h^2} \right). \quad (2.3.32)$$

Substituting equation (2.3.14) into equations (2.3.31) and (2.3.32) gives

$$\nabla\phi_A(x(s), y(s)) = \left(\frac{2(s-1)}{h}, 0 \right) \quad (2.3.33)$$

and

$$\nabla\phi_1(x(s), y(s)) = \left(\frac{2(1-s)}{h}, 0 \right). \quad (2.3.34)$$

Substituting equations (2.3.29), (2.3.30), (2.3.33) and (2.3.34) into equation (2.3.26) gives

$$b_1^{(n)} = h \left(\frac{4}{3} - \frac{2}{15}q^2 \right) U_A.$$

Now from equation (2.3.25) let us consider $b_m^{(n)}$ at element $e = M + 2$ (see Fig-

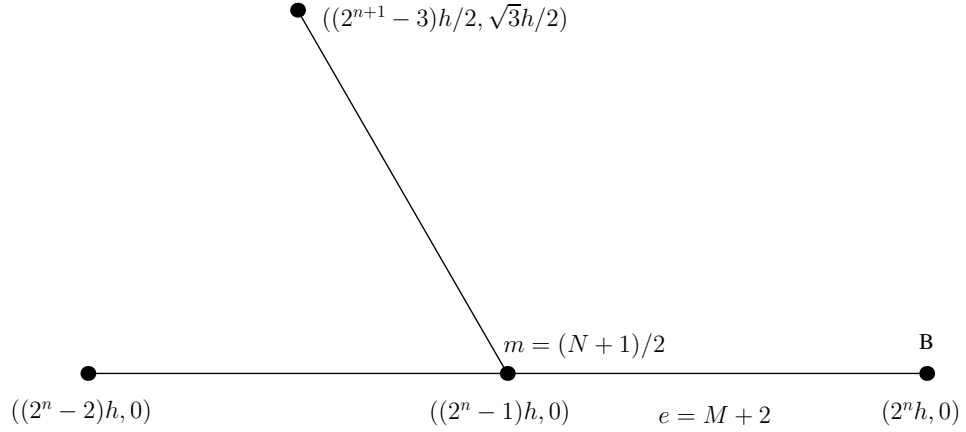


Figure 2.8: The boundary element for $e = M + 2$

ure 2.8), which is connected between vertex m at $(x_m, y_m) = ((2^n - 1)h, 0)$ and vertex B at $(x_B, y_B) = (2^n h, 0)$. From equation (2.3.14) we get $(x(s), y(s)) = ((x_B - x_m)s + x_m, (y_B - y_m)s + y_m) = ((s + 2^n - 1)h, 0)$ and $d\underline{x} = h ds$, gives

$$b_m^{(n)} = -h \left(\int_{M+2} (q^2 \phi_B \phi_m + h^2 \nabla \phi_B \cdot \nabla \phi_m) ds \right) U_B. \quad (2.3.35)$$

From equation (2.3.10) the basis functions at vertex B in element $e = M + 2$ is

$$\phi_B(x, y) = \frac{-(2^n - 1)^2 h^2 + x^2 + y^2}{(2^{n+1} - 1)h^2} \quad (2.3.36)$$

and at vertex m is

$$\phi_m(x, y) = 2^n(2 - 2^n) + \frac{2(2^n - 1)x}{h} - \frac{x^2 + y^2}{h^2}. \quad (2.3.37)$$

Substituting equation (2.3.14) into equations (2.3.36) and (2.3.37) gives

$$\phi_B(x(s), y(s)) = \frac{s(s + 2^{n+1} - 2)}{2^{n+1} - 1} \quad (2.3.38)$$

and

$$\phi_m(x(s), y(s)) = 1 - s^2. \quad (2.3.39)$$

From equation (2.3.11), equations (2.3.36) and (2.3.37) gives

$$\nabla\phi_B(x, y) = \left(\frac{2x}{(2^{n+1} - 1)h^2}, \frac{2y}{(2^{n+1} - 1)h^2} \right) \quad (2.3.40)$$

and

$$\nabla\phi_m(x, y) = \left(\frac{2(2^n - 1)}{h} - \frac{2x}{h^2}, \frac{-2y}{h^2} \right). \quad (2.3.41)$$

Substituting equation (2.3.14) into equations (2.3.40) and (2.3.41) gives

$$\nabla\phi_B(x(s), y(s)) = \left(\frac{2(s + 2^n - 1)}{(2^{n+1} - 1)h}, 0 \right) \quad (2.3.42)$$

and

$$\nabla\phi_m(x(s), y(s)) = \left(\frac{-2s}{h}, 0 \right). \quad (2.3.43)$$

Substituting equations (2.3.38), (2.3.39), (2.3.42) and (2.3.43) into equation (2.3.35) gives

$$b_m^{(n)} = h \left(1 + \frac{1}{3(2^{n+1} - 1)} + \frac{(11 - 15 \times 2^n)}{30(2^{n+1} - 1)} q^2 \right) U_B.$$

A similar calculation, for $b_N^{(n)}$ at element $e = M + 3$ shows

$$b_j^{(n)} = h \begin{cases} \eta_j^{(n)} U_A, & j = 1 \\ \eta_j^{(n)} U_B, & j = m \\ \eta_j^{(n)} U_C, & j = N \\ 0 & \text{otherwise,} \end{cases} \quad (2.3.44)$$

where

$$\eta_j^{(n)} = \begin{cases} \frac{4}{3} - \frac{2}{15}q^2, & j = 1 \\ 1 + \frac{1}{3(2^{n+1}-1)} + \frac{(11-15 \times 2^n)}{30(2^{n+1}-1)}q^2, & j = m \text{ or } N. \end{cases} \quad (2.3.45)$$

Note that the value of $\eta_j^{(n)}$ where $j \in \{m, N\}$ is dependent on the generation level n . For generation level $n = 1$,

$$b_j^{(1)} = h \begin{cases} (\frac{4}{3} - \frac{2}{15}q^2)U_A, & j = 1 \\ (\frac{10}{9} - \frac{19}{90}q^2)U_B, & j = 2 \\ (\frac{10}{9} - \frac{19}{90}q^2)U_C, & j = 3 \\ 0 & \text{otherwise,} \end{cases}$$

and for generation level $n = 2$,

$$b_j^{(2)} = h \begin{cases} (\frac{4}{3} - \frac{2}{15}q^2)U_A, & j = 1 \\ (\frac{22}{21} - \frac{7}{30}q^2)U_B, & j = 5 \\ (\frac{22}{21} - \frac{7}{30}q^2)U_C, & j = 9 \\ 0 & \text{otherwise.} \end{cases}$$

2.3.1 Application of the mechanical boundary conditions

Mechanical and electrical loads will be introduced to the transducer at its boundaries as displayed in Figure 2.9. In the mechanical load at the front face of the

transducer the governing equation is [3]

$$\rho_L \frac{\partial^2 u_L}{\partial t^2} = \mu_L \frac{\partial^2 u_L}{\partial x_L^2},$$

where ρ_L is the density of the load material, u_L is its displacement and μ_L is its shear modulus. That is

$$\frac{\partial^2 u_L}{\partial t^2} = \frac{\mu_L}{\rho_L} \frac{\partial^2 u_L}{\partial x_L^2}$$

and so, nondimensionalising in a similar fashion to equation (2.2.12), gives

$$\frac{\partial^2 u_L}{\partial \theta^2} = \left(\frac{hc_L}{c_T} \right)^2 \frac{\partial^2 u_L}{\partial x_L^2}$$

where c_L is the wave speed in the load ($c_L^2 = \mu_L/\rho_L$). Taking Laplace transforms as was done in equation (2.2.13) gives

$$\frac{d^2 \bar{u}_L}{dx_L^2} - \left(\frac{qc_T}{hc_L} \right)^2 \bar{u}_L = 0.$$

Hence, the displacement in the load is

$$\bar{u}_L(x_L) = A_L e^{(-qc_T x_L/hc_L)} + B_L e^{(qc_T x_L/hc_L)}, \quad (2.3.46)$$

where A_L, B_L are constants (A_L is the amplitude of the incoming wave that is received by the transducer (in transmission mode A_L is zero) and B_L is the amplitude of the transmitted wave (transmission mode) or reflected wave (in reception mode)) and x_L is the local coordinate in the mechanical load (see Figure 2.10). Similarly the displacement in the backing layer (subscript B) is given by

$$\bar{u}_B(x_B) = A_B e^{(-qc_T x_B/hc_B)} + B_B e^{(qc_T x_B/hc_B)},$$

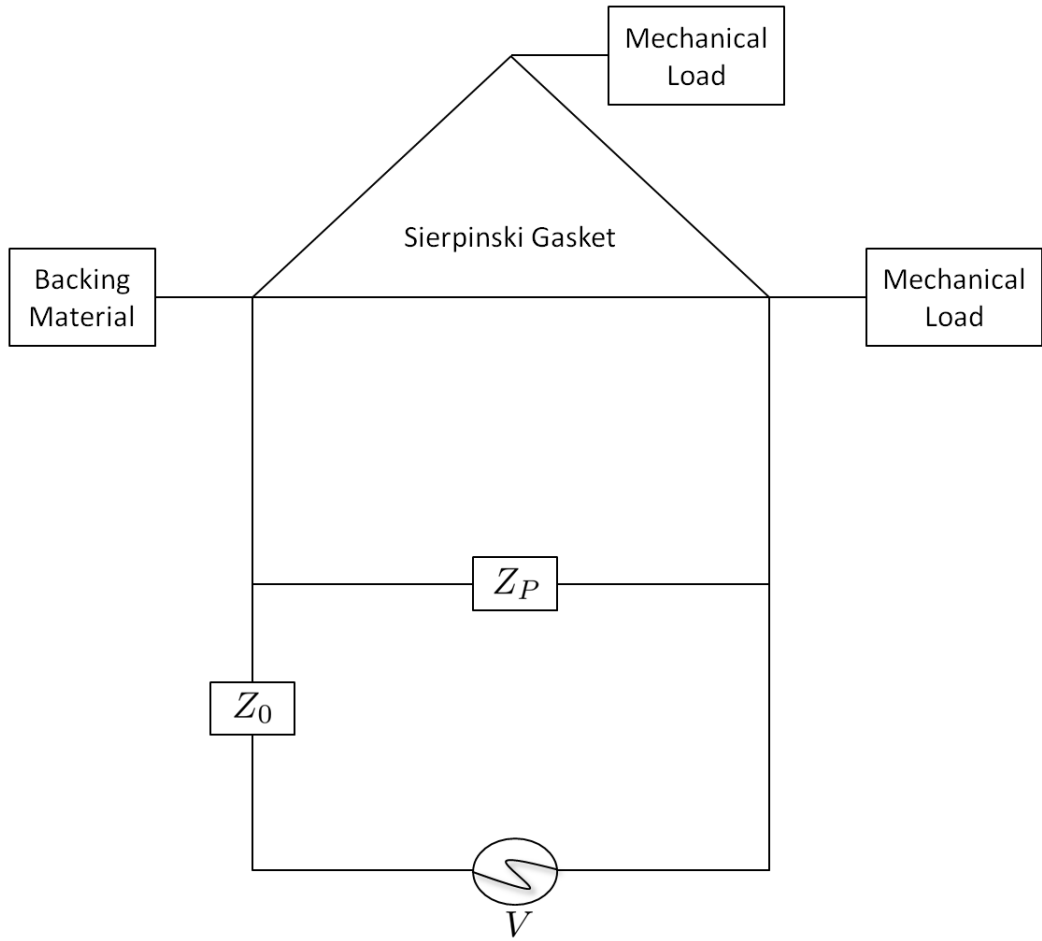


Figure 2.9: Physical layout of the fractal transducer.

where A_B , B_B are constants (in both transmission and reception modes A_B is the amplitude of the wave transmitted into the backing material and B_B is the amplitude of the incoming wave), x_B is the local coordinate in the backing material and c_B is the wave speed in the backing material. As the backing layer is highly attenuative it is assumed that there is only a wave travelling away from the piezoelectric layer (SG(3)) interface ($x_B = 0$) in the direction of increasing x_B , and so we set $B_B = 0$. Continuity of displacement at the transducer-mechanical

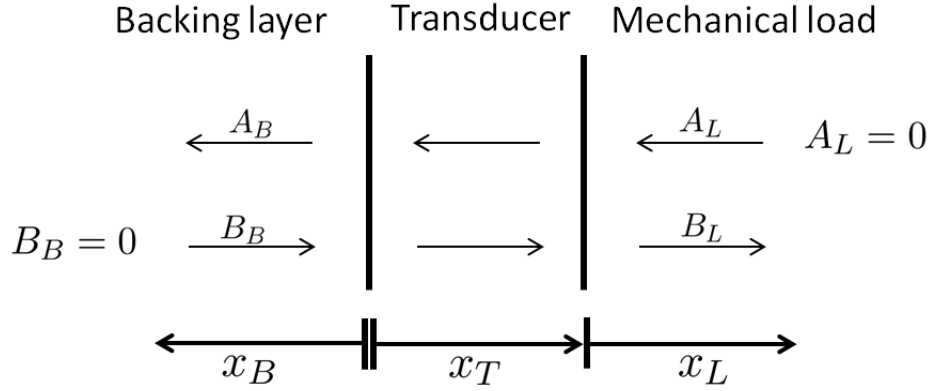


Figure 2.10: The multilayer model.

load interface and the symmetry of the SG(3) graph give

$$U_A = \bar{u}_B(0) = A_B, \quad (2.3.47)$$

$$U_B = \bar{u}_L(0) = A_L + B_L, \quad (2.3.48)$$

$$U_C = \bar{u}_L(0) = A_L + B_L. \quad (2.3.49)$$

The force F on each vertex is given by $F = A_r T$, where $A_r = \xi L / (2^n - 1) = \xi h^{(n)}$ is the cross-sectional area (A_r) of each edge of the fractal graph. Recall that in this chapter we will be restricting attention to a transducer composed of a piezoelectric material alone (so single phase and no polymer phase).

From equation (2.2.8) only $u_{3,1}$ and $u_{3,2}$ are nonzero and so the only nonzero components of equation (2.2.1) and due to the properties of PZT-5H (see Appendix A.4) [147,148], we get

$$T_{11} = T_{12} = T_{21} = T_{22} = T_{33} = 0,$$

and

$$T_{13} = T_{31} = c_{1313} S_{13} + c_{1331} S_{31} - e_{113} E_1.$$

That is

$$T_5 = c_{55}^T (S_{13} + S_{31}) - e_{15} E_1,$$

and, using equation (2.2.3), since from equation (2.2.8) $u_{1,3} = 0$, then

$$T_5 = c_{44}^T u_{3,1} - e_{24} E_1,$$

since $c_{55}^T = c_{44}^T$ and $e_{15} = e_{24}$. Similarly we get

$$T_{23} = T_{32} = c_{3223} S_{23} + c_{3232} S_{32} - e_{232} E_2,$$

that is

$$T_4 = c_{44}^T u_{3,2} - e_{24} E_2.$$

Similarly, from equation (2.2.2), for PZT-5H, the only nonzero components are

$$D_1 = e_{24} u_{3,1} + \varepsilon_{11}^T E_1,$$

and

$$D_2 = e_{24} u_{3,2} + \varepsilon_{11}^T E_2,$$

where D_3 is zero. Given the geometry of the graph, the positioning of the boundary vertices, and the load conditions there is a line of symmetry given by $x_1 = x_2$ (see Figure 2.11). Hence, $E_1 = E_2 = E$ and $u_{3,1} = u_{3,2}$ then $D_1 = D_2 = D$ and $T_5 = T_4 = T$, and so

$$D = e_{24} u_{3,1} + \varepsilon_{11}^T E.$$

That is

$$E = -\zeta S + \frac{D}{\varepsilon_{11}^T} \tag{2.3.50}$$

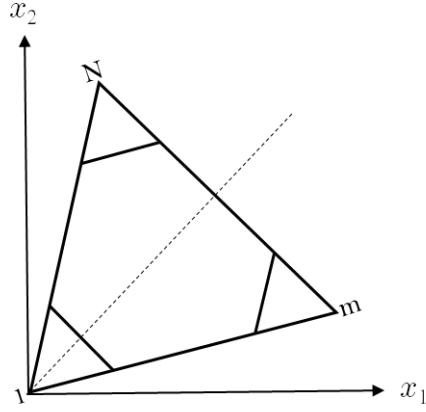


Figure 2.11: The line of symmetry given by $x_1 = x_2$

where $\zeta = e_{24}/\varepsilon_{11}^T$ and $S = u_{3,1} = d\bar{u}/dx$. Also, we have

$$T = c_{44}^T u_{3,1} - e_{24} E$$

and substituting equation (2.3.50) gives

$$T = \left(c_{44}^T + \frac{e_{24}^2}{\varepsilon_{11}^T} \right) u_{3,1} - \frac{e_{24}}{\varepsilon_{11}^T} D.$$

That is

$$T = \mu_T S - \zeta D. \quad (2.3.51)$$

Hence, from equation (2.3.51),

$$F = A_r T = A_r \mu_T S - \zeta D A_r.$$

By applying an electrical charge Q at one of the transducer-electrical load interfaces then Gauss' law (equation (2.2.5)) gives $D = Q/A_r$. Since $S = d\bar{u}/dx$, then

$$F = A_r \mu_T \frac{d\bar{u}}{dx} - \zeta Q. \quad (2.3.52)$$

So from the continuity of force we get $F(\bar{u}_m) = F_L(\bar{u}_{\partial\Omega}) = F_L(x_L = 0)$, where F_L is the force in the mechanical load. That is, from equation (2.3.46),

$$A_r\mu_T\frac{(U_B - U_m)}{h} - \zeta Q = A_r\mu_L\left(\frac{qc_T}{hc_L}\right)(-A_L + B_L), \quad (2.3.53)$$

and so

$$U_B - U_m - \frac{\zeta Q}{\mu_T}\left(\frac{h}{A_r}\right) = \frac{Z_L}{Z_T}q(-A_L + B_L), \quad (2.3.54)$$

where the mechanical impedance of the load is $Z_L = \mu_L A_r / c_L$ and of the transducer is $Z_T = \mu_T A_r / c_T$. At each generation level of the Sierpinski gasket transducer the ratio of the cross-sectional area of each edge to its length is denoted by $\xi = A_r / h^{(n)}$. The overall extent of the SG(3) is fixed and so the length of the edges will steadily decrease and, by fixing ξ , the cross-sectional area will also decrease as the fractal generation level increases. Hence, equation (2.3.54), and its equivalent at the front face of the transducer, can be written

$$U_1 - U_A - \frac{\zeta Q}{\mu_T \xi} = \frac{Z_B}{Z_T}q(-A_B), \quad (2.3.55)$$

$$U_B - U_m - \frac{\zeta Q}{\mu_T \xi} = \frac{Z_L}{Z_T}q(-A_L + B_L), \quad (2.3.56)$$

Z_B is the mechanical impedance of the backing material. Substituting equation (2.3.47) into equation (2.3.55) gives $U_A = \gamma_1 U_1 + \delta_1$ and substituting equations (2.3.48) and (2.3.49) into equation (2.3.56) gives

$$U_B = \gamma_m U_m + \delta_m = U_C = \gamma_N U_N + \delta_N, \quad (2.3.57)$$

where

$$\gamma_j = \begin{cases} (1 - q^{\frac{Z_B}{Z_T}})^{-1}, & j = 1 \\ (1 - q^{\frac{Z_L}{Z_T}})^{-1}, & j = m \text{ or } N \\ 0 & \text{otherwise} \end{cases} \quad (2.3.58)$$

and

$$\delta_j = \begin{cases} -\gamma_1 \frac{\zeta Q}{\mu_T \xi}, & j = 1 \\ \gamma_m \left(\frac{\zeta Q}{\mu_T \xi} - 2A_L q^{\frac{Z_L}{Z_T}} \right), & j = m \text{ or } N \\ 0 & \text{otherwise.} \end{cases} \quad (2.3.59)$$

Hence, equation (2.3.44) becomes

$$b_j^{(n)} = h\bar{\gamma}_j^{(n)}U_j + h\bar{\delta}_j^{(n)} \quad j = 1, m \text{ or } N \quad (2.3.60)$$

where $\bar{\gamma}_j^{(n)} = \eta_j^{(n)}\gamma_j$ and $\bar{\delta}_j^{(n)} = \eta_j^{(n)}\delta_j$. Putting equation (2.3.60) into equation (2.3.4) gives

$$\hat{A}_{ji}^{(n)}U_i = \bar{\gamma}_j^{(n)}U_j + \bar{\delta}_j^{(n)}.$$

Hence,

$$(\hat{A}_{ji}^{(n)} - \hat{B}_{ji}^{(n)})U_i = \bar{\delta}_j^{(n)}, \quad i = 1, m \text{ or } N$$

where

$$\hat{B}_{ji}^{(n)} = \begin{bmatrix} \bar{\gamma}_1 & 0 & \cdots & & \cdots & 0 \\ 0 & 0 & \ddots & & & \vdots \\ \vdots & \ddots & \ddots & & & \\ & & & 0 & 0 & \\ & & & & \bar{\gamma}_m & \\ & & & 0 & 0 & \\ & & & & & \ddots & \ddots & \vdots \\ \vdots & & & & & \ddots & 0 & 0 \\ 0 & \cdots & & & \cdots & 0 & \bar{\gamma}_N \end{bmatrix}. \quad (2.3.61)$$

That is

$$F_{ji}^{(n)} U_i = \bar{\delta}_j^{(n)},$$

and so

$$U_i = G_{ji}^{(n)} \bar{\delta}_j^{(n)}, \quad (2.3.62)$$

where

$$G_{ji}^{(n)} = \left(F_{ji}^{(n)} \right)^{-1} = \left(\hat{A}_{ji}^{(n)} - \hat{B}_{ji}^{(n)} \right)^{-1} \quad (2.3.63)$$

represents the Green's transfer matrix.

2.4 Renormalisation

From equation (2.3.62) the desired basis function weightings in equation (2.3.2) at each vertex in Ω are then given by

$$U_j^{(n)} = G_{j1}^{(n)} \bar{\delta}_1^{(n)} + G_{jm}^{(n)} \bar{\delta}_m^{(n)} + G_{jN}^{(n)} \bar{\delta}_N^{(n)}. \quad (2.4.1)$$

In particular we will be interested in $U_1^{(n)}, U_m^{(n)}$ and $U_N^{(n)}$ and so we only need to be able to calculate the pivotal Green's functions $G_{ij}^{(n)}$, $i, j \in \{1, m, N\}$. If

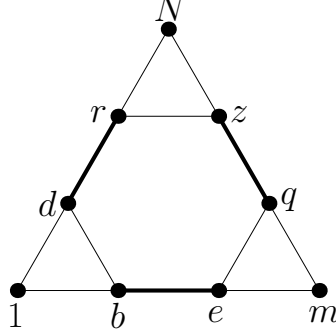


Figure 2.12: Three Sierpinski Gasket graphs of generation level $n-1$ are connected by the edges in bold ($(dr), (be), (qz)$) to create the Sierpinski Gasket graph at generation level n .

we temporarily ignore matrix \hat{B} in equation (2.3.63) (this matrix originates from consideration of the boundary conditions) then, due to the symmetries of the SG(3) graph (and hence in matrix $A^{(n)}$), we have

$$\hat{G}_{ii}^{(n)} = \hat{G}_{jj}^{(n)} = \hat{x}, \text{ say, where } i, j \in \{1, m, N\} \quad (2.4.2)$$

(i.e corner-to-same-corner), and

$$\hat{G}_{jk}^{(n)} = \hat{G}_{hk}^{(n)} = \hat{y}, \text{ say, where } j, k, h \in \{1, m, N\}, j \neq k \neq h \quad (2.4.3)$$

(i.e corner-to-other-corner), where

$$\hat{G}^{(n)} = \left(\hat{A}^{(n)} \right)^{-1}. \quad (2.4.4)$$

For clarity, at level $n+1$, we denote, $\hat{X} = \hat{G}_{ii}^{(n+1)}$ and $\hat{Y} = \hat{G}_{ji}^{(n+1)}$ where $j, i \in \{1, m, N\}, j \neq i$. The matrix is symmetrical and consequently, $\hat{G}_{ij}^{(n)} = \hat{G}_{ji}^{(n)}$. From

equation (2.2.12), since

$$\theta^{(n)} = \frac{c_T}{h^{(n)}} t, \quad (2.4.5)$$

then $\mathcal{L} : \theta^{(n)} \rightarrow q^{(n)}$ where $q^{(n)} = i\hat{\omega}^{(n)} = i2\pi\hat{f}^{(n)} = i2\pi (c_T/h^{(n)})^{-1} f^{(n)}$, $\hat{f}^{(n)}$ is the nondimensionalised natural frequency, $\hat{\omega}^{(n)}$ is the nondimensionalised angular frequency and $f^{(n)}$, and $\omega^{(n)}$ are the dimensionalised equivalents. In order to use the renormalisation approach detailed below then we set $q = q^{(n)} = q^{(n+1)}$. This simply means that the output from the renormalisation methodology (and hence the electrical impedance and transmission/reception sensitivities) at a given q (fixed) is then that quantity at frequency $f^{(n)}$ at fractal generation level n . So when comparing outputs at different fractal generation levels one must ensure that the frequency is scaled appropriately (by $(c_T/h^{(n)})^{-1}$) when re-dimensionalising. An iterative procedure can be developed from equation (2.3.24) which can be written as

$$\hat{A}^{(n+1)} = \bar{\hat{A}}^{(n)} + \beta V^{(n+1)}, \quad n \geq 1.$$

where $V_{ji}^{(n)} = \mathbf{1}_{D^{(n)}}(ji)$, $D^{(n)} = \{\{b, e\}, \{d, r\}, \{q, z\}, \{e, b\}, \{r, d\}, \{z, q\}\}$ (see Figure 2.12). Since $\bar{\hat{G}}^{(n)}$ is a block-diagonal matrix and from equation (2.4.4) then

$$\left(\hat{G}^{(n+1)}\right)^{-1} = \left(\bar{\hat{G}}^{(n)}\right)^{-1} + \beta V^{(n+1)}.$$

That is

$$\left(\bar{\hat{G}}^{(n)}\right)^{-1} = \left(\hat{G}^{(n+1)}\right)^{-1} - \beta V^{(n+1)}.$$

Hence, using the $N_{n \times 1} \times N_{n \times 1}$ identity matrix denoted by I_{n+1} ,

$$\begin{aligned} I_{n+1} &= \bar{\hat{G}}^{(n)} \left(\left(\hat{G}^{(n+1)} \right)^{-1} - \beta V^{(n+1)} \right) \\ &= \bar{\hat{G}}^{(n)} \left(\left(\hat{G}^{(n+1)} \right)^{-1} - \beta V^{(n+1)} \hat{G}^{(n+1)} \left(\hat{G}^{(n+1)} \right)^{-1} \right) \\ &= \bar{\hat{G}}^{(n)} \left(I_{n+1} - \beta V^{(n+1)} \hat{G}^{(n+1)} \right) \left(\hat{G}^{(n+1)} \right)^{-1}. \end{aligned}$$

Hence,

$$\hat{G}^{(n+1)} = \bar{\hat{G}}^{(n)} - \beta \bar{\hat{G}}^{(n)} V^{(n+1)} \hat{G}^{(n+1)}. \quad (2.4.6)$$

To calculate $G_{ji}^{(n)}$ the boundary conditions must be reintroduced. From equation (2.3.63),

$$\left(G^{(n)} \right)^{-1} = \hat{A}^{(n)} - \hat{B}^{(n)}.$$

Now, from equation (2.4.4)

$$\left(G^{(n)} \right)^{-1} = \left(\hat{G}^{(n)} \right)^{-1} - \hat{B}^{(n)}.$$

Hence,

$$I_n = \left(\hat{G}^{(n)} \right)^{-1} G^{(n)} - \hat{B}^{(n)} G^{(n)},$$

and so

$$\hat{G}^{(n)} = G^{(n)} - \hat{G}^{(n)} \hat{B}^{(n)} G^{(n)}.$$

Hence,

$$G^{(n)} = \hat{G}^{(n)} + \hat{G}^{(n)} \hat{B}^{(n)} G^{(n)}. \quad (2.4.7)$$

2.4.1 Derivation of the pivotal recursion relationships

The $(i, j)^{th}$ element of the matrix equation (2.4.6) can be written as,

$$\hat{G}_{ij}^{(n+1)} = \bar{\hat{G}}_{ij}^{(n)} - \sum_{h,k} \beta \bar{\hat{G}}_{ih}^{(n)} V_{hk}^{(n)} \hat{G}_{kj}^{(n+1)}. \quad (2.4.8)$$

The system of linear equations in $\hat{G}_{ij}^{(n+1)}$ will create the renormalisation recursion relationships for the pivotal Green's functions. However, these recursions do not include the boundary conditions. Since the subgraphs of Figure 2.12 only connect to each other at the corners, it will transpire that the recursions in equation (2.4.8) only involve two pivotal Green's functions, namely, corner-to-same-corner and corner-to-other-corner; the so called input/output vertices. To proceed, we now need to determine \hat{x} and \hat{y} as defined in equations (2.4.2) and (2.4.3). Using equation (2.4.8) we get

$$\hat{G}_{11}^{(n+1)} = \bar{\hat{G}}_{11}^{(n)} - \sum_{h,k} \beta \bar{\hat{G}}_{1h}^{(n)} V_{hk}^{(n)} \hat{G}_{k1}^{(n+1)},$$

where $\bar{\hat{G}}_{ij}^{(n)}$ is a block-diagonal matrix where each block has dimensions $d \times d$ so $\bar{\hat{G}}_{ij}^{(n)} = 0, \forall j > d$. Also $V_{hk}^{(n)} = \mathbb{1}_{D^{(n)}}(hk)$ is the adjacency matrix for the subgraph of $SG^{(n)}(3)$ consisting of the edges $D^{(n)}$ that connect each of the three $SG^{(n-1)}(3)$ graphs ($D^{(n)} = \{\{d, r\}, \{b, e\}, \{q, z\}, \{r, d\}, \{e, b\}, \{z, q\}\}$ (see Figure 2.12)) and .

So, we get

$$\hat{G}_{11}^{(n+1)} = \hat{G}_{11}^{(n)} - \beta \bar{\hat{G}}_{1d}^{(n)} V_{dr}^{(n)} \hat{G}_{r1}^{(n+1)} - \beta \bar{\hat{G}}_{1b}^{(n)} V_{be}^{(n)} \hat{G}_{e1}^{(n+1)}$$

and

$$\hat{G}_{11}^{(n+1)} = \hat{G}_{11}^{(n)} - \beta \hat{G}_{1N}^{(n)} \hat{G}_{r1}^{(n+1)} - \beta \hat{G}_{1m}^{(n)} \hat{G}_{e1}^{(n+1)}$$

since, by symmetry $\bar{G}_{1d}^{(n)} = \hat{G}_{1N}^{(n)}$, $\hat{G}_{1N}^{(n)} = \hat{G}_{1m}^{(n)}$ and $\hat{G}_{r1}^{(n+1)} = \hat{G}_{e1}^{(n+1)}$. That is

$$\hat{X} = \hat{x} - 2\beta\hat{y}\hat{G}_{e1}^{(n+1)}, \quad (2.4.9)$$

since, $\hat{G}_{11}^{(n)} = \hat{x}$ (corner-to-same-corner), $\hat{G}_{1N}^{(n)} = \hat{G}_{1m}^{(n)} = \hat{y}$ (corner-to-other-corner); and so at generation level $n + 1$, $\hat{G}_{11}^{(n+1)} = \hat{X}$ (see equation (2.4.4)). Similarly,

$$\begin{aligned} \hat{G}_{e1}^{(n+1)} &= \bar{G}_{e1}^{(n)} - \sum_{h,k} \beta \bar{G}_{eh}^{(n)} V_{hk}^{(n)} \hat{G}_{k1}^{(n+1)} \\ &= -\beta \bar{G}_{ee}^{(n)} V_{eb}^{(n)} \hat{G}_{b1}^{(n+1)} - \beta \bar{G}_{eq}^{(n)} V_{qz}^{(n)} \hat{G}_{z1}^{(n+1)} \\ &= -\beta \hat{G}_{11}^{(n)} \hat{G}_{b1}^{(n+1)} - \beta \hat{G}_{1N}^{(n)} \hat{G}_{z1}^{(n+1)}. \end{aligned}$$

Therefore

$$\hat{G}_{e1}^{(n+1)} = -\beta\hat{x}\hat{G}_{b1}^{(n+1)} - \beta\hat{y}\hat{G}_{z1}^{(n+1)}. \quad (2.4.10)$$

Also

$$\begin{aligned} \hat{G}_{b1}^{(n+1)} &= \bar{G}_{b1}^{(n)} - \sum_{h,k} \beta \bar{G}_{bh}^{(n)} V_{hk}^{(n)} \hat{G}_{k1}^{(n+1)} \\ &= \hat{G}_{m1}^{(n)} - \beta \bar{G}_{bb}^{(n)} V_{be}^{(n)} \hat{G}_{e1}^{(n+1)} - \beta \bar{G}_{bd}^{(n)} V_{dr}^{(n)} \hat{G}_{r1}^{(n+1)} \\ &= \hat{y} - \beta \hat{G}_{mm}^{(n)} \hat{G}_{e1}^{(n+1)} - \beta \hat{G}_{mN}^{(n)} \hat{G}_{e1}^{(n+1)}. \end{aligned}$$

Hence

$$\hat{G}_{b1}^{(n+1)} = \hat{y} - \beta \hat{G}_{e1}^{(n+1)} (\hat{x} + \hat{y}), \quad (2.4.11)$$

since $\hat{G}_{r1}^{(n+1)} = \hat{G}_{e1}^{(n+1)}$. Finally,

$$\begin{aligned}\hat{G}_{z1}^{(n+1)} &= \bar{\bar{G}}_{z1}^{(n)} - \sum_{h,k} \beta \bar{\bar{G}}_{zh}^{(n)} V_{hk}^{(n)} \hat{G}_{k1}^{(n+1)} \\ &= -\beta \bar{\bar{G}}_{zr}^{(n)} V_{rd}^{(n)} \hat{G}_{d1}^{(n+1)} - \beta \bar{\bar{G}}_{zz}^{(n)} V_{zq}^{(n)} \hat{G}_{q1}^{(n+1)} \\ &= -\beta \hat{G}_{m1}^{(n)} \hat{G}_{b1}^{(n+1)} - \beta \hat{G}_{mm}^{(n)} \hat{G}_{z1}^{(n+1)}.\end{aligned}$$

Therefore

$$\hat{G}_{z1}^{(n+1)} = -\beta \hat{y} \hat{G}_{b1}^{(n+1)} - \beta \hat{x} \hat{G}_{z1}^{(n+1)}, \quad (2.4.12)$$

since $\hat{G}_{d1}^{(n+1)} = \hat{G}_{b1}^{(n+1)}$ and $\hat{G}_{q1}^{(n+1)} = \hat{G}_{z1}^{(n+1)}$. Equations (2.4.9) to (2.4.12) provide four equations in the four unknowns \hat{X} , $\hat{G}_{e1}^{(n+1)}$, $\hat{G}_{b1}^{(n+1)}$ and $\hat{G}_{z1}^{(n+1)}$ which can be written in matrix form as

$$\begin{bmatrix} 1 & 2\beta\hat{y} & 0 & 0 \\ 0 & 1 & \beta\hat{x} & \beta\hat{y} \\ 0 & \beta(\hat{x} + \hat{y}) & 1 & 0 \\ 0 & \beta\hat{x} & \beta\hat{y} & 1 \end{bmatrix} \begin{bmatrix} \hat{X} \\ \hat{G}_{e1}^{(n+1)} \\ \hat{G}_{b1}^{(n+1)} \\ \hat{G}_{z1}^{(n+1)} \end{bmatrix} = \begin{bmatrix} \hat{x} \\ 0 \\ \hat{y} \\ 0 \end{bmatrix}. \quad (2.4.13)$$

So, solving this by the augmented matrix approach and back-substitution we get,

$$\hat{X} = \hat{x} + \frac{2\beta^2\hat{y}^2 (\hat{x} + \beta\hat{x}^2 - \beta\hat{y}^2)}{(1 + \beta\hat{x} + \beta\hat{y})(1 - \beta^2\hat{x}^2 - \beta\hat{y} + \beta^2\hat{y}^2)}, \quad (2.4.14)$$

$$\hat{G}_{e1}^{(n+1)} = \frac{-\beta\hat{y} (\hat{x} + \beta\hat{x}^2 - \beta\hat{y}^2)}{(1 + \beta\hat{x} + \beta\hat{y})(1 - \beta^2\hat{x}^2 - \beta\hat{y} + \beta^2\hat{y}^2)},$$

$$\hat{G}_{b1}^{(n+1)} = \frac{\hat{y}(1 + \beta\hat{x})}{(1 + \beta\hat{x} + \beta\hat{y})(1 - \beta^2\hat{x}^2 - \beta\hat{y} + \beta^2\hat{y}^2)}, \quad (2.4.15)$$

and

$$\hat{G}_{z1}^{(n+1)} = \frac{-\beta\hat{y}^2}{(1 + \beta\hat{x} + \beta\hat{y})(1 - \beta^2\hat{x}^2 - \beta\hat{y} + \beta^2\hat{y}^2)}. \quad (2.4.16)$$

Now, for $\hat{Y} = \hat{G}_{m1}^{(n+1)}$, equation (2.4.8) gives

$$\begin{aligned}
\hat{G}_{m1}^{(n+1)} &= \bar{\hat{G}}_{m1}^{(n)} - \sum_{h,k} \beta \bar{\hat{G}}_{mh}^{(n)} V_{hk}^{(n)} \hat{G}_{k1}^{(n+1)} \\
&= -\beta \bar{\hat{G}}_{me}^{(n)} V_{eb}^{(n)} \hat{G}_{b1}^{(n+1)} - \beta \bar{\hat{G}}_{mq}^{(n)} V_{qz}^{(n)} \hat{G}_{z1}^{(n+1)} \\
&= -\beta \hat{G}_{m1}^{(n)} \hat{G}_{b1}^{(n+1)} - \beta \hat{G}_{mN}^{(n)} \hat{G}_{z1}^{(n+1)}.
\end{aligned}$$

Therefore

$$\hat{Y} = -\beta \hat{y} \left(\hat{G}_{b1}^{(n+1)} + \hat{G}_{z1}^{(n+1)} \right). \quad (2.4.17)$$

Putting equations (2.4.15) and (2.4.16) into equation (2.4.17) gives

$$\hat{Y} = \frac{-\beta \hat{y}^2 (1 + \beta \hat{x} - \beta \hat{y})}{(1 + \beta \hat{x} + \beta \hat{y}) (1 - \beta^2 \hat{x}^2 - \beta \hat{y} + \beta^2 \hat{y}^2)}. \quad (2.4.18)$$

The boundary conditions can now be considered by rewriting the $(i, j)^{th}$ element of the matrix equation (2.4.7) as,

$$G_{ij}^{(n)} = \hat{G}_{ij}^{(n)} + \sum_{h,k} \hat{G}_{ih}^{(n)} \hat{B}_{hk}^{(n)} G_{kj}^{(n)}$$

and so we have,

$$\begin{aligned}
G_{11}^{(n)} &= \hat{G}_{11}^{(n)} + \sum_{h,k} \hat{G}_{ih}^{(n)} \hat{B}_{hk}^{(n)} G_{k1}^{(n)} \\
&= \hat{G}_{11}^{(n)} + \hat{G}_{11}^{(n)} \hat{B}_{11}^{(n)} G_{11}^{(n)} + \hat{G}_{1m}^{(n)} \hat{B}_{mm}^{(n)} G_{m1}^{(n)} + \hat{G}_{1N}^{(n)} \hat{B}_{NN}^{(n)} G_{N1}^{(n)}.
\end{aligned}$$

Therefore

$$x = \hat{x} + \hat{x} \bar{\gamma}_1 x + 2 \hat{y} \bar{\gamma}_m y \quad (2.4.19)$$

since $\hat{B}_{11}^{(n)} = \bar{\gamma}_1, \hat{B}_{mm}^{(n)} = \hat{B}_{NN}^{(n)} = \bar{\gamma}_m$ from equation (2.3.61). Similarly,

$$\begin{aligned} G_{1m}^{(n)} &= \hat{G}_{1m}^{(n)} + \sum_{h,k} \hat{G}_{mh}^{(n)} \hat{B}_{hk}^{(n)} G_{k1}^{(n)} \\ &= \hat{G}_{m1}^{(n)} + \hat{G}_{m1}^{(n)} \hat{B}_{11}^{(n)} G_{11}^{(n)} + \hat{G}_{mm}^{(n)} \hat{B}_{mm}^{(n)} G_{m1}^{(n)} + \hat{G}_{mN}^{(n)} \hat{B}_{NN}^{(n)} G_{N1}^{(n)}. \end{aligned}$$

Hence

$$y = \hat{y} + \hat{y}\bar{\gamma}_1x + \hat{x}\bar{\gamma}_my + \hat{y}\bar{\gamma}_my. \quad (2.4.20)$$

Letting $G_{mm}^{(n)} = z$ and $G_{mN}^{(n)} = r$ then,

$$\begin{aligned} G_{mm}^{(n)} &= \hat{G}_{mm}^{(n)} + \sum_{h,k} \hat{G}_{mh}^{(n)} \hat{B}_{hk}^{(n)} G_{km}^{(n)} \\ &= \hat{G}_{mm}^{(n)} + \hat{G}_{m1}^{(n)} \hat{B}_{11}^{(n)} G_{1m}^{(n)} + \hat{G}_{mm}^{(n)} \hat{B}_{mm}^{(n)} G_{mm}^{(n)} + \hat{G}_{mN}^{(n)} \hat{B}_{NN}^{(n)} G_{Nm}^{(n)}. \end{aligned}$$

Therefore

$$z = \hat{x} + \hat{y}\bar{\gamma}_1y + \hat{x}\bar{\gamma}_mz + \hat{y}\bar{\gamma}_mr. \quad (2.4.21)$$

Finally,

$$\begin{aligned} G_{mN}^{(n)} &= \hat{G}_{mN}^{(n)} + \sum_{h,k} \hat{G}_{mh}^{(n)} \hat{B}_{hk}^{(n)} G_{kN}^{(n)} \\ &= \hat{G}_{mN}^{(n)} + \hat{G}_{m1}^{(n)} \hat{B}_{11}^{(n)} G_{1N}^{(n)} + \hat{G}_{mm}^{(n)} \hat{B}_{mm}^{(n)} G_{mN}^{(n)} + \hat{G}_{mN}^{(n)} \hat{B}_{NN}^{(n)} G_{NN}^{(n)}. \end{aligned}$$

Hence

$$r = \hat{y} + \hat{y}\bar{\gamma}_1y + \hat{x}\bar{\gamma}_mr + \hat{y}\bar{\gamma}_mz. \quad (2.4.22)$$

The four equations (2.4.19),(2.4.20),(2.4.21) and (2.4.22) can be solved to express x, y, r, z in terms of $\hat{x}, \hat{y}, \bar{\gamma}_1, \bar{\gamma}_m$. Solving equations (2.4.19),(2.4.20) for x and y gives

$$x = \frac{\hat{x} + 2\hat{y}\bar{\gamma}_my}{1 - \hat{x}\bar{\gamma}_1}. \quad (2.4.23)$$

Substituting equation (2.4.23) into equation (2.4.20) gives

$$y = \hat{y} + \hat{y}\bar{\gamma}_1 \left(\frac{\hat{x} + 2\hat{y}\bar{\gamma}_m y}{1 - \hat{x}\bar{\gamma}_1} \right) + \hat{x}\bar{\gamma}_m y + \hat{y}\bar{\gamma}_m y.$$

Therefore

$$y = \frac{\hat{y}}{(1 - \hat{x}\bar{\gamma}_1)(1 - \bar{\gamma}_m(\hat{x} + \hat{y})) - 2\hat{y}^2\bar{\gamma}_1\bar{\gamma}_m}. \quad (2.4.24)$$

Rearranging equation (2.4.21) we get

$$z(1 - \hat{x}\bar{\gamma}_m) = \hat{x} + \hat{y}\bar{\gamma}_1 y + \hat{y}\bar{\gamma}_m r.$$

That is

$$z = \frac{\hat{x} + \hat{y}\bar{\gamma}_1 y + \hat{y}\bar{\gamma}_m r}{1 - \hat{x}\bar{\gamma}_m}. \quad (2.4.25)$$

Substituting this equation into (2.4.22) gives

$$r(1 - \hat{x}\bar{\gamma}_m) = \hat{y} + \hat{y}\bar{\gamma}_1 y + \hat{y}\bar{\gamma}_m \left(\frac{\hat{x} + \hat{y}\bar{\gamma}_1 y + \hat{y}\bar{\gamma}_m r}{1 - \hat{x}\bar{\gamma}_m} \right)$$

which can be written as

$$r = \frac{\hat{y}(1 + \bar{\gamma}_1 y)}{1 - \hat{x}\bar{\gamma}_m} + \frac{\hat{y}\bar{\gamma}_m(\hat{x} + \hat{y}(\bar{\gamma}_1 y + \bar{\gamma}_m r))}{(1 - \hat{x}\bar{\gamma}_m)^2}.$$

Therefore

$$r = \frac{\hat{y}(1 + \bar{\gamma}_1 y(1 + \bar{\gamma}_m(\hat{y} - \hat{x})))}{(\hat{x}\bar{\gamma}_m - 1 + \hat{y}\bar{\gamma}_m)(\hat{x}\bar{\gamma}_m - 1 - \hat{y}\bar{\gamma}_m)}. \quad (2.4.26)$$

2.5 Electrical impedance and transmission sensitivity

In transmission mode there is no force incident on the front face of the transducer and so in equation (2.3.59) $A_L = 0$. Consider one edge in the graph connecting vertex 1 to vertex N , and apply a charge Q at vertex N . The voltage V is defined as follows

$$V = \int_0^L E dx$$

and using equation (2.3.50)

$$\begin{aligned} V &= \int_0^L \left(-\zeta S + \frac{D}{\varepsilon_{11}^T} \right) dx \\ &= \int_0^L \left(-\zeta \frac{d\bar{u}}{dx} + \frac{D}{\varepsilon_{11}^T} \right) dx. \end{aligned}$$

Now integrating and using $D = Q/A_r$ as used in equation (2.3.52) gives

$$\begin{aligned} V &= -\zeta(U_N - U_1) + \frac{QL}{A_r \varepsilon_{11}^T} \\ &= -\zeta(U_N - U_1) + \frac{Q}{C_0} \end{aligned} \tag{2.5.1}$$

where the transducer capacitance is given by $C_0 = A_r \varepsilon_{11}^T / L$. Since the charge $Q = \int I_T dt = \sqrt{(\rho_T / \mu_T)} h \int I_T d\theta$ where I_T is the current and $\theta = c_T t / h$ then, by taking Laplace transforms, gives

$$Q = \sqrt{\frac{\rho_T}{\mu_T}} h \frac{I_T}{q}.$$

That is

$$I_T = \frac{qQ\mu_T\xi}{Z_T}, \tag{2.5.2}$$

where $Z_T = \sqrt{\mu_T \rho_T} A_r$. The electrical impedance of the device, denoted by Z_E , is given by

$$Z_E = \frac{V}{I_T}, \quad (2.5.3)$$

substituting equations (2.5.1) and (2.5.2) into equation (2.5.3) gives

$$Z_E = \frac{Z_T}{C_0 q \mu_T \xi} \left(1 - \frac{\zeta C_0 (U_N - U_1)}{Q} \right). \quad (2.5.4)$$

Now using equation (2.4.1)

$$\begin{aligned} U_1^{(n)} &= G_{11}^{(n)} \bar{\delta}_1^{(n)} + G_{1m}^{(n)} \bar{\delta}_m^{(n)} + G_{1N}^{(n)} \bar{\delta}_N^{(n)} \\ &= G_{11}^{(n)} \bar{\delta}_1^{(n)} + \bar{\delta}_m^{(n)} \left(G_{1m}^{(n)} + G_{1N}^{(n)} \right) \\ &= G_{11}^{(n)} \bar{\delta}_1^{(n)} + 2G_{1m}^{(n)} \bar{\delta}_m^{(n)} \end{aligned}$$

since $G_{1m}^{(n)} = G_{1N}^{(n)}$ and $\bar{\delta}_N^{(n)} = \bar{\delta}_m^{(n)}$. This can be calculated since $G_{11}^{(n)} = x$ is given by equations (2.4.14) and (2.4.23) and $G_{1m}^{(n)} = y$ is given by equations (2.4.18) and (2.4.24). From equation (2.3.59) and the definition of $\bar{\delta}_j^{(n)}$ in equation (2.3.60) gives

$$U_1^{(n)} = -\frac{\zeta Q}{\mu_T \xi} \left(\eta_1^{(n)} \gamma_1 G_{11}^{(n)} - 2\eta_m^{(n)} \gamma_m G_{1m}^{(n)} \right). \quad (2.5.5)$$

Note that in equation (2.3.59) $\delta_m = \gamma_m \zeta Q / (\mu_T \xi)$ since $A_L = 0$. Similarly,

$$\begin{aligned} U_N^{(n)} &= G_{N1}^{(n)} \bar{\delta}_1^{(n)} + G_{Nm}^{(n)} \bar{\delta}_m^{(n)} + G_{NN}^{(n)} \bar{\delta}_N^{(n)} \\ &= G_{N1}^{(n)} \bar{\delta}_1^{(n)} + \bar{\delta}_m^{(n)} \left(G_{Nm}^{(n)} + G_{NN}^{(n)} \right). \end{aligned}$$

Therefore

$$U_N^{(n)} = -\frac{\zeta Q}{\mu_T \xi} \left(\eta_1^{(n)} \gamma_1 G_{N1}^{(n)} - \eta_m^{(n)} \gamma_m \left(G_{Nm}^{(n)} + G_{NN}^{(n)} \right) \right). \quad (2.5.6)$$

Substituting equations (2.5.5) and (2.5.6) into equation (2.5.4) gives

$$Z_E = \frac{Z_T}{C_0 q \mu_T \xi} \left(1 + \frac{\zeta^2 C_0}{\mu_T \xi} \left(\gamma_1 \eta_1^{(n)} \left(G_{N1}^{(n)} - G_{11}^{(n)} \right) + \gamma_m \eta_m^{(n)} \left(-G_{Nm}^{(n)} - G_{NN}^{(n)} + 2G_{1m}^{(n)} \right) \right) \right),$$

and so

$$Z_E = \frac{Z_T}{C_0 q \mu_T \xi} \left(1 + \frac{\zeta^2 C_0}{\mu_T \xi} (\sigma_1 + \sigma_2) \right)$$

where

$$\sigma_1 = \gamma_1 \eta_1^{(n)} \left(G_{N1}^{(n)} - G_{11}^{(n)} \right) \quad \text{and} \quad \sigma_2 = \gamma_m \eta_m^{(n)} \left(-G_{Nm}^{(n)} - G_{NN}^{(n)} + 2G_{1m}^{(n)} \right),$$

and $G_{N1}^{(n)} = G_{Nm}^{(n)} = G_{1m}^{(n)} = y$ is given by equations (2.4.18) and (2.4.24) and $G_{11}^{(n)} = G_{NN}^{(n)} = x$ is given by equations (2.4.14) and (2.4.23). Hence, the non-dimensionalised electrical impedance (\hat{Z}_E) is given by

$$\hat{Z}_E(f; n) = \frac{Z_E}{Z_0} = \frac{Z_T}{C_0 q \mu_T \xi Z_0} \left(1 + \frac{\zeta^2 C_0}{\mu_T \xi} (\sigma_1 + \sigma_2) \right) \quad (2.5.7)$$

where Z_0 is the series electrical impedance load in the connecting circuitry. This can be compared with the non-dimensionalised form for the electrical impedance of the standard (Euclidean) transducer ($\bar{\bar{Z}}_E$) [6,8,149]

$$\bar{\bar{Z}}_E(f) = \frac{1}{q C_0 Z_0} \left(1 - \frac{\zeta^2 C_0}{2q Z_T} (K_F T_F + K_B T_B) \right), \quad (2.5.8)$$

where $T_F = 2Z_T/(Z_T + Z_L)$, $T_B = 2Z_T/(Z_T + Z_B)$ are non-dimensional transmission coefficients, K_F and K_B are also non-dimensional and are given by

$$K_F = \frac{(1 - e^{-q\tau})(1 - R_B e^{-q\tau})}{(1 - R_F R_B e^{-2q\tau})}$$

and

$$K_B = \frac{(1 - e^{-q\tau})(1 - R_F e^{-q\tau})}{(1 - R_F R_B e^{-2q\tau})}$$

where $R_F = (Z_T - Z_L)/(Z_T + Z_L)$, $R_B = (Z_T - Z_B)/(Z_T + Z_B)$ are non-dimensionalised reflection coefficients and $\tau = L/c_T$ is the wave transit time across the device. In order to calculate the transmission sensitivity, consider the circuit shown in Figure 2.9. The current across the transducer I_T is given by [8]

$$I_T = \frac{aV}{Z_E + b} \quad (2.5.9)$$

where $a = Z_P/(Z_0 + Z_P)$, $b = Z_0 Z_P/(Z_0 + Z_P)$ and Z_P is parallel electrical impedance load. Continuity of force at the front face given by equation (2.3.53) and continuity of displacement given by equation (2.3.49) (with $A_L = 0$) gives

$$F_F = F_L(x_L = 0) = A_r \mu_L \left(\frac{qc_T}{hc_L} \right) U_C. \quad (2.5.10)$$

Substituting equation (2.3.57) into equation (2.5.10) gives

$$F_F = A_r \mu_L \left(\frac{qc_T}{hc_L} \right) (\gamma_m U_m + \delta_m).$$

From equations (2.3.58) and (2.3.59) with $A_L = 0$ then

$$F_F = A_r \mu_L \left(\frac{qc_T}{hc_L} \right) \left(\gamma_m U_m + \gamma_m \frac{\zeta Q}{\mu_T \xi} \right).$$

Therefore

$$F_F = \frac{\xi \mu_L qc_T}{c_L} \gamma_m \left(U_m + \frac{\zeta Q}{\mu_T \xi} \right), \quad (2.5.11)$$

since $\xi = A_r/h$. To obtain U_m we make use of equation (2.4.1) to obtain

$$U_m^{(n)} = -\frac{\zeta Q}{\mu_T \xi} \left(\eta_1^{(n)} \gamma_1 G_{m1}^{(n)} - \eta_m^{(n)} \gamma_m \left(G_{mm}^{(n)} + G_{mN}^{(n)} \right) \right).$$

Therefore equation (2.5.11) becomes

$$F_F = \frac{\mu_L q c_T}{c_L} \left(\frac{\zeta Q}{\mu_T} \right) \gamma_m \left(-\eta_1^{(n)} \gamma_1 G_{m1}^{(n)} + \eta_m^{(n)} \gamma_m \left(G_{mm}^{(n)} + G_{mN}^{(n)} \right) + 1 \right). \quad (2.5.12)$$

Substituting equation (2.5.9) into equation (2.5.2) gives

$$Q = \frac{aV Z_T}{(Z_E + b)q\mu_T \xi}, \quad (2.5.13)$$

then substituting this into equation (2.5.12) gives

$$\frac{F_F}{V} = \frac{Z_L \zeta a}{(Z_E + b)\mu_T \xi} \gamma_m \left(-\eta_1^{(n)} \gamma_1 G_{m1}^{(n)} + \eta_m^{(n)} \gamma_m \left(G_{mm}^{(n)} + G_{mN}^{(n)} \right) + 1 \right),$$

since $Z_L = \mu_L A_r / c_L$, and so

$$\frac{F_F}{V} = \frac{Z_L \zeta a}{(Z_E + b)\mu_T \xi} K^{(n)}$$

where

$$K^{(n)} = \gamma_m \left(-\eta_1^{(n)} \gamma_1 G_{m1}^{(n)} + \eta_m^{(n)} \gamma_m \left(G_{mm}^{(n)} + G_{mN}^{(n)} \right) + 1 \right).$$

The non-dimensionalised transmission sensitivity (ψ_F) is then given by

$$\psi_F(f; n) = \frac{F_F}{V} \left(\frac{1}{\zeta C_0} \right) = \frac{aZ_L}{(Z_E + b)\mu_T \xi C_0} K^{(n)}. \quad (2.5.14)$$

This expression can be compared to the equivalent transmission sensitivity (ψ_E) in the standard (Euclidean) design [6,8,149]

$$\psi_E(f) = \frac{F_E}{V} \left(\frac{1}{\zeta C_0} \right) = -\frac{aA_T \hat{\lambda} K_F}{2C_0} \left(1 - \frac{\zeta^2 \hat{\lambda} (K_F T_F + K_B T_B)}{2qZ_T} \right)^{-1}, \quad (2.5.15)$$

where F_E the force produced at the front face of the standard transducer, $\hat{\lambda} = C_0/(1 + qC_0b)$ and $A_T = 2Z_L/(Z_L + Z_T)$ are dimensionless constants.

2.6 Reception sensitivity

In reception mode A_L is now non zero because the front face will be subject to a force (given by the incoming signal). From equations (2.3.59) and (2.3.62)

$$U_1^{(n)} = -\frac{\zeta Q}{\mu_T \xi} \eta_1^{(n)} \gamma_1 G_{11}^{(n)} + \left(\frac{\zeta Q}{\mu_T \xi} - 2A_L q \frac{Z_L}{Z_T} \right) 2\eta_m^{(n)} \gamma_m G_{1m}^{(n)}$$

and

$$U_N^{(n)} = -\frac{\zeta Q}{\mu_T \xi} \eta_1^{(n)} \gamma_1 G_{N1}^{(n)} + \left(\frac{\zeta Q}{\mu_T \xi} - 2A_L q \frac{Z_L}{Z_T} \right) \eta_m^{(n)} \gamma_m \left(G_{Nm}^{(n)} + G_{NN}^{(n)} \right).$$

Putting these into equation (2.5.1) gives

$$\begin{aligned} V_F &= \frac{\zeta^2 Q}{\mu_T \xi} \eta_1^{(n)} \gamma_1 \left(G_{N1}^{(n)} - G_{11}^{(n)} \right) + \left(\frac{\zeta^2 Q}{\mu_T \xi} - 2\zeta A_L q \frac{Z_L}{Z_T} \right) \eta_m^{(n)} \gamma_m \\ &\quad \left(2G_{1m}^{(n)} - G_{Nm}^{(n)} - G_{NN}^{(n)} \right) + \frac{Q}{C_0}. \end{aligned}$$

Then

$$V_F = \frac{\zeta^2 Q}{\mu_T \xi} \sigma_1 + \frac{\zeta^2 Q}{\mu_T \xi} \sigma_2 - 2\zeta A_L q \frac{Z_L}{Z_T} \sigma_2 + \frac{Q}{C_0}$$

and so

$$V_F = Q \left(\frac{\zeta^2}{\mu_T \xi} (\sigma_1 + \sigma_2) + \frac{1}{C_0} \right) - 2\zeta A_L q \frac{Z_L}{Z_T} \sigma_2. \quad (2.6.1)$$

From equation (2.3.52) the force in the load ($\zeta = 0$) is given by

$$F = A_r \mu_L \frac{d\bar{u}_L}{dx_L}. \quad (2.6.2)$$

From equation (2.3.46)

$$\frac{d\bar{u}_L}{dx_L} = \left(\frac{qc_T}{hc_L} \right) (B_L e^{(qc_T x_L / hc_L)} - A_L e^{(-qc_T x_L / hc_L)}),$$

and so, at $x_L = 0$,

$$\frac{d\bar{u}_L}{dx_L} = \left(\frac{qc_T}{hc_L} \right) (-A_L),$$

since in receiving mode $B_L = 0$. Substituting this into equation (2.6.2) we get

$$F = \frac{\xi qc_T Z_L}{A_r} (-A_L).$$

Then

$$A_L = \frac{-F A_r}{\xi qc_T Z_L}.$$

Substituting this and equation (2.5.13) into equation (2.6.1) becomes

$$V_F = \frac{a V_F Z_T}{(Z_E + b) q \mu_T \xi} \left(\frac{\zeta^2}{\mu_T \xi} (\sigma_1 + \sigma_2) + \frac{1}{C_0} \right) + \frac{2F \zeta \sigma_2}{\xi \mu_T},$$

since $\mu_T = Z_T c_T / A_r$, and so

$$V_F \left(1 - \frac{a Z_T}{(Z_E + b) q \mu_T \xi} \left(\frac{\zeta^2}{\mu_T \xi} (\sigma_1 + \sigma_2) + \frac{1}{C_0} \right) \right) = \frac{2F \zeta \sigma_2}{\xi \mu_T},$$

and hence

$$\frac{V_F}{F} = \frac{2\zeta\sigma_2}{\xi\mu_T} \left(1 - \frac{aZ_T\zeta^2(\sigma_1 + \sigma_2)}{(Z_E + b)q\mu_T^2\xi^2} - \frac{aZ_T}{(Z_E + b)q\mu_T\xi C_0} \right)^{-1}.$$

The non-dimensionalised reception sensitivity (ϕ_F) is then

$$\begin{aligned} \phi_F(f; n) &= \frac{V_F}{F}(e_{24}L) \\ &= \frac{2\zeta e_{24}L\sigma_2}{\xi\mu_T} \left(1 - \frac{aZ_T\zeta^2(\sigma_1 + \sigma_2)}{(Z_E + b)q\mu_T^2\xi^2} - \frac{aZ_T}{(Z_E + b)q\mu_T\xi C_0} \right)^{-1}. \end{aligned} \quad (2.6.3)$$

This expression can be compared to the equivalent reception sensitivity (ϕ_E) in the standard (Euclidean) design [6,8,149]

$$\phi_E(f) = \frac{V_E}{F}(e_{24}L) = \frac{-\zeta T_F K_F \hat{\lambda}_* e_{24}L}{qZ_T} \left(1 - \frac{\zeta^2 \hat{\lambda}_* (K_F T_F + K_B T_B)}{2q^2 Z_T Z_E} \right)^{-1}, \quad (2.6.4)$$

where V_E the voltage produced by the standard transducer and $\hat{\lambda}_* = qC_0b/(1 + qC_0b)$. Having derived expressions for the main operating characteristics of this new device it is necessary to compare these with those of a standard device to assess any practical benefits arising from this novel design.

2.7 Steady state solutions

The fractal case arises when we allow the generation level n to tend to infinity and we assume that the recursion relationships converge to a steady state (we denote these steady state solutions by a * superscript). Note we will examine the convergence of these recursion relationships later when we consider the pre-fractal SG(3) transducer (finite generation levels).

Case A: $\hat{y}^* = 0$

If $\hat{y}^* = 0$ then equation (2.4.9) is automatically satisfied (since $\hat{X} = \hat{x} = \hat{x}^*$) and from equations (2.4.10) and (2.4.11) we get

$$\hat{G}_{e1}^* = -\beta\hat{x}^*\hat{G}_{b1}^* \quad (2.7.1)$$

and

$$\hat{G}_{b1}^* = -\beta\hat{x}^*\hat{G}_{e1}^*. \quad (2.7.2)$$

Substituting equation (2.7.1) into equation (2.7.2) gives

$$\hat{G}_{b1}^* (1 - \beta^2\hat{x}^{*2}) = 0.$$

Therefore $\hat{G}_{b1}^* = 0$ or $\hat{x}^* = \pm 1/\beta$. In the former case then $\hat{G}_{e1}^* = 0$ and in the latter case $\hat{G}_{b1}^* = \mp\hat{G}_{e1}^*$. From equation (2.4.12) we get

$$\hat{G}_{z1}^*(1 + \beta\hat{x}^*) = 0.$$

Therefore $\hat{G}_{z1}^* = 0$ or $\hat{x}^* = -1/\beta$. Now bringing in the boundary conditions equation (2.4.25) gives

$$z = \frac{\hat{x}^*}{1 - \hat{x}^*\bar{\gamma}_m}$$

where $\hat{x}^* \neq 1/\bar{\gamma}_m$. From equation (2.4.23) we get

$$x = \frac{\hat{x}^*}{1 - \hat{x}^*\bar{\gamma}_1}$$

where $\hat{x}^* \neq 1/\bar{\gamma}_1$. From equation (2.4.20) we get

$$y = \hat{x}^*\bar{\gamma}_m y.$$

That is

$$y = 0$$

since $\hat{x}^* \neq 1/\bar{\gamma}_m$. From equation (2.4.22) we get

$$w = \hat{x}^* \bar{\gamma}_m w.$$

That is

$$w = 0$$

since $\hat{x}^* \neq 1/\bar{\gamma}_m$. In the case where $\hat{G}_{b1}^* = \hat{G}_{e1}^* = \hat{G}_{z1}^* = 0$ we denote the solution as $x^* = \chi$, $\chi \in \mathbb{C}$ and in the case where $\hat{x}^* = \pm 1/\beta$ we denote the solutions as $\hat{G}_{b1}^* = \mp \lambda$, $\hat{G}_{e1}^* = \mp \lambda$ and $\hat{G}_{z1}^* = \theta$ (or 0 when $\hat{x}^* = 1/\beta$) where $\lambda, \theta \in \mathbb{C}$. The full set of solutions are summarised in the table below.

Case	\hat{x}^*	\hat{y}^*	\hat{G}_{b1}^*	\hat{G}_{e1}^*	\hat{G}_{z1}^*	x	y	w	z	note
A1	$\frac{-1}{\beta}$	0	λ	$-\lambda$	θ	$\frac{-1}{\beta + \bar{\gamma}_1}$	0	0	$\frac{-1}{\beta + \bar{\gamma}_m}$	$\beta \neq \bar{\gamma}_1, \beta \neq \bar{\gamma}_m$
A2	$\frac{1}{\beta}$	0	$-\lambda$	λ	0	$\frac{1}{\beta - \bar{\gamma}_1}$	0	0	$\frac{1}{\beta - \bar{\gamma}_m}$	$\beta \neq \bar{\gamma}_1, \beta \neq \bar{\gamma}_m$
A3	χ	0	0	0	0	$\frac{\chi}{1 - \chi \bar{\gamma}_1}$	0	0	$\frac{\chi}{1 - \chi \bar{\gamma}_m}$	$\bar{\gamma}_1 \neq \frac{1}{\chi}, \bar{\gamma}_m \neq \frac{1}{\chi}, \chi \neq \pm \frac{1}{\beta}$

Case B: $\hat{y}^* \neq 0$

If $\hat{y}^* \neq 0$ then from equation (2.4.9) we get

$$-2\beta \hat{y}^* \hat{G}_{e1}^* = 0$$

since $\hat{X} = \hat{x} = \hat{x}^*$ and $\hat{Y} = \hat{y} = \hat{y}^*$. That is

$$\hat{G}_{\epsilon 1}^* = 0$$

since $\beta \neq 0$, $\hat{y}^* \neq 0$. Substituting this into equations (2.4.10) and (2.4.11) we get

$$\hat{x}^* \hat{G}_{b1}^* + \hat{y}^* \hat{G}_{z1}^* = 0 \quad (2.7.3)$$

and

$$\hat{G}_{b1}^* = \hat{y}^*. \quad (2.7.4)$$

Substituting equation (2.7.4) into equation (2.7.3) gives

$$\hat{G}_{z1}^* = -\hat{x}^*. \quad (2.7.5)$$

Substituting equations (2.7.4) and (2.7.5) into equation (2.4.12) gives

$$\hat{x}^* + \beta \hat{x}^{*2} - \beta \hat{y}^{*2} = 0. \quad (2.7.6)$$

Note that $\hat{x}^* \neq 0$ since this would imply that \hat{y}^* was zero. Also substituting equations (2.7.4) and (2.7.5) into equation (2.4.17) gives

$$\hat{y}^* = -\beta \hat{y}^* (\hat{y}^* - \hat{x}^*).$$

That is

$$\hat{y}^* = \hat{x}^* - \frac{1}{\beta}. \quad (2.7.7)$$

Putting this into equation (2.7.6) gives

$$\hat{x}^* = \frac{1}{3\beta}. \quad (2.7.8)$$

Putting this into equation (2.7.7) gives

$$\hat{y}^* = \frac{-2}{3\beta}. \quad (2.7.9)$$

Now putting equations (2.7.8) and (2.7.9) into the boundary conditions equation (2.4.24) gives

$$y = \frac{-2\beta}{3\beta^2 - 3\bar{\gamma}_1\bar{\gamma}_m + \beta(-\bar{\gamma}_1 + \bar{\gamma}_m)}. \quad (2.7.10)$$

Putting equations (2.7.8),(2.7.9) and (2.7.10) into equations (2.4.23) and (2.4.26) gives

$$x = \frac{\beta + 3\bar{\gamma}_m}{3\beta^2 - \beta\bar{\gamma}_1 + \beta\bar{\gamma}_m - 3\bar{\gamma}_1\bar{\gamma}_m}$$

and

$$w = \frac{-2\beta(\beta - \bar{\gamma}_1)}{(\beta - \bar{\gamma}_m)(3\beta^2 - 3\bar{\gamma}_1\bar{\gamma}_m + \beta(-\bar{\gamma}_1 - \bar{\gamma}_m))}. \quad (2.7.11)$$

Substituting equations (2.7.8),(2.7.9),(2.7.10) and (2.7.11) into equation (2.4.25) gives

$$z = \frac{\beta^2 - 3\bar{\gamma}_1\bar{\gamma}_m + \beta(\bar{\gamma}_1 + \bar{\gamma}_m)}{(\beta - \bar{\gamma}_m)(3\beta^2 - 3\bar{\gamma}_1\bar{\gamma}_m + \beta(-\bar{\gamma}_1 + \bar{\gamma}_m))}.$$

Note that from equation (2.4.5), $h^{(n)} \rightarrow 0$ and $q^{(n)} \rightarrow 0$ as $n \rightarrow \infty$, and so from equation (2.5.7) the non-dimensionalised electrical impedance tends to infinity ($(\hat{Z}_E(f; n)) \rightarrow \infty$), from equation (2.5.14) the non-dimensionalised transmission sensitivity tends to zero ($\psi_F(f; n) \rightarrow 0$), and from equation (2.3.58) $\gamma_j \rightarrow 1$ and

from equation (2.3.60) $\bar{\gamma}_j \rightarrow \eta_j^*$. From equation (2.3.45) we get

$$\eta_j^* = \begin{cases} \frac{4}{3}, & j = 1 \\ 1, & j = m \text{ or } N. \end{cases}$$

From equation (2.6.3) the non-dimensionalised reception sensitivity is

$$\phi_F^*(f; n) = \frac{2\zeta e_{24} L \sigma_2^*}{\xi \mu_T} \left(1 - \frac{a Z_T (\mu_T \xi + C_0 \zeta^2 (\sigma_1^* + \sigma_2^*))}{\mu_T Z_T \xi + C_0 b q \xi^2 \mu_T^2 + C_0 \zeta^2 Z_T (\sigma_1^* + \sigma_2^*)} \right)^{-1},$$

and, since $q^{(n)} \rightarrow 0$, then

$$\phi_F^*(f; n) = \frac{2\zeta e_{24} L \sigma_2^*}{\xi \mu_T (1 - a)},$$

where

$$\sigma_2^* = \begin{cases} \frac{1}{1+\beta}, & \text{in case A1} \\ \frac{1}{1-\beta}, & \text{in case A2} \\ \frac{\chi}{\chi-1}, & \text{in case A3} \\ \frac{-3(3\beta+4)}{9\beta^2+\beta-12}, & \text{in case B.} \end{cases}$$

2.8 Results

From a practical perspective, these fractal transducers will only be able to be manufactured at low generation levels. The formulation presented above will allow us to compare the fractal design with a conventional (Euclidean) design in terms of the key operating characteristics of the transmission and reception sensitivity spectra [150]. Within each, the presence of higher amplitudes, multiple resonances, and improved bandwidth (the range of frequencies over which the performance exceeds a certain decibel level) are the key performance indicators of interest in this section. The model (equations (2.2.1), (2.2.2), (2.2.4) and (2.2.5)) has been imple-

mented in Mathematica [150]. We have started from fractal generation level $n = 1$ and formed its matrix (equation (2.3.22)). Since this has a very low dimension we simply invert it to produce the initial conditions for the renormalisation equations. These are then iterated to the desired fractal generation level (equations (2.4.2), (2.4.3), (2.4.14) and (2.4.18)) and then put into the electrical impedance, transmission and reception sensitivities (equations (2.5.7), (2.5.14) and (2.6.3)).

2.8.1 Electrical impedance and transmission/reception sensitivities

In Figure 2.13 the overall trend of the curve is that of a capacitor ($1/(C_0 f)$ profile where C_0 is the transducer capacitance and f is the frequency) with prominent resonances. The important features of this plot, that the design engineer is interested in, are the location and magnitude of the first minimum (f_r) and the first maximum (f_a) turning points. The first minimum is where the mechanical resonance (or series resonance) occurs and, as this provides the least resistance to the electrical energy being supplied, is the frequency at which the device should be used in transmission mode; this device will produce its maximum force on the mechanical load at this frequency. The absolute value of the electrical impedance at this frequency ($\hat{Z}_E(f_r)$) is also important since, the lower ($\hat{Z}_E(f_r)$) is, the higher will be the peak transmission sensitivity of the device ($\psi(f_r)$). The first maximum (known as the anti-resonance or parallel resonance frequency) is where the electrical impedance of the device peaks and is therefore the optimal frequency to operate the device in reception mode. From the parameter values for PZT5-H then the piezoelectrically stiffened velocity (c_T) in equation (2.2.11) is approximately 2370 m/s and, with an overall device length of $L = 1$ mm, then the corresponding frequency is approximately $f_a = c_T/(2L) = 1.2$ MHz. This agrees reasonably well

with the reception sensitivity maximum for the homogenised estimate for f_a (the full line in Figure 2.13). Let us start by examining the performance of the first generation graph ($n = 1$).

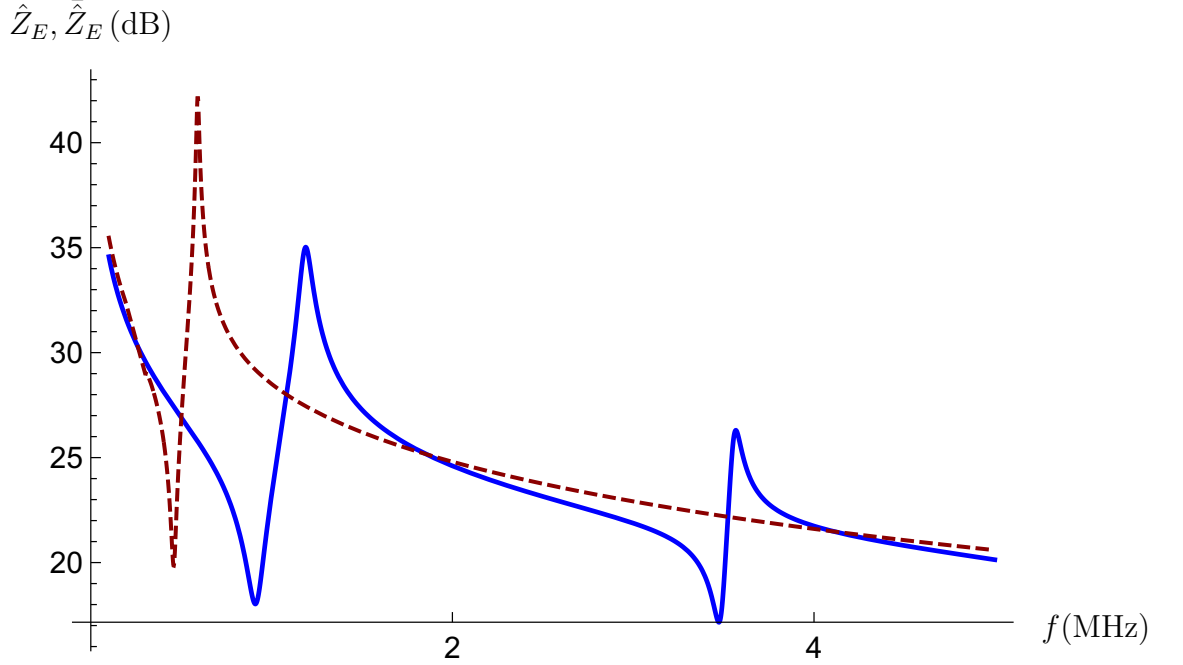


Figure 2.13: Non-dimensionalised electrical impedance (equation (2.5.7)) versus frequency for the SG(3) graph transducer (\hat{Z}_E) at fractal generation level $n = 1$ (dashed line). The non-dimensionalised electrical impedance of the standard (Euclidean) transducer (\tilde{Z}_E) (equation (2.5.8)) is plotted for comparison (full line). Parameter values are given in Appendix A.5.

Figure 2.13 shows that for the standard (Euclidean) design (full line), the mechanical resonance is $f_r = 0.9$ MHz and the electrical resonance is $f_a = 1.2$ MHz. The electrical impedance of the fractal graph has its first resonance at around 0.5 MHz (at a lower frequency than the Euclidean case) and any higher frequency resonances are absent at this stage.

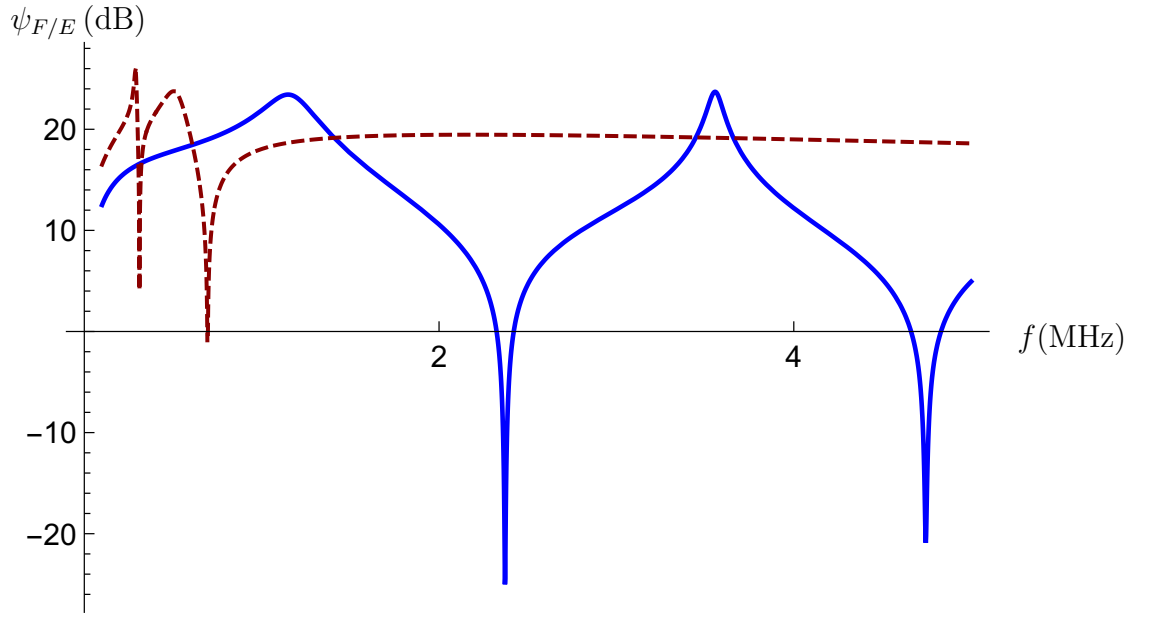


Figure 2.14: Non-dimensionalised transmission sensitivity (equation (2.5.14)) versus frequency for the SG(3) graph transducer (ψ_F) at fractal generation level $n = 1$ (dashed line). The non-dimensionalised transmission sensitivity of the standard (Euclidean) transducer (ψ_E) (equation (2.5.15)) is plotted for comparison (full line). Parameter values are given in Appendix A.5.

As discussed above, the frequency of the first minimum (f_r) in the electrical impedance, corresponds precisely to the first maximum in the transmission sensitivity as shown in Figure 2.14 where the first maximum appears at 0.9 MHz. The transmission sensitivity at generation level $n = 1$ has a maximum amplitude (gain) that is higher than the Euclidean case (standard design) at its lower operating frequency (26 dB at 0.3 MHz compared to 24 dB at 0.9 MHz for the Euclidean case). Although the bandwidth around this peak sensitivity is smaller than that of the Euclidean case. It can be seen, unusually, that the fractal device has a very flat response from 2 MHz upwards at a sensitivity level of 19 dB albeit at a much reduced decibel level from the main peak.

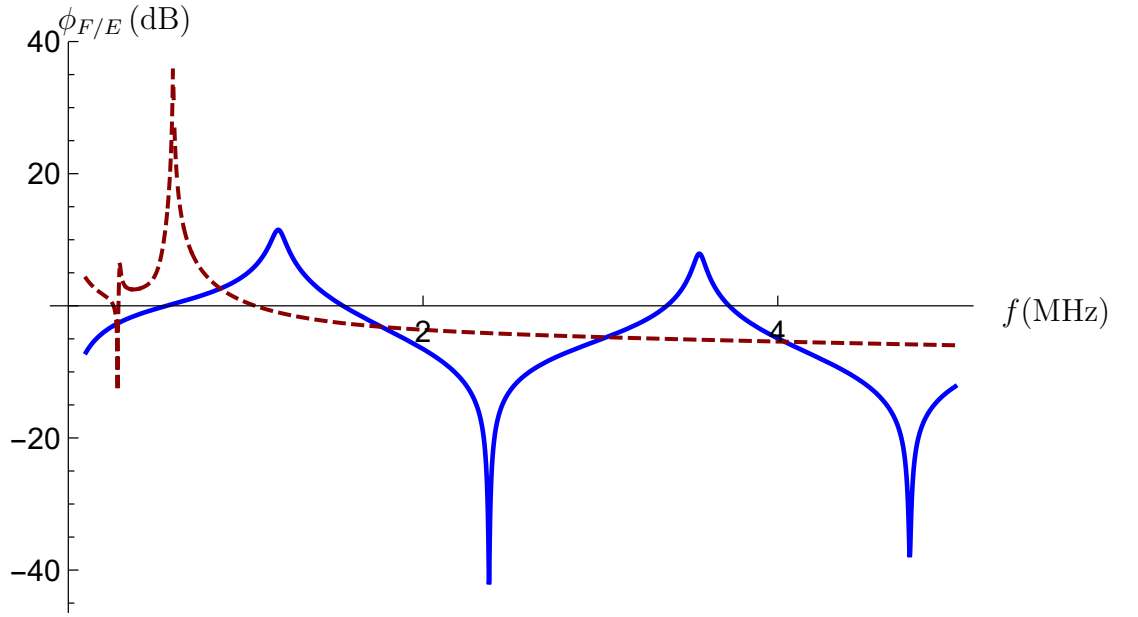


Figure 2.15: Non-dimensionalised reception sensitivity (equation (2.6.3)) versus frequency for the SG(3) graph transducer (ϕ_F) at fractal generation level $n = 1$ (dashed line). The non-dimensionalised reception sensitivity of the standard (Euclidean) transducer (ϕ_E) (equation (2.6.4)) is plotted for comparison (full line). Parameter values are given in Appendix A.5.

Also, the frequency of the first maximum (f_a) of the electrical impedance, corresponds precisely to the first maximum in the reception sensitivity as shown in Figure 2.15, where the first maximum appears at 1.2 MHz. With regard to the reception sensitivity the fractal design at generation level $n = 1$ does show some encouraging results with a much higher peak amplitude than that of the Euclidean case and at a lower operating frequency (at 0.6 MHz its sensitivity is 36 dB whereas the peak sensitivity of the standard device is 12 dB at 1.2 MHz).

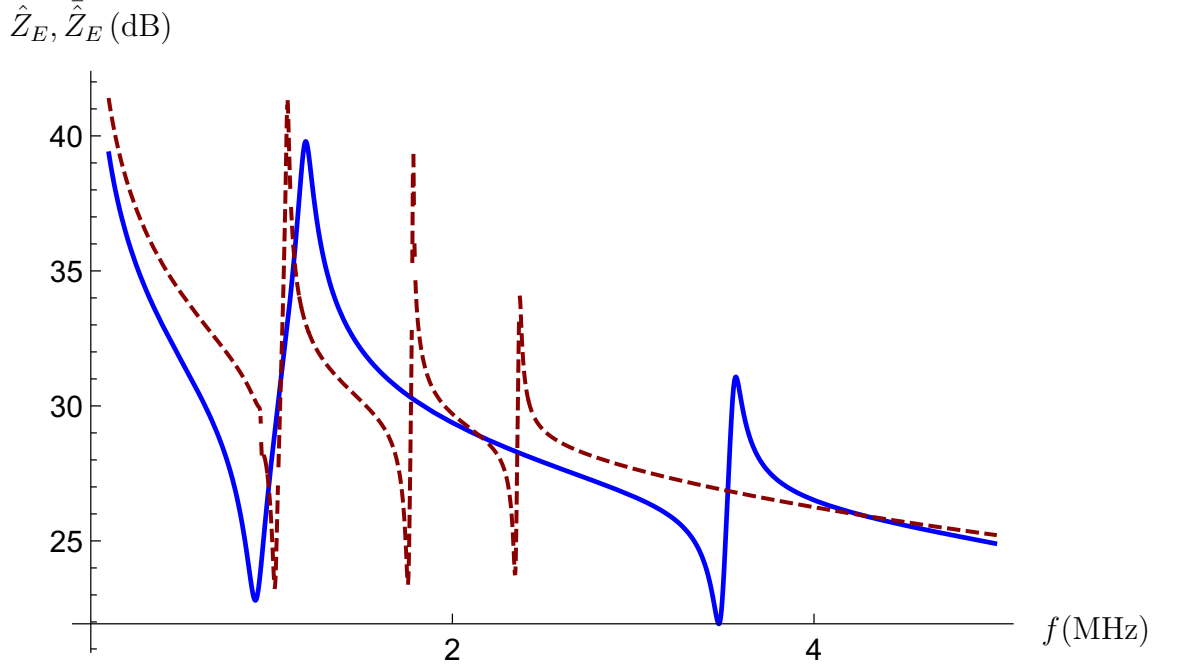


Figure 2.16: Non-dimensionalised electrical impedance (equation (2.5.7)) versus frequency for the SG(3) graph transducer (\hat{Z}_E) at fractal generation level $n = 2$ (dashed line). The non-dimensionalised electrical impedance of the standard (Euclidean) transducer (\bar{Z}_E) (equation (2.5.8)) is plotted for comparison (full line). Parameter values are given in Appendix A.5.

The electrical impedance profile of the fractal design at generation level $n = 2$ and the standard design follow a similar profile with more resonances being present in the fractal case due to the presence of a range of length scales in the new design. Indeed, for all the results that we will show, the resonant modes occur at higher frequencies as the generation level increases (that is, as the length scale of the graph edges decreases).

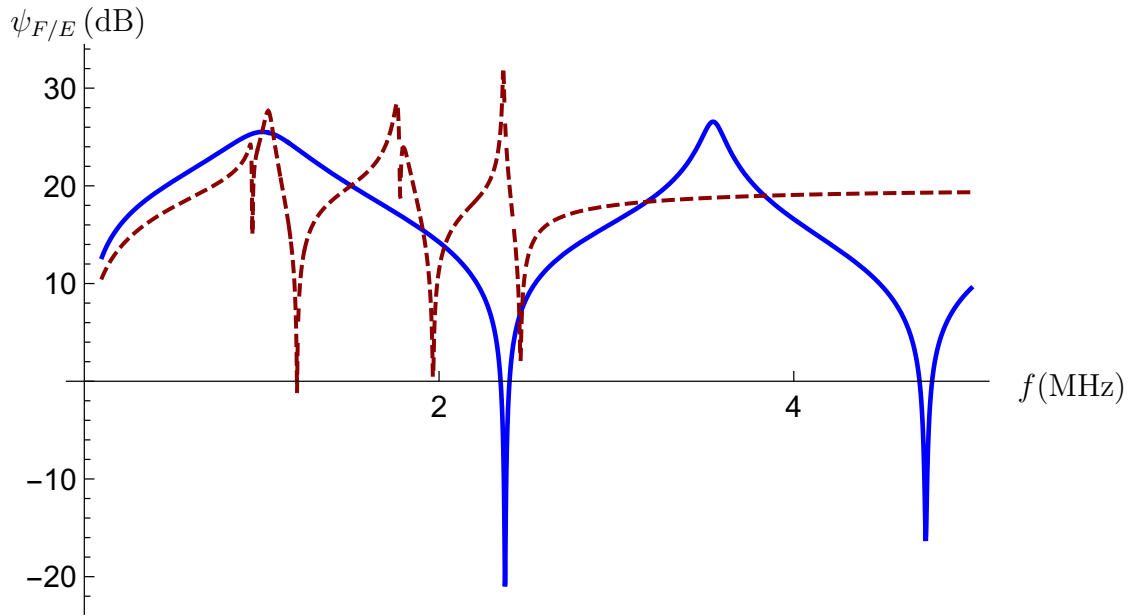


Figure 2.17: Non-dimensionalised transmission sensitivity (equation (2.5.14)) versus frequency for the SG(3) graph transducer (ψ_F) at fractal generation level $n = 2$ (dashed line). The non-dimensionalised transmission sensitivity of the standard (Euclidean) transducer (ψ_E) (equation (2.5.15)) is plotted for comparison (full line). Parameter values are given in Appendix A.5.

In terms of the transmission sensitivity at generation level $n = 2$, the maximum amplitude is somewhat higher in the fractal design than the Euclidean case (32 dB at 2.4 MHz compared to 27 dB at 3.5 MHz for the Euclidean case). Once again the bandwidth around this peak sensitivity is smaller than that of the Euclidean case.

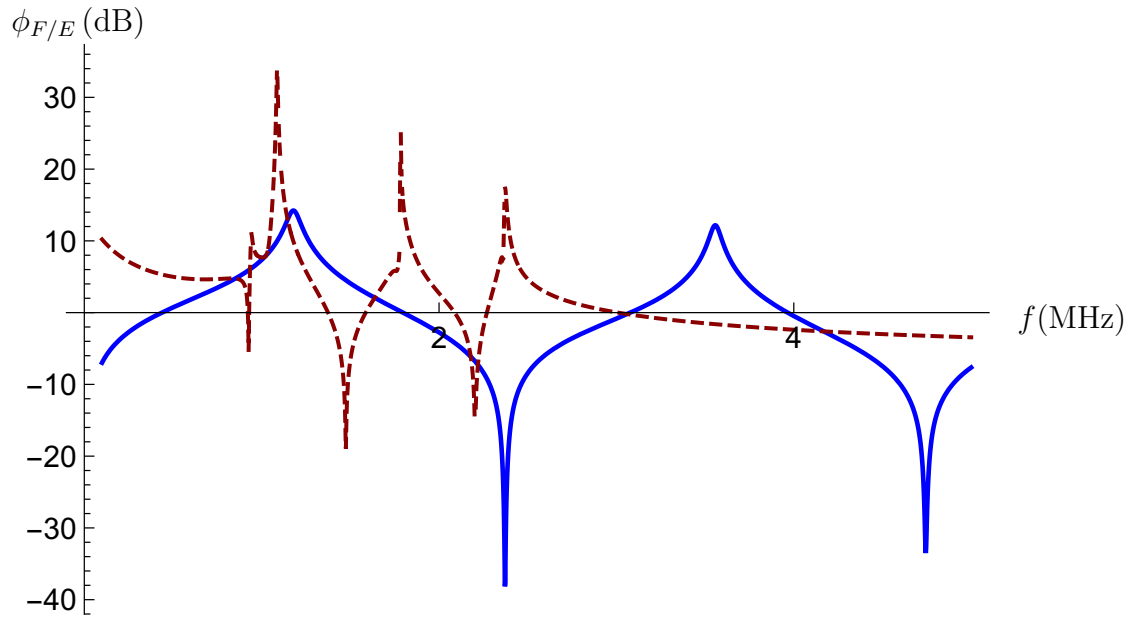


Figure 2.18: Non-dimensionalised reception sensitivity (equation (2.6.3)) versus frequency for the SG(3) graph transducer (ϕ_F) at fractal generation level $n = 2$ (dashed line). The non-dimensionalised reception sensitivity of the standard (Euclidean) transducer (ϕ_E) (equation (2.6.4)) is plotted for comparison (full line). Parameter values are given in Appendix A.5.

The reception sensitivity at generation level $n = 2$ has again a much higher peak amplitude than that of the Euclidean case at its lower operating frequency (at 1 MHz its sensitivity is 34 dB whereas the peak sensitivity of the standard (Euclidean) device is 15 dB at 1.2 MHz).

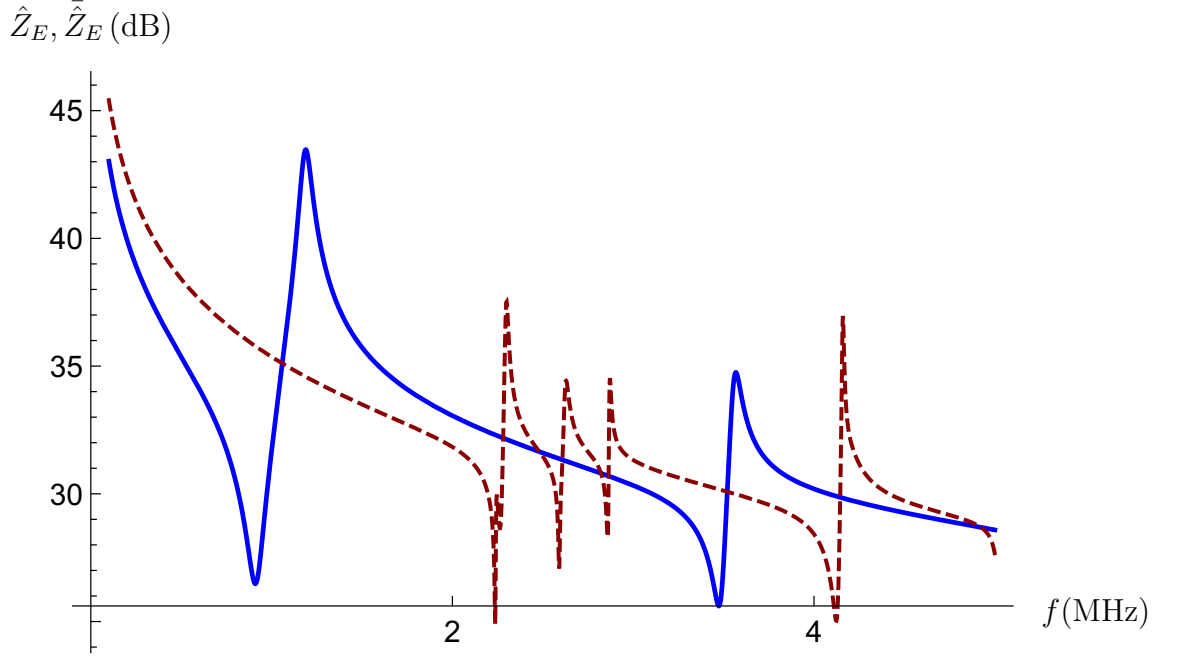


Figure 2.19: Non-dimensionalised electrical impedance (equation (2.5.7)) versus frequency for the SG(3) graph transducer (\hat{Z}_E) at fractal generation level $n = 3$ (dashed line). The non-dimensionalised electrical impedance of the standard (Euclidean) transducer (\tilde{Z}_E) (equation (2.5.8)) is plotted for comparison (full line). Parameter values are given in Appendix A.5.

As the generation level increases a greater range of length scales exist within the fractal design and so an increasing number of resonant modes emerge. For the fractal design the electrical impedance profile has many resonance frequencies at generation level $n = 3$ ($f_r^{(3)} = 2.2$ MHz and $f_a^{(3)} = 2.3$ MHz) and this suggests that it is a complex interaction between the edge lengths in the graph associated with the various generation levels that are causing these resonances; so the internal geometry is dictating the device behaviour as anticipated.

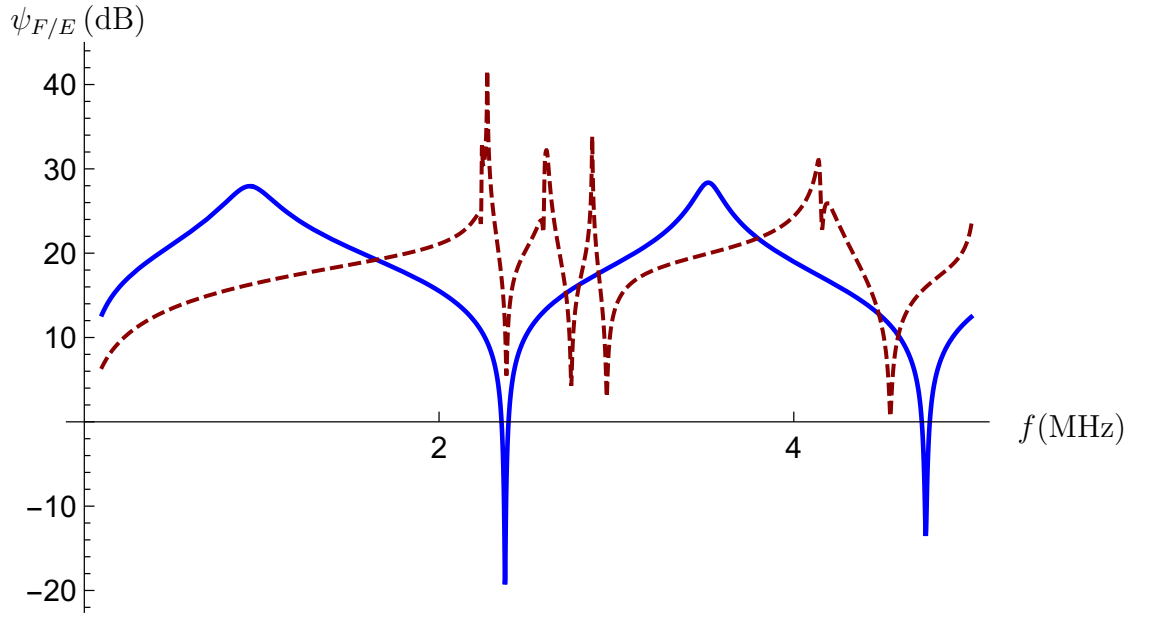


Figure 2.20: Non-dimensionalised transmission sensitivity (equation (2.5.14)) versus frequency for the SG(3) graph transducer (ψ_F) at fractal generation level $n = 3$ (dashed line). The non-dimensionalised transmission sensitivity of the standard (Euclidean) transducer (ψ_E) (equation (2.5.15)) is plotted for comparison (full line). Parameter values are given in Appendix A.5.

As before the transmission sensitivity maximum amplitude at fractal generation level $n = 3$ is higher than the Euclidean case (43 dB at 2.3 MHz compared to 28 dB at 3.5 MHz for the Euclidean case). However, this peak in the transmission sensitivity results in a reduced bandwidth; if we take the noise floor to be 3 dB below the peak gain of the standard transducer (that is 25 dB) then the operational bandwidth of the standard transducer is 0.25 MHz whereas the fractal transducer only has an operational bandwidth of around 0.07 MHz.

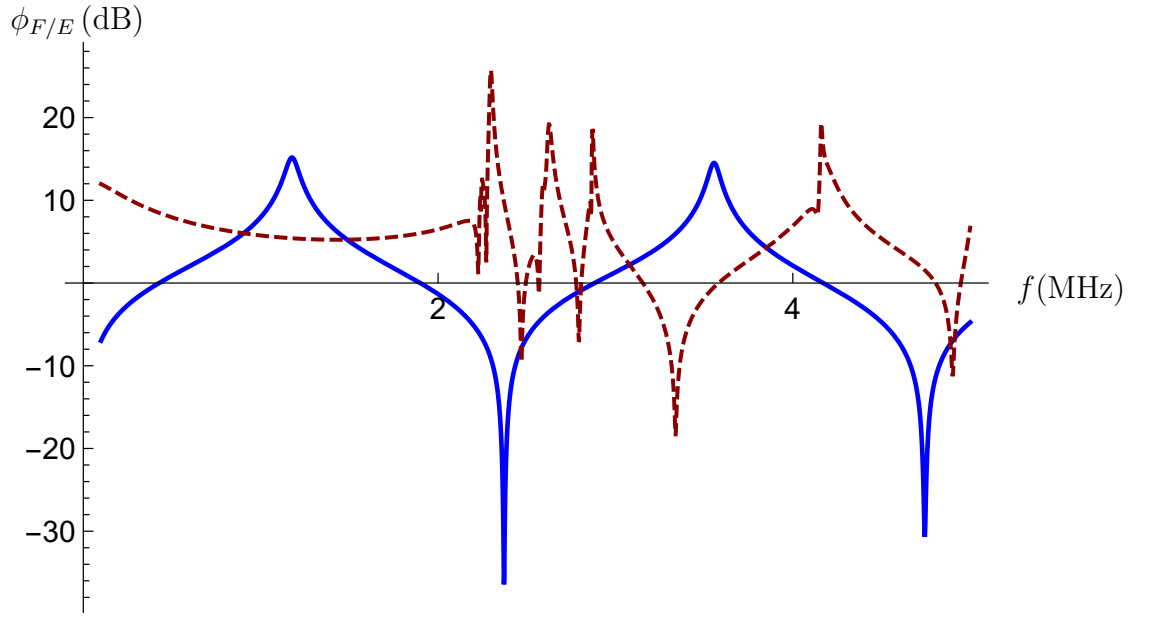


Figure 2.21: Non-dimensionalised reception sensitivity (equation (2.6.3)) versus frequency for the SG(3) graph transducer (ϕ_F) at fractal generation level $n = 3$ (dashed line). The non-dimensionalised reception sensitivity of the standard (Euclidean) transducer (ϕ_E) (equation (2.6.4)) is plotted for comparison (full line). Parameter values are given in Appendix A.5.

The reception sensitivity at fractal generation level $n = 3$ is now more closely matched to the standard design in terms of peak amplitude (at 2.3 MHz its sensitivity is 25 dB and the peak sensitivity of the standard (Euclidean) device is 15 dB at 1.2 MHz). Again, if we take the noise floor to be around 3 dB lower than the peak gain of the standard design (so a 12 dB level) then the operational bandwidth of the fractal design is 0.11 MHz compared to 0.19 MHz from the standard design.

2.8.2 Convergence

The norm of the difference between the energy in the power spectrum at successive generation levels, integrated with respect to frequency, is calculated for the

transmission/reception sensitivities, as follows

$$\sum_{i=1}^m |\psi_F(f_i; n) - \psi_F(f_i; n + 1)| = \psi_F^*(n), \quad (2.8.1)$$

and

$$\sum_{i=1}^m |\phi_F(f_i; n) - \phi_F(f_i; n + 1)| = \phi_F^*(n). \quad (2.8.2)$$

where $\psi_F^*(n)$ and $\phi_F^*(n)$ record the convergence of the transmission and reception sensitivities respectively as the fractal generation level increases. Figures 2.22 and 2.23 shows the dependence of these norms on the generation level.

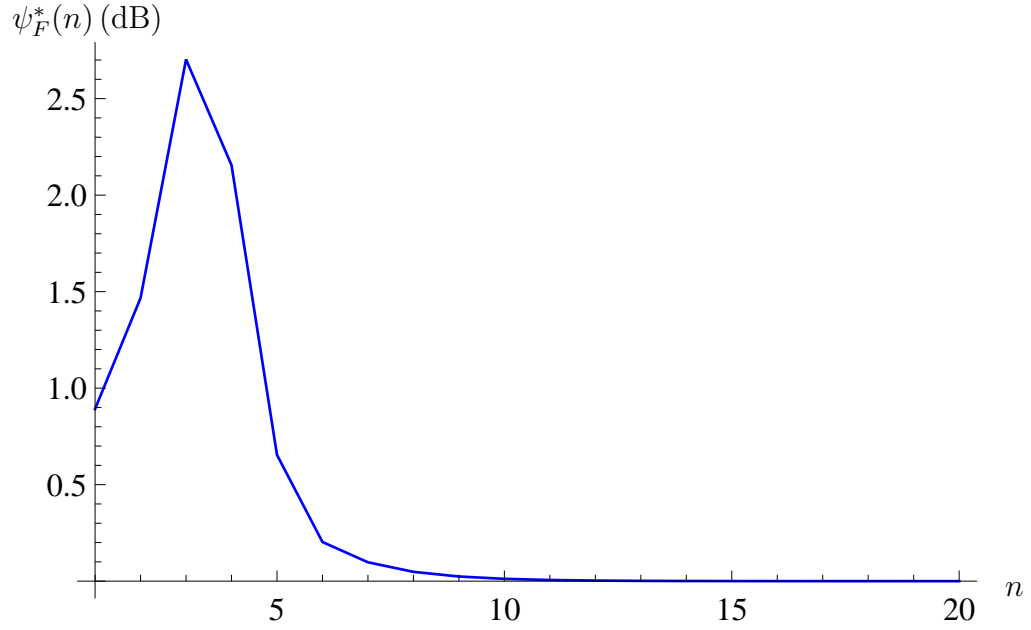


Figure 2.22: Non-dimensionalised transmission sensitivity ($\psi_F^*(n)$) (equation (2.8.1)) converges as the fractal generation level increases. This sensitivity converges by generation level $n = 10$ over this frequency range where $f_i \in [0.1, 10]$ MHz.

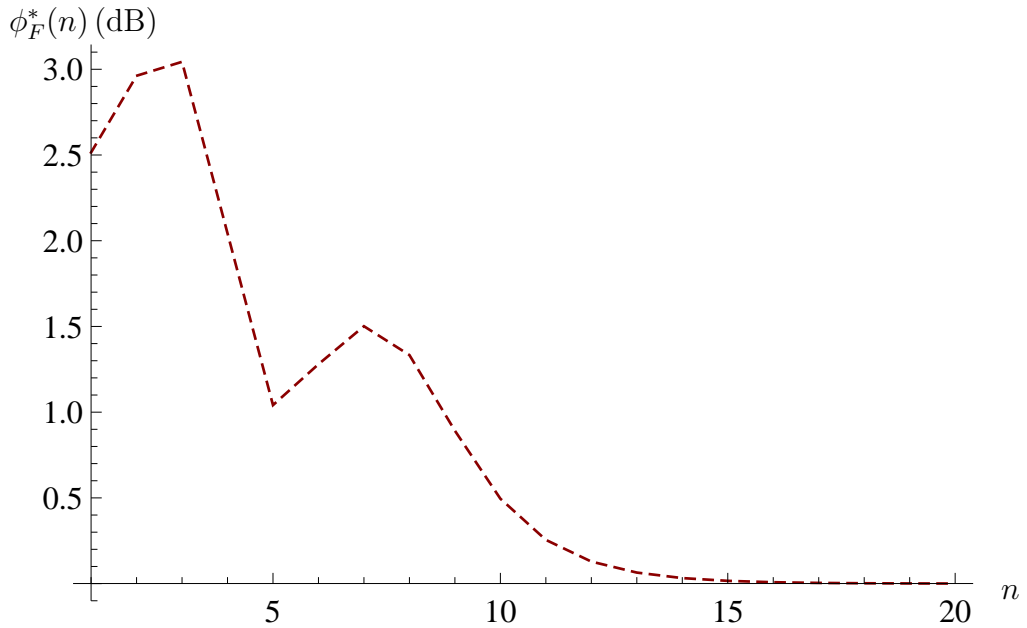


Figure 2.23: Non-dimensionalised reception sensitivity ($\phi_F^*(n)$) (equation (2.8.2)) versus successive generation levels. This sensitivity converges by generation level $n = 16$ over this frequency range where $f_i \in [0.1, 10]$ MHz.

2.9 Conclusions

A model of a piezoelectric ultrasound transducer with a fractal geometry has been constructed and its operational qualities compared with that of a standard (Euclidean) design. The fractal that was used to simulate this self-similar transducer was the Sierpinski gasket [144]. The graph counterpart of the Sierpinski gasket SG(3) [145] was used to express the electrical and mechanical fields in terms of a finite element methodology [7]. As this was the first time that a finite element analysis has been performed on this structure then some new basis functions were derived. The fractal design has multiple length scales (the standard design typically has a single length scale) and, since these are resonating devices, this resulted in a rich set of resonating frequencies. Indeed the broadband resonators found in

nature and in musical instruments rely on this principle. The finite element formulation resulted in a matrix equation whose solution yielded to a renormalisation approach. This is turn led to a small set of recursion relationships for the pivotal Green's functions that drive the calculation of the transmission/reception sensitivities of the device. The focus was on low generation levels of the fractal as these are most likely to adhere to manufacturing constraints. The results showed that the fractal transducer resonates at many more frequencies than the standard (Euclidean) transducer. Importantly, the fractal transducer gave rise to a significantly higher amplitude transmission and reception sensitivity than the standard (Euclidean) design. The convergence of the fractal device's performance as the fractal generation level increases was also considered. It was seen that, in both transmission and reception modes, the outputs converge by generation levels $n = 10$ and $n = 16$ respectively. These encouraging results suggest that it will be worthwhile studying other fractal transducer designs.

Chapter 3

A fractal ultrasonic transducer based on the Sierpinski gasket with both piezoelectric and polymer phases

3.1 Introduction

This chapter builds a model of a composite fractal ultrasound transducer and compare this model's operational qualities with that of a standard (simple) design. We will use a finite element methodology and introduce new basis functions to express the wave fields within the graph. This Galerkin approach leads to a discrete formulation that lends itself to a renormalisation approach. The Sierpinski gasket will be used for the simulation of a self-similar transducer in this chapter [9,10,144,145]. Such an ultrasonic transducer would start with an equilateral triangle of piezoelectric crystal. This equilateral triangle is composed of four

identical equilateral sub-triangles whose side length is half of the original. The first generation ($n = 1$) would be obtained by replacing the central sub-triangle by a polymer material. This process is then repeated for several generations with the removed sub-triangles from the smallest triangles being filled with a polymer (see Figure 3.1). The associated graph is constructed by a process which starts from the order $n = 1$ design (which consists of three piezoelectric triangles and one polymer triangle), assigns a vertex to the centre of each of these triangles and, by connecting these vertices together with edges, the SG(3,4) graph at generation level $n = 1$ is constructed (see Figure 3.2). The polymer triangle has a vertex denoted by a non-filled circle which has degree 3 whereas each piezoelectric triangle has a vertex denoted by a filled circle and has degree 4. The graph has side length L units which remains constant as the generation level n increases. Therefore, as n increases, the length of the edge between adjacent vertices tends to zero and in this limit the graph will perfectly match the space filling properties of the original Sierpinski gasket [7]. The total number of vertices is $3^n + 3^{n-1} = N^{(n)} + 1$ where $N^{(1)} = 3$ and $N^{(2)} = 11$ (see Figures 3.3 and 3.4) and $h^{(n)} = L/(2^n - 1)$ is the edge length between any two adjacent piezoelectric vertices. The piezoelectric vertex degree is 4 (apart from the boundary vertices (input/output vertices) which have degree 3) and $M = (5 \times 3^n - 3)/2$ denotes the total number of edges. These boundary vertices will be used to interact with external loads (both electrical and mechanical) and so we introduce fictitious vertices A, B and C to accommodate these interfacial boundary conditions (see Figures 3.3 and 3.4). Denote by Ω the set of points lying on the edges or vertices of SG(3,4) and denote the region's boundary by $\partial\Omega$. Note that the edges joining the piezoelectric vertices to the polymer vertices are composed of a piezoelectric section (shown by the full line in Figure 3.3 along the edge joining vertex 1 to 4) and a polymer section (shown by

the dashed line along this same edge). In what follows we will retain the freedom to vary the fraction of piezoelectric material in this edge from $\nu = 1$ (piezoelectric material only) to $\nu = 0$ (polymer material only).

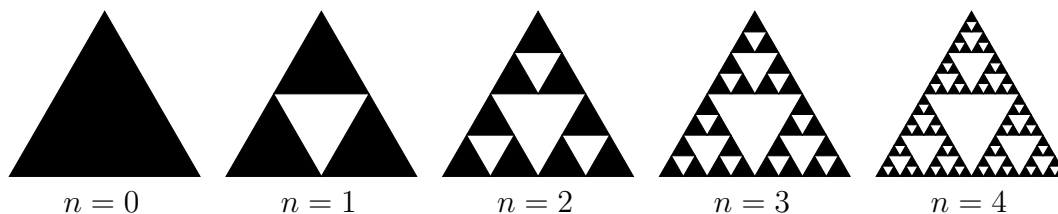


Figure 3.1: The first few generations of the Sierpinski gasket. The black triangles are a piezoelectric material and the *smallest* white triangles are a polymer material.

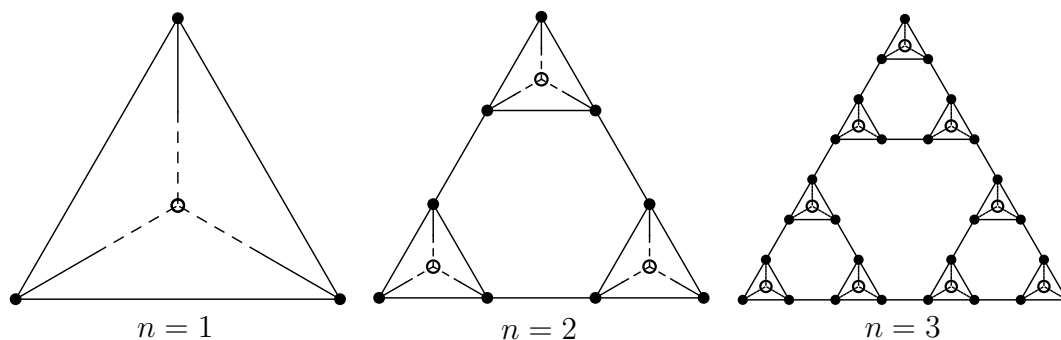


Figure 3.2: The first few generations of the Sierpinski gasket graph $SG(3,4)$.

By introducing the non-dimensionalised variable $\theta = ct/h$ then (temporarily dropping the subscript on u and the superscript on h)

$$\frac{\partial^2 u}{\partial \theta^2} = \frac{h^2}{c_T^2} c^2 \nabla^2 u. \quad (3.1.1)$$

Applying the Laplace transform $\mathcal{L} : \theta \rightarrow q$ then gives

$$q^2 \bar{u} = \frac{h^2}{c_T^2} c^2 \nabla^2 \bar{u}. \quad (3.1.2)$$

We will seek a weak solution $\bar{u} \in H^1(\Omega)$ where on the boundary $\bar{u} = \bar{u}_{\partial\Omega} \in H^1(\partial\Omega)$. Now multiplying by a test function $w \in H_B^1(\Omega)$, where $H_B^1(\Omega) := \{w \in H^1(\Omega) : w = 0 \text{ on } \partial\Omega\}$, integrating over the region Ω , and using Green's first identity $\int_{\Omega} \psi \nabla^2 \phi \, dv = \oint_{\partial\Omega} \psi (\nabla \phi \cdot \underline{n}) \, dr - \int_{\Omega} \nabla \phi \cdot \nabla \psi \, dv$, where \underline{n} is the outward pointing unit normal of surface element dr , gives

$$\int_{\Omega} q^2 \bar{u} w \, d\underline{x} = \frac{h^2}{c_T^2} c^2 \oint_{\partial\Omega} w (\nabla \bar{u} \cdot \underline{n}) \, dr - \frac{h^2}{c_T^2} c^2 \int_{\Omega} \nabla \bar{u} \cdot \nabla w \, d\underline{x}.$$

Now $h^2 \oint_{\partial\Omega} w (\nabla \bar{u} \cdot \underline{n}) \, dr$ is zero since $w = 0$ on $\partial\Omega$ and so, we seek $\bar{u} \in H^1(\Omega)$ such that

$$q^2 \int_{\Omega} \bar{u} w \, d\underline{x} = -\frac{h^2}{c_T^2} c^2 \int_{\Omega} \nabla \bar{u} \cdot \nabla w \, d\underline{x}$$

where $w \in H_B^1(\Omega)$.

3.2 Galerkin discretisation

Using a standard Galerkin method we replace $H^1(\Omega)$ and $H_B^1(\Omega)$ by the finite dimensional subspaces S_S and $S_B = S_S \cap H_B^1(\Omega)$. Let $U_B \in S_S$ be a function that approximates $\bar{u}_{\partial\Omega}$ on $\partial\Omega$, then the discretised problem involves finding $\bar{U} \in S_S$ such that

$$q^2 \int_{\Omega} \bar{U} W \, d\underline{x} = -\frac{h^2}{c_T^2} c^2 \int_{\Omega} \nabla \bar{U} \cdot \nabla W \, d\underline{x},$$

where W is the test function expressed in this finite dimensional space. Let $\{\phi_1, \phi_2, \dots, \phi_N, \phi_{N+1}\}$ form a basis of S_B and set $W = \phi_j$, then

$$q^2 \int_{\Omega} \bar{U} \phi_j \, d\underline{x} = -\frac{h^2}{c_T^2} c^2 \int_{\Omega} \nabla \bar{U} \cdot \nabla \phi_j \, d\underline{x}, \quad j = 1, \dots, N+1. \quad (3.2.1)$$

Furthermore, let ψ_I , $I = \{N + 2, N + 3, N + 4\}$ form a basis for the boundary vertices and let

$$\bar{U} = \sum_{i=1}^{N+1} U_i \phi_i + \sum_{i \in I} U_{B_i} \psi_i. \quad (3.2.2)$$

Hence, equation (3.2.1) becomes

$$\begin{aligned} & \sum_{i=1}^{N+1} \left(q^2 \int_{\Omega} \phi_i \phi_j d\underline{x} + \frac{h^2}{c_T^2} c^2 \int_{\Omega} \nabla \phi_i \cdot \nabla \phi_j d\underline{x} \right) U_i = \\ & - \sum_{i \in I} \left(q^2 \int_{\Omega} \psi_i \phi_j d\underline{x} + \frac{h^2}{c_T^2} c^2 \int_{\Omega} \nabla \psi_i \cdot \nabla \phi_j d\underline{x} \right) U_{B_i} \end{aligned} \quad (3.2.3)$$

where $j \in \{1, 2, \dots, N, N + 1\}$. That is

$$A_{ji} U_i = b_j \quad (3.2.4)$$

where

$$A_{ji} = q^2 \int_{\Omega} \phi_i \phi_j d\underline{x} + \frac{h^2}{c_T^2} c^2 \int_{\Omega} \nabla \phi_i \cdot \nabla \phi_j d\underline{x}, \quad (3.2.5)$$

and

$$b_j = - \sum_{i \in I} \left(q^2 \int_{\Omega} \psi_i \phi_j d\underline{x} + \frac{h^2}{c_T^2} c^2 \int_{\Omega} \nabla \psi_i \cdot \nabla \phi_j d\underline{x} \right) U_{B_i}. \quad (3.2.6)$$

It is important to now explicitly record the fractal generation level n and so equation (3.2.5) can be written

$$A_{ji}^{(n)} = q^2 H_{ji}^{(n)} + \frac{(h^{(n)})^2}{c_T^2} K_{ji}^{(n)}, \quad (3.2.7)$$

where

$$H_{ji}^{(n)} = \int_{\Omega} (\phi_j \phi_i) d\underline{x}, \quad (3.2.8)$$

and

$$K_{ji}^{(n)} = c^2 \int_{\Omega} (\nabla \phi_j \cdot \nabla \phi_i) d\underline{x}. \quad (3.2.9)$$

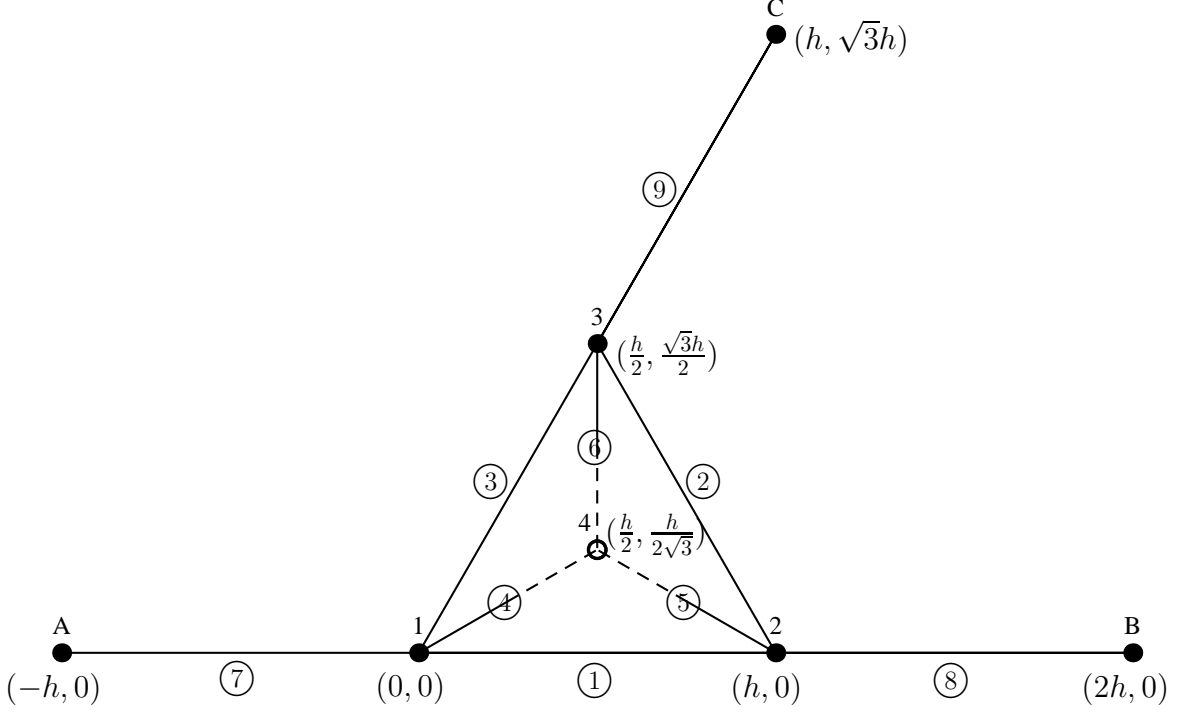


Figure 3.3: The modified Sierpinski Gasket graph SG(3,4) at generation level $n = 1$. Vertices 1, 2 and 3 are the input/output piezoelectric vertices, vertex 4 is a polymer vertex, and vertices A (or 5), B (or 6) and C (or 7) are fictitious vertices used to accommodate the boundary conditions. The graph has 9 elements (circled numbers), with two vertices adjacent to each element.

3.2.1 Transformations of the fundamental basis functions

In this section we will consider transformations of some fundamental basis functions $\hat{\phi}_J$, $\hat{\phi}_K$ and $\hat{\psi}_I$ (see Figures 3.5, 3.6 and 3.7) to get basis functions ϕ_J , ϕ_K and ψ_I at each vertex in the graph. These basis functions will be based on a fundamental basis function for the interior piezoelectric vertices (J), one for the interior polymer vertices (K) and one for the exterior piezoelectric vertices (I).

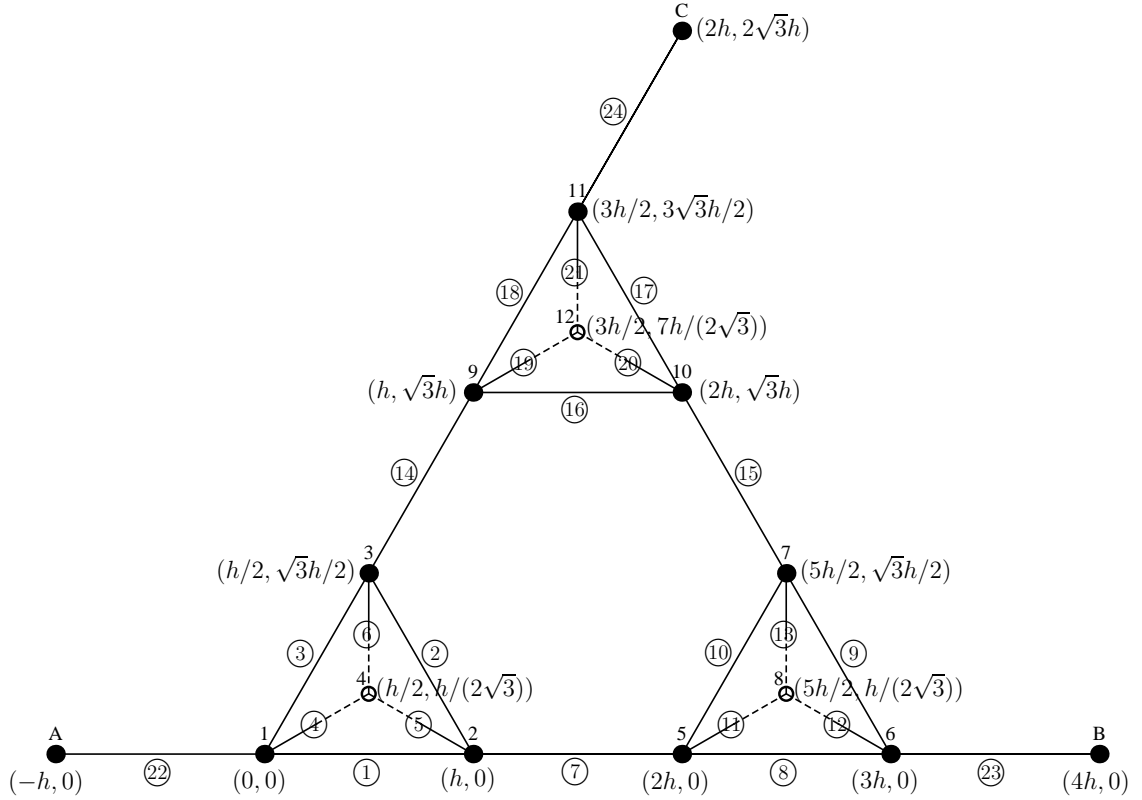


Figure 3.4: The modified Sierpinski Gasket graph $SG(3,4)$ at generation level $n = 2$. Vertices A (or 13), B (or 14) and C (or 15) are fictitious vertices used to accommodate the boundary conditions. The graph has 24 elements (circled numbers), with two vertices adjacent to each element.

We choose the design of the fundamental basis functions $\hat{\phi}_J$ as shown in Figure 3.5 with vertices $(\sqrt{3}h/2, h/2)$, $(\sqrt{3}h/2, -h/2)$, $(h/\sqrt{3}, 0)$ and $(-\sqrt{3}h/2, h/2)$. The $\hat{\phi}_J$ basis function is defined such that (we ease the notation by setting $x_1 = x$, and $x_2 = y$)

$$\hat{\phi}_j(x, y) = \begin{cases} 1 & \text{if } (x, y) = (x_j, y_j) \\ 0 & \text{if } (x, y) = \text{coordinates of vertices adjacent to vertex } j. \end{cases} \quad (3.2.10)$$

The basis functions have a compact support and are identically zero outside the edges that are incident upon the particular vertex.

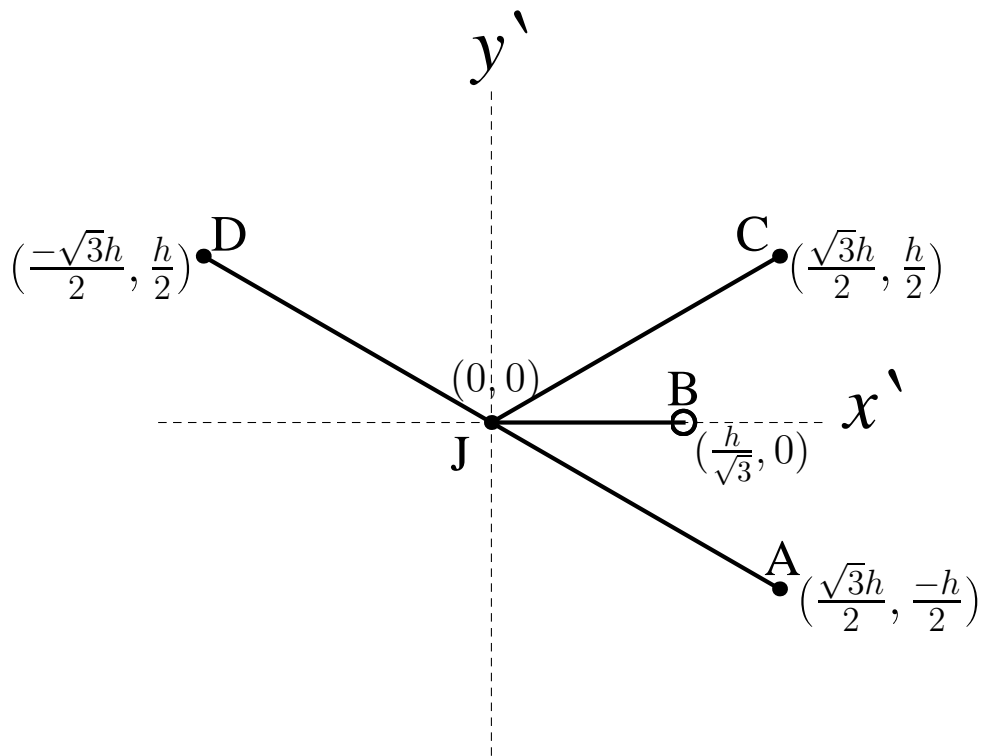


Figure 3.5: Plan view of $\hat{\phi}_J$, the fundamental basis function for the piezoelectric vertices; it is symmetric with respect to the x' axis.

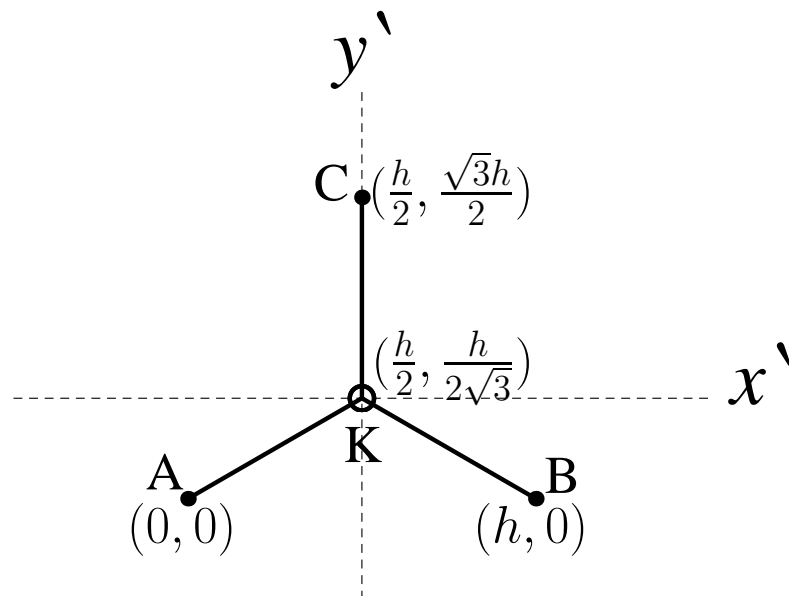


Figure 3.6: Plan view of $\hat{\phi}_K$, the fundamental basis function for the polymer vertices.

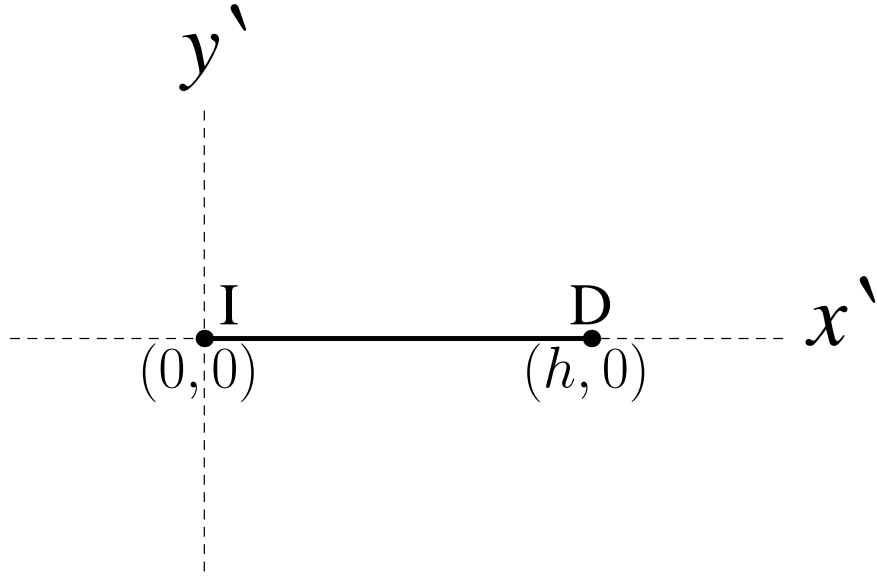


Figure 3.7: Plan view of $\hat{\phi}_I$, the fundamental basis function.

For the fundamental basis functions $\hat{\phi}_J$ (see Figure 3.5) we have five vertices and so the functional form has five unknowns. Setting

$$\hat{\phi}_J(x, y) = a + bx + cy + dx^2 + ey^2, \quad (3.2.11)$$

then, by applying equation (3.2.10), we get

$$\hat{\phi}_J(0, 0) = a = 1, \quad (3.2.12)$$

$$\hat{\phi}_J\left(\frac{h}{\sqrt{3}}, 0\right) = 1 + \frac{h}{\sqrt{3}}b + \frac{h^2}{3}d = 0, \quad (3.2.13)$$

$$\hat{\phi}_J\left(\frac{\sqrt{3}h}{2}, \frac{h}{2}\right) = 1 + \frac{\sqrt{3}}{2}hb + \frac{h}{2}c + \frac{3}{4}h^2d + \frac{h^2}{4}e = 0, \quad (3.2.14)$$

$$\hat{\phi}_J\left(\frac{\sqrt{3}h}{2}, -\frac{h}{2}\right) = 1 + \frac{\sqrt{3}}{2}hb - \frac{h}{2}c + \frac{3}{4}h^2d + \frac{h^2}{4}e = 0 \quad (3.2.15)$$

and

$$\hat{\phi}_J\left(\frac{-\sqrt{3}h}{2}, \frac{h}{2}\right) = 1 - \frac{\sqrt{3}}{2}hb + \frac{h}{2}c + \frac{3}{4}h^2d + \frac{h^2}{4}e = 0. \quad (3.2.16)$$

Equations (3.2.13) to (3.2.16) provide four equations in the four unknowns b, c, d and e , which give $b = 0, c = 0, d = -3/h^2$ and $e = 5/h^2$ and substituting these into equation (3.2.11) gives

$$\hat{\phi}_J(x, y) = 1 - \frac{3}{h^2}x^2 + \frac{5}{h^2}y^2. \quad (3.2.17)$$

Similarly, for the fundamental basis function $\hat{\phi}_K$ (see Figure 3.6), we have four vertices, so we need to form an equation with four unknowns, so consider

$$\hat{\phi}_K(x, y) = a + bx + cy + d(x^2 + y^2). \quad (3.2.18)$$

By applying equation (3.2.10), then we get

$$\hat{\phi}_K(0, 0) = a = 0, \quad (3.2.19)$$

$$\hat{\phi}_K(h, 0) = hb + h^2d = 0, \quad (3.2.20)$$

$$\hat{\phi}_K\left(\frac{h}{2}, \frac{\sqrt{3}h}{2}\right) = \frac{h}{2}b + \frac{\sqrt{3}h}{2}c + h^2d = 0 \quad (3.2.21)$$

and

$$\hat{\phi}_K\left(\frac{h}{2}, \frac{h}{2\sqrt{3}}\right) = \frac{h}{2}b + \frac{h}{2\sqrt{3}}c + \frac{h^2}{3}d = 1. \quad (3.2.22)$$

Equations (3.2.20) to (3.2.22) provide three equations in the three unknowns b, c and d , which gives $b = 3/h, c = \sqrt{3}/h$ and $d = -3/h^2$, and substituting these into equations (3.2.18) gives

$$\hat{\phi}_K(x, y) = \frac{3}{h}x + \frac{\sqrt{3}}{h}y - \frac{3}{h^2}(x^2 + y^2). \quad (3.2.23)$$

Similarly, for the fundamental basis functions $\hat{\psi}_I$ (see Figure 3.7), we have two

vertices, so consider

$$\hat{\psi}_I(x, y) = a + d(x^2 + y^2). \quad (3.2.24)$$

By applying equation (3.2.10), we get

$$\hat{\psi}_I(0, 0) = a = 1$$

and

$$\hat{\psi}_I(h, 0) = 1 + h^2d = 0.$$

This equation gives $d = -1/h^2$, and substituting this into equation (3.2.24) gives

$$\hat{\psi}_I(x, y) = 1 - \frac{1}{h^2}(x^2 + y^2). \quad (3.2.25)$$

Having established the fundamental (canonical) basis functions for each type of vertex in the graph we now need to calculate the specific basis functions for each vertex. In order to do this each fundamental basis function is mapped onto the specific vertex by a series of transformations such as a translation, a rotation, or a reflection in the x or y axis. This has to be performed for each vertex in the graph and below we illustrate the process by detailing the transformations for a small subset of these vertices. The form of the basis function centred on vertex 1 at fractal generation level $n = 1$ is obtained by relating it to the canonical basis function $\hat{\phi}_J$ shown in Figure 3.5 as given by equation (3.2.17) (with respect to the (x', y') coordinate frame shown in red in Figure 3.8).

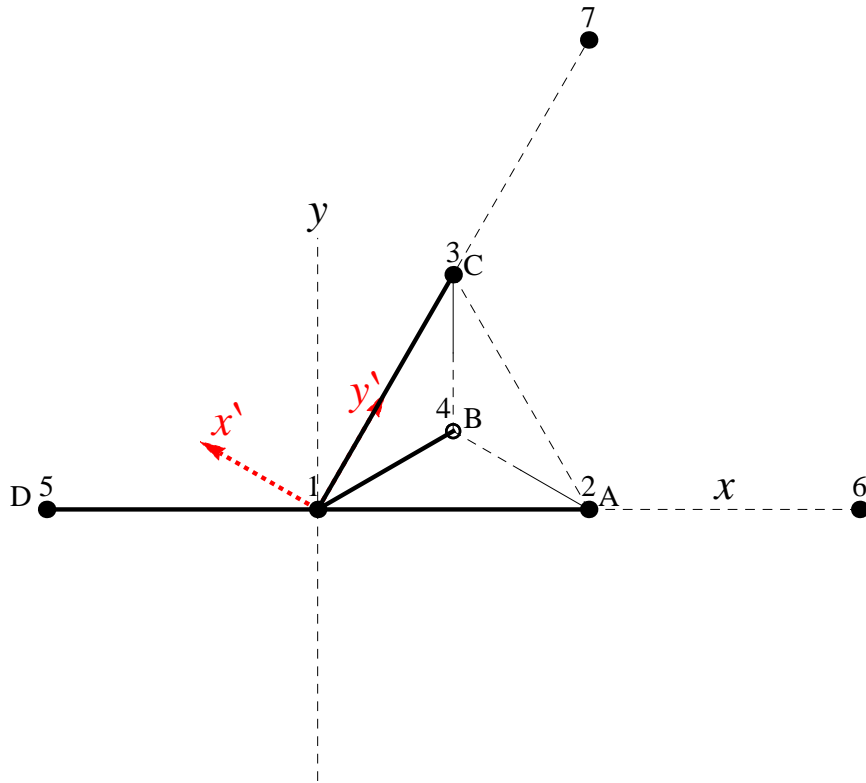


Figure 3.8: The plan view of the basis function ϕ_1 , before transformation. The coordinate axis x' lies along the edge JD in Figure 3.5.

The one step in transforming ϕ_1 to the canonical basis function $\hat{\phi}_J$ is via a rotation of $-\pi/6$ (clockwise) (see Figure 3.9). The anticlockwise rotation by an amount θ is obtained by multiplying the basis vectors by the matrix

$$R_\theta = \begin{pmatrix} \cos \theta & -\sin \theta \\ \sin \theta & \cos \theta \end{pmatrix}.$$

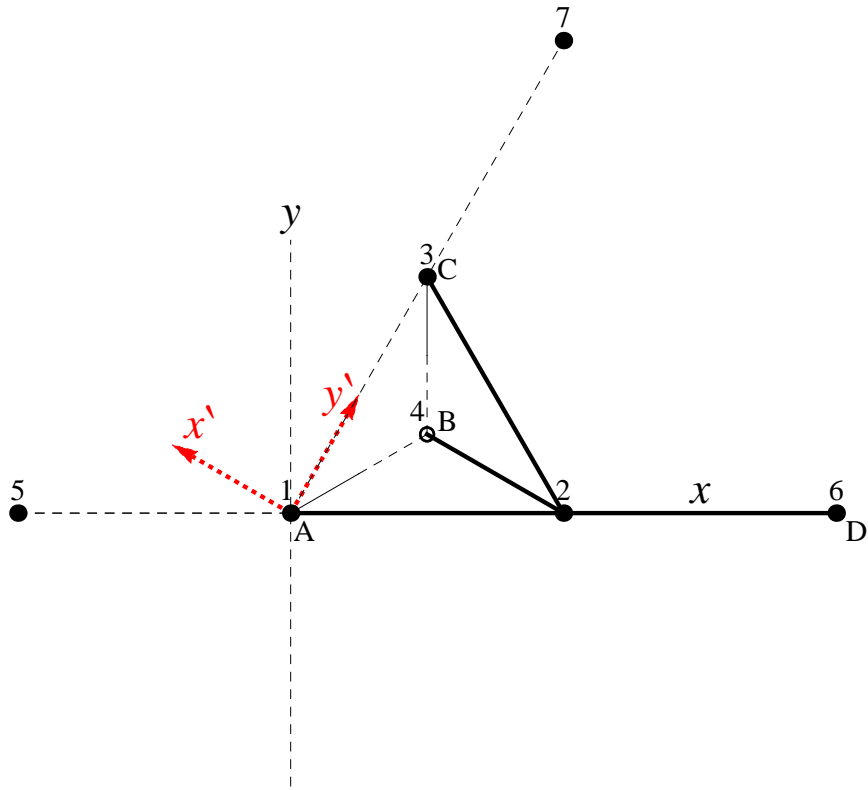


Figure 3.10: The plan view of the basis function ϕ_2 , before transformation.

In Figure 3.10 the plan view of the basis function centred on vertex 2 at fractal generation level $n = 1$ is shown. To transform this plan view of ϕ_2 to the plan view of $\hat{\phi}_J$ then we simply need to transform the (x, y) axis in Figure 3.10 to the (x', y') axis in Figure 3.5. So the first step is via a translation of $x_2 = (h, 0)$ to $x'_2 = (0, 0)$ (see Figure 3.11). In general, the translation of the basis vectors to the point (x_j, y_j) is given by the transformation

$$R_T(\underline{x}_j) = \begin{pmatrix} x - x_j \\ y - y_j \end{pmatrix}.$$

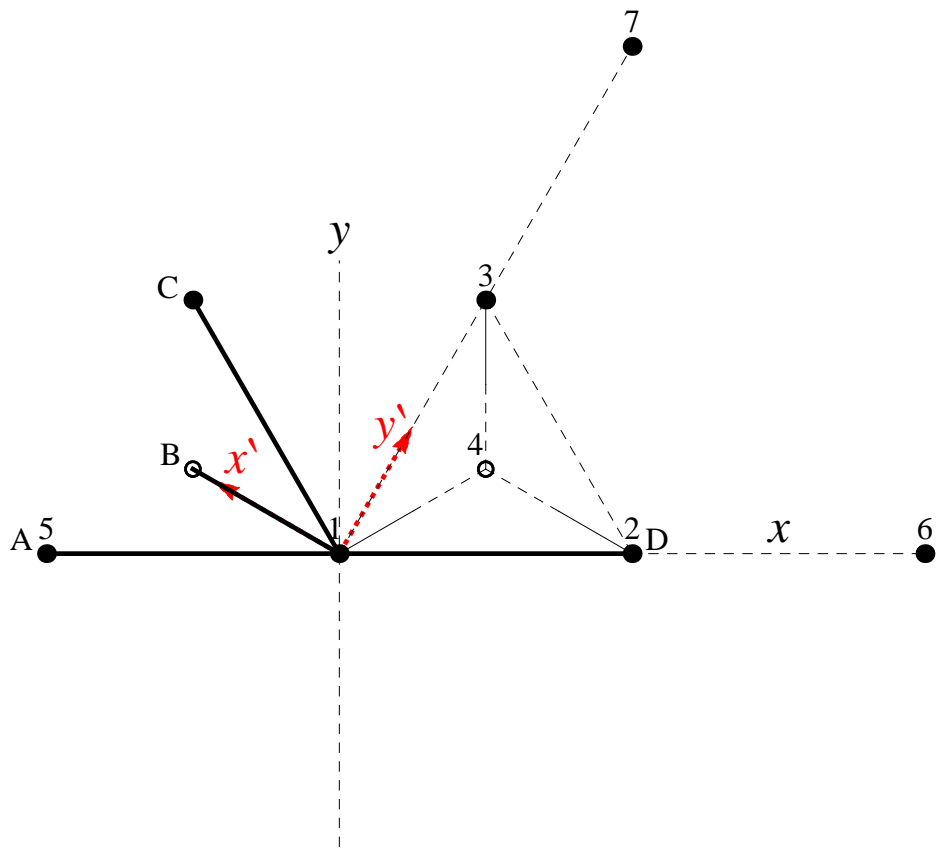


Figure 3.11: The plan view of ϕ_2 , after the first transformation.

The second step in transforming ϕ_2 to $\hat{\phi}_J$ is via a reflection in the (y axis) (see Figure 3.12). Reflection in the y axis can be obtained by multiplying the basis vectors by the matrix

$$R_R = \begin{pmatrix} -1 & 0 \\ 0 & 1 \end{pmatrix}.$$

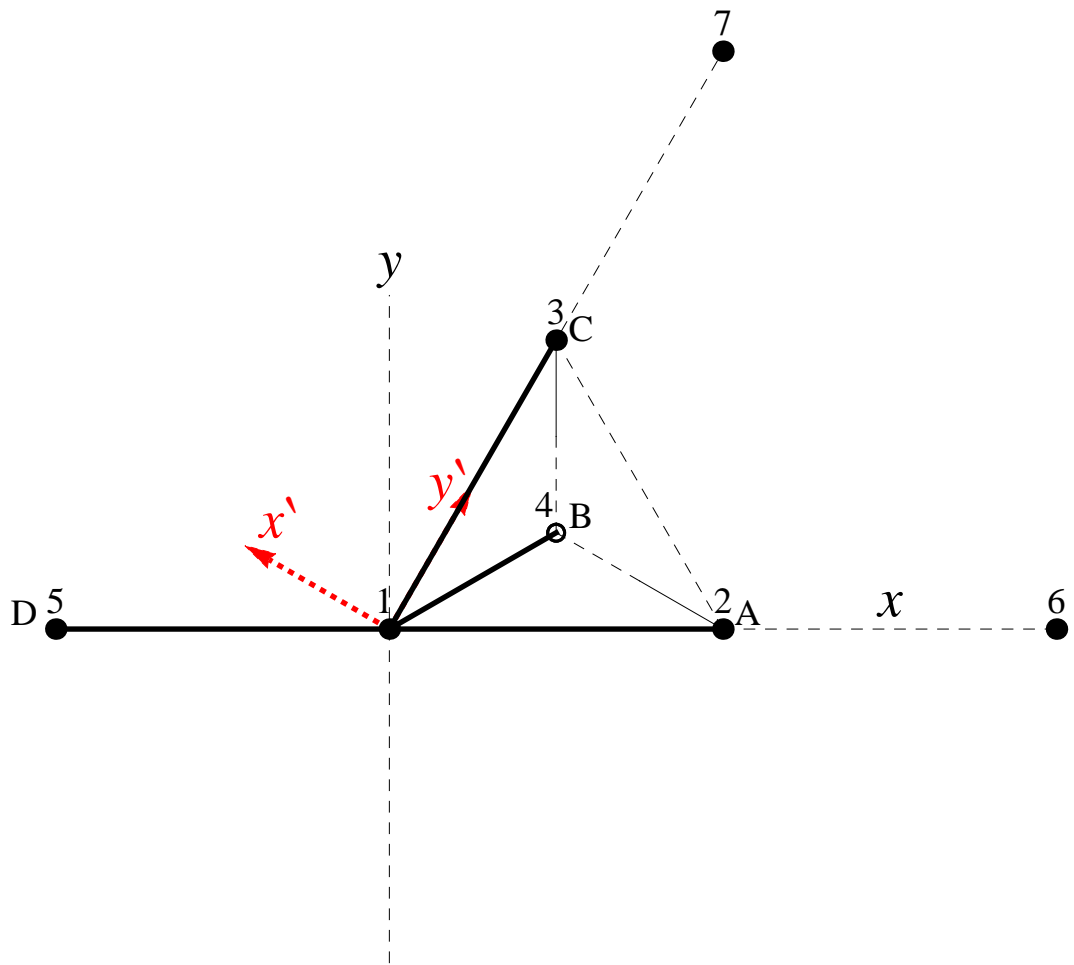


Figure 3.12: The plan view of ϕ_2 , after the second transformation.

Then from this plan view of ϕ_2 , the third (final) step in transforming ϕ_2 to $\hat{\phi}_J$ is via a rotation of $-\pi/6$ (clockwise) (see Figure 3.13).

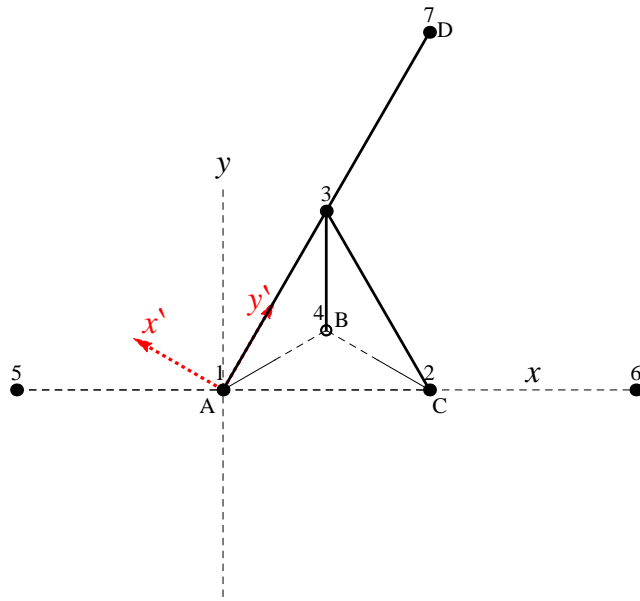


Figure 3.14: The plan view the basis function ϕ_3 , before transformation.

To transform ϕ_3 (see Figure 3.14) to the canonical basis function $\hat{\phi}_J$ (see Figure 3.5) we need a translation of $x_3 = (h/2, \sqrt{3}h/2)$ (see Figure 3.15).

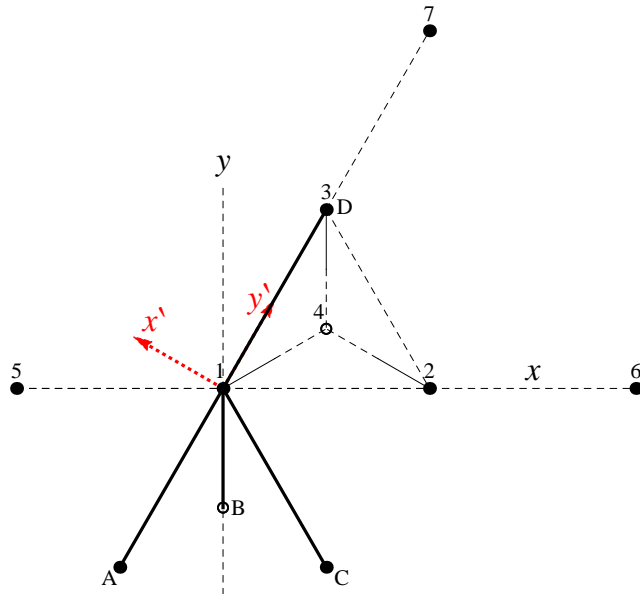


Figure 3.15: The plan view of ϕ_3 , after the first step of transformation.

The second (final) step in transforming ϕ_3 to $\hat{\phi}_J$ is via a rotation of $\pi/2$ (anticlockwise) (see Figure 3.16).

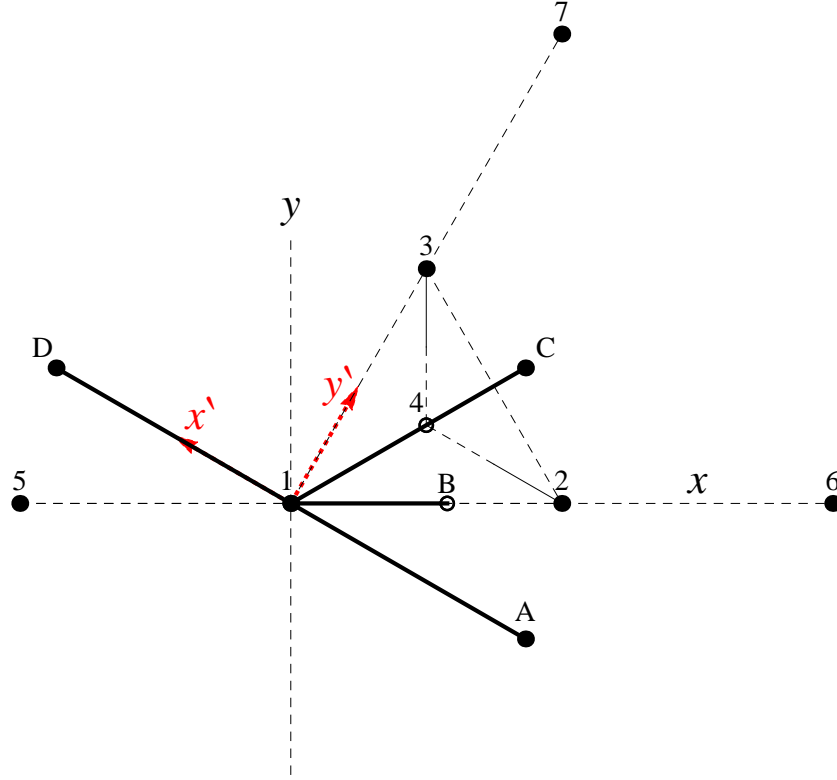


Figure 3.16: The plan view of ϕ_3 , after the second step of transformation.

So,

$$\begin{aligned}
 \phi_3 &= R_{\frac{\pi}{2}} \circ R_T(\underline{x}_3) \hat{\phi}_J(x, y) \\
 &= R_{\frac{\pi}{2}} \hat{\phi}_J \left(x - \frac{h}{2}, y - \frac{\sqrt{3}h}{2} \right) \\
 &= \hat{\phi}_J \left(-y + \frac{\sqrt{3}h}{2}, x - \frac{h}{2} \right) \\
 &= 1 - \frac{3}{h^2} \left(-y + \frac{\sqrt{3}h}{2} \right)^2 + \frac{5}{h^2} \left(x - \frac{h}{2} \right)^2 \\
 &= -\frac{5}{h}x + \frac{3\sqrt{3}}{h}y + \frac{5}{h^2}x^2 - \frac{3}{h^2}y^2.
 \end{aligned} \tag{3.2.28}$$

To transform the basis function ψ_5 (see Figure 3.17) to the canonical basis function $\hat{\psi}_I$ shown in Figure 3.7 as given by equation (3.2.25). So the one step is via a translation of $x_5 = (-h, 0)$ to $x'_5 = (0, 0)$ (see Figure 3.18).

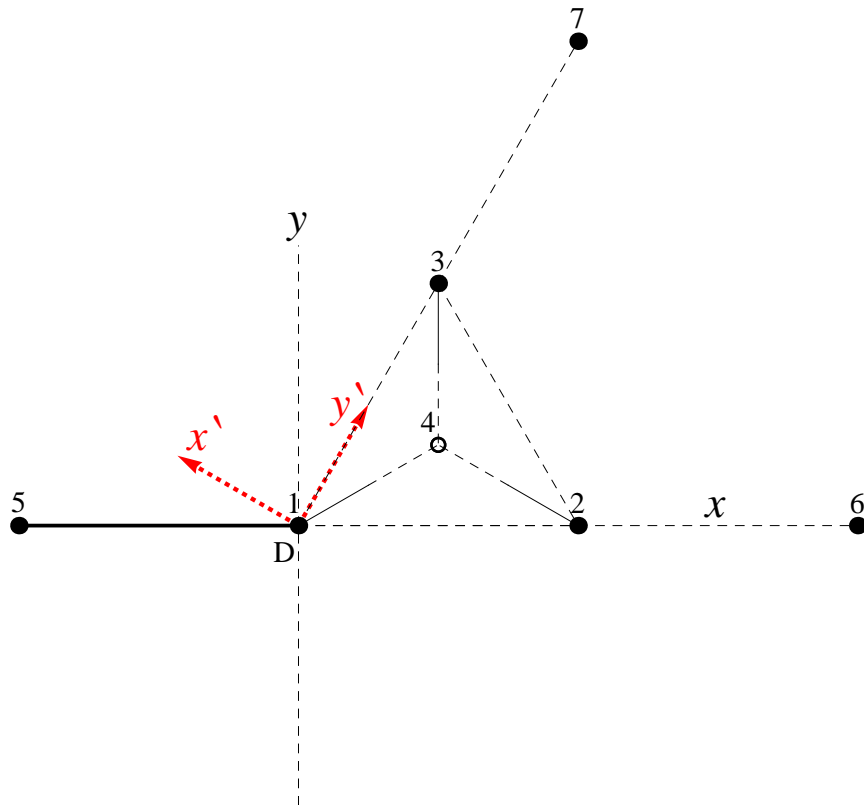


Figure 3.17: The plan view of the basis function ψ_5 , before transformation.

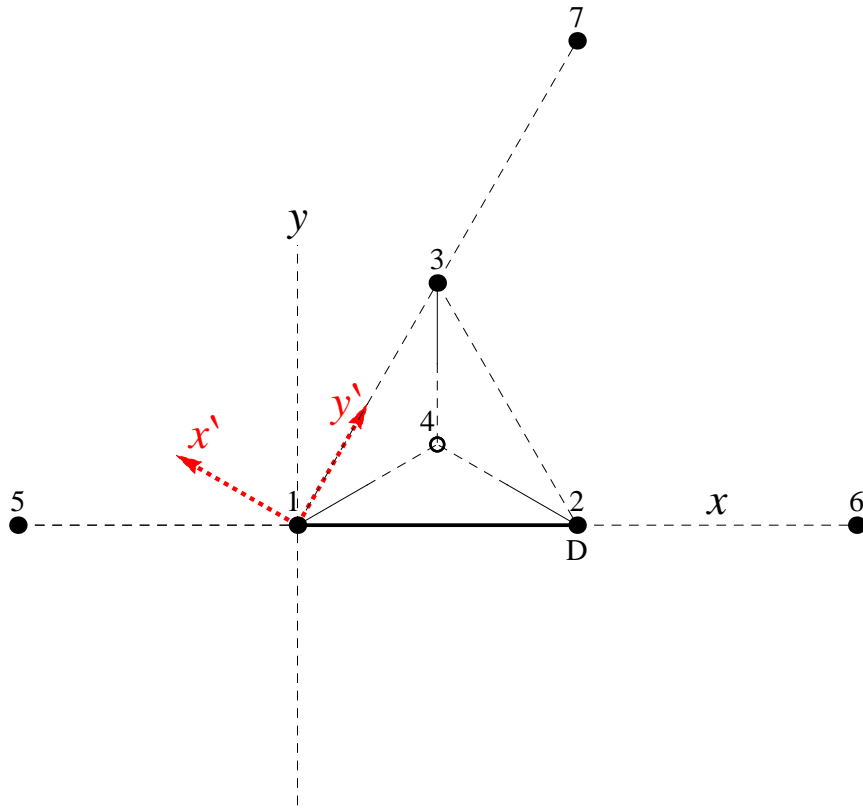


Figure 3.18: The plan view of ψ_5 , after the translation (final transformation).

So, for example, at fractal generation level $n = 1$,

$$\begin{aligned}
 \psi_5 &= R_T(\underline{x}_5)\hat{\psi}_I(x, y) \\
 &= \hat{\psi}_I(x + h, y) \\
 &= 1 - \frac{1}{h^2}((x + h)^2 + y^2) \\
 &= -\frac{2}{h}x - \frac{1}{h^2}x^2 - \frac{1}{h^2}y^2.
 \end{aligned} \tag{3.2.29}$$

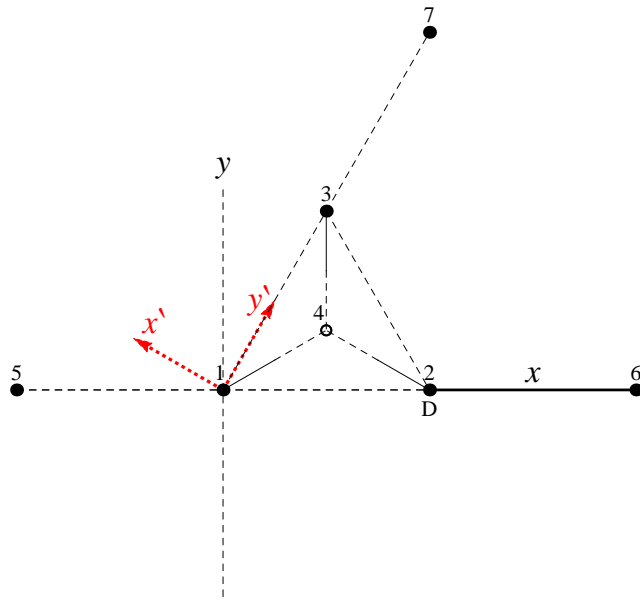


Figure 3.19: The plan view of the basis function ψ_6 , before transformation.

To transform the basis function ψ_6 (see Figure 3.19) to the canonical basis function $\hat{\psi}_I$ (see Figure 3.7), the first step is a translation of $x_6 = (2h, 0)$ (see Figure 3.20).

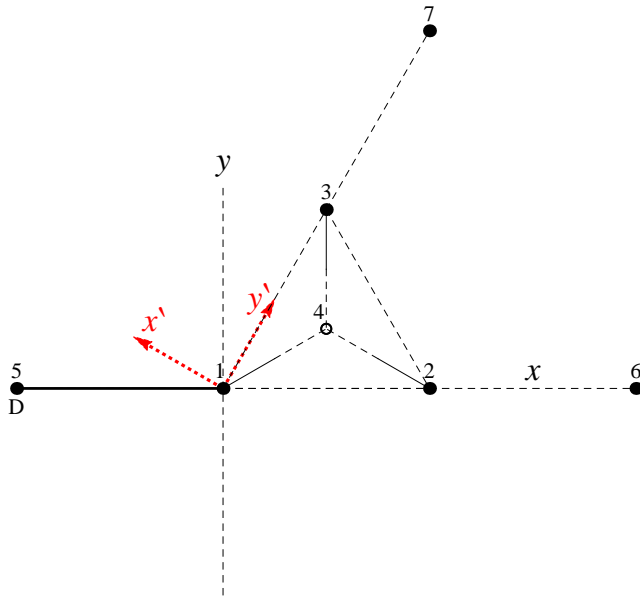


Figure 3.20: The plan view of ψ_6 , after the first step of transformation.

The second (final) step in transforming ψ_6 to the canonical basis function $\hat{\psi}_I$ is via a rotation of π (see Figure 3.21).

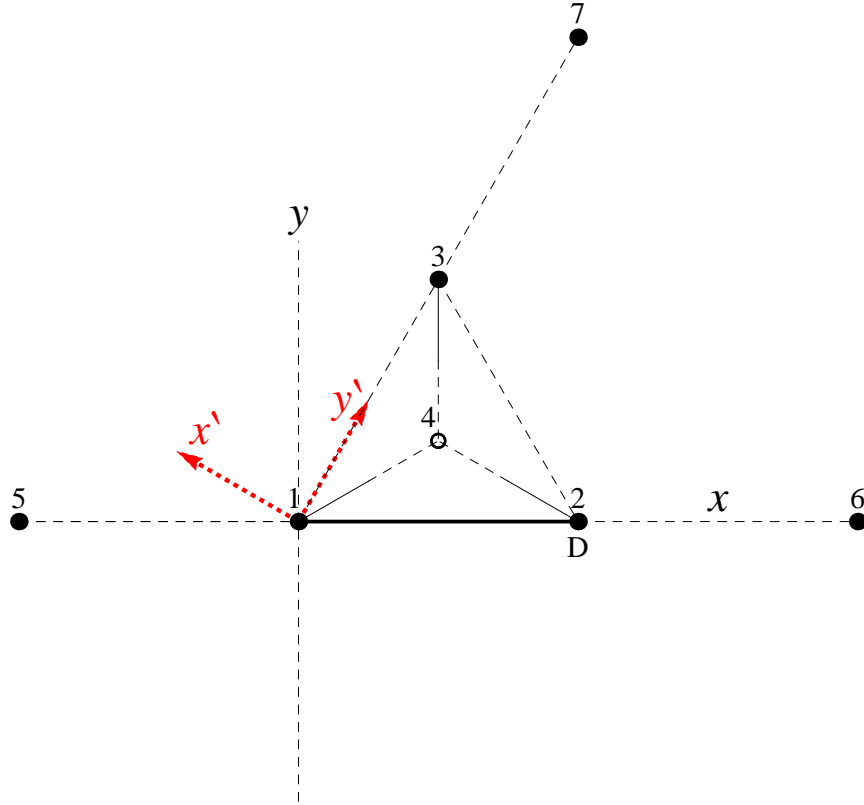


Figure 3.21: The plan view of ψ_6 , after the second (final) step of transformation.

So,

$$\begin{aligned}
 \psi_6 &= R_\pi \circ R_T(\underline{x}_6)\hat{\psi}_I(x, y) \\
 &= R_\pi\hat{\psi}_I(x - 2h, y) \\
 &= \hat{\psi}_I(-x + 2h, -y) \\
 &= -3 + \frac{4}{h}x - \frac{1}{h^2}x^2 - \frac{1}{h^2}y^2.
 \end{aligned} \tag{3.2.30}$$

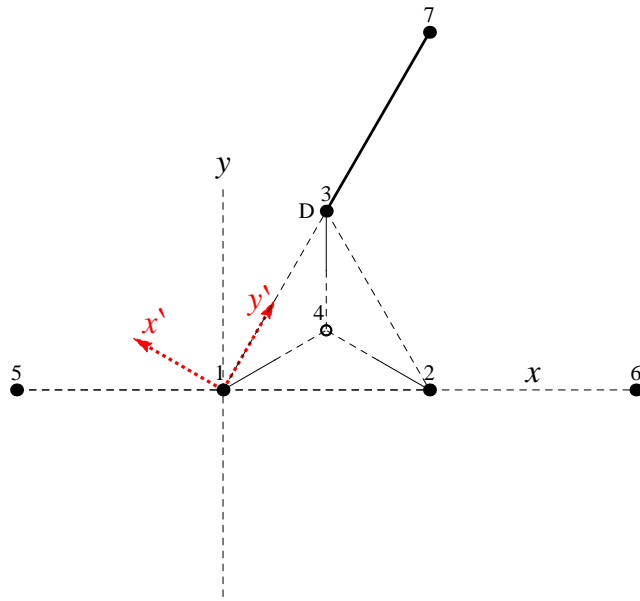


Figure 3.22: The plan view of the basis function ψ_7 , before transformation.

To transform ψ_7 (see Figure 3.22) to the canonical basis function $\hat{\psi}_I$ (see Figure 3.7), the first step is a translation of $x_7 = (h, \sqrt{3}h)$ (see Figure 3.23).

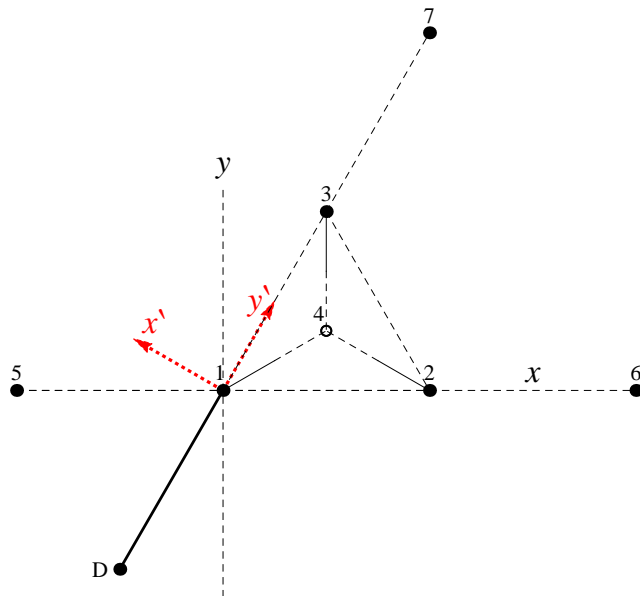


Figure 3.23: The plan view of ψ_7 , after the first step of transformation.

The second (final) step in transforming ψ_7 to $\hat{\psi}_I$ is via a rotation of $2\pi/3$ (anti-clockwise) (see Figure 3.24).

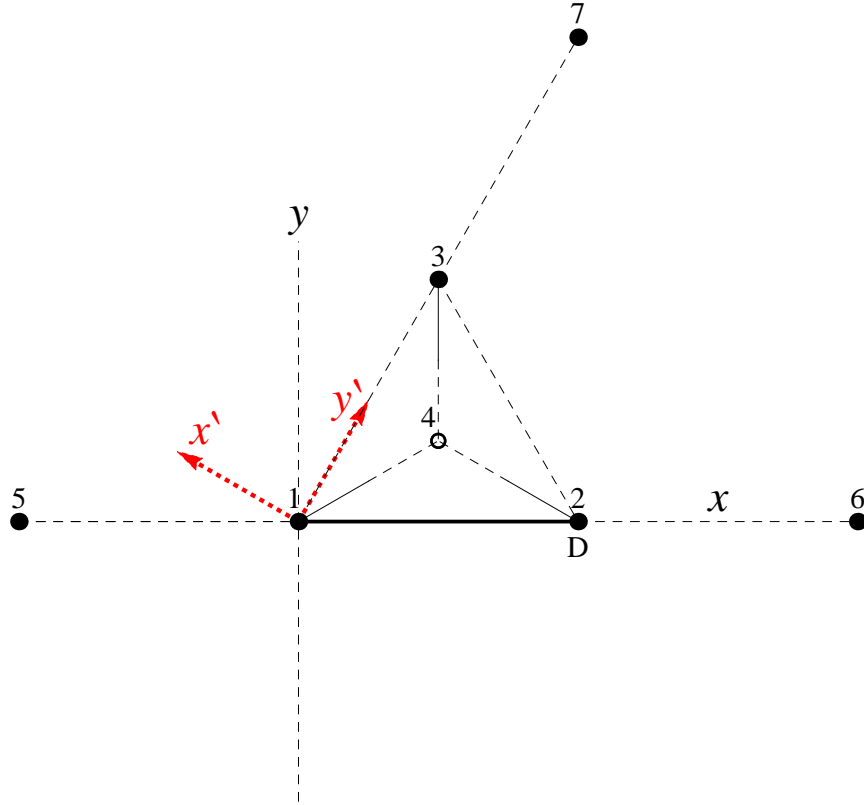


Figure 3.24: The plan view of ψ_7 , after the second (final) step of transformation.

So,

$$\begin{aligned}
 \psi_7 &= R_{\frac{2\pi}{3}} \circ R_T(\underline{x}_7) \hat{\psi}_I(x, y) \\
 &= R_{\frac{2\pi}{3}} \hat{\psi}_I(x - h, y - \sqrt{3}h) \\
 &= \hat{\psi}_I \left(-\frac{1}{2}(x - h) - \frac{\sqrt{3}}{2}(y - \sqrt{3}h), \frac{\sqrt{3}}{2}(x - h) - \frac{1}{2}(y - \sqrt{3}h) \right) \\
 &= -3 + \frac{2}{h}x + \frac{2\sqrt{3}}{h}y - \frac{1}{h^2}x^2 - \frac{1}{h^2}y^2. \tag{3.2.31}
 \end{aligned}$$

j	Related steps from ϕ_j and ψ_j to their respective canonical basis function		
	(1) Translation (R_T)	(2) Reflection (R_R)	(3) Rotation (R_θ)
1	—	—	$-\pi/6$
2	$(h, 0)$	y axis	$-\pi/6$
3	$(\frac{h}{2}, \frac{\sqrt{3}h}{2})$	—	$\pi/2$
4	—	—	—
5	$(-h, 0)$	—	—
6	$(2h, 0)$	—	π
7	$(h, \sqrt{3}h)$	—	$2\pi/3$

Table 3.1: The related steps of the transformation from ϕ_j , $j = 1, \dots, 4$ and ψ_j , $j = 5, 6, 7$ to their respective canonical basis function in fractal generation level $n = 1$.

A summary of the transformations required for each basis function at fractal generation level $n = 1$ is given in Table 3.1. A table summarising the coefficients that subsequently arise for each basis function is given in Appendix A.2.

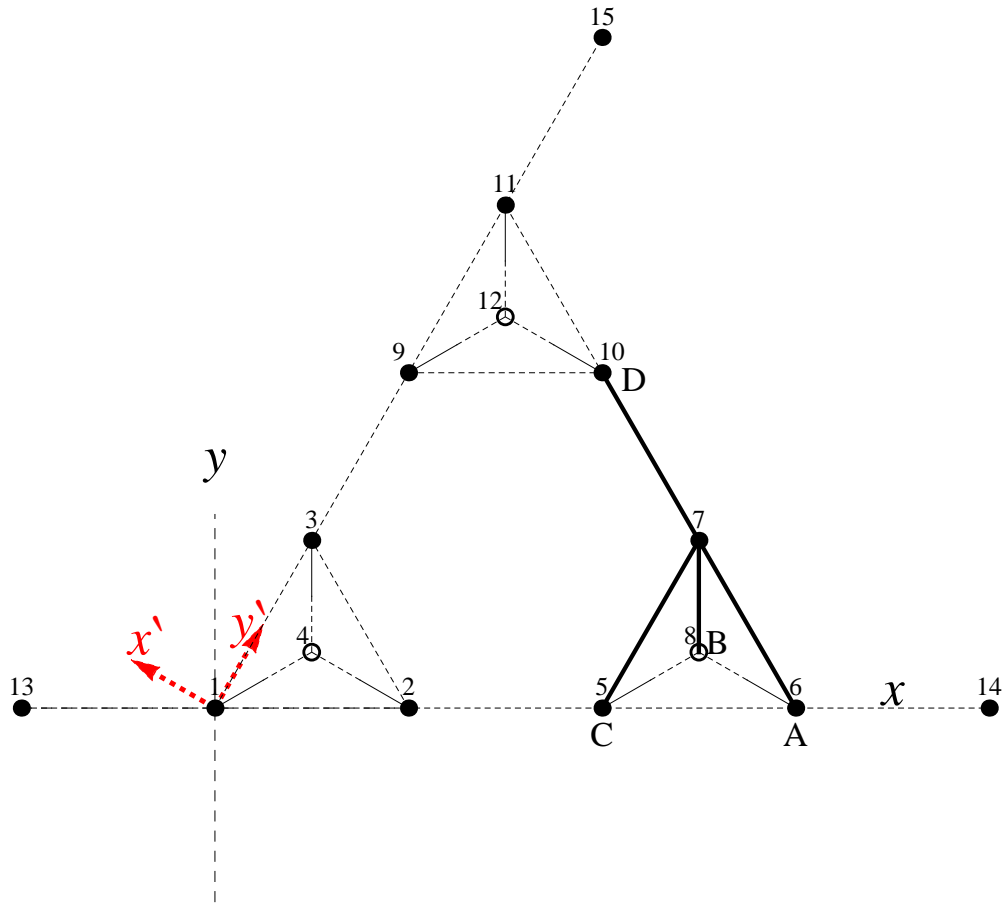


Figure 3.25: The plan view of the basis function ϕ_7 , before transformation.

The above process can then be repeated for fractal generation level $n = 2$. Recall that at each generation level the overall length of the graph remains fixed (L) and the edge length h decreases. As such the canonical basis function given by equation (3.2.17) can still be applied here since it will be automatically scaled as its coefficients depend on h . For example, to transform ϕ_7 (see Figure 3.25) to $\hat{\phi}_J$ (see Figure 3.5), the first step is a translation of $x_7 = (5h/2, \sqrt{3}h/2)$ (see Figure 3.26).

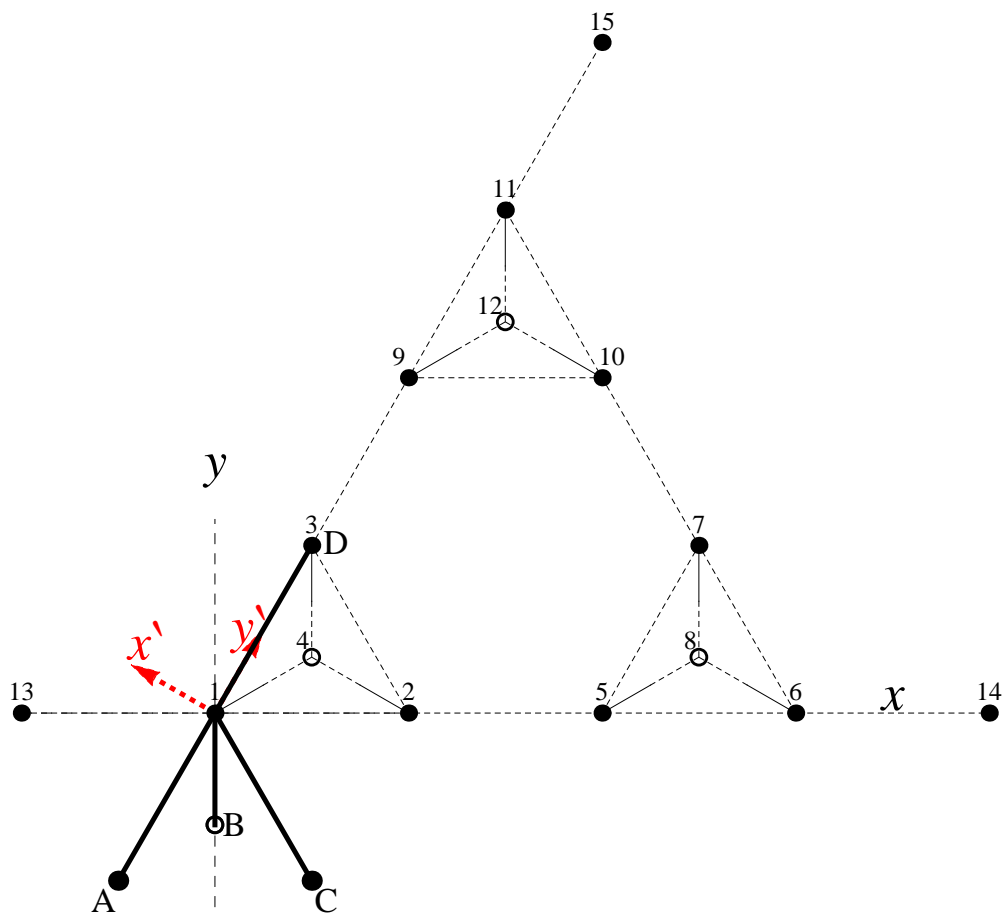


Figure 3.27: The plan view of ϕ_7 , after the second transformation.

Then from this plan view of ϕ_7 , the third (final) step in transforming ϕ_7 to $\hat{\phi}_J$ is via a rotation of $\pi/2$ (anticlockwise) (see Figure 3.28).

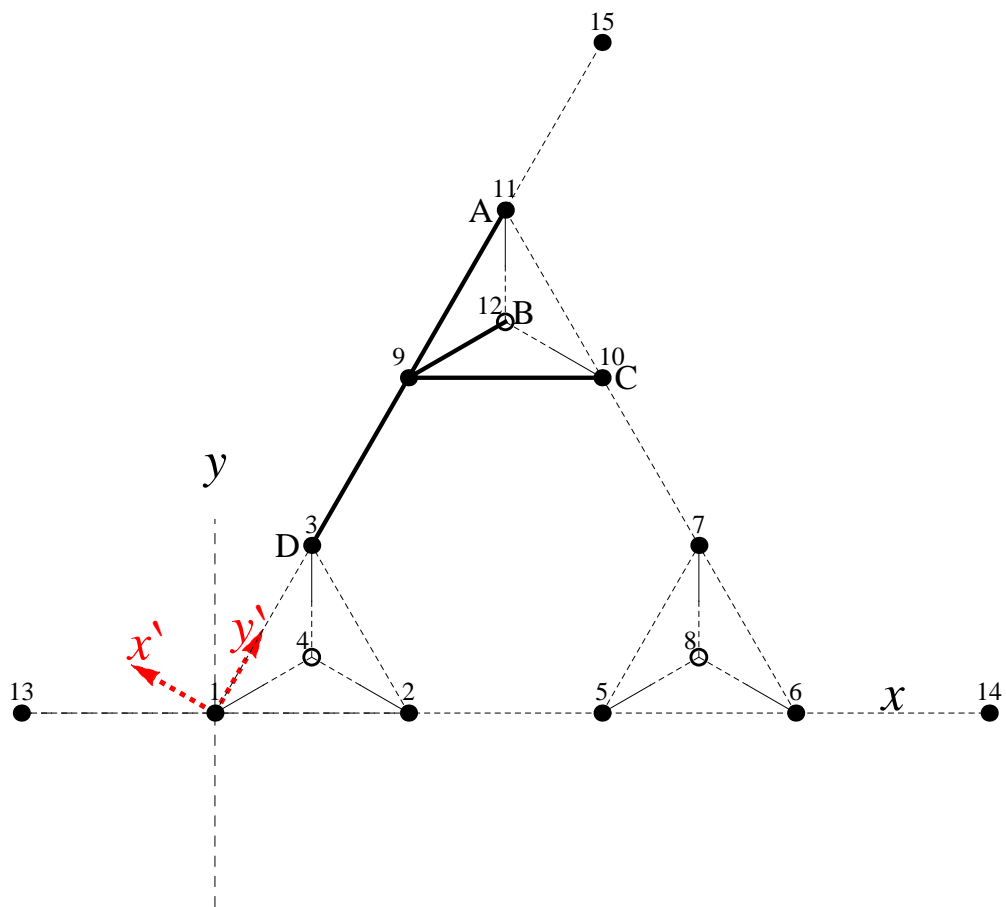


Figure 3.29: The plan view of the basis function ϕ_9 , before transformation.

To transform ϕ_9 (see Figure 3.29) to $\hat{\phi}_J$ (see Figure 3.5) the first step is a translation of $x_9 = (h, \sqrt{3}h)$ (see Figure 3.30).

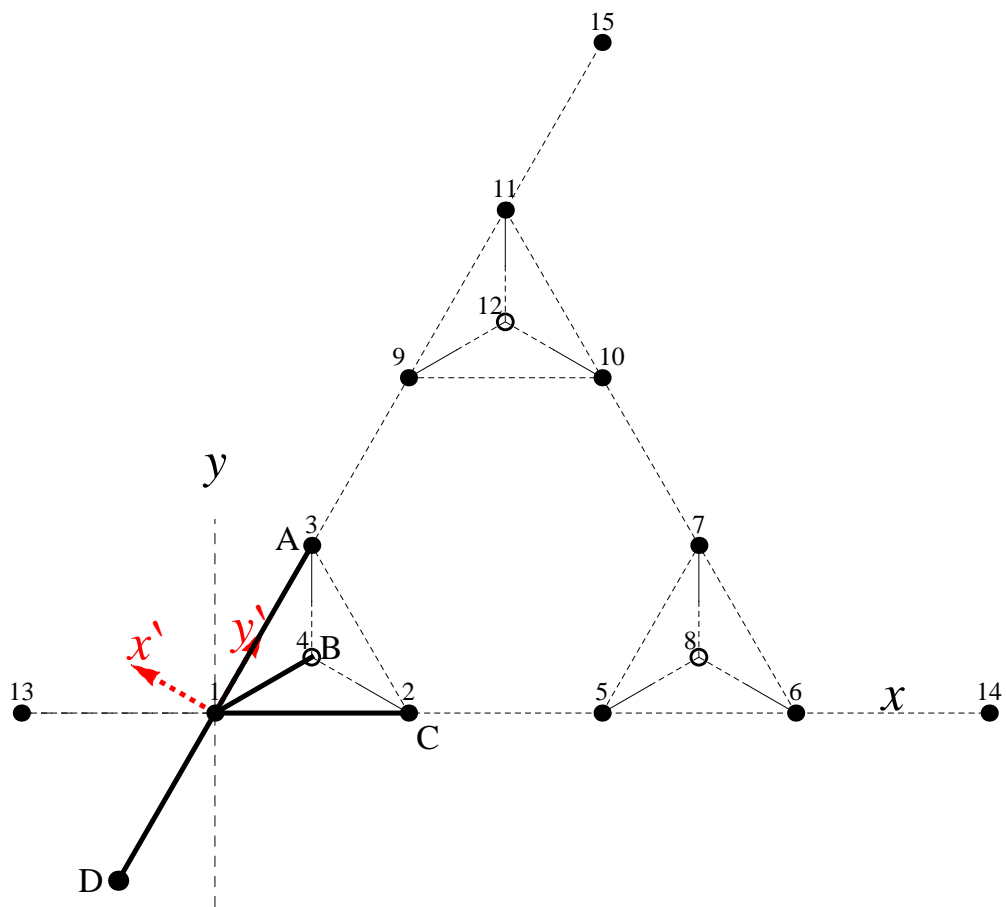


Figure 3.30: The plan view of ϕ_9 , after the first transformation.

The second related step is a reflection in the (y axis) (see Figure 3.31).

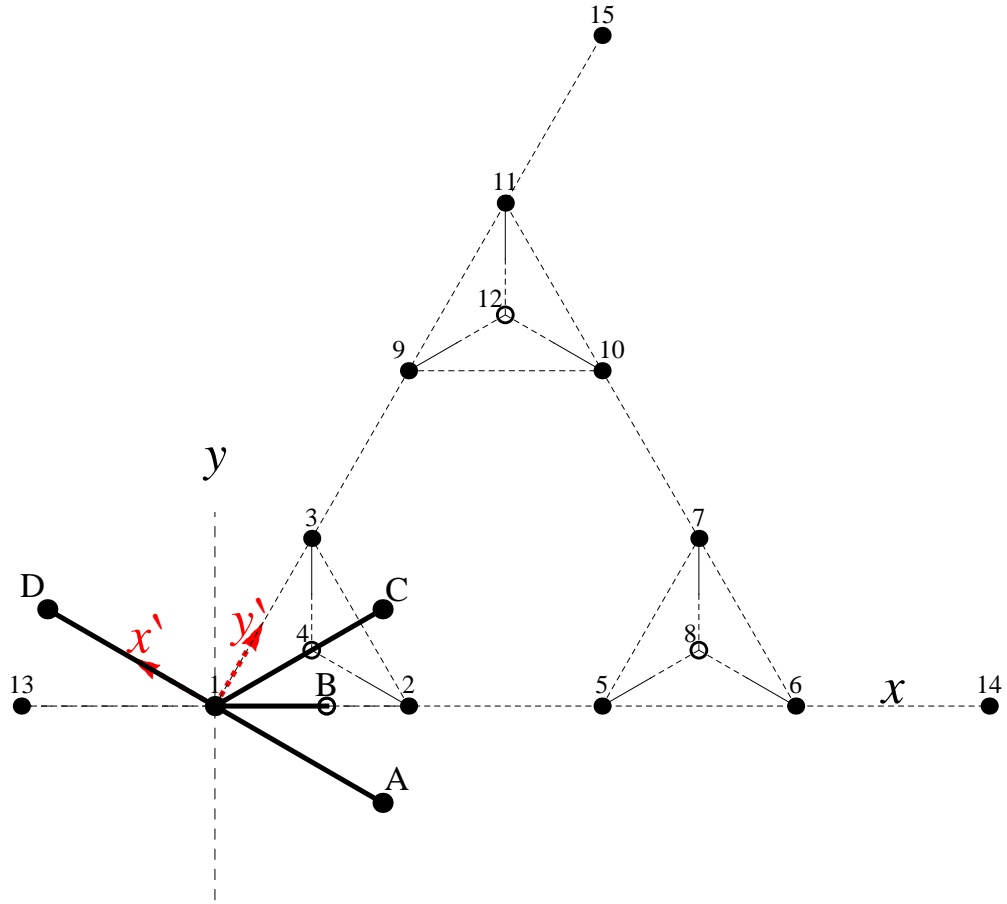


Figure 3.32: The plan view of ϕ_9 , after the third (final) transformation.

Hence,

$$\begin{aligned}
\phi_9 &= R_{-\frac{5\pi}{6}} \circ R_R \circ R_T(\underline{x}_9) \hat{\phi}_J(x, y) \\
&= R_{-\frac{5\pi}{6}} \circ R_R \hat{\phi}_J(x - h, y - \sqrt{3}h) \\
&= R_{-\frac{5\pi}{6}} \hat{\phi}_J(-x + h, y - \sqrt{3}h) \\
&= \hat{\phi}_J \left(\frac{\sqrt{3}}{2}x - \frac{\sqrt{3}h}{2} + \frac{1}{2}y - \frac{\sqrt{3}h}{2}, \frac{1}{2}x - \frac{h}{2} - \frac{\sqrt{3}}{2}y + \frac{3h}{2} \right) \\
&= 1 - \frac{3}{h^2} \left(\frac{\sqrt{3}}{2}x + \frac{1}{2}y - \sqrt{3}h \right)^2 + \frac{5}{h^2} \left(\frac{1}{2}x - \frac{\sqrt{3}}{2}y + h \right)^2 \\
&= -3 + \frac{14}{h}x - \frac{2\sqrt{3}}{h}y - \frac{1}{h^2}x^2 + \frac{3}{h^2}y^2 - \frac{4\sqrt{3}}{h^2}xy. \tag{3.2.33}
\end{aligned}$$

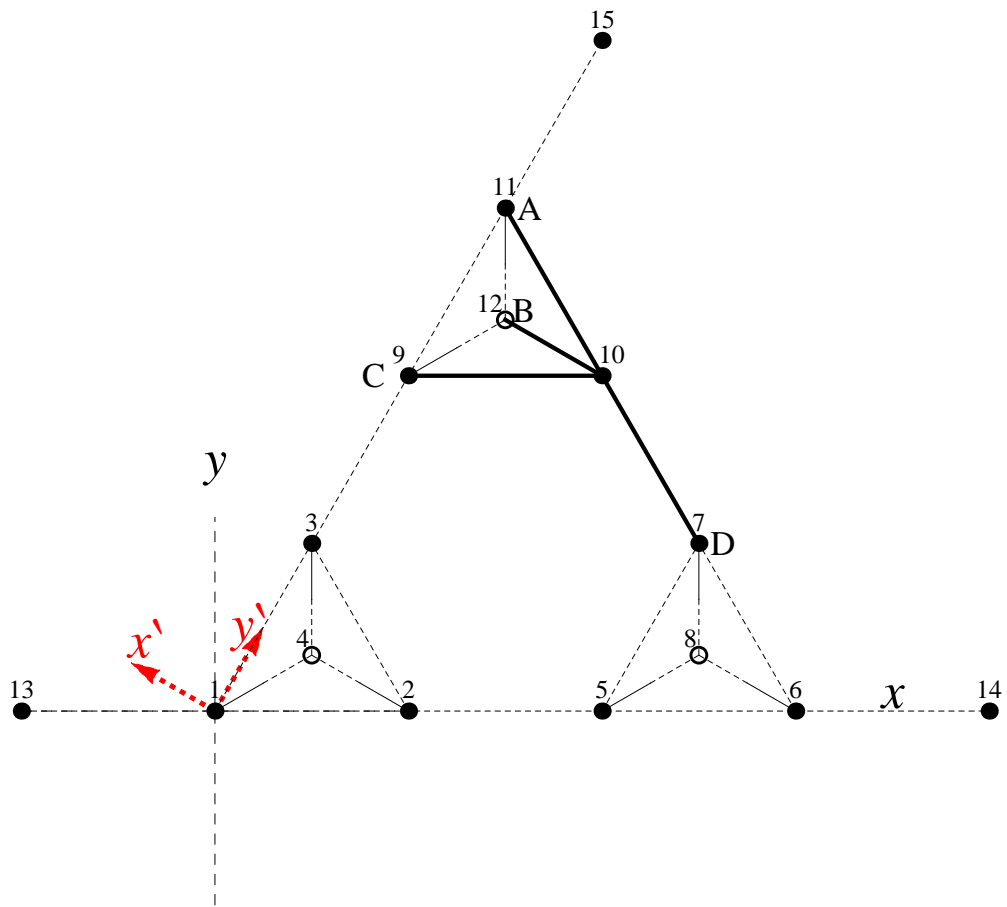


Figure 3.33: The plan view of the basis function ϕ_{10} , before transformation.

To transform ϕ_{10} (see Figure 3.33) to $\hat{\phi}_J$ (see Figure 3.5) the first step is a translation of $x_{10} = (2h, \sqrt{3}h)$ (see Figure 3.34).

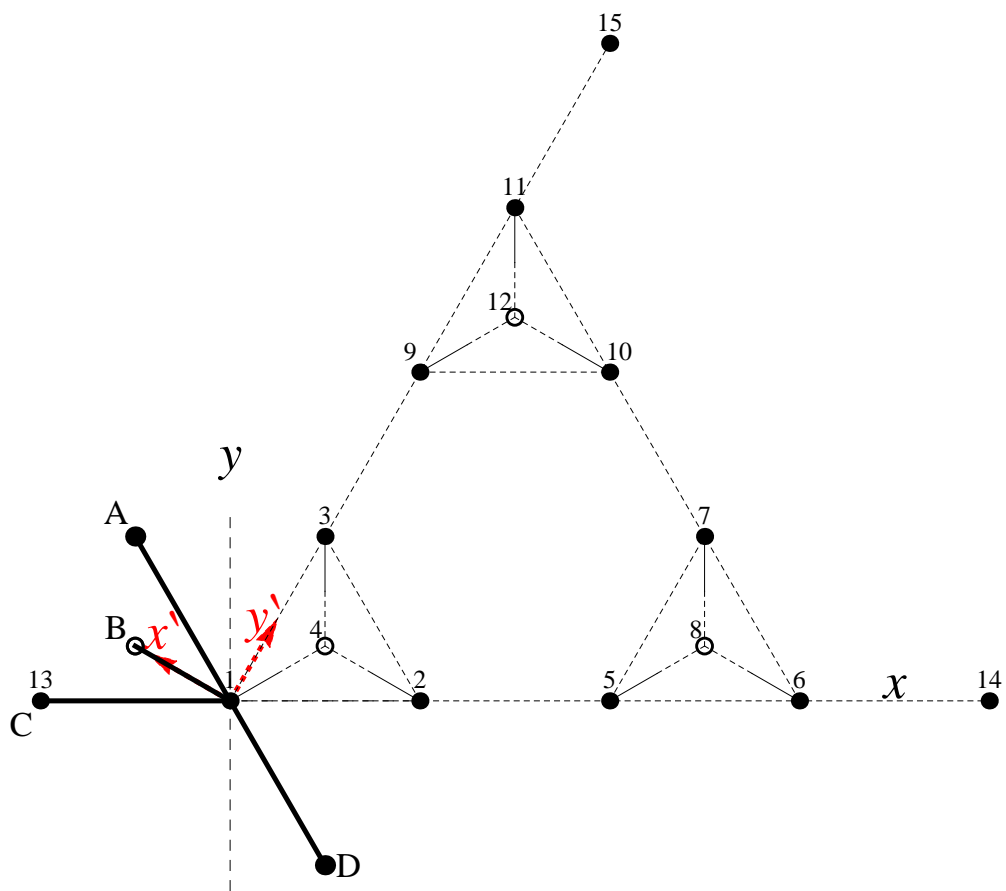


Figure 3.34: The plan view of ϕ_{10} , after the first transformation.

The second (final) step is a rotation of $-5\pi/6$ (clockwise) (see Figure 3.35).

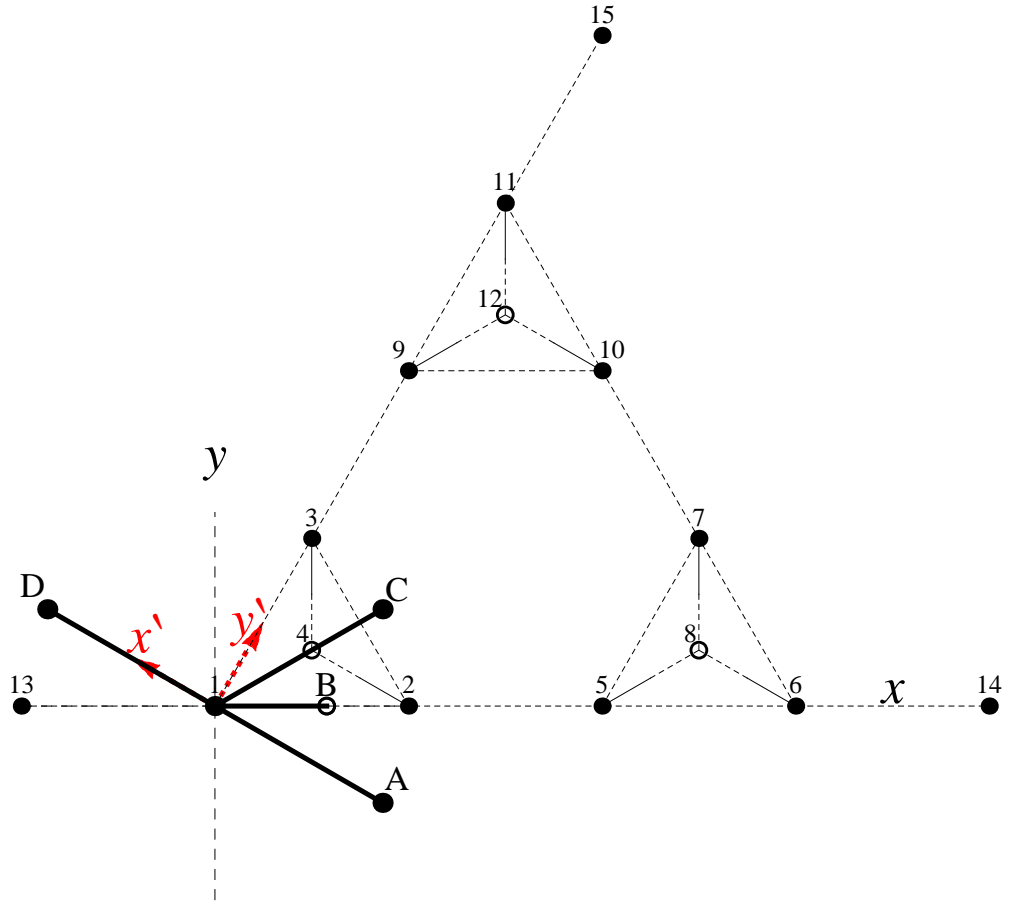


Figure 3.35: The plan view of ϕ_{10} , after the second (final) transformation.

So,

$$\begin{aligned}
\phi_{10} &= R_{-\frac{5\pi}{6}} \circ R_T(\underline{x}_{10})\hat{\phi}_J(x, y) \\
&= R_{-\frac{5\pi}{6}}\hat{\phi}_J(x - 2h, y - \sqrt{3}h) \\
&= \hat{\phi}_J\left(-\frac{\sqrt{3}}{2}x + \sqrt{3}h + \frac{y}{2} - \frac{\sqrt{3}h}{2}, -\frac{1}{2}x + h - \frac{\sqrt{3}}{2}y + \frac{3h}{2}\right) \\
&= 1 - \frac{3}{h^2}\left(-\frac{\sqrt{3}}{2}x + \frac{1}{2}y + \frac{\sqrt{3}h}{2}\right)^2 + \frac{5}{h^2}\left(-\frac{1}{2}x - \frac{\sqrt{3}}{2}y + \frac{5h}{2}\right)^2 \\
&= 30 - \frac{8}{h}x - \frac{14\sqrt{3}}{h}y - \frac{1}{h^2}x^2 + \frac{3}{h^2}y^2 + \frac{4\sqrt{3}}{h^2}xy. \tag{3.2.34}
\end{aligned}$$

j	Related steps from ϕ_j and ψ_j to their respective canonical basis function		
	(1) Translation (R_T)	(2) Reflection (R_R)	(3) Rotation (R_θ)
1	—	—	$-\pi/6$
2	$\lambda(h, 0)$	y axis	$-\pi/6$
3	$\lambda(\frac{h}{2}, \frac{\sqrt{3}h}{2})$	—	$\pi/2$
4	—	—	—
5	$\lambda(2h, 0)$	—	$-\pi/6$
6	$\lambda(3h, 0)$	y axis	$-\pi/6$
7	$\lambda(\frac{5h}{2}, \frac{\sqrt{3}h}{2})$	y axis	$\pi/2$
8	$\lambda(\frac{5h}{2}, \frac{h}{2\sqrt{3}})$	—	—
9	$\lambda(h, \sqrt{3}h)$	y axis	$-5\pi/6$
10	$\lambda(2h, \sqrt{3}h)$	—	$-5\pi/6$
11	$\lambda(\frac{3h}{2}, \frac{3\sqrt{3}h}{2})$	—	$\pi/2$
12	$\lambda(\frac{3h}{2}, \frac{7h}{2\sqrt{3}})$	—	—
13	$\lambda(-h, 0)$	—	—
14	$\lambda(4h, 0)$	—	π
15	$\lambda(2h, 2\sqrt{3}h)$	—	$2\pi/3$

Table 3.2: The related steps of the transformation from ϕ_j , $j = 1, \dots, 12$ and ψ_j , $j = 13, 14, 15$ to their respective canonical basis function in fractal generation level $n = 2$, where $\lambda = 1/3$.

A table showing all the transformations required to create the basis functions, for fractal generation level $n = 2$, is shown in Table 3.2. Another table showing the coefficients that arise from this process for each basis function is given in Appendix A.2. To aid in the visualisation of these basis functions an example is provided in the graph below, which shows the graph basis functions ϕ_j where $j = 1, 2$ and 3 , which are the interior PZT-5H vertices at fractal generation level $n = 1$ (see Figure 3.3). The graph basis functions ϕ_1 at vertex $(0, 0)$ (as shown in green in Figure 3.36) is connected to vertex 2 through element 1, vertex A through element 7, vertex 3 through element 3 and vertex 4 through element 4. The graph basis functions ϕ_2 at vertex $(h, 0)$ (as shown in blue in Figure 3.36) is connected to vertex 1 through element 1, vertex B through element 8, vertex 3 through element 2 and vertex 4 through element 5. The graph basis functions ϕ_3

at vertex $(h/2, \sqrt{3}h/2)$ (as shown in blue in Figure 3.36) is connected to vertex 1 through element 3, vertex 2 through element 2, vertex C through element 9, and vertex 4 through element 6.

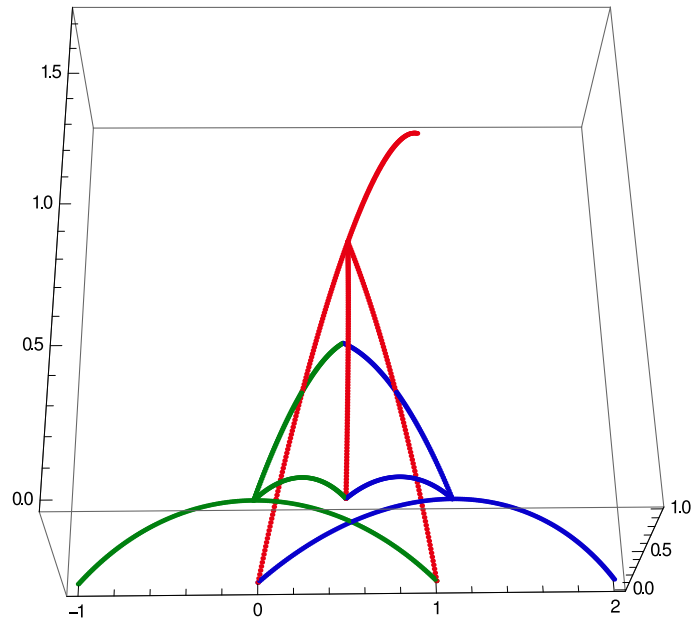


Figure 3.36: The basis functions ϕ_j where $j = 1, 2$ and 3 at fractal generation level $n = 1$.

The graph below shows the graph basis functions ϕ_4 which is the interior polymer vertex at fractal generation level $n = 1$ (see Figure 3.3). The graph basis functions ϕ_4 at vertex $(h/2, h/2\sqrt{3})$ (as shown at Figure 3.37) is connected to vertex 1 through element 4, vertex 2 through element 5 and vertex 3 through element 6.

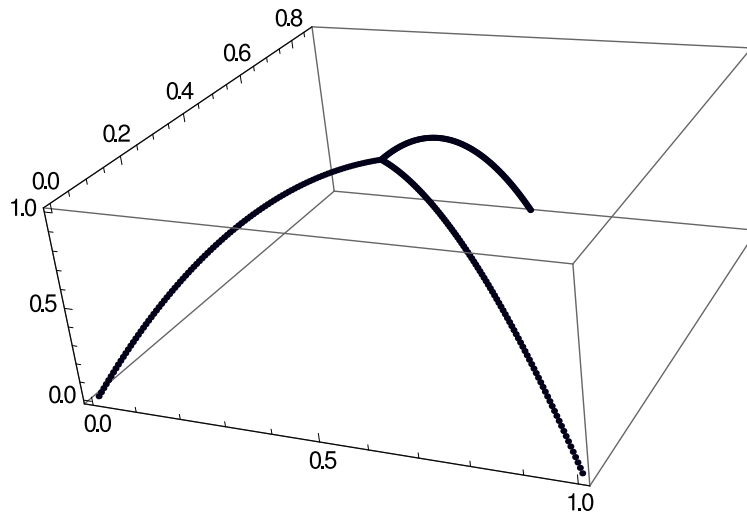


Figure 3.37: The basis function ϕ_4 at fractal generation level $n = 1$.

The graph below shows the graph basis functions ψ_j where $j = 5, 6$ and 7 which are the exterior vertices at fractal generation level $n = 1$ (see Figure 3.3). The graph basis functions ψ_5 at vertex $(-h, 0)$ (as shown in red in Figure 3.38) is connected to vertex 1 through element 7. The graph basis functions ψ_6 at vertex $(2h, 0)$ (as shown in blue in Figure 3.38) is connected to vertex 2 through element 8. The graph basis functions ψ_7 at vertex $(h, \sqrt{3}h)$ (as shown in green in Figure 3.38) is connected to vertex 3 through element 9.

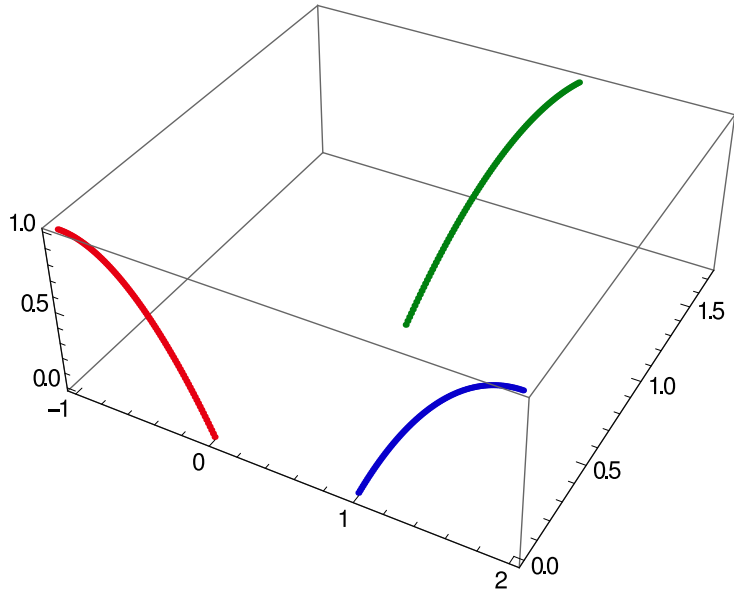


Figure 3.38: The basis functions ψ_j where $j = 5, 6$ and 7 at fractal generation level $n = 1$.

The graph below shows the graph basis functions ϕ_j where $j = 1, 2$ and 3 which are some of the interior PZT-5H vertices at fractal generation level $n = 2$ (see Figure 3.4). The graph basis functions ϕ_1 at vertex $(0, 0)$ (as shown in green in Figure 3.39) is connected to vertex 2 through element 1, vertex A (that is, vertex 13) through element 22, vertex 3 through element 3, and vertex 4 through element 4. The graph basis functions ϕ_2 at vertex $(h, 0)$ (as shown in blue in Figure 3.39) is connected to vertex 1 through element 1, vertex 5 through element 7, vertex 3 through element 2, and vertex 4 through element 5. The graph basis functions ϕ_3 at vertex $(h/2, \sqrt{3}h/2)$ (as shown in blue in Figure 3.39) is connected to vertex 1 through element 3, vertex 2 through element 2, vertex 9 through element 14, and vertex 4 through element 6.

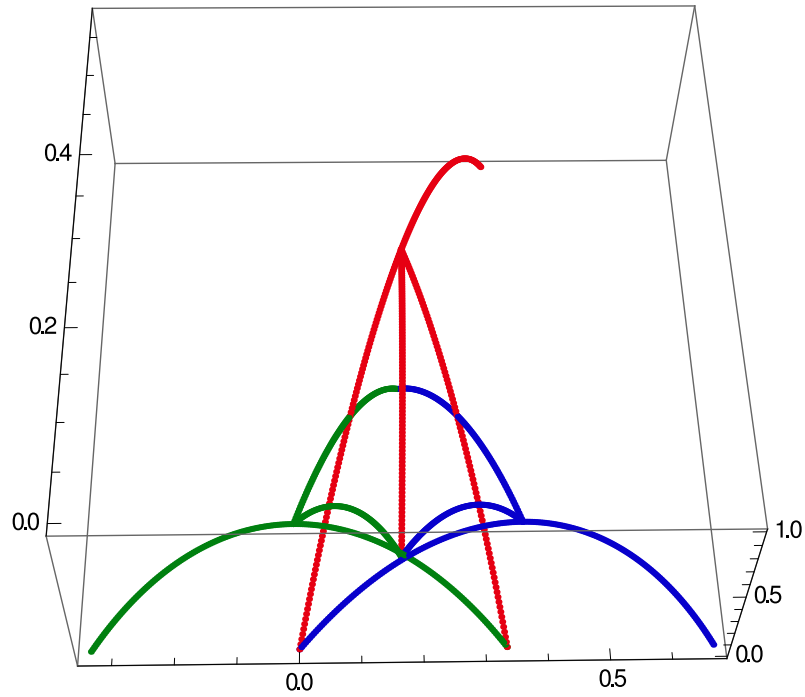


Figure 3.39: The basis functions ϕ_j where $j = 1, 2$ and 3 at fractal generation level $n = 2$.

The graph below shows the graph basis functions ϕ_j where $j = 5, 6$ and 7 which are some of the interior PZT-5H vertices at fractal generation level $n = 2$ (see Figure 3.4). The graph basis functions ϕ_5 at vertex $(2h, 0)$ (as shown in green in Figure 3.40) is connected to vertex 2 through element 7, vertex 6 through element 8, vertex 7 through element 10, and vertex 8 through element 11. The graph basis functions ϕ_6 at vertex $(3h, 0)$ (as shown in blue in Figure 3.40) is connected to vertex 5 through element 8, vertex B (that is, vertex 14) through element 23, vertex 7 through element 9, and vertex 8 through element 12. The graph basis functions ϕ_7 at vertex $(5h/2, \sqrt{3}h/2)$ (as shown in blue in Figure 3.40) is connected to vertex 5 through element 10, vertex 6 through element 9, vertex 10 through element 15, and vertex 8 through element 13.

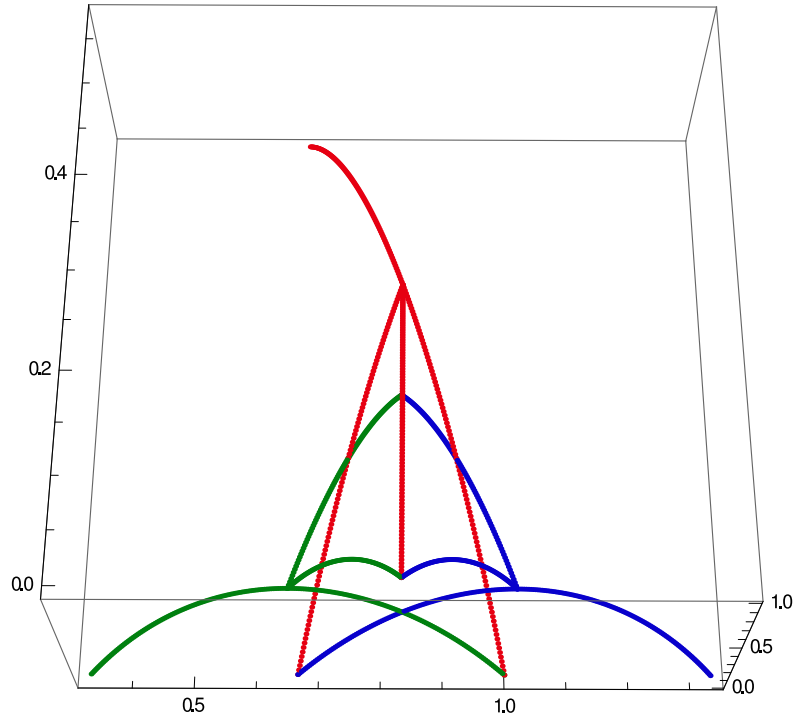


Figure 3.40: The basis functions ϕ_j where $j = 5, 6$ and 7 at fractal generation level $n = 2$.

The graph below shows the graph basis functions ϕ_j where $j = 9, 10$ and 11 which are some of the interior PZT-5H vertices at fractal generation level $n = 2$ (see Figure 3.4). The graph basis functions ϕ_9 at vertex $(h, \sqrt{3}h)$ (as shown in green in Figure 3.41) is connected to vertex 3 through element 14, vertex 10 through element 16, vertex 11 through element 18, and vertex 12 through element 19. The graph basis functions ϕ_{10} at vertex $(2h, \sqrt{3}h)$ (as shown in blue in Figure 3.41) is connected to vertex 7 through element 15, vertex 9 through element 16, vertex 11 through element 17, and vertex 12 through element 20. The graph basis functions ϕ_{11} at vertex $(3h/2, 3\sqrt{3}h/2)$ (as shown in blue in Figure 3.40) is connected to vertex 9 through element 18, vertex 10 through element 17, vertex C (that is, vertex 15) through element 24, and vertex 12 through element 21.

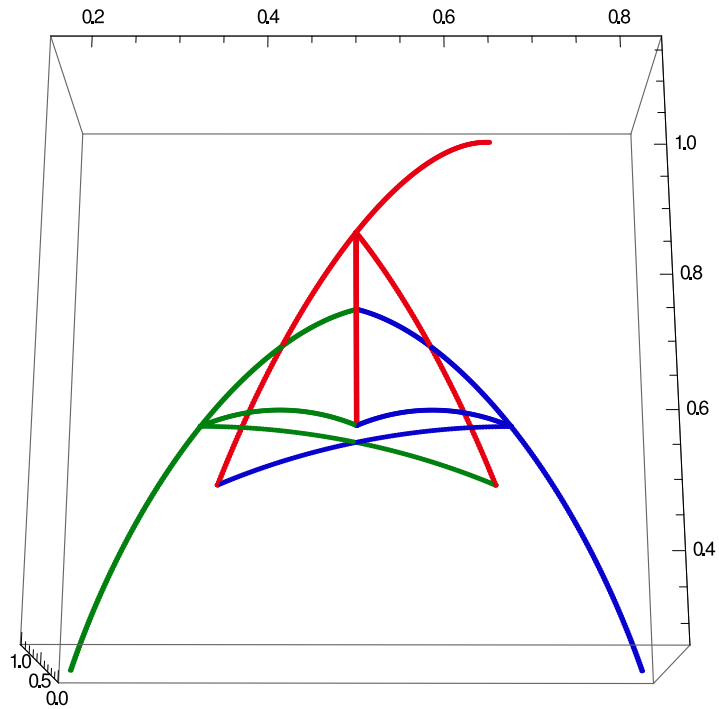


Figure 3.41: The basis functions ϕ_j where $j = 9, 10$ and 11 at fractal generation level $n = 2$.

The graph below shows the graph basis functions ϕ_j where $j = 4, 8$ and 12 which are the interior polymer vertices at fractal generation level $n = 2$ (see Figure 3.4). The graph basis functions ϕ_4 at vertex $(h/2, h/2\sqrt{3})$ (as shown in green in Figure 3.42) is connected to vertex 1 through element 4, vertex 2 through element 5 and vertex 3 through element 6. The graph basis functions ϕ_8 at vertex $(5h/2, h/2\sqrt{3})$ (as shown in blue in Figure 3.42) is connected to vertex 5 through element 11, vertex 6 through element 12 and vertex 7 through element 13. The graph basis functions ϕ_{12} at vertex $(3h/2, 7h/2\sqrt{3})$ (as shown in red in Figure 3.42) is connected to vertex 9 through element 19, vertex 10 through element 20 and vertex 11 through element 21.

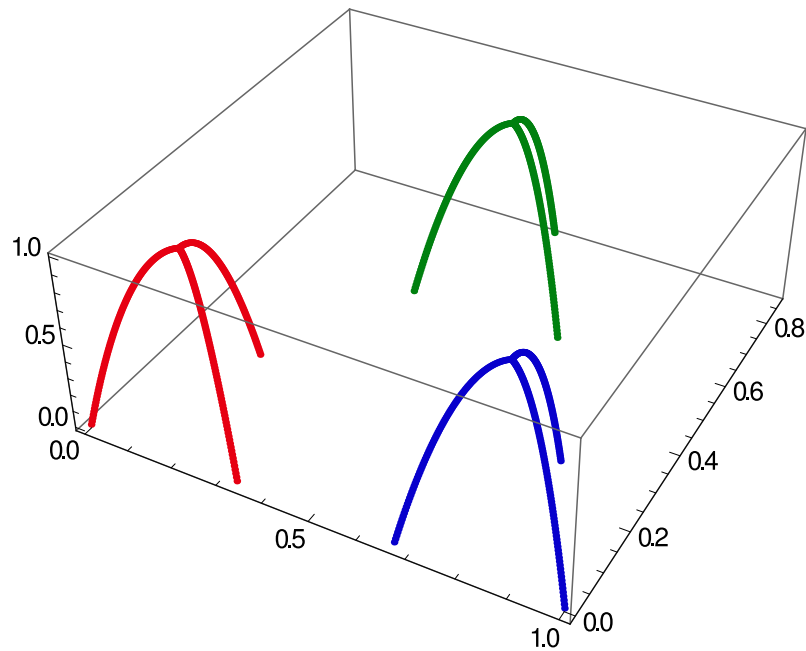


Figure 3.42: The basis functions ϕ_j where $j = 4, 8$ and 12 at fractal generation level $n = 2$.

The graph below shows the graph basis functions ψ_j where $j = 13, 14$ and 15 which are the exterior vertices at fractal generation level $n = 2$ (see Figure 3.4). The graph basis functions ψ_{13} at vertex $(-h, 0)$ (as shown in green in Figure 3.43) is connected to vertex 1 through element 22. The graph basis functions ψ_{14} at vertex $(4h, 0)$ (as shown in blue in Figure 3.43) is connected to vertex 6 through element 23. The graph basis functions ψ_{15} at vertex $(2h, 2\sqrt{3}h)$ (as shown in red in Figure 3.43) is connected to vertex 11 through element 24.

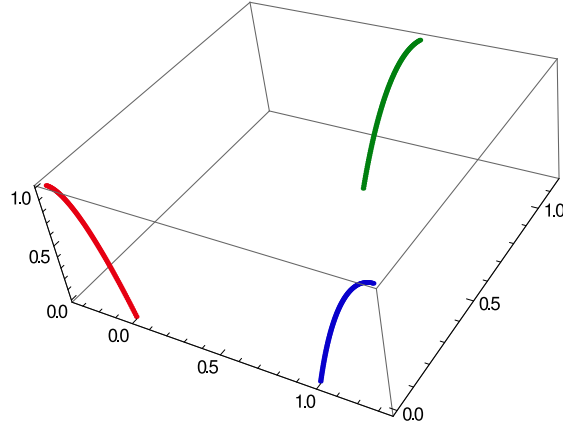


Figure 3.43: The basis functions ψ_j where $j = 13, 14$ and 15 at fractal generation level $n = 2$.

The fundamental (canonical) basis function $\hat{\phi}_J$ (see equation (3.2.11)) has five unknowns because we have four adjacent vertices and hence five conditions on this function and this leads to equation (3.2.17). Similarly, $\hat{\phi}_K$ has four unknowns and four conditions (as these vertices are degree 3) and $\hat{\psi}_I$ has two unknowns and two conditions (as there are degree 1). However, after we use the above transformations, the graph basis function appear more complicated, for example some now have terms in x, y and xy non-zero coefficients. Hence the graph basis functions are given by

$$\phi_j(x, y) = \begin{cases} a_j + b_jx + c_jy + d_jx^2 + f_jy^2 + g_jxy & j \in J \\ a_j + b_jx + c_jy + d_j(x^2 + y^2) & j \in K \end{cases} \quad (3.2.35)$$

and

$$\psi_j(x, y) = a_j + b_jx + c_jy + d_j(x^2 + y^2) \quad j \in I \quad (3.2.36)$$

where $(x, y) \in \Omega$ and a, b, c, d, f and $g \in \mathbb{R}$ are coefficients to be determined by transforming equations (3.2.17), (3.2.23) and (3.2.25) (see Appendix A.2) and $J = \{1, 2, 3\}$ at $n = 1$, $J = \{1, 2, 3, 5, 6, 7, 9, 10, 11\}$ at $n = 2$ which are the interior

piezoelectric vertices, $K = \{4\}$ at $n = 1$ and $K = \{4, 8, 12\}$ at $n = 2$ which are the polymer vertices and $I = \{5, 6, 7\}$ at $n = 1$, $I = \{13, 14, 15\}$ at $n = 2$ which are the exterior piezoelectric vertices. Hence

$$\nabla\phi_j(x, y) = \begin{cases} (b_j + 2d_jx + g_jy, c_j + 2f_jy + g_jx) & j \in J \\ (b_j + 2d_jx, c_j + 2d_jy) & j \in K \end{cases} \quad (3.2.37)$$

and

$$\nabla\psi_j(x, y) = (b_j + 2d_jx, c_j + 2e_jy) \quad j \in I. \quad (3.2.38)$$

For each element (edge) e where $e \in M_J$ (which is the set of elements in the interior that are piezoelectric), for ${}^eH_{ji}^{(n)}$ where $j, i \in \{1, 2, \dots, N, N + 1\}$ we can write equation (3.2.8) (using equation (3.2.35)) as

$$\begin{aligned} {}^{M_J}H_{ji}^{(n)} &= \int_e \left((a_j + b_jx + c_jy + d_jx^2 + f_jy^2 + g_jxy) \right. \\ &\quad \left. \cdot (a_i + b_ix + c_iy + d_ix^2 + f_iy^2 + g_ixy) \right) d\underline{x} \\ &= \int_e \left(a_ja_i + (a_jb_i + a_ib_j)x + (a_jc_i + a_ic_j)y + (a_jd_i + a_id_j + b_jb_i)x^2 \right. \\ &\quad \left. + (a_jf_i + a_if_j + c_jc_i)y^2 + (a_jg_i + a_ig_j + b_jc_i + b_ic_j)xy + (b_jd_i + \right. \\ &\quad \left. b_id_j)x^3 + (c_jf_i + c_if_j)y^3 + (b_jf_i + b_if_j + c_jg_i + c_ig_j)xy^2 + (b_jg_i + \right. \\ &\quad \left. b_ig_j + c_jd_i + c_id_j)x^2y + (f_jg_i + f_ig_j)xy^3 + (d_jg_i + d_ig_j)x^3y + (d_jf_i \right. \\ &\quad \left. + d_if_j + g_jg_i)x^2y^2 + d_jd_ix^4 + f_jf_jy^4 \right) d\underline{x}. \end{aligned} \quad (3.2.39)$$

Similarly, for each element (edge) e where $e \in M_K$ (which is the set of elements in

the interior that are a polymer - piezoelectric mix), then

$$\begin{aligned}
M_K H_{ji}^{(n)} &= \int_e \left((a_j + b_j x + c_j y + d_j x^2 + f_j y^2 + g_j xy) \cdot (a_i + b_i x + c_i y + \right. \\
&\quad \left. d_i(x^2 + y^2)) \right) d\underline{x} \\
&= \int_e \left(a_j a_i + (a_j b_i + a_i b_j) x + (a_j c_i + a_i c_j) y + (b_i b_j + a_j d_i + a_i d_j) x^2 \right. \\
&\quad \left. + (c_i c_j + a_j d_i + a_i f_j) y^2 + (b_i c_j + b_j c_i + a_i g_j) xy + (b_j d_i + b_i d_j) x^3 + \right. \\
&\quad \left. (c_j d_i + c_i f_j) y^3 + (b_j d_i + b_i f_j + c_i g_j) xy^2 + (c_j d_i + c_i d_j + b_i g_j) x^2 y + \right. \\
&\quad \left. d_i g_j xy^3 + d_i g_j x^3 y + (d_i d_j + d_i f_j) x^2 y^2 + d_i d_j x^4 + d_i f_j y^4 \right) d\underline{x}. \quad (3.2.40)
\end{aligned}$$

For the boundary elements $e \in M_I$ (which is the set of elements that connect to the exterior) note that $M_I H_{ii}^{(n)} = M_J H_{ii}^{(n)}$ where $i \in J$ (corner vertices). For

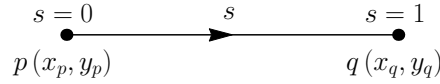


Figure 3.44: An isoparametric element (edge) between piezoelectric vertices $p(x_p, y_p)$ and $q(x_q, y_q)$.

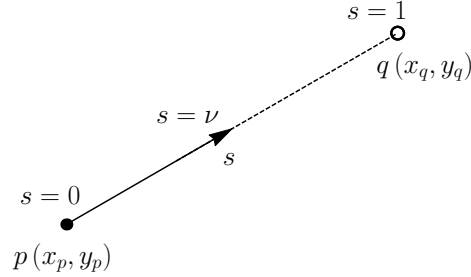


Figure 3.45: An isoparametric element (edge) between piezoelectric vertex $p(x_p, y_p)$ and polymer vertex $q(x_q, y_q)$. The fraction of piezoelectric material in this edge is given by ν .

a piezoelectric element lying between vertex p and vertex q the isoparametric representation, given by

$$(x(s), y(s)) = ((x_j - x_i)s + x_i, (y_j - y_i)s + y_i) \quad (3.2.41)$$

is employed, where $s = 0$ and $s = 1$ and $d\underline{x} = h ds$ (see Figure 3.44). For the elements that join a piezoelectric vertex to a polymer vertex a similar representation is used but here $d\underline{x} = h/\sqrt{3} ds$ and the region between $s = 0$ and $s = \nu$ is piezoelectric and that between $s = \nu$ and $s = 1$ is polymer (see Figure 3.45). Substituting this into equations (3.2.39) and (3.2.40) gives

$$H_{ji}^{(n)} = \begin{cases} h \int_0^1 \phi_j \phi_i ds & \text{if } e \in M_J \\ \frac{h}{\sqrt{3}} \int_0^1 \phi_j \phi_i ds & \text{if } e \in M_K \\ h \int_0^1 \phi_j \phi_i ds & \text{if } e \in M_I. \end{cases} \quad (3.2.42)$$

Let us start with an interior piezoelectric element ($e \in M_J$), say $e = 1 \in M_J$ which is connected between vertex 1 at $(x_i, y_i) = (0, 0)$ and vertex 2 at $(x_j, y_j) = (h, 0)$. From equation (3.2.41) we get $(x(s), y(s)) = (hs, 0)$ and then from equations (3.2.35) and (3.2.42) we get

$$\begin{aligned} {}^{e=1}H_{11}^{(1)} &= h \int_0^1 \phi_1(hs, 0) \phi_1(hs, 0) ds \\ &= h \int_0^1 (1 - s^2)^2 ds \\ &= \frac{h}{30}(16). \end{aligned}$$

Similarly,

$$\begin{aligned} {}^{e=1}H_{12}^{(1)} &= h \int_0^1 \phi_1(hs, 0) \phi_2(hs, 0) ds \\ &= h \int_0^1 (1 - s^2) (2s - s^2) ds \\ &= h \int_0^1 (1 - s^2) (2 - s) s ds \\ &= \frac{h}{30}(11), \end{aligned}$$

where we note that ${}^{e=1}H_{21}^{(1)} = {}^{e=1}H_{12}^{(1)}$. Also

$$\begin{aligned}
{}^{e=1}H_{22}^{(1)} &= h \int_0^1 \phi_2(hs, 0) \phi_2(hs, 0) ds \\
&= h \int_0^1 (2s - s^2)^2 ds \\
&= h \int_0^1 (2 - s)^2 s^2 ds \\
&= \frac{h}{30}(16).
\end{aligned}$$

So for each interior piezoelectric element ($e \in M_J$),

$$M_J H_{ji}^{(n)} = \frac{h}{30} \begin{cases} 16 & \text{if } j = i \\ 11 & \text{if } j \neq i \\ 0 & \text{otherwise.} \end{cases} \quad (3.2.43)$$

For a piezoelectric - polymer element ($e \in M_K$), let us take the example $e = 5 \in M_K$ which is connected between vertex 2 at $(x_i, y_j) = (h, 0)$ and vertex 4 at $(x_j, y_j) = (h/2, h/(2\sqrt{3}))$. From equation (3.2.41) we get $(x(s), y(s)) = (-h/2s + h, h/(2\sqrt{3})s)$ and then from equations (3.2.35) and (3.2.42) we get

$$\begin{aligned}
{}^{e=5}H_{22}^{(1)} &= \frac{h}{\sqrt{3}} \int_0^1 \phi_2\left(\frac{-h}{2}s + h, \frac{h}{2\sqrt{3}}s\right) \phi_2\left(\frac{-h}{2}s + h, \frac{h}{2\sqrt{3}}s\right) ds \\
&= \frac{h}{\sqrt{3}} \int_0^1 (1 - s^2)^2 ds \\
&= \frac{h}{30\sqrt{3}}(16).
\end{aligned}$$

Similarly,

$$\begin{aligned}
{}^{e=5}H_{24}^{(1)} &= \frac{h}{\sqrt{3}} \int_0^1 \phi_2 \left(\frac{-h}{2}s + h, \frac{h}{2\sqrt{3}}s \right) \phi_4 \left(\frac{-h}{2}s + h, \frac{h}{2\sqrt{3}}s \right) ds \\
&= \frac{h}{\sqrt{3}} \int_0^1 (1-s^2)(2-s)s ds \\
&= \frac{h}{30\sqrt{3}}(11),
\end{aligned}$$

where we note that ${}^{e=5}H_{42}^{(1)} = {}^{e=5}H_{24}^{(1)}$. Also

$$\begin{aligned}
{}^{e=5}H_{44}^{(1)} &= \frac{h}{\sqrt{3}} \int_0^1 \phi_4 \left(\frac{-h}{2}s + h, \frac{h}{2\sqrt{3}}s \right) \phi_4 \left(\frac{-h}{2}s + h, \frac{h}{2\sqrt{3}}s \right) ds \\
&= \frac{h}{\sqrt{3}} \int_0^1 (2-s)^2 s^2 ds \\
&= \frac{h}{30\sqrt{3}}(16).
\end{aligned}$$

So, for each piezoelectric - polymer element ($e \in M_K$),

$${}_{M_K}H_{ji}^{(n)} = \frac{h}{30\sqrt{3}} \begin{cases} 16 & \text{if } j = i \\ 11 & \text{if } j \neq i \\ 0 & \text{otherwise.} \end{cases} \quad (3.2.44)$$

Note that from equation (3.2.7) since ${}_{M_K}H_{ji}^{(n)} = h/\sqrt{3}(\int_0^\nu \phi_j \phi_i dx + \int_\nu^1 \phi_j \phi_i dx) = h/\sqrt{3} \int_0^1 \phi_j \phi_i dx$, then ν does not explicitly appear. On the edges in M_K there will be a jump in the material properties and hence a jump in the observed dynamics in each section of the edge. However, as our basis functions are only defined at vertices at the extremities of these edges then, as a modelling assumption, this phenomenon is simply averaged out (so it is just the volume fraction of polymer that is modelled rather than the spatial location of a jump in material properties). Hence we have used quadratic polynomials as our basis functions. It would be

possible to put two elements with a vertex at the interface between the piezoelectric and the polymer material on these edges to capture this jump. We will see later that for $c^2 K_{ji}^{(n)}$ for $e \in M_K$, we need to apply equation (2.2.11) where ${}^{M_K} c^2 K_{ji}^{(n)} = h/\sqrt{3}(c_T^2 \int_0^\nu \nabla \phi_j \cdot \nabla \phi_i ds + c_P^2 \int_\nu^1 \nabla \phi_j \cdot \nabla \phi_i ds)$ and so ν does appear explicitly in that case. For exterior piezoelectric elements ($e \in M_I = \{M + 1, M + 2, M + 3\}$), let us take the example for one element that is $e = 7 \in M_I$ which is connected between vertex 1 at $(x_i, y_j) = (0, 0)$ and vertex 5 at $(x_j, y_j) = (-h, 0)$ and apply equation (3.2.41) to get $(x(s), y(s)) = (hs, 0)$. Then from equations (3.2.35) and (3.2.42) we get

$$\begin{aligned} {}^{e=7} H_{11}^{(1)} &= h \int_0^1 \phi_1(hs, 0) \phi_1(hs, 0) ds \\ &= h \int_0^1 (1 - s^2)^2 ds \\ &= \frac{h}{30}(16). \end{aligned}$$

Similarly, for each exterior piezoelectric element ($e \in M_I$),

$${}^{M_I} H_{ji}^{(n)} = \frac{h}{30} \begin{cases} 16 & \text{if } j = i = q \\ 0 & \text{otherwise} \end{cases} \quad (3.2.45)$$

where q is the corner vertex of the SG(3,4) graph connected to element e (for $n = 1$, $q \in \{1, 2, 3\}$, and for $n = 2$, $q \in \{1, 6, 11\}$). The left hand side of equation (3.2.3) does not involve the basis functions (ψ_I) which are located at boundary vertices I . As such the integrals are zero unless $\phi_i = \phi_j$ where $i, j \in \{1, m, N\}$.

Assembling the full matrix in equation (3.2.8) gives, for generation level $n = 1$

$$H_{ji}^{(1)} = h \begin{bmatrix} \frac{8}{45}(9 + \sqrt{3}) & \frac{11}{30} & \frac{11}{30} & \frac{11}{30\sqrt{3}} \\ \frac{11}{30} & \frac{8}{45}(9 + \sqrt{3}) & \frac{11}{30} & \frac{11}{30\sqrt{3}} \\ \frac{11}{30} & \frac{11}{30} & \frac{8}{45}(9 + \sqrt{3}) & \frac{11}{30\sqrt{3}} \\ \frac{11}{30\sqrt{3}} & \frac{11}{30\sqrt{3}} & \frac{11}{30\sqrt{3}} & \frac{48}{30\sqrt{3}} \end{bmatrix} = h \hat{H}_{ji}^{(1)} \quad (3.2.46)$$

and at generation level $n = 2$,

$$H_{ji}^{(2)} = h \begin{bmatrix} & & & & 0 & 0 & 0 & 0 & 0 & 0 & 0 & 0 \\ & & & & \frac{11}{30} & 0 & 0 & 0 & 0 & 0 & 0 & 0 \\ & & & & 0 & 0 & 0 & 0 & \frac{11}{30} & 0 & 0 & 0 \\ & & & & 0 & 0 & 0 & 0 & 0 & 0 & 0 & 0 \\ 0 & \frac{11}{30} & 0 & 0 & & & & & 0 & 0 & 0 & 0 \\ 0 & 0 & 0 & 0 & & \hat{H}_{ji}^{(1)} & & & 0 & 0 & 0 & 0 \\ 0 & 0 & 0 & 0 & & & & & 0 & \frac{11}{30} & 0 & 0 \\ 0 & 0 & 0 & 0 & & & & & 0 & 0 & 0 & 0 \\ 0 & 0 & \frac{11}{30} & 0 & 0 & 0 & 0 & 0 & & & & \\ 0 & 0 & 0 & 0 & 0 & 0 & \frac{11}{30} & 0 & & \hat{H}_{ji}^{(1)} & & \\ 0 & 0 & 0 & 0 & 0 & 0 & 0 & 0 & & & & \\ 0 & 0 & 0 & 0 & 0 & 0 & 0 & 0 & & & & \end{bmatrix}. \quad (3.2.47)$$

So, from equations (3.2.46) and (3.2.47), we can write matrix H , for $n \geq 2$ as

$$H_{ji}^{(n)} = h \begin{bmatrix} \hat{H}_{ji}^{(n-1)} & \frac{11}{30}V_{ji}^{(n)} & \frac{11}{30}V_{ji}^{(n)} \\ \frac{11}{30}V_{ji}^{(n)} & \hat{H}_{ji}^{(n-1)} & \frac{11}{30}V_{ji}^{(n)} \\ \frac{11}{30}V_{ji}^{(n)} & \frac{11}{30}V_{ji}^{(n)} & \hat{H}_{ji}^{(n-1)} \end{bmatrix},$$

where $\hat{H}_{ji}^{(n-1)} = H_{ji}^{(n-1)}/h$ and $V_{ji}^{(n)} = \mathbb{1}_{D^{(n)}}(ji)$ is the adjacency matrix for the subgraph of $\text{SG}^{(n)}(3)$ consisting of the edges $D^{(n)}$ that connect each of the three $\text{SG}^{(n-1)}(3)$ graphs (for $n = 2$, $D^{(2)} = \{\{2, 5\}, \{3, 9\}, \{7, 10\}\}$ (see Figure 3.4), and for $n = 3$, $D^{(3)} = \{\{6, 13\}, \{11, 25\}, \{23, 30\}\}$). (where $\mathbb{1}_{\{A\}}(a)$ is the indicator function which equals 1 if $a \in A$, and 0 otherwise). That is,

$$H_{ji}^{(n)} = h \left(\bar{\hat{H}}_{ji}^{(n-1)} + \frac{11}{30}V_{ji}^{(n)} \right), \quad (3.2.48)$$

where $\bar{\hat{H}}_{ji}^{(n-1)}$ is a block diagonal matrix consisting of three blocks of matrix $\hat{H}_{ji}^{(n-1)}$.

Similarly for ${}^e K_{ji}^{(n)}$ we can write equation (3.2.9) (using equation (3.2.37)) as

$$\begin{aligned} {}^{M_J} K_{ji}^{(n)} &= c^2 \int_e ((b_j + 2d_jx + g_jy, c_j + 2f_jy + g_jx) \cdot (b_i + 2d_ix + g_iy, c_i + 2f_iy + g_ix)) d\underline{x} \\ &= c^2 \int_e (b_jb_i + 2(b_jd_i + b_id_j)x + (b_jg_i + b_ig_j)y + 4d_jd_ix^2 + g_jg_iy^2 \\ &\quad + 2(d_jg_i + d_ig_j)xy + c_jc_i + (c_jg_i + c_ig_j)x + 2(c_jf_i + c_if_j)y + g_jg_ix^2 \\ &\quad + 4f_jf_iy^2 + 2(f_jg_i + f_ig_j)xy) d\underline{x}. \end{aligned}$$

For each element (edge) e where $e \in M_K$ or $e \in M_I$

$$\begin{aligned} {}^{M_K}K_{ji}^{(n)} = {}^{M_I}K_{ji}^{(n)} &= c^2 \int_e (b_j + 2d_jx, c_j + 2d_jy) \cdot (b_i + 2d_ix, c_i + 2d_iy) d\underline{x}, \\ &= c^2 \int_e \left(b_ib_j + 2(d_jb_i + d_ib_j)x + 4d_id_jx^2 + c_ic_j + 2(d_ic_j + d_jc_i)y \right. \\ &\quad \left. + 4d_id_jy^2 \right) d\underline{x}. \end{aligned}$$

By using the definition of c in equation (2.2.11) and using equation (3.2.41) then we can write equation (3.2.9) as

$$K_{ji}^{(n)} = \begin{cases} hc_T^2 \int_0^1 \nabla \phi_j \cdot \nabla \phi_i ds & \text{if } e \in M_J \\ \frac{h}{\sqrt{3}} \left(c_T^2 \int_0^\nu \nabla \phi_j \cdot \nabla \phi_i ds + c_P^2 \int_\nu^1 \nabla \phi_j \cdot \nabla \phi_i ds \right) & \text{if } e \in M_K \\ hc_T^2 \int_0^1 \nabla \phi_j \cdot \nabla \phi_i ds & \text{if } e \in M_I, \end{cases} \quad (3.2.49)$$

where ν is a parameter indicating the volume fraction of piezoelectric material in edge $e \in M_K$. For $e \in M_J$, from equations (3.2.37) and (3.2.49) we get

$${}^{M_J}K_{ji}^{(n)} = hc_T^2 \begin{cases} \frac{52}{h^2} \int_0^1 s^2 ds & \text{if } j = i = p \\ \frac{-44}{h^2} \int_0^1 s(s-1) ds & \text{if } j, i \in \{p, q\}, j \neq i \\ \frac{52}{h^2} \int_0^1 (s-1)^2 ds & \text{if } j = i = q \\ 0 & \text{otherwise.} \end{cases}$$

That is

$${}^{M_J}K_{ji}^{(n)} = \frac{2}{3h} c_T^2 \begin{cases} 26 & \text{if } j = i = p \\ 11 & \text{if } j, i \in \{p, q\}, j \neq i \\ 26 & \text{if } j = i = q \\ 0 & \text{otherwise.} \end{cases}$$

Similarly for $e \in M_K$,

$$M_K K_{ji}^{(n)} = \frac{h}{\sqrt{3}} \begin{cases} \frac{12}{h^2} (c_T^2 \int_0^\nu s^2 ds + c_P^2 \int_\nu^1 s^2 ds) & \text{if } j = i = p \\ \frac{12}{h^2} (c_T^2 \int_0^\nu s(s-1) ds + c_P^2 \int_\nu^1 s(s-1) ds) & \text{if } j, i \in \{p, q\}, j \neq i \\ \frac{12}{h^2} (c_T^2 \int_0^\nu (s-1)^2 ds + c_P^2 \int_\nu^1 (s-1)^2 ds) & \text{if } j = i = q \\ 0 & \text{otherwise.} \end{cases}$$

That is

$$M_K K_{ji}^{(n)} = \frac{2}{3h} c_T^2 \begin{cases} 2\sqrt{3} \left(\nu^3 + \frac{c_P^2}{c_T^2} (1 - \nu^3) \right) & \text{if } j = i = p \\ \sqrt{3} \left(\nu^2 (2\nu - 3) - \frac{c_P^2}{c_T^2} (\nu - 1)^2 (1 + 2\nu) \right) & \text{if } j, i \in \{p, q\}, j \neq i \\ 2\sqrt{3} \left(\nu (\nu^2 - 3\nu + 3) - \frac{c_P^2}{c_T^2} (\nu - 1)^3 \right) & \text{if } j = i = q \\ 0 & \text{otherwise.} \end{cases}$$

Similarly for $e \in M_I$,

$$M_I K_{ji}^{(n)} = hc_T^2 \begin{cases} \frac{52}{h^2} \int_0^1 s^2 ds & \text{if } j = i = q \\ 0 & \text{otherwise.} \end{cases}$$

That is

$$M_I K_{ji}^{(n)} = \frac{2}{3h} c_T^2 \begin{cases} 26 & \text{if } j = i = q \\ 0 & \text{otherwise.} \end{cases}$$

Assembling the full matrix in equation (3.2.9) gives, for generation level $n = 1$

$$K_{ji}^{(1)} = \frac{c_T^2}{h} \begin{bmatrix} D & \frac{22}{3} & \frac{22}{3} & R \\ \frac{22}{3} & D & \frac{22}{3} & R \\ \frac{22}{3} & \frac{22}{3} & D & R \\ R & R & R & E \end{bmatrix} = \frac{c_T^2}{h} \hat{K}_{ji}^{(1)}, \quad (3.2.50)$$

where $\hat{K}_{ji}^{(n-1)} = h K_{ji}^{(n-1)} / c_T^2$. That is,

$$K_{ji}^{(n)} = \frac{1}{h} \left(\bar{K}_{ji}^{(n-1)} + \frac{22}{3} V_{ji}^{(n)} \right), \quad (3.2.52)$$

where $\bar{K}_{ji}^{(n-1)}$ is a block diagonal matrix consisting of three blocks of matrix $\hat{K}_{ji}^{(n-1)}$.

Combining equations (3.2.46) and (3.2.50) gives equation (3.2.7) as

$$A_{ji}^{(1)} = h \begin{bmatrix} \alpha & \beta & \beta & \mathcal{P} \\ \beta & \alpha & \beta & \mathcal{P} \\ \beta & \beta & \alpha & \mathcal{P} \\ \mathcal{P} & \mathcal{P} & \mathcal{P} & \vartheta \end{bmatrix} = h \hat{A}_{ji}^{(1)}, \quad (3.2.53)$$

where $\alpha = (q^2/30) (48 + (16/\sqrt{3})) + 52 + (4/\sqrt{3}) (\nu^3 + c_P^2/c_T^2(1 - \nu^3))$, $\beta = 11q^2/30 + 22/3$, $\mathcal{P} = 11q^2/30\sqrt{3} + (2/\sqrt{3}) (\nu^2(2\nu - 3) - c_P^2/c_T^2(\nu - 1)^2(1 + 2\nu))$ and $\vartheta = 48q^2/30\sqrt{3} + (4\sqrt{3}) (\nu(\nu^2 - 3\nu + 3) - c_P^2/c_T^2(\nu - 1)^3)$. Similarly, for generation

level $n = 2$,

$$A_{ji}^{(2)} = h \begin{bmatrix} & & & & 0 & 0 & 0 & 0 & 0 & 0 & 0 & 0 \\ & & & & \beta & 0 & 0 & 0 & 0 & 0 & 0 & 0 \\ & & & & 0 & 0 & 0 & 0 & \beta & 0 & 0 & 0 \\ & & & & 0 & 0 & 0 & 0 & 0 & 0 & 0 & 0 \\ \hline 0 & \beta & 0 & 0 & & & & & 0 & 0 & 0 & 0 \\ 0 & 0 & 0 & 0 & & \hat{A}_{ji}^{(1)} & & & 0 & 0 & 0 & 0 \\ 0 & 0 & 0 & 0 & & & & & 0 & \beta & 0 & 0 \\ 0 & 0 & 0 & 0 & & & & & 0 & 0 & 0 & 0 \\ \hline 0 & 0 & \beta & 0 & 0 & 0 & 0 & 0 & & & & \\ 0 & 0 & 0 & 0 & 0 & 0 & \beta & 0 & & \hat{A}_{ji}^{(1)} & & \\ 0 & 0 & 0 & 0 & 0 & 0 & 0 & 0 & & & & \\ 0 & 0 & 0 & 0 & 0 & 0 & 0 & 0 & & & & \end{bmatrix}. \quad (3.2.54)$$

So, from equations (3.2.53) and (3.2.54), we can write matrix A , for $n \geq 2$ as

$$A_{ji}^{(n)} = h \begin{bmatrix} & & & \hat{A}_{ji}^{(n-1)} & \beta V_{ji}^{(n)} & \beta V_{ji}^{(n)} \\ \hline \beta V_{ji}^{(n)} & \hat{A}_{ji}^{(n-1)} & \beta V_{ji}^{(n)} & & & \\ \hline \beta V_{ji}^{(n)} & \beta V_{ji}^{(n)} & \hat{A}_{ji}^{(n-1)} & & & \end{bmatrix},$$

where $\hat{A}_{ji}^{(n-1)} = A_{ji}^{(n-1)}/h$. That is,

$$A_{ji}^{(n)} = h \left(\bar{A}_{ji}^{(n-1)} + \beta V_{ji}^{(n)} \right), \quad (3.2.55)$$

where $\bar{A}_{ji}^{(n-1)}$ is a block diagonal matrix consisting of three blocks of matrix $\hat{A}_{ji}^{(n-1)}$.

A similar treatment, can be given to equation (3.2.6) by using the definition of c that appears in equation (2.2.11) to give (where $m = (N + 1)/2$)

$$b_j^{(n)} = \begin{cases} - \left(\int_{e_{M+1}} (q^2 \psi_{N+2} \phi_j + h^2 \nabla \psi_{N+2} \cdot \nabla \phi_j) d\underline{x} \right) U_A, & j = 1 \\ - \left(\int_{e_{M+2}} (q^2 \psi_{N+3} \phi_j + h^2 \nabla \psi_{N+3} \cdot \nabla \phi_j) d\underline{x} \right) U_B, & j = m \\ - \left(\int_{e_{M+3}} (q^2 \psi_{N+4} \phi_j + h^2 \nabla \psi_{N+4} \cdot \nabla \phi_j) d\underline{x} \right) U_C, & j = N \\ 0 & \text{otherwise,} \end{cases} \quad (3.2.56)$$

where $M + 1, M + 2$ and $M + 3$ are the set of edges M_I, U_A, U_B and U_C are the mechanical displacements at the fictitious vertices A, B and C respectively. Now consider equation (3.2.56) to find $b_m^{(n)}$ at element $e = M + 2$ (see Fig-

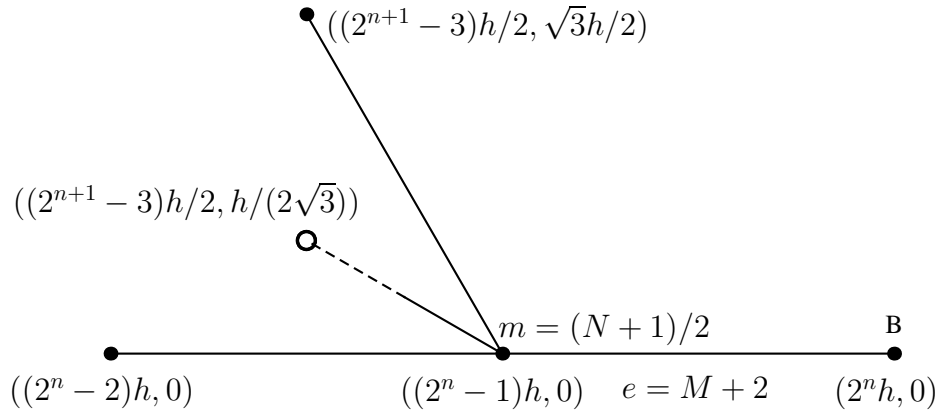


Figure 3.46: The boundary element for $e = M + 2$

ure 3.46), which is connected between vertex m at $(x_m, y_m) = ((2^n - 1)h, 0)$ and vertex B at $(x_B, y_B) = (2^n h, 0)$. From equation (3.2.41) we get $(x(s), y(s)) =$

$((x_B - x_m)s + x_m, (y_B - y_m)s + y_m) = ((s + 2^n - 1)h, 0)$ and $d\mathbf{x} = h ds$, gives

$$b_m^{(n)} = -h \left(\int_{M+2} (q^2 \psi_B \phi_m + h^2 \nabla \psi_B \cdot \nabla \phi_m) ds \right) U_B. \quad (3.2.57)$$

From equation (3.2.36) the basis functions at vertex B in element $e = M + 2$ is

$$\psi_B(x, y) = 1 - \frac{(x - 2^n h)^2 + y^2}{h^2} \quad (3.2.58)$$

and from equation (3.2.35) the basis functions at vertex m is

$$\phi_m(x, y) = \frac{(2^{n+1} - 2^{2n})h^2 - x^2 + 4\sqrt{3}xy + 3y^2 + (2^{n+1} - 2)h(x - 2\sqrt{3}y)}{h^2}. \quad (3.2.59)$$

Substituting equation (3.2.41) into equations (3.2.58) and (3.2.59) gives

$$\psi_B(x(s), y(s)) = (2 - s)s \quad (3.2.60)$$

and

$$\phi_m(x(s), y(s)) = 1 - s^2. \quad (3.2.61)$$

From equations (3.2.37) and (3.2.38), equations (3.2.58) and (3.2.59) gives

$$\nabla \psi_B(x, y) = \left(\frac{2(2^n h - x)}{h^2}, \frac{-2y}{h^2} \right) \quad (3.2.62)$$

and

$$\nabla \phi_m(x, y) = \left(\frac{(2^{n+1} - 2)h - 2x + 4\sqrt{3}y}{h^2}, \frac{4\sqrt{3}(1 - 2^n)h + 4\sqrt{3}x + 6y}{h^2} \right). \quad (3.2.63)$$

Substituting equation (3.2.41) into equations (3.2.62) and (3.2.63) gives

$$\nabla\psi_B(x(s), y(s)) = \left(\frac{2-2s}{h}, 0 \right) \quad (3.2.64)$$

and

$$\nabla\phi_m(x(s), y(s)) = \left(\frac{-2s}{h}, \frac{4\sqrt{3}s}{h} \right). \quad (3.2.65)$$

Substituting equations (3.2.60), (3.2.61), (3.2.64) and (3.2.65) into equation (3.2.57) gives

$$b_m^{(n)} = h \left(\frac{2}{3} - \frac{11}{30}q^2 \right) U_B.$$

A similar calculation, for $b_1^{(n)}$ at element $e = M + 1$ and $b_N^{(n)}$ at element $e = M + 3$ shows

$$b_j^{(n)} = h\eta \begin{cases} U_A, & j = 1 \\ U_B, & j = m \\ U_C, & j = N \\ 0 & \text{otherwise,} \end{cases} \quad (3.2.66)$$

where

$$\eta = \frac{2}{3} - \frac{11}{30}q^2. \quad (3.2.67)$$

For generation level $n = 1$,

$$b_j^{(1)} = h \left(\frac{2}{3} - \frac{11}{30}q^2 \right) \begin{cases} U_A, & j = 1 \\ U_B, & j = 2 \\ U_C, & j = 3 \\ 0 & \text{otherwise,} \end{cases}$$

and for generation level $n = 2$,

$$b_j^{(2)} = h \left(\frac{2}{3} - \frac{11}{30} q^2 \right) \begin{cases} U_A, & j = 1 \\ U_B, & j = 6 \\ U_C, & j = 11 \\ 0 & \text{otherwise.} \end{cases}$$

3.3 A Homogenised model of the transducer

In this section we introduce a homogenised model of this composite transducer [8,151–153] that will be compared with the renormalisation approach being developed here; this comparison being made at a low number of fractal generation levels (these are the most interesting cases as these are potentially manufacturable). The

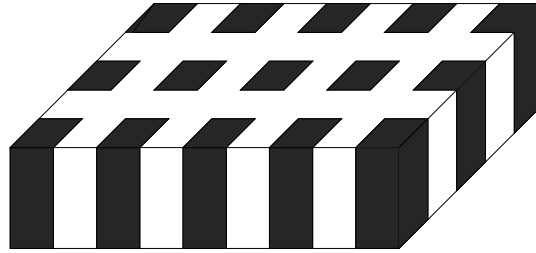


Figure 3.47: Illustration of a standard 1-3 composite transducer where the ceramic is black and the polymer is white. It clearly shows the regularity in the structure and the reliance on a single length scale.

homogenised model described below can be thought of as the operating characteristics that one would obtain from a conventional (i.e. non-fractal) 1-3 composite transducer as illustrated in Figure 3.47. The constitutive relations for the individual phases have a compact form, within the ceramic (E) phase, and within the polymer (P) phase [147,148]. From equation (2.2.1), and due to the properties of

PZT-5H (see Appendix A.4), we get

$$T_{11} = T_{12} = T_{21} = T_{22} = T_{33} = 0,$$

and

$$T_{13} = T_{31} = c_{1313}S_{13} + c_{1331}S_{31} - e_{113}E_1.$$

That is

$$T_5 = c_{55}(S_{13} + S_{31}) - e_{15}E_1,$$

and, using equation (2.2.3), since from equation (2.2.8) $u_{1,3} = 0$, then

$$T_5 = c_{44}u_{3,1} - e_{24}E_1, \quad (3.3.1)$$

since $c_{55} = c_{44}$ and $e_{15} = e_{24}$. Similarly we get

$$T_{23} = T_{32} = c_{3223}S_{23} + c_{3232}S_{32} - e_{232}E_2,$$

that is

$$T_4 = c_{44}u_{3,2} - e_{24}E_2. \quad (3.3.2)$$

So we rewrite equations (3.3.1) and (3.3.2), for the piezoelectric phase as

$$T_5^T = c_{44}^T u_{3,1}^T - e_{24}^T E_1^T$$

and

$$T_4^T = c_{44}^T u_{3,2}^T - e_{24}^T E_2^T. \quad (3.3.3)$$

Similarly, for polymer phase we get

$$T_5^P = c_{44}^P u_{3,1}^P,$$

and

$$T_4^P = c_{44}^P u_{3,2}^P, \quad (3.3.4)$$

since there is no piezoelectric effect in the polymer phase. From equation (2.2.2) we get for the piezoelectric phase

$$D_1^T = e_{24} u_{3,1}^T + \varepsilon_{11}^T E_1^T, \quad (3.3.5)$$

and

$$D_2^T = e_{24} u_{3,2}^T + \varepsilon_{11}^T E_2^T,$$

and for the polymer phase we get

$$D_1^P = \varepsilon_{11}^P E_1^P, \quad (3.3.6)$$

and

$$D_2^P = \varepsilon_{11}^P E_2^P,$$

where D_3^T , D_3^P are zero and ε_{11}^P is an element of the permittivity tensor of polymer. We assume uniform fields in each phase that any movement (strain) in the polymer phase is compensated by a strain in the piezoelectric phase, and so we can write

$$\bar{u}_{3,1} = v u_{3,1}^T + \bar{v} u_{3,1}^P, \quad (3.3.7)$$

and

$$\bar{u}_{3,2} = v u_{3,2}^T + \bar{v} u_{3,2}^P, \quad (3.3.8)$$

where v is the volume fraction of the piezoelectric phase where this is calculated via

$$v^{(n)} = \frac{\frac{3}{2}(3^n - 1) \left(\frac{L}{2^n - 1}\right) + 3^n \left(\frac{L}{(2^n - 1)\sqrt{3}}\right) \nu}{\frac{3}{2}(3^n - 1) \left(\frac{L}{2^n - 1}\right) + 3^n \left(\frac{L}{(2^n - 1)\sqrt{3}}\right)}$$

where $3(3^n - 1)/2$ is the number of elements that are piezoelectric (M_J), 3^n is the number of elements that are a polymer-piezoelectric composite (M_K), $L/(2^n - 1)$ is the length of elements M_J , $L/((2^n - 1)\sqrt{3})$ is the length of elements M_K and ν as defined in equation (3.2.49). That is

$$v^{(n)} = \frac{\frac{3}{2}(3^n - 1) + 3^{n-\frac{1}{2}}\nu}{\frac{3}{2}(3^n - 1) + 3^{n-\frac{1}{2}}},$$

and $\bar{v}^{(n)} = 1 - v^{(n)}$ is the volume fraction of the polymer phase. For example at generation level ($n = 1$) if $\nu = 1$ then $v = 1$ and if $\nu = 0$ then $v = 3/(3 + \sqrt{3})$. Assuming the electric fields are similarly averaged then

$$\bar{E}_1 = v E_1^T + \bar{v} E_1^P, \quad (3.3.9)$$

and

$$\bar{E}_2 = v E_2^T + \bar{v} E_2^P. \quad (3.3.10)$$

Assuming that the stresses in each phase are equal then

$$\bar{T}_4 = T_4^T = T_4^P \quad (3.3.11)$$

and

$$\bar{T}_5 = T_5^T = T_5^P.$$

If the electrical displacements are also equal in each phase then

$$\bar{D}_1 = D_1^T = D_1^P \quad (3.3.12)$$

and

$$\bar{D}_2 = D_2^T = D_2^P.$$

From the symmetry of the SG(3,4) graph (see Figure 2.11) then we have

$$\bar{u}_{3,2} = \bar{u}_{3,1} = \bar{u}, \quad (3.3.13)$$

since $u_{3,2}^T = u_{3,1}^T = u^T$, and $u_{3,2}^P = u_{3,1}^P = u^P$. We take the electric fields to be the same in both phases, namely,

$$\bar{E}_1 = \bar{E}_2 = \bar{E}, \quad (3.3.14)$$

since $E_1^T = E_2^T = E^T$, and $E_1^P = E_2^P = E^P$. Also

$$\bar{T}_4 = \bar{T}_5 = \bar{T}, \quad (3.3.15)$$

and

$$\bar{D}_1 = \bar{D}_2 = \bar{D}. \quad (3.3.16)$$

From equations (3.3.11), (3.3.15), (3.3.13) and (3.3.14) we can write equation (3.3.3) as

$$\bar{T} = c_{44}^T u^T - e_{24} E^T, \quad (3.3.17)$$

and from equations (3.3.12), (3.3.16), (3.3.13) and (3.3.14) we can write equation (3.3.5) as

$$\bar{D} = e_{24}u^T + \varepsilon_{11}^T E^T. \quad (3.3.18)$$

For the polymer phase, we have from equations (3.3.11), (3.3.15) and (3.3.13) that we can write equation (3.3.4) as

$$\bar{T} = c_{44}^P u^P, \quad (3.3.19)$$

and from equations (3.3.12), (3.3.16) and (3.3.14) we can write equation (3.3.6) as

$$\bar{D} = \varepsilon_{11}^P E^P. \quad (3.3.20)$$

From equation (3.3.13) we can write equations (3.3.8) and (3.3.7) as

$$\bar{u} = \bar{S} = v u^T + \bar{v} u^P, \quad (3.3.21)$$

and from equation (3.3.14) we can write equations (3.3.9) and (3.3.10) as

$$\bar{E} = v E^T + \bar{v} E^P. \quad (3.3.22)$$

From equation (3.3.19) we get

$$u^P = \frac{\bar{T}}{c_{44}^P}, \quad (3.3.23)$$

and from equation (3.3.20) we get

$$E^P = \frac{\bar{D}}{\varepsilon_{11}^P}. \quad (3.3.24)$$

Hence, from equations (3.3.21) and (3.3.23) we get

$$u^T = \frac{1}{v} \left(\bar{S} - \bar{v} \frac{\bar{T}}{c_{44}^P} \right), \quad (3.3.25)$$

and from equations (3.3.22) and (3.3.24) we get

$$E^T = \frac{1}{v} \left(\bar{E} - \bar{v} \frac{\bar{D}}{\varepsilon_{11}^P} \right). \quad (3.3.26)$$

Substituting equations (3.3.25) and (3.3.26) into equation (3.3.17) gives

$$\bar{T} = c_{44}^T \frac{1}{v} \left(\bar{S} - \bar{v} \frac{\bar{T}}{c_{44}^P} \right) - e_{24} \frac{1}{v} \left(\bar{E} - \bar{v} \frac{\bar{D}}{\varepsilon_{11}^P} \right).$$

That is

$$\bar{T} \left(1 + \frac{\bar{v} c_{44}^T}{v c_{44}^P} \right) = \frac{c_{44}^T}{v} \bar{S} - \frac{e_{24}}{v} \bar{E} + \frac{\bar{v} e_{24}}{v \varepsilon_{11}^P} \bar{D}. \quad (3.3.27)$$

Also, substituting equations (3.3.25) and (3.3.26) into equation (3.3.18) gives

$$\bar{D} = \frac{e_{24}}{v} \left(\bar{S} - \bar{v} \frac{\bar{T}}{c_{44}^P} \right) + \frac{\varepsilon_{11}^T}{v} \left(\bar{E} - \bar{v} \frac{\bar{D}}{\varepsilon_{11}^P} \right).$$

That is

$$\bar{D} \left(1 + \frac{\bar{v} \varepsilon_{11}^T}{v \varepsilon_{11}^P} \right) = \frac{e_{24}}{v} \bar{S} - \frac{\bar{v} e_{24}}{v c_{44}^P} \bar{T} + \frac{\varepsilon_{11}^T}{v} \bar{E}.$$

Hence,

$$\bar{D} = \frac{\varepsilon_{11}^P e_{24}}{v \varepsilon_{11}^P + \bar{v} \varepsilon_{11}^T} \bar{S} - \frac{\bar{v} e_{24} \varepsilon_{11}^P}{c_{44}^P (v \varepsilon_{11}^P + \bar{v} \varepsilon_{11}^T)} \bar{T} + \frac{\varepsilon_{11}^P \varepsilon_{11}^T}{v \varepsilon_{11}^P + \bar{v} \varepsilon_{11}^T} \bar{E}.$$

That is

$$\bar{D} = \frac{\varepsilon_{11}^P e_{24}}{\bar{\varepsilon}^*} \bar{S} - \frac{\bar{v} e_{24} \varepsilon_{11}^P}{c_{44}^P \bar{\varepsilon}^*} \bar{T} + \frac{\varepsilon_{11}^P \varepsilon_{11}^T}{\bar{\varepsilon}^*} \bar{E}, \quad (3.3.28)$$

where $\bar{\varepsilon}^* = v\varepsilon_{11}^P + \bar{v}\varepsilon_{11}^T$. Putting this into equation (3.3.27) gives

$$\bar{T} \left(1 + \frac{\bar{v}c_{44}^T}{vc_{44}^P} \right) = \frac{c_{44}^T}{v} \bar{S} - \frac{e_{24}}{v} \bar{E} + \frac{\bar{v}e_{24}^2}{v\bar{\varepsilon}^*} \bar{S} - \frac{\bar{v}^2 e_{24}^2}{vc_{44}^P \bar{\varepsilon}^*} \bar{T} + \frac{\bar{v}e_{24}\varepsilon_{11}^T}{v\bar{\varepsilon}^*} \bar{E}$$

that is

$$\bar{T} \left(1 + \frac{\bar{v}c_{44}^T}{vc_{44}^P} + \frac{\bar{v}^2 e_{24}^2}{vc_{44}^P \bar{\varepsilon}^*} \right) = \left(\frac{c_{44}^T}{v} + \frac{\bar{v}e_{24}^2}{v\bar{\varepsilon}^*} \right) \bar{S} + \left(\frac{\bar{v}e_{24}\varepsilon_{11}^T}{v\bar{\varepsilon}^*} - \frac{e_{24}}{v} \right) \bar{E},$$

and so

$$\bar{T} (vc_{44}^P \bar{\varepsilon}^* + \bar{v}c_{44}^T \bar{\varepsilon}^* + \bar{v}^2 e_{24}^2) = (c_{44}^T c_{44}^P \bar{\varepsilon}^* + \bar{v}c_{44}^P e_{24}^2) \bar{S} + (\bar{v}c_{44}^P e_{24} \varepsilon_{11}^T - c_{44}^P e_{24} \bar{\varepsilon}^*) \bar{E}.$$

That is

$$\bar{T} = \bar{c}_{44} \bar{S} - \bar{e}_{24} \bar{E}, \quad (3.3.29)$$

since $\bar{c}_{44} = (c_{44}^T c_{44}^P \bar{\varepsilon}^* + \bar{v}c_{44}^P e_{24}^2) / (vc_{44}^P \bar{\varepsilon}^* + \bar{v}c_{44}^T \bar{\varepsilon}^* + \bar{v}^2 e_{24}^2)$ and $\bar{e}_{24} = (c_{44}^P e_{24} v \varepsilon_{11}^P) / (vc_{44}^P \bar{\varepsilon}^* + \bar{v}c_{44}^T \bar{\varepsilon}^* + \bar{v}^2 e_{24}^2)$. Substituting this into equation (3.3.28) gives

$$\bar{D} = \frac{\varepsilon_{11}^P e_{24}}{\bar{\varepsilon}^*} \bar{S} + \frac{\varepsilon_{11}^P \varepsilon_{11}^T}{\bar{\varepsilon}^*} \bar{E} - \frac{\bar{v}e_{24}\varepsilon_{11}^P}{c_{44}^P \bar{\varepsilon}^*} (\bar{c}_{44} \bar{S} - \bar{e}_{24} \bar{E}),$$

that is

$$\bar{D} = \left(\frac{\varepsilon_{11}^P e_{24}}{\bar{\varepsilon}^*} - \frac{\bar{v}e_{24}\varepsilon_{11}^P \bar{c}_{44}}{c_{44}^P \bar{\varepsilon}^*} \right) \bar{S} + \left(\frac{\varepsilon_{11}^P \varepsilon_{11}^T}{\bar{\varepsilon}^*} + \frac{\bar{v}e_{24}\varepsilon_{11}^P \bar{e}_{24}}{c_{44}^P \bar{\varepsilon}^*} \right) \bar{E}.$$

Now

$$\begin{aligned} \frac{\varepsilon_{11}^P e_{24}}{\bar{\varepsilon}^*} - \frac{\bar{v}e_{24}\varepsilon_{11}^P \bar{c}_{44}}{c_{44}^P \bar{\varepsilon}^*} &= \frac{\varepsilon_{11}^P e_{24}}{\bar{\varepsilon}^*} - \frac{\bar{v}e_{24}\varepsilon_{11}^P (c_{44}^T c_{44}^P \bar{\varepsilon}^* + \bar{v}c_{44}^P e_{24}^2)}{c_{44}^P \bar{\varepsilon}^* (vc_{44}^P \bar{\varepsilon}^* + \bar{v}c_{44}^T \bar{\varepsilon}^* + \bar{v}^2 e_{24}^2)} \\ &= \frac{c_{44}^P e_{24} v \varepsilon_{11}^P}{vc_{44}^P \bar{\varepsilon}^* + \bar{v}c_{44}^T \bar{\varepsilon}^* + \bar{v}^2 e_{24}^2} = \bar{e}_{24}. \end{aligned}$$

So

$$\bar{D} = \bar{e}_{24}\bar{S} + \bar{\varepsilon}_{11}\bar{E},$$

where $\bar{\varepsilon}_{11} = (\varepsilon_{11}^P \varepsilon_{11}^T) / \bar{\varepsilon}^* + (\bar{v} e_{24} \varepsilon_{11}^P \bar{e}_{24}) / (c_{44}^P \bar{\varepsilon}^*)$. We then have

$$\bar{E} = \frac{\bar{D}}{\bar{\varepsilon}_{11}} - \frac{\bar{e}_{24}}{\bar{\varepsilon}_{11}} \bar{S}, \quad (3.3.30)$$

and so we can rewrite equation (3.3.29) as

$$\bar{T} = \bar{c}_{44}\bar{S} - \bar{e}_{24} \left(\frac{\bar{D}}{\bar{\varepsilon}_{11}} - \frac{\bar{e}_{24}}{\bar{\varepsilon}_{11}} \bar{S} \right).$$

That is

$$\bar{T} = \bar{\mu}_T \bar{S} - \bar{\zeta} \bar{D}, \quad (3.3.31)$$

where $\bar{\mu}_T = \bar{c}_{44} + \bar{e}_{24}^2 / \bar{\varepsilon}_{11}$ and $\bar{\zeta} = \bar{e}_{24} / \bar{\varepsilon}_{11}$. The specific acoustic impedance of the composite is then [151],

$$\bar{Z}_T = \sqrt{\bar{\mu}_T \bar{\rho}_T}$$

where $\bar{\rho}_T = v \rho_T + \bar{v} \rho_P$ is the average density, and the longitudinal velocity is [151],

$$\bar{c}_T = \sqrt{\frac{\bar{\mu}_T}{\bar{\rho}_T}}.$$

In order to calculate the transmission sensitivity, consider the circuit shown in Figure 2.9. The current across the transducer \bar{I}_T is given by [8]

$$\bar{I}_T = \frac{a \bar{V}}{Z_E + b} \quad (3.3.32)$$

where $a = Z_P / (Z_0 + Z_P)$, $b = Z_0 Z_P / (Z_0 + Z_P)$, Z_0 is the series electrical impedance load in the connecting circuitry and Z_P is the parallel electrical load. In a similar

way to equation (2.5.8) the non-dimensionalised form for the electrical impedance of the standard (Euclidean) transducer (\bar{Z}_E) is then [8]

$$\bar{Z}_E(f) = \frac{1}{q\bar{C}_0 Z_0} \left(1 - \frac{\bar{\zeta}^2 \bar{C}_0}{2q\bar{Z}_T} (\bar{K}_F \bar{T}_F + \bar{K}_B \bar{T}_B) \right), \quad (3.3.33)$$

where $\bar{T}_F = 2\bar{Z}_T/(\bar{Z}_T + Z_L)$, $\bar{T}_B = 2\bar{Z}_T/(\bar{Z}_T + Z_B)$ are non-dimensional transmission coefficients, \bar{K}_F and \bar{K}_B are also non-dimensional and are given by

$$\bar{K}_F = \frac{(1 - e^{-q\bar{\tau}})(1 - \bar{R}_B e^{-q\bar{\tau}})}{(1 - \bar{R}_F \bar{R}_B e^{-2q\bar{\tau}})}$$

and

$$\bar{K}_B = \frac{(1 - e^{-q\bar{\tau}})(1 - \bar{R}_F e^{-q\bar{\tau}})}{(1 - \bar{R}_F \bar{R}_B e^{-2q\bar{\tau}})}$$

where $\bar{R}_F = (\bar{Z}_T - Z_L)/(\bar{Z}_T + Z_L)$, $\bar{R}_B = (\bar{Z}_T - Z_B)/(\bar{Z}_T + Z_B)$ are non-dimensionalised reflection coefficients and $\bar{\tau} = L/\bar{c}_T$ is the wave transit time across the device. Note that the capacitance of the device is given by $\bar{C}_0 = A_r \bar{\epsilon}_{11}/L$. The non-dimensionalised transmission sensitivity for the standard (Euclidean) transducer (ψ_E) (similar to equation (2.5.15)) is then [149]

$$\psi_E(f) = \frac{F_E}{V} \left(\frac{1}{\bar{\zeta} \bar{C}_0} \right) = -\frac{a \bar{A}_T \bar{\lambda} \bar{K}_F}{2\bar{C}_0} \left(1 - \frac{\bar{\zeta}^2 \bar{\lambda} (\bar{K}_F \bar{T}_F + \bar{K}_B \bar{T}_B)}{2q\bar{Z}_T} \right)^{-1}, \quad (3.3.34)$$

where F_E the force produced at the front face of the standard transducer, $\bar{\lambda} = \bar{C}_0/(1 + q\bar{C}_0 b)$ and $\bar{A}_T = 2Z_L/(Z_L + \bar{Z}_T)$ are dimensionless constants. The non-dimensionalised reception sensitivity for the standard (Euclidean) transducer (ϕ_E) (similar to equation (2.6.4)) is then [6]

$$\phi_E(f) = \frac{V_E}{F} (\bar{e}_{24} L) = \frac{-\bar{\zeta} \bar{T}_F \bar{K}_F \bar{\lambda} \bar{e}_{24} L}{q\bar{Z}_T} \left(1 - \frac{\bar{\zeta}^2 \bar{\lambda} (\bar{K}_F \bar{T}_F + \bar{K}_B \bar{T}_B)}{2q^2 \bar{Z}_T Z_E} \right)^{-1}, \quad (3.3.35)$$

where V_E the voltage produced by the standard transducer and $\bar{\lambda}_* = q\bar{C}_0b/(1 + q\bar{C}_0b)$. Having derived expressions for the main operating characteristics of a homogenised device these will be used to compare with the characteristics of the fractal device using the renormalisation approach. This will allow us to assess any practical benefits arising from this novel design.

3.4 Renormalisation model of the transducer operating characteristics

The transducer is electrically coupled to a power supply and is immersed in a mechanical load and appropriate electrical and mechanical boundary conditions can be applied. The derivation follows similar lines to those in Section 2.3.1. In this chapter, the force F on each vertex is given by $F = A_r\bar{T}$. Hence, from equations (2.3.52) and (3.3.31), applying an electrical charge \bar{Q} at one of the transducer-electrical load interfaces then

$$F = A_r\bar{\mu}_T \frac{d\bar{u}}{dx} - \bar{\zeta}\bar{Q}. \quad (3.4.1)$$

So from the continuity of force we get $F(\bar{u}_m) = F_L(\bar{u}_{\partial\Omega}) = F_L(x_L = 0)$, where F_L is the force in the mechanical load. That is, from equation (2.3.46),

$$A_r\bar{\mu}_T \frac{(U_B - U_m)}{h} - \bar{\zeta}\bar{Q} = A_r\mu_L \left(\frac{qc_T}{hc_L} \right) (-A_L + B_L), \quad (3.4.2)$$

and so

$$U_B - U_m - \frac{\bar{\zeta}\bar{Q}}{\bar{\mu}_T} \left(\frac{h}{A_r} \right) = \frac{Z_L}{\bar{Z}_T} q(-A_L + B_L), \quad (3.4.3)$$

where the mechanical impedance of the load is $Z_L = \mu_L A_r / c_L$ and of the transducer is $\bar{\bar{Z}}_T = A_r \bar{\mu}_T / c_T$. At each generation level of the Sierpinski gasket transducer the ratio of the cross-sectional area of each edge to its length is denoted by $\xi = A_r / h^{(n)}$. The overall extent of the SG(3,4) is fixed and so the length of the edges will steadily decrease and, by fixing ξ , the cross-sectional area will also decrease as the fractal generation level increases. Hence, equation (3.4.3), and its equivalent at the front face of the transducer, can be written

$$U_1 - U_A - \frac{\bar{\zeta} \bar{Q}}{\bar{\mu}_T \xi} = \frac{Z_B}{\bar{\bar{Z}}_T} q(-A_B), \quad (3.4.4)$$

$$U_B - U_m - \frac{\bar{\zeta} \bar{Q}}{\bar{\mu}_T \xi} = \frac{Z_L}{\bar{\bar{Z}}_T} q(-A_L + B_L), \quad (3.4.5)$$

Z_B is the mechanical impedance of the backing material. Substituting equation (2.3.47) into equation (3.4.4) gives $U_A = \gamma_1 U_1 + \delta_1$ and substituting equations (2.3.48) and (2.3.49) into equation (3.4.5) gives

$$U_B = \gamma_m U_m + \delta_m = U_C = \gamma_N U_N + \delta_N, \quad (3.4.6)$$

where

$$\gamma_j = \begin{cases} \left(1 - q Z_B / \bar{\bar{Z}}_T\right)^{-1}, & j = 1 \\ \left(1 - q Z_L / \bar{\bar{Z}}_T\right)^{-1}, & j = m \text{ or } N \\ 0 & \text{otherwise} \end{cases} \quad (3.4.7)$$

and

$$\delta_j = \begin{cases} -\gamma_1 \bar{\zeta} \bar{Q} / (\bar{\mu}_T \xi), & j = 1 \\ \gamma_m \left(\bar{\zeta} \bar{Q} / (\bar{\mu}_T \xi) - 2 A_L q Z_L / \bar{\bar{Z}}_T \right), & j = m \text{ or } N \\ 0 & \text{otherwise.} \end{cases} \quad (3.4.8)$$

Hence, equation (3.2.66) becomes

$$b_j^{(n)} = h\bar{\gamma}_j U_j + h\bar{\delta}_j \quad j = 1, m \text{ or } N \quad (3.4.9)$$

where $\bar{\gamma}_j = \eta\gamma_j$ and $\bar{\delta}_j = \eta\delta_j$. Putting equation (3.4.9) into equation (3.2.4) gives

$$\hat{A}_{ji}^{(n)} U_i = \bar{\gamma}_j U_j + \bar{\delta}_j.$$

Hence,

$$\left(\hat{A}_{ji}^{(n)} - \hat{B}_{ji}^{(n)} \right) U_i = \bar{\delta}_j, \quad i = 1, m \text{ or } N$$

where

$$\hat{B}_{ji}^{(n)} = \begin{bmatrix} \bar{\gamma}_1 & 0 & \cdots & & \cdots & 0 \\ 0 & 0 & \ddots & & & \vdots \\ \vdots & \ddots & \ddots & & & \\ & & & 0 & 0 & \\ & & & & \bar{\gamma}_m & \\ & & & 0 & 0 & \\ & & & & & \ddots & \ddots & \vdots \\ \vdots & & & & & \ddots & 0 & 0 \\ 0 & \cdots & & & \cdots & 0 & \bar{\gamma}_N \end{bmatrix}. \quad (3.4.10)$$

That is

$$F_{ji}^{(n)} U_i = \bar{\delta}_j,$$

and so

$$U_i = G_{ji}^{(n)} \bar{\delta}_j, \quad (3.4.11)$$

where

$$G_{ji}^{(n)} = \left(F_{ji}^{(n)} \right)^{-1} = \left(\hat{A}_{ji}^{(n)} - \hat{B}_{ji}^{(n)} \right)^{-1} \quad (3.4.12)$$

represents the Green's transfer matrix.

The calculation of the pivotal elements of $G_{ji}^{(n)}$ in equation (3.4.11) can be conducted as before in Section 2.4.1 using renormalisation. Due to the block structure of $A_{ji}^{(n)}$ as described in equation (3.2.55) being so similar to that in equation (2.3.24) the derivation of the renormalisation equation is identical and leads to equations (2.4.14) and (2.4.18), and also when the boundary conditions are included from equations (2.4.23) to (2.4.26). The major difference however is that the initialisation of these recursion relationships is different since $A_{ji}^{(1)}$ given by equation (3.2.53) is different from $A_{ji}^{(1)}$ given by equation (2.3.22).

3.5 Electrical impedance and transmission and reception sensitivities

The derivation of the electric impedance and the transmission and reception sensitivities follow a very similar derivation to that in Sections 2.5 and 2.6. We simply need to replace ζ by $\bar{\zeta}$ (using equation (3.3.31)), C_0 by $\bar{C}_0 = A_r \bar{\epsilon}_{11} / L$ (using equation (3.3.33)) and μ_T by $\bar{\mu}_T$ (using equation (3.3.31)) to give the non-dimensionalised electrical impedance (\hat{Z}_E) as

$$\hat{Z}_E(f; n) = \frac{Z_E}{Z_0} = \frac{Z_T}{\bar{C}_0 q \mu_T \xi Z_0} \left(1 + \frac{\bar{\zeta}^2 \bar{C}_0 \eta}{\bar{\mu}_T \xi} (\sigma_1 + \sigma_2) \right) \quad (3.5.1)$$

where

$$\sigma_1 = \gamma_1 \left(G_{N1}^{(n)} - G_{11}^{(n)} \right) \quad \text{and} \quad \sigma_2 = \gamma_m \left(-G_{Nm}^{(n)} - G_{NN}^{(n)} + 2G_{1m}^{(n)} \right),$$

and γ_j is given by equation (3.4.7), η is given by equation (3.2.67), $G_{11}^{(n)} = G_{NN}^{(n)} = x$ is given by equations (2.4.14) and (2.4.23) and $G_{N1}^{(n)} = G_{Nm}^{(n)} = G_{1m}^{(n)} = y$ is given by equations (2.4.18) and (2.4.24). Similarly, the non-dimensionalised transmission sensitivity (ψ_F) is then given by

$$\psi_F(f; n) = \frac{F_F}{\bar{V}} \left(\frac{1}{\bar{\zeta}\bar{C}_0} \right) = \frac{aZ_L Z_T}{\bar{Z}_T(Z_E + b)\mu_T \xi \bar{C}_0} K^{(n)}, \quad (3.5.2)$$

where

$$K^{(n)} = \gamma_m \left(-\eta \left(\gamma_1 G_{m1}^{(n)} - \gamma_m \left(G_{mm}^{(n)} + G_{mN}^{(n)} \right) \right) + 1 \right),$$

and \bar{Z}_T is given by equation (3.4.3). Similarly, the non-dimensionalised reception sensitivity (ϕ_F) is then given by

$$\begin{aligned} \phi_F(f; n) &= \frac{\bar{V}_F}{F} (\bar{e}_{24} L) \\ &= \frac{2\bar{\zeta}\bar{e}_{24} L \eta \sigma_2}{\xi \bar{\mu}_T} \left(1 - \frac{aZ_T \bar{\zeta}^2 \eta (\sigma_1 + \sigma_2)}{(Z_E + b) q \mu_T \bar{\mu}_T \xi^2} - \frac{aZ_T}{(Z_E + b) q \mu_T \xi \bar{C}_0} \right)^{-1}. \end{aligned} \quad (3.5.3)$$

3.6 Steady state solutions

The true fractal case arises when we allow the fractal generation level n to tend to infinity and we assume that the renormalisation recursion relationships converge to a steady state (we denote these steady state solutions by a * superscript). Note we will examine the convergence of these recursion relationships later (see section 3.7.3) when we consider the pre-fractal SG(3,4) transducer (at increasing but finite fractal generation levels).

Case A: $\hat{y}^* = 0$

If $\hat{y}^* = 0$ then equation (2.4.9) is automatically satisfied (since $\hat{X} = \hat{x} = \hat{x}^*$) and from equations (2.4.10) and (2.4.11) we get

$$\hat{G}_{e1}^* = -\beta\hat{x}^*\hat{G}_{b1}^* \quad (3.6.1)$$

and

$$\hat{G}_{b1}^* = -\beta\hat{x}^*\hat{G}_{e1}^*. \quad (3.6.2)$$

Substituting equation (3.6.1) into equation (3.6.2) gives

$$\hat{G}_{b1}^* (1 - \beta^2\hat{x}^{*2}) = 0.$$

Therefore $\hat{G}_{b1}^* = 0$ or $\hat{x}^* = \pm 1/\beta$. In the former case then $\hat{G}_{e1}^* = 0$ and in the latter case $\hat{G}_{b1}^* = \mp\hat{G}_{e1}^*$. From equation (2.4.12) we get

$$\hat{G}_{z1}^* (1 + \beta\hat{x}^*) = 0.$$

Therefore $\hat{G}_{z1}^* = 0$ or $\hat{x}^* = -1/\beta$. Now bringing in the boundary conditions equation (2.4.25) gives

$$z = \frac{\hat{x}^*}{1 - \hat{x}^*\bar{\gamma}_m}$$

where $\hat{x}^* \neq 1/\bar{\gamma}_m$. From equation (2.4.23) we get

$$x = \frac{\hat{x}^*}{1 - \hat{x}^*\bar{\gamma}_1}$$

where $\hat{x}^* \neq 1/\bar{\gamma}_1$. From equation (2.4.20) we get

$$y = \hat{x}^*\bar{\gamma}_m y.$$

That is

$$y = 0$$

and from equation (2.4.22) we get

$$w = \hat{x}^* \bar{\gamma}_m w,$$

giving

$$w = 0.$$

In the case where $\hat{G}_{b1}^* = \hat{G}_{e1}^* = \hat{G}_{z1}^* = 0$ we denote the solution as $x^* = \chi$, $\chi \in \mathbb{C}$ and in the case where $\hat{x}^* = \pm 1/\beta$ we denote the solutions as $\hat{G}_{b1}^* = \mp \lambda$, $\hat{G}_{e1}^* = \mp \lambda$ and $\hat{G}_{z1}^* = \theta$ (or 0 when $\hat{x}^* = 1/\beta$) where $\lambda, \theta \in \mathbb{C}$. The full set of steady state solutions for this branch of solutions are summarised in the table below.

Case	\hat{x}^*	\hat{y}^*	\hat{G}_{b1}^*	\hat{G}_{e1}^*	\hat{G}_{z1}^*	x	y	w	z	note
A1	$\frac{-1}{\beta}$	0	λ	$-\lambda$	θ	$\frac{-1}{\beta + \bar{\gamma}_1}$	0	0	$\frac{-1}{\beta + \bar{\gamma}_m}$	$\beta \neq \bar{\gamma}_1, \beta \neq \bar{\gamma}_m$
A2	$\frac{1}{\beta}$	0	$-\lambda$	λ	0	$\frac{1}{\beta - \bar{\gamma}_1}$	0	0	$\frac{1}{\beta - \bar{\gamma}_m}$	$\beta \neq \bar{\gamma}_1, \beta \neq \bar{\gamma}_m$
A3	χ	0	0	0	0	$\frac{\chi}{1 - \chi \bar{\gamma}_1}$	0	0	$\frac{\chi}{1 - \chi \bar{\gamma}_m}$	$\bar{\gamma}_1 \neq \frac{1}{\chi}, \bar{\gamma}_m \neq \frac{1}{\chi}, \chi \neq \pm \frac{1}{\beta}$

Case B: $\hat{y}^* \neq 0$

If $\hat{y}^* \neq 0$ then from equation (2.4.9) we get

$$-2\beta \hat{y}^* \hat{G}_{e1}^* = 0,$$

and so

$$\hat{G}_{e1}^* = 0.$$

Substituting this into equations (2.4.10) and (2.4.11) we get

$$\hat{x}^* \hat{G}_{b1}^* + \hat{y}^* \hat{G}_{z1}^* = 0 \quad (3.6.3)$$

and

$$\hat{G}_{b1}^* = \hat{y}^*. \quad (3.6.4)$$

Substituting this equation into equation (3.6.3) gives

$$\hat{G}_{z1}^* = -\hat{x}^*. \quad (3.6.5)$$

Substituting equations (3.6.4) and (3.6.5) into equation (2.4.12) gives

$$\hat{x}^* + \beta \hat{x}^{*2} - \beta \hat{y}^{*2} = 0. \quad (3.6.6)$$

Note that $\hat{x}^* \neq 0$ since this would imply that \hat{y}^* was zero. Also substituting equations (3.6.4) and (3.6.5) into equation (2.4.17) gives

$$\hat{y}^* = -\beta \hat{y}^* (\hat{y}^* - \hat{x}^*).$$

That is

$$\hat{y}^* = \hat{x}^* - \frac{1}{\beta}. \quad (3.6.7)$$

Putting this into equation (3.6.6) gives

$$\hat{x}^* = \frac{1}{3\beta}. \quad (3.6.8)$$

Putting this into equation (3.6.7) gives

$$\hat{y}^* = \frac{-2}{3\beta}. \quad (3.6.9)$$

Now putting equations (3.6.8) and (3.6.9) into the boundary conditions equation (2.4.24) gives

$$y = \frac{-2\beta}{3\beta^2 - 3\bar{\gamma}_1\bar{\gamma}_m + \beta(-\bar{\gamma}_1 + \bar{\gamma}_m)}. \quad (3.6.10)$$

Putting equations (3.6.8),(3.6.9) and (3.6.10) into equations (2.4.23) and (2.4.26) gives

$$x = \frac{\beta + 3\bar{\gamma}_m}{3\beta^2 - \beta\bar{\gamma}_1 + \beta\bar{\gamma}_m - 3\bar{\gamma}_1\bar{\gamma}_m}$$

and

$$w = \frac{-2\beta(\beta - \bar{\gamma}_1)}{(\beta - \bar{\gamma}_m)(3\beta^2 - 3\bar{\gamma}_1\bar{\gamma}_m + \beta(-\bar{\gamma}_1 - \bar{\gamma}_m))}. \quad (3.6.11)$$

Substituting equations (3.6.8),(3.6.9),(3.6.10) and (3.6.11) into equation (2.4.25) gives

$$z = \frac{\beta^2 - 3\bar{\gamma}_1\bar{\gamma}_m + \beta(\bar{\gamma}_1 + \bar{\gamma}_m)}{(\beta - \bar{\gamma}_m)(3\beta^2 - 3\bar{\gamma}_1\bar{\gamma}_m + \beta(-\bar{\gamma}_1 + \bar{\gamma}_m))}.$$

Note that from equation (2.4.5), $h^{(n)} \rightarrow 0$ and $q^{(n)} \rightarrow 0$ as $n \rightarrow \infty$, and so from equation (3.5.1) the non-dimensionalised electrical impedance tends to infinity ($(\hat{Z}_E(f; n)) \rightarrow \infty$), from equation (3.5.2) the non-dimensionalised transmission sensitivity tends to zero ($\psi_F(f; n) \rightarrow 0$), and from equation (3.4.7) $\gamma_j \rightarrow 1$ and from equation (3.4.9) $\bar{\gamma}_j \rightarrow \eta^*$. From equation (3.2.67) we get

$$\eta^* = \frac{2}{3}.$$

From equation (3.5.3) the non-dimensionalised reception sensitivity is

$$\phi_F^*(f; n) = \frac{2\bar{\zeta}\bar{e}_{24}L\eta^*\sigma_2^*}{\xi\bar{\mu}_T} \left(1 - \frac{aZ_T(\xi\bar{\mu}_T + \bar{C}_0\bar{\zeta}^2\eta^*(\sigma_1^* + \sigma_2^*))}{\xi\bar{\mu}_TZ_T + \xi^2\mu_T\bar{\mu}_Tbq\bar{C}_0 + \bar{C}_0\bar{\zeta}^2\eta^*Z_T(\sigma_1^* + \sigma_2^*)} \right)^{-1},$$

and, since $q^{(n)} \rightarrow 0$, then

$$\phi_F^*(f; n) = \frac{4\bar{\zeta}\bar{e}_{24}L\sigma_2^*}{3\xi\bar{\mu}_T(1-a)},$$

where

$$\sigma_2^* = \begin{cases} \frac{1}{1+\beta}, & \text{in case A1} \\ \frac{1}{1-\beta}, & \text{in case A2} \\ \frac{\chi}{\chi-1}, & \text{in case A3} \\ \frac{-3(3\beta+4)}{9\beta^2+\beta-12} & \text{in case B.} \end{cases}$$

3.7 Results

As in Section 2.8 we will compare the fractal design with a conventional (Euclidean) design in terms of the key operating characteristics of the transmission and reception sensitivity spectra [150]. A careful examination of the transmission and reception sensitivities of the fractal device as the fractal generation level is increased has been performed. However, to keep the presentation here succinct and to produce results that are pertinent to devices that can be physically produced, we will focus on fractal generation levels $n = 4$, $n = 5$ and $n = 6$.

3.7.1 Electrical impedance and transmission/reception sensitivities

A typical profile of the electrical impedance spectrum (magnitude) given by equation (3.5.1) is shown in Figures 3.48 ($n = 4$), 3.51 ($n = 5$) and 3.54 ($n = 6$) (dashed line); it is compared to the equivalent profile given by a model of the traditional design (3.3.33) (full line). Similar to the discussion in Section 2.8.1, it can be seen in

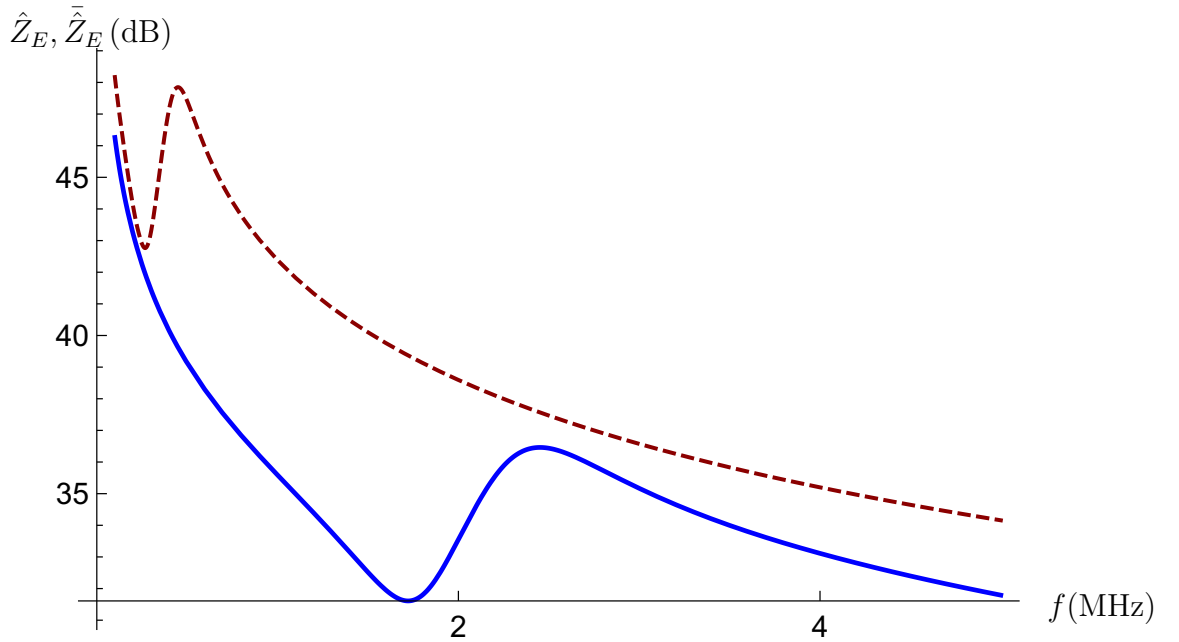


Figure 3.48: Non-dimensionalised electrical impedance (equation (3.5.1)) versus frequency for the SG(3,4) graph transducer (\hat{Z}_E) at fractal generation level $n = 4$ (dashed line). The non-dimensionalised electrical impedance of the standard (Euclidean) transducer (\bar{Z}_E) (equation (3.3.33)) is plotted for comparison (full line). Parameter values are given in Appendix A.5.

Figures 3.48, 3.51 and 3.54 that, for the standard design (full line), the mechanical resonance $f_r = 1.7$ MHz and the electrical resonance $f_a = 2.4$ MHz. These frequencies correspond precisely to the first maximum in the transmission sensitivity plots (Figures 3.49, 3.52 and 3.55, full line) and the reception sensitivity plots (Figures 3.50, 3.53 and 3.56 full line). From the parameter values for PZT5-H then

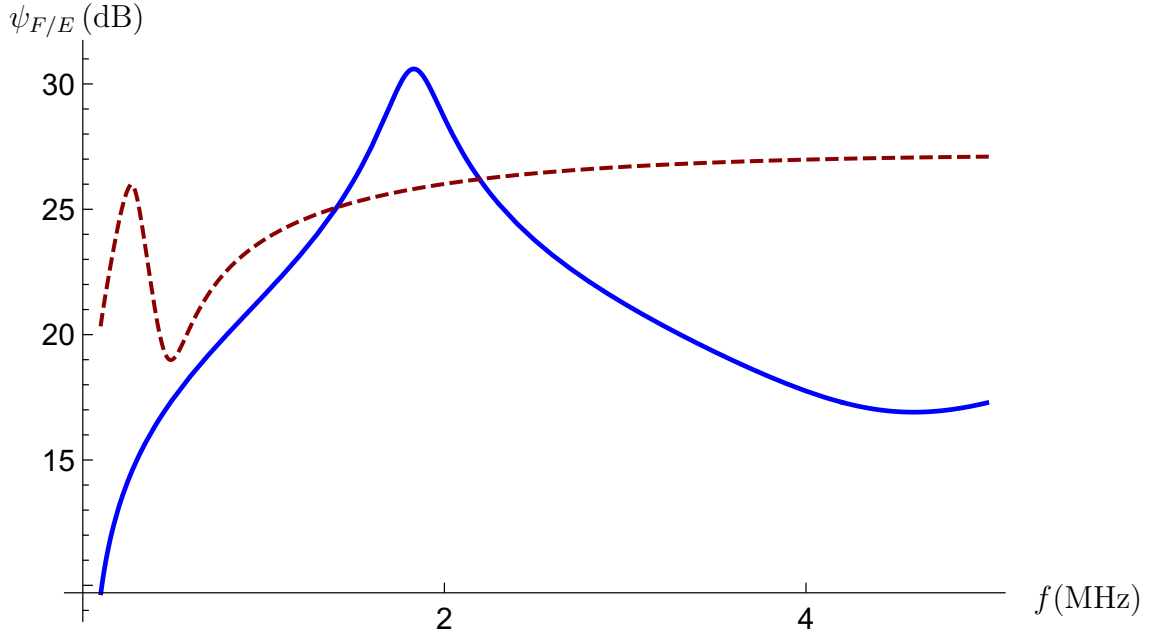


Figure 3.49: Non-dimensionalised transmission sensitivity (equation (3.5.2)) versus frequency for the SG(3,4) graph transducer (ψ_F) at fractal generation level $n = 4$ (dashed line). The non-dimensionalised transmission sensitivity of the standard (Euclidean) transducer (ψ_E) (equation (3.3.34)) is plotted for comparison (full line). Parameter values are given in Appendix A.5.

in equation (2.2.11) the piezoelectrically stiffened velocity (c_T) is approximately 2370 m/s and the polymer stiffened velocity (c_P) is approximately 992 m/s and, with an overall device length of $L = 0.5$ mm, then the corresponding frequency for low volume fractions of polymer is approximately $f_a = c_T/(2L) = 2.4$ MHz. This agrees reasonably well with the reception sensitivity maximum for the homogenised estimate for f_a (the full line in Figure 3.48). For the fractal design the electrical impedance resonance frequencies are actually lower in this case ($f_r^{(4)} = 0.25$ MHz, $f_r^{(5)} = 0.54$ MHz, $f_r^{(6)} = 1.2$ MHz and $f_a^{(4)} = 0.45$ MHz, $f_a^{(5)} = .93$ MHz, $f_a^{(6)} = 2$ MHz) and this suggests that the polymer phase is damping the higher resonances and also bringing the dominant resonances to lower frequencies due to the lower wave velocities it supports. Importantly, the magnitude of the electrical impedance at the electrical resonance frequency is higher than the traditional design; there

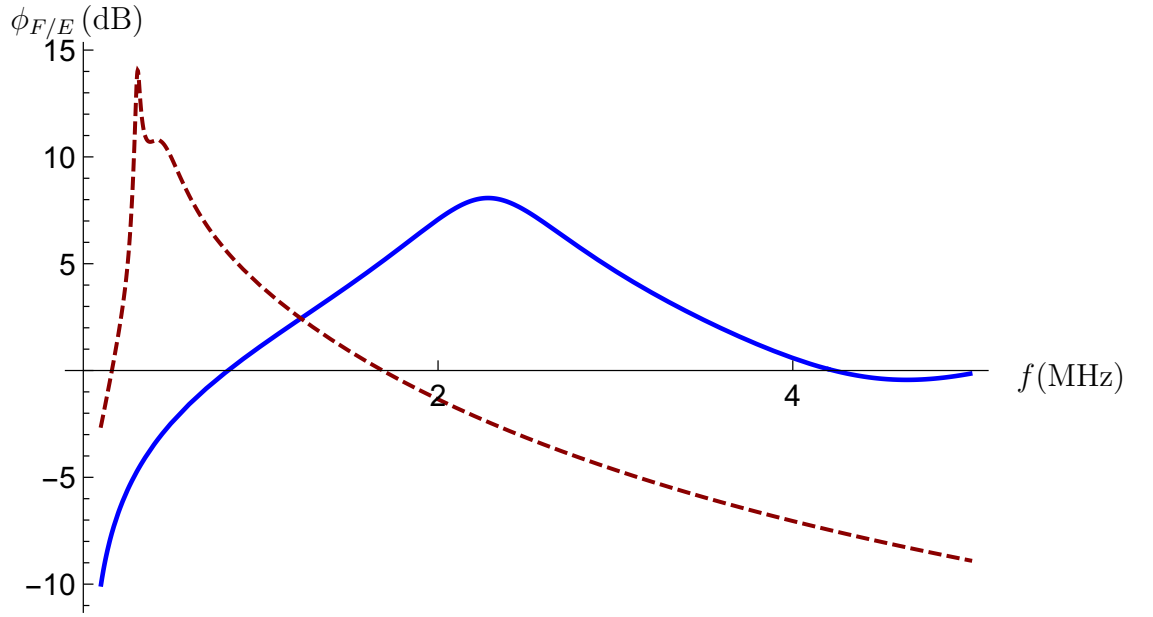


Figure 3.50: Non-dimensionalised reception sensitivity (equation (3.5.3)) versus frequency for the SG(3,4) graph transducer (ϕ_F) at fractal generation level $n = 4$ (dashed line). The non-dimensionalised reception sensitivity of the standard (Euclidean) transducer (ϕ_E) (equation (3.3.35)) is plotted for comparison (full line). Parameter values are given in Appendix A.5.

is about a 5 dB increase for $n = 6$. This results in the reception sensitivity spectrum having a much larger gain for $n = 6$; there is a 7 dB improvement in the reception sensitivity gain from the traditional design to the fractal design (see Figure 3.56). Importantly, this peak in the reception sensitivity also results in an enhanced bandwidth; if we take the noise floor to be 3 dB below the peak gain of the traditional design (that is 5 dB) then the operational bandwidth of the traditional design is 1.5 MHz whereas the fractal design has an operational bandwidth of around 3 MHz. It should be borne in mind of course that no matching layers (or indeed an optimised backing layer) have been used in this design, and that the transducer is solely composed of the piezoelectric-polymer composite material. Let us start by examining the performance of the first generation graph ($n = 4$). Figure 3.48 shows that the electrical impedance of the fractal graph has its first

resonance (the electrical resonance) around $f_r^{(4)} = 0.25$ MHz (at a lower frequency than the Euclidean case $f_r = 1.7$ MHz) and that the higher frequency resonances are absent. Figure 3.49 shows that the transmission sensitivity of the fractal design has a maximum amplitude (gain) that is lower than the Euclidean case (standard design) at its lower operating frequency (26 dB at 0.23 MHz compared to 31 dB at 1.7 MHz for the Euclidean case). If we take the noise floor to be 3 dB below the peak gain of the traditional design then the operational bandwidth of the traditional design is 0.5 MHz whereas the fractal design has no operational bandwidth. Figure 3.50 shows that the reception sensitivity of the fractal design does show some encouraging results with a much higher peak amplitude than that of the Euclidean case and at a lower operating frequency (at 0.32 MHz its sensitivity is 14 dB whereas the peak sensitivity of the standard device is 8 dB at 2.4 MHz). Following this is an examination of the next generation level ($n = 5$). Also in generation level $n = 5$ the electrical impedance of the fractal graph has its first resonance at around 0.5 MHz (at a lower frequency than the Euclidean case) and that the higher frequency resonances are absent.

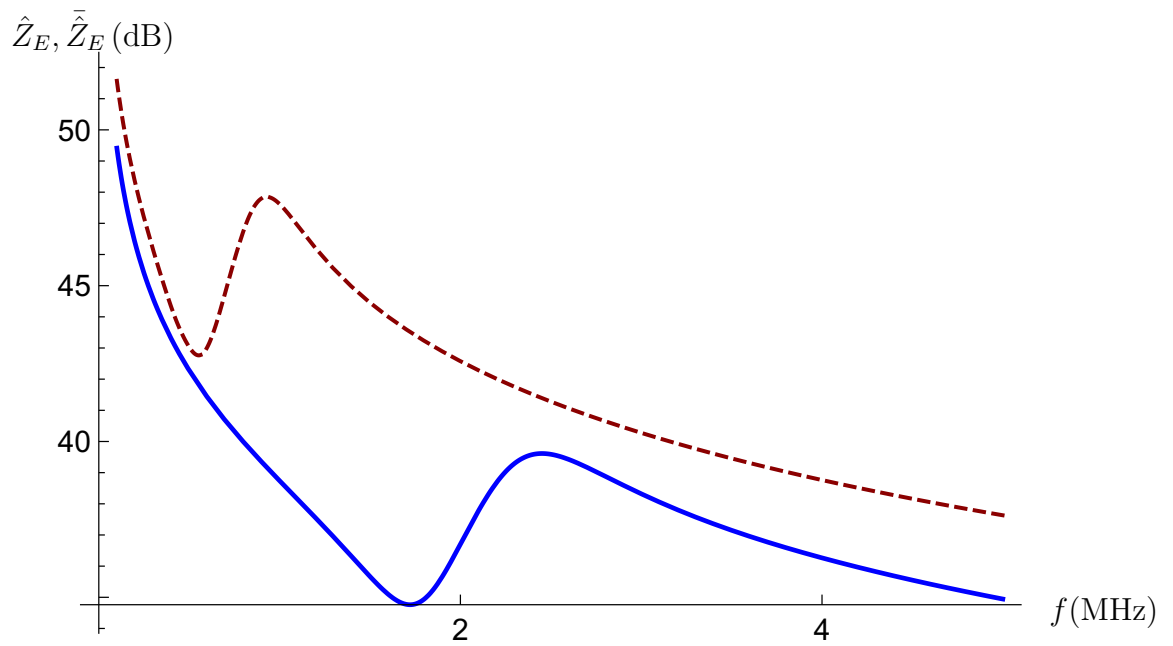


Figure 3.51: Non-dimensionalised electrical impedance (equation (3.5.1)) versus frequency for the SG(3,4) graph transducer (\hat{Z}_E) at fractal generation level $n = 5$ (dashed line). The non-dimensionalised electrical impedance of the standard (Euclidean) transducer ($\bar{\hat{Z}}_E$) (equation (3.3.33)) is plotted for comparison (full line). Parameter values are given in Appendix A.5.

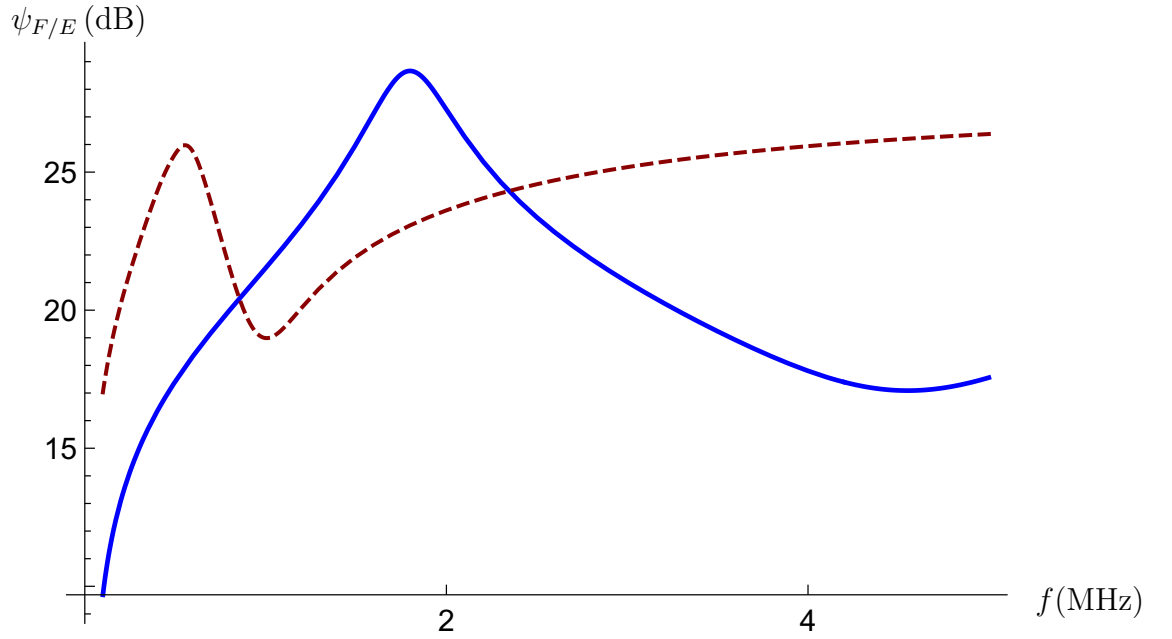


Figure 3.52: Non-dimensionalised transmission sensitivity (equation (3.5.2)) versus frequency for the SG(3,4) graph transducer (ψ_F) at fractal generation level $n = 5$ (dashed line). The non-dimensionalised transmission sensitivity of the standard (Euclidean) transducer (ψ_E) (equation (3.3.34)) is plotted for comparison (full line). Parameter values are given in Appendix A.5.

The transmission sensitivity of the fractal design in generation level $n = 5$ has a maximum amplitude (gain) that is lower than the homogenised case (standard Euclidean design) at its lower operating frequency (at 0.55 MHz its sensitivity is 26 dB and the peak sensitivity of the standard (Euclidean) device is 29 dB at 1.7 MHz). The bandwidth of around 25 dB is smaller than that of the Euclidean case (see Table 3.3).

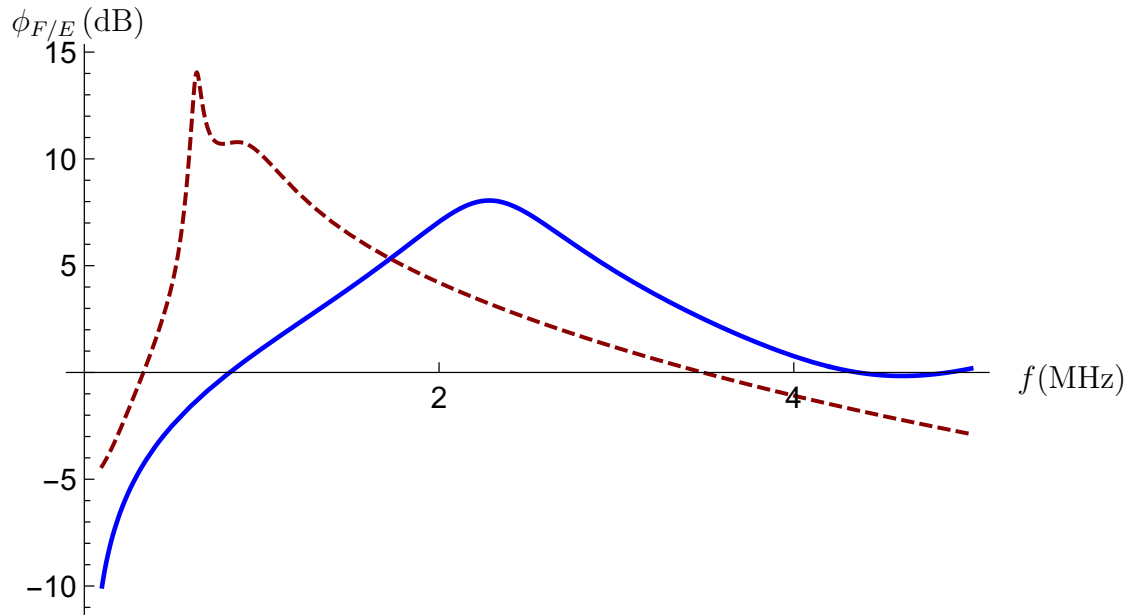


Figure 3.53: Non-dimensionalised reception sensitivity (equation (3.5.3)) versus frequency for the SG(3,4) graph transducer (ϕ_F) at fractal generation level $n = 5$ (dashed line). The non-dimensionalised reception sensitivity of the standard (Euclidean) transducer (ϕ_E) (equation (3.3.35)) is plotted for comparison (full line). Parameter values are given in Appendix A.5.

The reception sensitivity of the fractal design in generation level $n = 5$ has again a much higher peak amplitude than that of the Euclidean case at its lower operating frequency (at 0.6 MHz its sensitivity is 14 dB whereas the peak sensitivity of the standard (Euclidean) device is 8 dB at 2.4 MHz). This examination can continue and below we consider the sixth generation level ($n = 6$) performance.

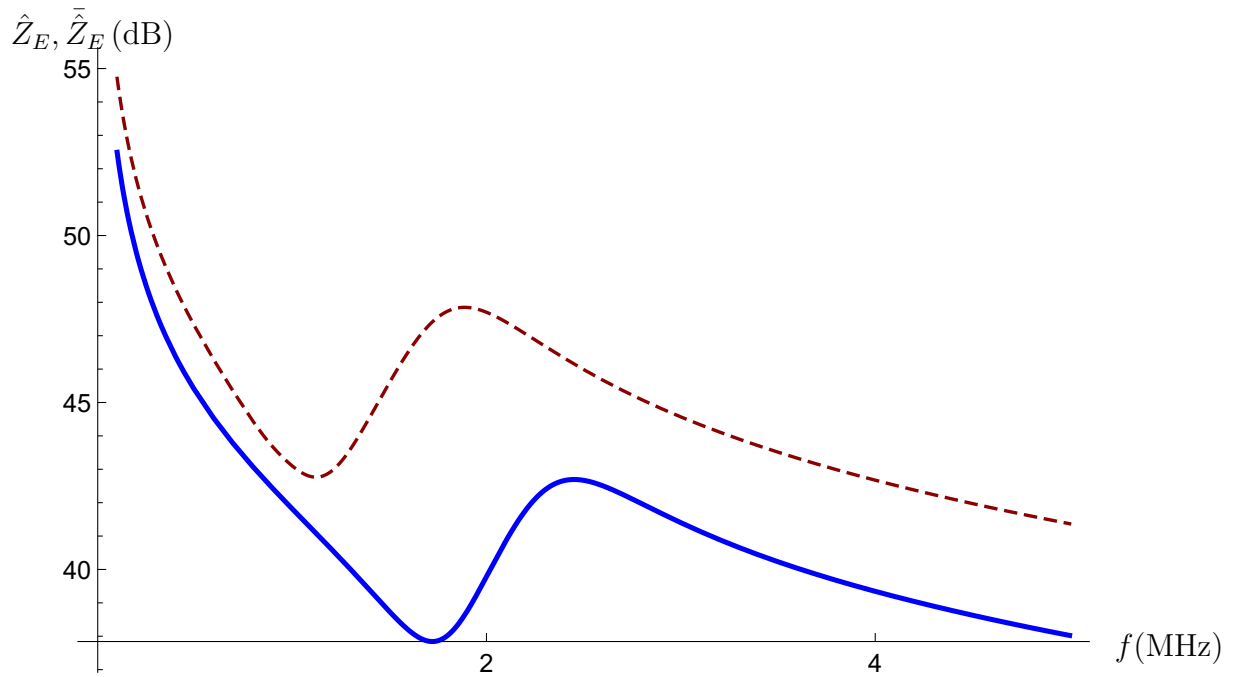


Figure 3.54: Non-dimensionalised electrical impedance (equation (3.5.1)) versus frequency for the SG(3,4) graph transducer (\hat{Z}_E) at fractal generation level $n = 6$ (dashed line). The non-dimensionalised electrical impedance of the standard (Euclidean) transducer (\tilde{Z}_E) (equation (3.3.33)) is plotted for comparison (full line). Parameter values are given in Appendix A.5.

At fractal generation level $n = 6$ the electrical impedance of the fractal graph has its first resonance at around 1.2 MHz. This is at a higher impedance gain than the Euclidean case (which resonates at a higher frequency) and again the higher frequency resonances are absent.

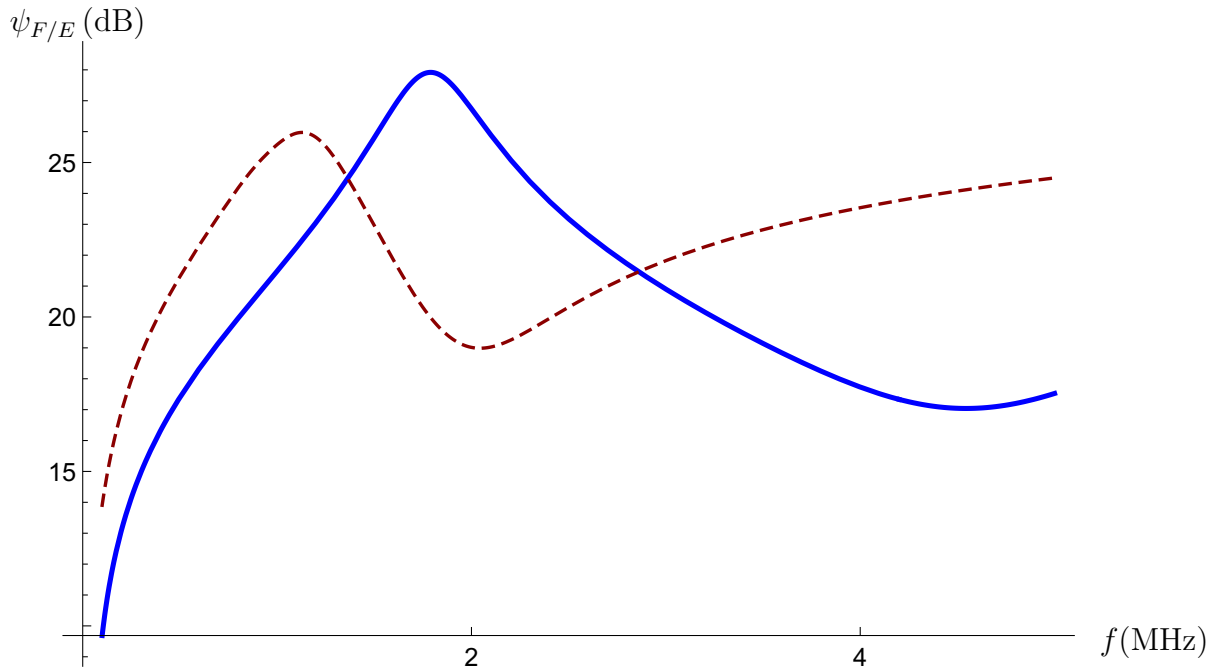


Figure 3.55: Non-dimensionalised transmission sensitivity (equation (3.5.2)) versus frequency for the SG(3,4) graph transducer (ψ_F) at fractal generation level $n = 6$ (dashed line). The non-dimensionalised transmission sensitivity of the standard (Euclidean) transducer (ψ_E) (equation (3.3.34)) is plotted for comparison (full line). Parameter values are given in Appendix A.5.

The transmission sensitivity of the fractal design in generation level $n = 6$ has a maximum amplitude (gain) that is lower than the Euclidean case (at 1.1 MHz its sensitivity is 26 dB and the peak sensitivity of the standard device is 28 dB at 1.7 MHz). Once again the bandwidth around 25 dB is smaller than that of the homogenised case.

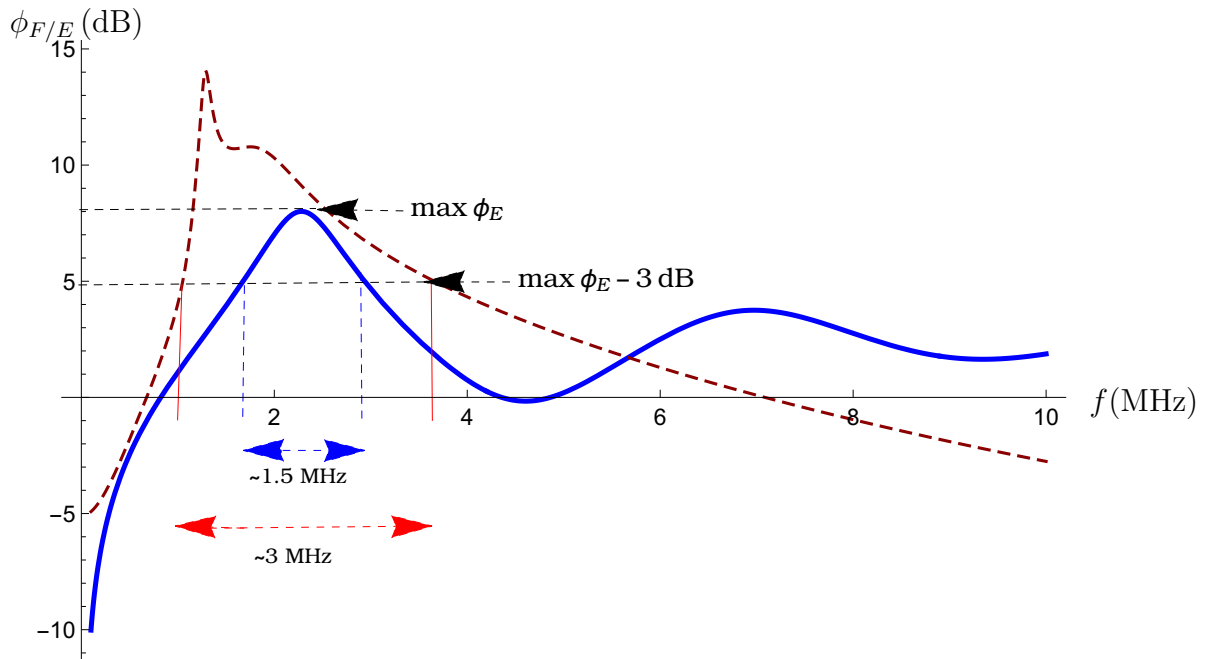


Figure 3.56: Non-dimensionalised reception sensitivity (equation (3.5.3)) versus frequency for the SG(3,4) graph transducer (ϕ_F) at fractal generation level $n = 6$ (dashed line). The non-dimensionalised reception sensitivity of the standard (Euclidean) transducer (ϕ_E) (equation (3.3.35)) is plotted for comparison (full line). The red arrow shows the bandwidth of the fractal transducer is around 3 MHz and the bandwidth of the Euclidean transducer is around 1.5 MHz as shown by the blue arrow (see Table 3.3). Parameter values are given in Appendix A.5.

As before the reception sensitivity maximum amplitude of the fractal design (in generation level $n = 6$) is higher than the Euclidean case (14 dB at 1.3 MHz compared to 8 dB at 2.4 MHz for the Euclidean case), with the bandwidth around this peak sensitivity being bigger than that of the Euclidean case.

Design (n)	f_r (MHz)	f_a (MHz)	ψ_{max} (dB)	ϕ_{max} (dB)	BW_T (MHz)	BW_R (MHz)
Fractal (4)	0.3	0.5	26.0	14.0	0	0.5
Standard	1.7	2.4	31.0	8.0	0.3	1.5
Fractal (5)	0.5	0.9	26.0	14.0	0.2	1.5
Standard	1.7	2.4	29.0	8.0	0.8	1.5
Fractal (6)	1.2	2.0	26.0	14.0	0.5	3.0
Standard	1.7	2.4	28.0	8.0	1.0	1.5

Table 3.3: A comparison between the operating characteristics of a fractal transducer and an equivalent standard design at fractal generation levels $n = 4, 5$ and 6 . The mechanical resonance frequency is denoted by f_r (MHz), the electrical resonance frequency is denoted by f_a (MHz), the transmission sensitivity gain is denoted by ψ_{max} (dB), the reception sensitivity gain is denoted by ϕ_{max} (dB), the transmission sensitivity bandwidth is denoted by BW_T (MHz) and the reception sensitivity bandwidth is denoted by BW_R (MHz).

3.7.2 Homogeneous Euclidean transducers

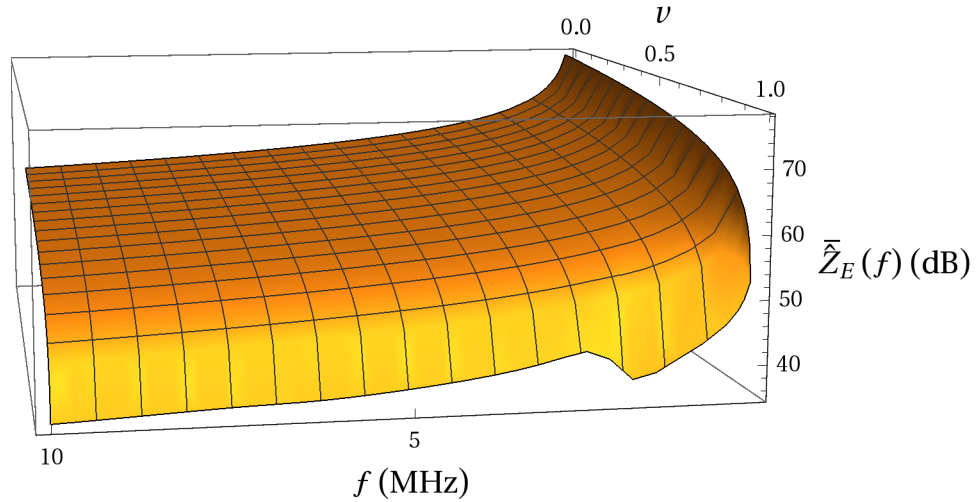


Figure 3.57: Non-dimensionalised electrical impedance of the standard (Euclidean) transducer $\bar{Z}_E(f)$ (dB) (equation (3.3.33)) versus frequency f (MHz) and volume fraction of ceramic ν for a 1-3 composite transducer. Parameter values are given in Appendix A.5.

The electrical impedance of the standard (Euclidean) design was calculated using

the homogenisation approach that led to equation (3.3.33). As can be seen in Figure 3.57 the resonances (peaks in the electrical impedance amplitude) only appear once the volume fraction of the polymer (ν) exceeds a threshold of roughly 0.95.

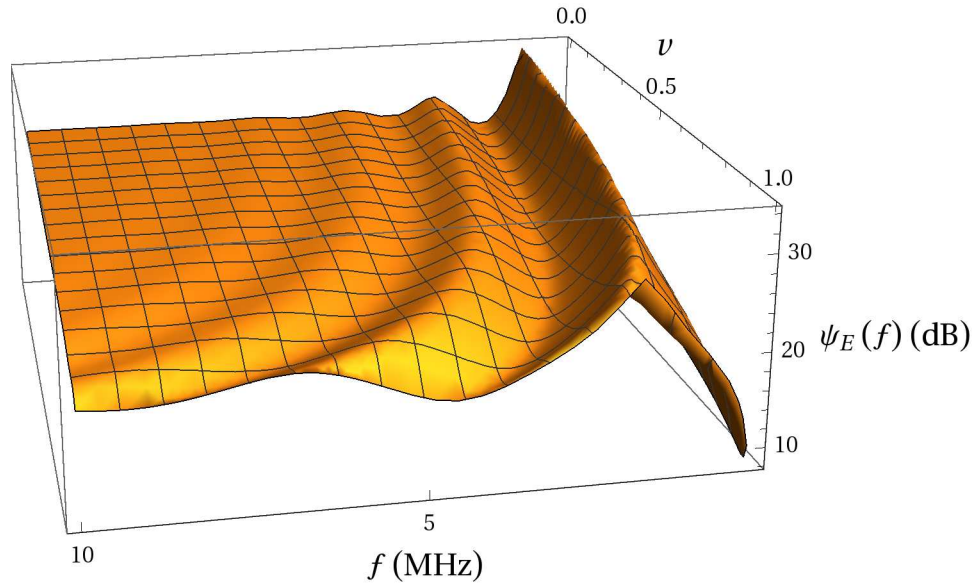


Figure 3.58: Non-dimensionalised transmission sensitivity of the standard (Euclidean) transducer $\psi_E(f)$ (dB) (equation (3.3.34)) versus frequency f (MHz) and volume fraction of ceramic ν for a 1-3 composite transducer. Parameter values are given in Appendix A.5.

At the low volume fraction of the polymer (ν) there is a number of resonances. As the volume fraction increases these resonances shift to higher frequencies. It can be seen that the peak sensitivity is 28 dB and the bandwidth around this peak sensitivity is bigger at the low volume fractions of the polymer (ν).

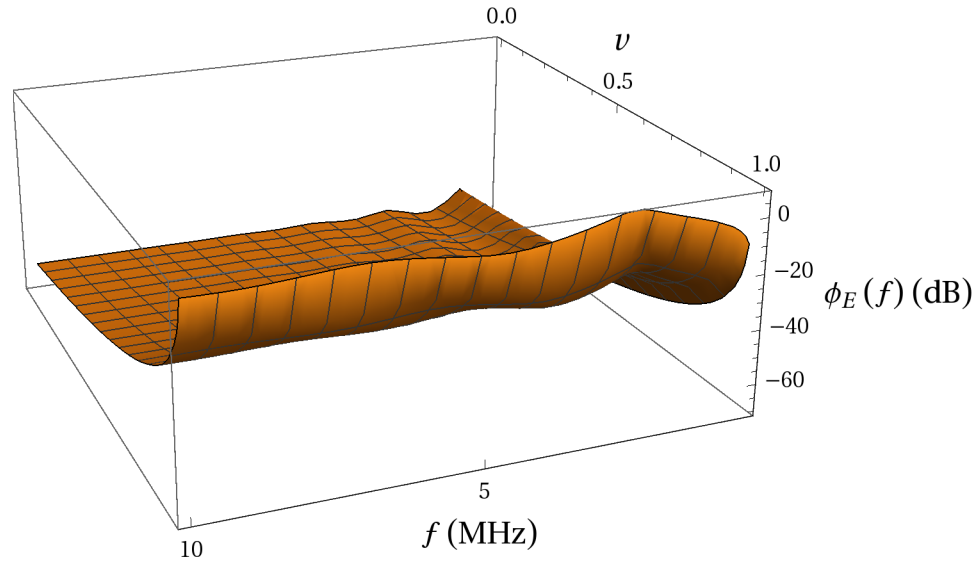


Figure 3.59: Non-dimensionalised reception sensitivity of the standard (Euclidean) transducer $\phi_E(f)$ (dB) (equation (3.3.35)) versus frequency f (MHz) and volume fraction of ceramic ν for a 1-3 composite transducer. Parameter values are given in Appendix A.5.

At low volume fractions of the polymer (ν) there are a number of resonances in the low frequency regime. As the volume fraction of ceramic increases the peak sensitivity increases as well.

3.7.3 Convergence

Similar to Section 2.8.2, the norm of the difference between the energy in the power spectrum at successive generation levels, integrated with respect to frequency, can be calculated for the transmission/reception sensitivities. Figure 3.60 shows the dependence of these norms on the generation level. Scrutiny of the underlying spectra shows that the transmission sensitivity accrues more and more resonances as the fractal generation n increases. As the length scale of the smallest edge is decreasing with n then resonances at higher frequencies appear; note that the lack of damping in the model permits these resonances to have amplitudes which

would not be present in an experimental setting. As n is increased further, then the various peaks become quite dense and a very flat response emerges which does not change over the frequency range of interest (up to 10 MHz). Hence, the successive spectra start to reach a steady state and this accounts for the steady state that is reached after $n = 10$. A similar story holds for the reception sensitivity.

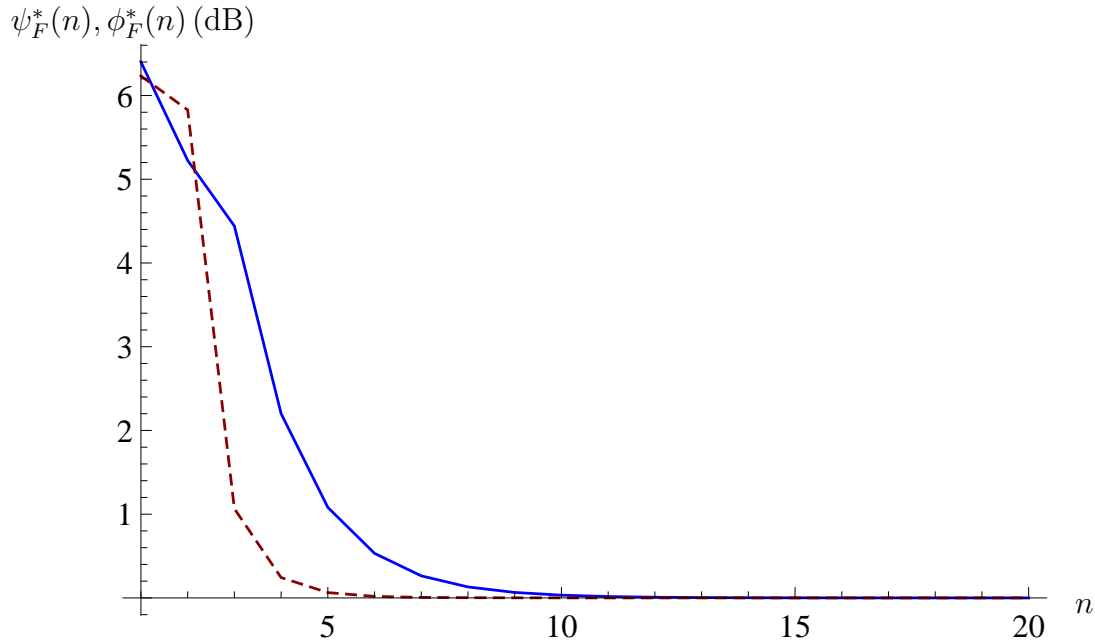


Figure 3.60: The convergence of the transmission and reception sensitivities is examined by plotting the differences in the energies in successive spectra as the fractal generation level increases. Non-dimensionalised transmission sensitivity ($\psi_F^*(n)$) (equation (2.8.1)) (full line) and non-dimensionalised reception sensitivity ($\phi_F^*(n)$) (equation (2.8.2)) (dashed line) versus the fractal generation level. The transmission sensitivity converges by generation level $n = 10$ and the reception sensitivity by generation level $n = 5$, over this frequency range where $f_i \in [0.1, 10]$ MHz.

3.8 Conclusions

The performance of a composite piezoelectric ultrasound transducer, where its internal architecture is a fractal, is compared with that of a traditional design. The

former case is modelled using a renormalisation approach whereas the latter case is modelled using homogenisation. In Chapter 2, only ceramic elements were used, however in this chapter, this was improved on by using a combination of ceramic and polymer elements. New basis functions for this two phase material whose support is the underlying fractal graph, were developed for the finite element analysis. To assess the performance of this new device a new model for a homogenised device was derived. This represents the standard designs that are commonly used whereby the piezoelectric and polymer constituents are on the same length scale and are often arranged in a periodic structure. Low fractal generation levels ($n = 4, 5$ and 6) of the fractal transducer was investigated as these are in the regime most likely to be amenable to manufacture. A significantly higher amplitude reception sensitivity was produced by the fractal transducer when compared to the standard design; note however that a lower transmission sensitivity amplitude resulted. The convergence of the fractal device's performance as the fractal generation level increases was also considered. It was seen that, in both transmission and reception modes, the outputs converge by generation level $n = 10$ and $n = 5$ respectively. The reception sensitivity also resulted in a wider bandwidth than the standard design; if we take the noise floor to be 3 dB below the peak gain of the traditional design (around 5 dB) the bandwidth of the fractal transducer is around 3 MHz but 1.5 MHz for the Euclidean transducer (see Figure 3.56 and Table 3.3).

Chapter 4

A fractal ultrasonic transducer based on the complement of the Sierpinski gasket

4.1 Introduction

This chapter derives a model of a fractal ultrasound transducer and compare its distinctive properties with that of a standard transducer design. The complement of the Sierpinski gasket fractal is utilized in this chapter to simulate this self-similar transducer [9,10,144]. This transducer starts off as an equilateral triangle of piezoelectric crystal, connected to three half sized copies of itself (see Figure 4.1). The next generation ($n = 2$) connects three half-sized copies of the smaller triangles to each of these triangles. Continuing in this way what we will call the complement (or dual) of the standard Sierpinski gasket is produced. Using the complement (the black triangles in Figure 4.1) should prove to be a significant advance as it has a range of triangle sizes whereas the Sierpinski gasket is composed of triangles

of the same size (the white triangles in Figure 4.1) for a given fractal generation level. The dual graph ($\overline{\text{SG}}(3)$) is introduced and constructed by a process which starts from the order $n = 1$ design (which consists of four piezoelectric triangles), assigns a vertex to the centre of each of the smaller triangles and, by connecting these vertices together with edges whose length is the side length of the larger triangle, the $\overline{\text{SG}}(3)$ weighted graph at generation level $n = 1$ is constructed (see Figure 4.2). The Sierpinski gasket has side length L units which remains constant as the generation level n increases. The length of the smallest edge in the weighted graph $\overline{\text{SG}}^{(n)}(3)$ is $h^{(n)} = L/2^n$ and the longest edge length that connects the three $\overline{\text{SG}}^{(n-1)}(3)$ graphs is $h^{(1)} = L/2$. Then the overall diameter of the graph is $L_{\text{SG}}^{(n)} = nL/2$ and the total number of vertices is $N_n = 3^n$. The vertex degree is 3 apart from the boundary vertices (input/output vertices) which have degree 2 and $M_n = 3(3^n - 1)/2$ denotes the total number of edges at generation level n . The boundary vertices are used to interact with external loads (both electrical and mechanical) and fictitious vertices A, B and C are introduced to cope with these interfacial boundary conditions later on (see Figures 4.3 and 4.4). Denote by Ω_n the set of points lying on the edges or vertices of the weighted graph $\overline{\text{SG}}^{(n)}(3)$ and denote the region's boundary by $\partial\Omega_n$.

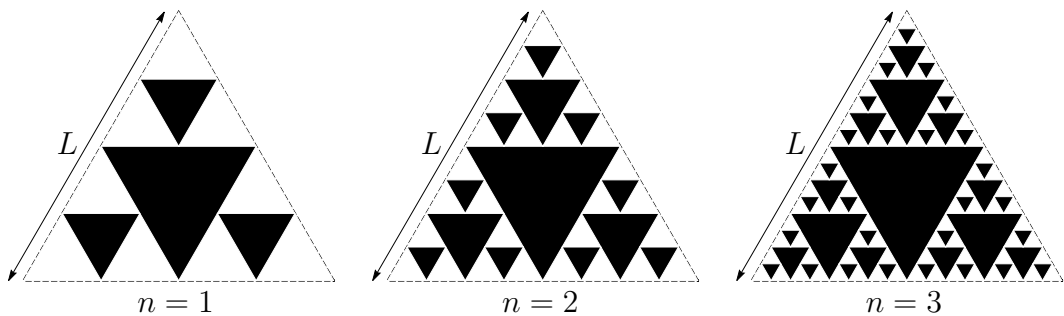


Figure 4.1: The first few generations of the Sierpinski gasket (white triangles). The black triangles (the complement of the Sierpinski gasket) consist of piezoelectric material. The side length of the Sierpinski gasket is L for all generation levels.

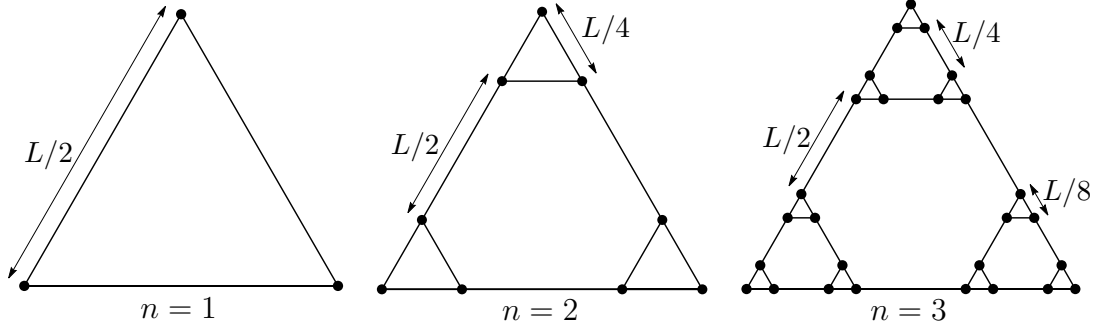


Figure 4.2: The first few generations of the weighted Sierpinski gasket graph $\overline{\text{SG}}(3)$.

By introducing the non-dimensionalised variable $\theta = c_T t / h^{(n)}$ then (temporarily dropping the subscript on u and the superscript on $h^{(n)}$)

$$\frac{\partial^2 u}{\partial \theta^2} = (h^{(n)})^2 \nabla^2 u. \quad (4.1.1)$$

Applying the Laplace transform $\mathcal{L} : \theta \rightarrow q$ then gives

$$q^2 \bar{u} = (h^{(n)})^2 \nabla^2 \bar{u}. \quad (4.1.2)$$

We will seek a weak solution $\bar{u} \in H^1(\Omega_n)$ where on the boundary $\bar{u} = \bar{u}_{\partial\Omega_n} \in H^1(\partial\Omega_n)$. Now multiplying by a test function $w \in H_B^1(\Omega_n)$, where $H_B^1(\Omega_n) := \{w \in H^1(\Omega_n) : w = 0 \text{ on } \partial\Omega_n\}$, integrating over the region Ω_n , and using Green's first identity $\int_{\Omega_n} \psi \nabla^2 \phi \, dv = \oint_{\partial\Omega_n} \psi (\nabla \phi \cdot \underline{n}) \, dr - \int_{\Omega_n} \nabla \phi \cdot \nabla \psi \, dv$, where \underline{n} is the outward pointing unit normal of surface element dr , gives

$$\int_{\Omega_n} q^2 \bar{u} w \, d\underline{x} = (h^{(n)})^2 \oint_{\partial\Omega_n} w (\nabla \bar{u} \cdot \underline{n}) \, dr - (h^{(n)})^2 \int_{\Omega_n} \nabla \bar{u} \cdot \nabla w \, d\underline{x}.$$

Now $(h^{(n)})^2 \oint_{\partial\Omega_n} w (\nabla \bar{u} \cdot \underline{n}) \, dr$ is zero since $w = 0$ on $\partial\Omega_n$ and so, we seek $\bar{u} \in$

$H^1(\Omega_n)$ such that

$$q^2 \int_{\Omega_n} \bar{u} w d\underline{x} = - (h^{(n)})^2 \int_{\Omega_n} \nabla \bar{u} \cdot \nabla w d\underline{x}$$

where $w \in H_B^1(\Omega_n)$.

4.2 Galerkin discretisation

Using a standard Galerkin method we replace $H^1(\Omega_n)$ and $H_B^1(\Omega_n)$ by the finite dimensional subspaces S_S and $S_B = S_S \cap H_B^1(\Omega_n)$. Let $U_B \in S_S$ be a function that approximates $\bar{u}_{\partial\Omega_n}$ on $\partial\Omega_n$, then the discretised problem involves finding $\bar{U} \in S_S$ such that

$$q^2 \int_{\Omega_n} \bar{U} W d\underline{x} = - (h^{(n)})^2 \int_{\Omega_n} \nabla \bar{U} \cdot \nabla W d\underline{x}, \quad (4.2.1)$$

where W is the test function expressed in this finite dimensional space.

Definition 4.2.1. Denote the set of vertices in Ω_n as V_{Ω_n} , the set of fictitious vertices as $V_{\partial\Omega_n}$ (these are vertices $N_n + 1, N_n + 2$ and $N_n + 3$), the set of interior vertices as $V_{\Omega_n^\circ}$ (so $V_{\Omega_n^\circ} = V_{\Omega_n} \setminus V_{\partial\Omega_n}$), and the set of input/output vertices as $V_{\partial\Omega_n^\circ}$ (these are vertices $1, m_n = (N_n + 1)/2$ and N_n). E_{Ω_n} is the set of edges in Ω_n , the set of edges joining vertices in $V_{\partial\Omega_n^\circ}$ to vertices in $V_{\partial\Omega_n}$ is denoted $E_{\partial\Omega_n}$ and $E_{\Omega_n^\circ}$ is the set of the interior edges ($E_{\Omega_n^\circ} = E_{\Omega_n} \setminus E_{\partial\Omega_n}$). Denote by $E_{\Omega_n^\circ}^{(p)}$ the set of edges in $E_{\Omega_n^\circ}$ of length $h^{(p)}$ and by $\bar{E}_{\Omega_n^\circ}^{(p)}$ three copies of $E_{\Omega_n^\circ}^{(p)}$ (the adjacency matrix for $\bar{E}_{\Omega_n^\circ}$ is a block diagonal matrix where each block is the adjacency matrix for $E_{\Omega_n^\circ}$). $E_{\Omega_n}^{(p)}$ and $\bar{E}_{\Omega_n}^{(p)}$ are defined similarly using the complete set of edges in Ω_n . Also $\bar{E}_{\partial\Omega_n}$ is three copies of the boundary edges $E_{\partial\Omega_n}$. Hence $\bar{E}_{\Omega_{n-1}}^{(p-1)} = E_{\Omega_n}^{(p)}$ if $p < n$, $\bar{E}_{\Omega_{n-1}}^{(p-1)} = E_{\Omega_n^\circ}^{(p)}$ for $p \leq n$ and $E_{\Omega_n}^{(p)} = E_{\Omega_n}^{(p)}$ if $p < n$.

Let $\phi_j, j \in V_{\Omega_n^\circ}$ form a basis of S_B and set $W = \phi_j$, then equation (4.2.1)

becomes

$$q^2 \int_{\Omega_n} \bar{U} \phi_j d\underline{x} = - (h^{(n)})^2 \int_{\Omega_n} \nabla \bar{U} \cdot \nabla \phi_j d\underline{x}. \quad (4.2.2)$$

Furthermore, let $\phi_i, i \in V_{\partial\Omega_n}$ form a basis for the boundary vertices and let

$$\bar{U} = \sum_{i=1}^{N_n} U_i \phi_i + \sum_{i \in V_{\partial\Omega_n}} U_{B_i} \phi_i. \quad (4.2.3)$$

Hence, equation (4.2.2) becomes

$$\begin{aligned} & \sum_{i=1}^{N_n} \left(\int_{\Omega_n} \left(q^2 \phi_j \phi_i + (h^{(n)})^2 \nabla \phi_j \cdot \nabla \phi_i \right) d\underline{x} \right) U_i = \\ & - \sum_{i \in V_{\partial\Omega_n}} \left(\int_{\Omega_n} \left(q^2 \phi_j \phi_i + (h^{(n)})^2 \nabla \phi_j \cdot \nabla \phi_i \right) d\underline{x} \right) U_{B_i} \end{aligned} \quad (4.2.4)$$

where $j \in V_{\Omega_n}$. That is

$$A_{ji} U_i = b_j \quad (4.2.5)$$

where

$$A_{ji} = q^2 \int_{\Omega_n} \phi_j \phi_i d\underline{x} + (h^{(n)})^2 \int_{\Omega_n} \nabla \phi_j \cdot \nabla \phi_i d\underline{x}, \quad (4.2.6)$$

and

$$b_j = - \sum_{i \in V_{\partial\Omega_n}} \left(\int_{\Omega_n} \left(q^2 \phi_j \phi_i + (h^{(n)})^2 \nabla \phi_j \cdot \nabla \phi_i \right) d\underline{x} \right) U_{B_i}. \quad (4.2.7)$$

It is important to now explicitly record the fractal generation level n and so equation (4.2.6) can be written

$$A_{ji}^{(n)} = q^2 H_{ji}^{(n)} + (h^{(n)})^2 K_{ji}^{(n)}, \quad (4.2.8)$$

where

$$H_{ji}^{(n)} = \int_{\Omega_n} (\phi_j \phi_i) d\underline{x}. \quad (4.2.9)$$

and

$$K_{ji}^{(n)} = \int_{\Omega_n} (\nabla \phi_j \cdot \nabla \phi_i) d\mathbf{x}. \quad (4.2.10)$$

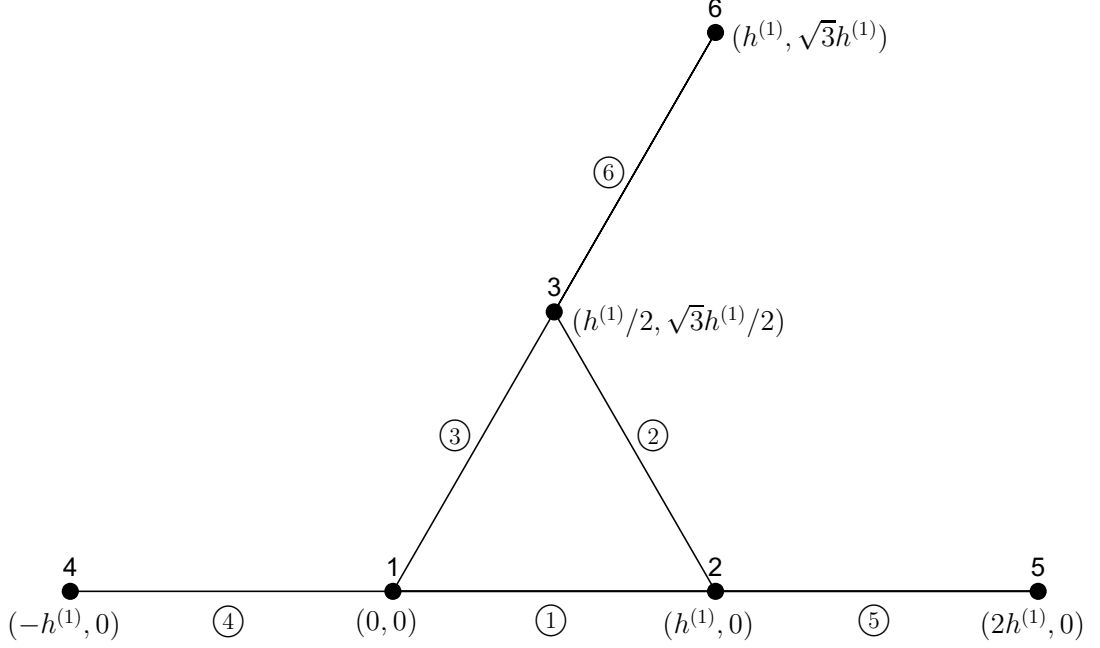


Figure 4.3: The Sierpinski Gasket dual graph $\overline{SG}(3)$ at generation level $n = 1$. Vertices $\{1, 2, 3\} \in V_{\Omega_n}$ or $V_{\partial\Omega_n}$ in this level $n = 1$ are the input/output vertices, and vertices $\{4, 5, 6\} \in V_{\partial\Omega_n}$ are fictitious vertices used to accommodate the boundary conditions. The graph has 6 elements (circled numbers), with two vertices adjacent to each element.

Lemma 4.2.1. *The basis function ϕ_j for vertex j in the element (the edge) joining vertices j and k at fractal generation level n is given by*

$$\begin{aligned} \phi_j(x, y, x_j, y_j, x_k, y_k, x_m, y_m, x_l, y_l) = & \left((y - y_k)(x_m + x_l) - (x - x_k)(y_m + y_l) \right. \\ & + 2(xy_k - x_ky) + x_jy - x_jy_k - xy_j + x_ky_j + xy_k - x_ky \\ & \left. - (x_j - x_k)(y_m + y_l) + 2(x_jy_k - x_ky_j) \right) / \left((y_j - y_k)(x_m + x_l) \right. \\ & \left. - (x_j - x_k)(y_m + y_l) + 2(x_jy_k - x_ky_j) \right) \end{aligned} \quad (4.2.11)$$

where, for edges of length greater than $h^{(n)}$ and $n \geq 2$, the two other adjacent

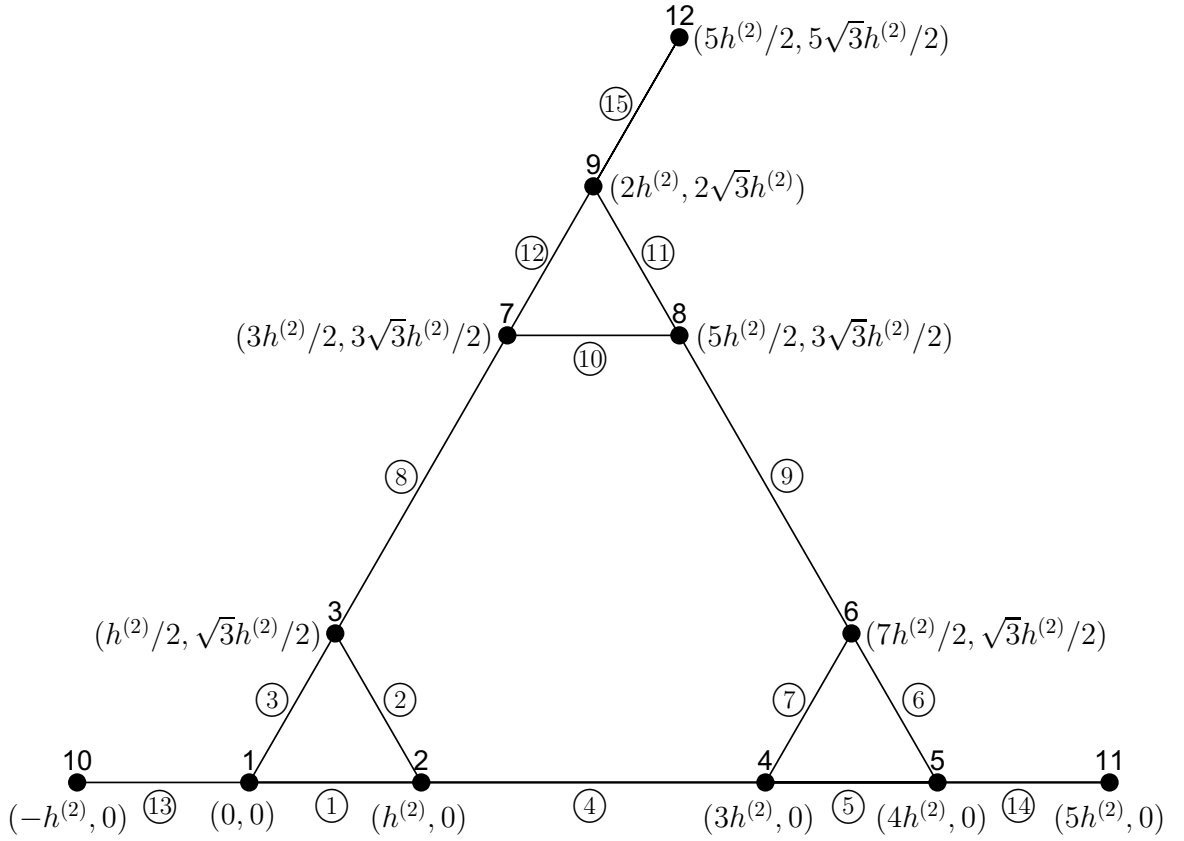


Figure 4.4: The Sierpinski Gasket dual graph $\overline{\text{SG}}(3)$ at generation level $n = 2$. Vertices $\{1, \dots, 9\} \in V_{\Omega_n^o}$ and vertices $\{1, 5, 9\} \in V_{\partial\Omega_n^o}$. Vertices $\{10, 11, 12\} \in V_{\partial\Omega_n}$ are fictitious vertices used to accommodate the boundary conditions. The graph has 15 elements (circled numbers), with two vertices adjacent to each element.

vertices to vertex j are l and m . For interior edges of length $h^{(n)}$ and $n \geq 1$ then vertex l is equal to vertex j and vertex m is the vertex that is connected to vertex j by the other edge of length $h^{(n)}$ (for exterior edges (these will have length $h^{(n)}$) then vertices l and m are also the two interior vertices adjacent to vertex j). Hence,

$$\nabla\phi_j(x, y, x_j, y_j, x_k, y_k, x_m, y_m, x_l, y_l) = \left(\frac{-(y_j + y_m + y_l) + 3y_k}{(y_j - y_k)(x_m + x_l) - (x_j - x_k)(y_m + y_l) + 2(x_j y_k - x_k y_j)}, \frac{x_j + x_m + x_l - 3x_k}{(y_j - y_k)(x_m + x_l) - (x_j - x_k)(y_m + y_l) + 2(x_j y_k - x_k y_j)} \right). \quad (4.2.12)$$

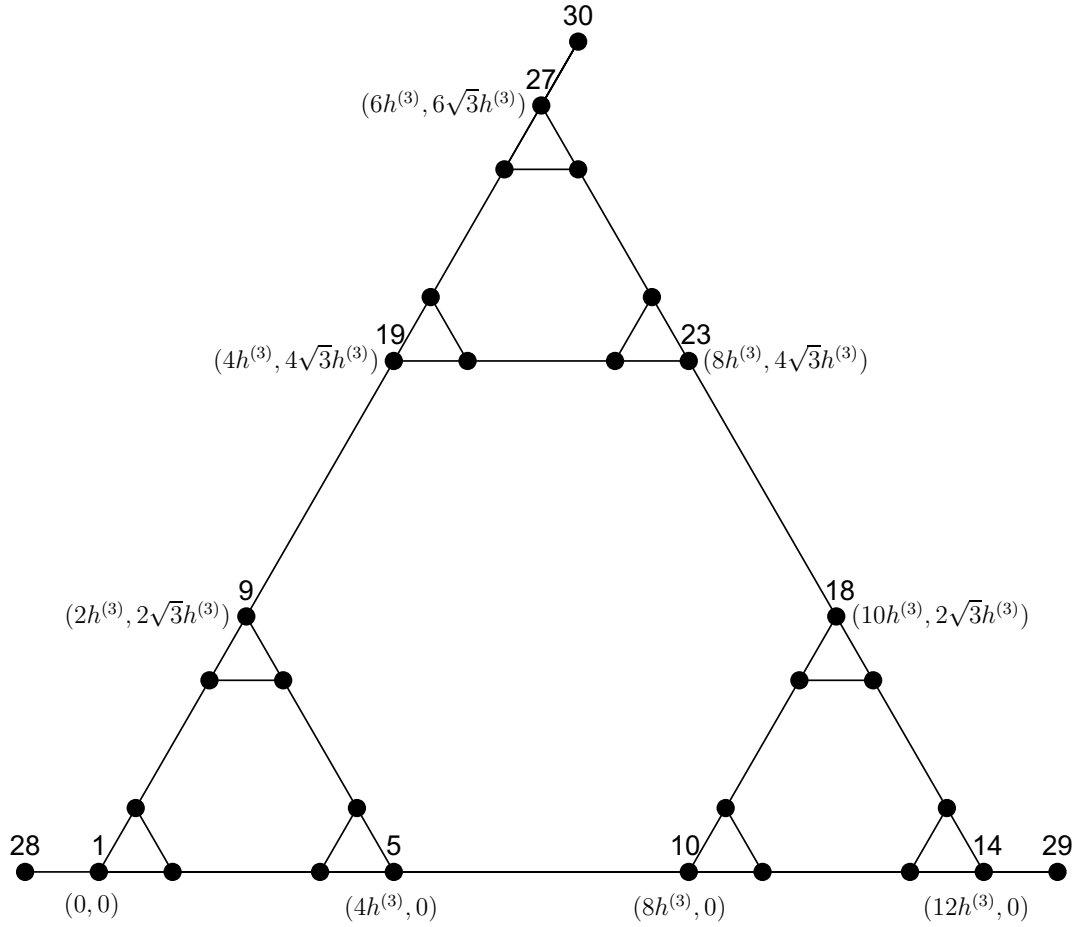


Figure 4.5: The Sierpinski Gasket dual graph $\overline{\text{SG}}(3)$ at generation level $n = 3$. Vertices $\{28, 29, 30\} \in V_{\partial\Omega_n}$ are fictitious vertices used to accommodate the boundary conditions. The graph has 42 elements, with two vertices adjacent to each element.

Proof. The basis function is chosen to be linear having a value of one at vertex j and a value of zero at vertex k . So $\phi_j^{(n)}$ is a straight line lying in a plane S_P containing the points $P_2 = (x_k, y_k, 0)$ and $P_1 = (x_j, y_j, 1)$ (see Figure 4.6). To make this plane unique a third point is required. When edge jk is longer than $h^{(n)}$ then, to retain the symmetry inherent to the $\overline{\text{SG}}$ graph this third point is chosen as the centroid of the triangle formed by the two other vertices (\underline{x}_m and \underline{x}_l) connected to vertex j and vertex j itself. When an interior edge jk has length $h^{(n)}$ then this third point is chosen as the centroid of the triangle formed by the two interior vertices that are connected to vertex j by edges of length $h^{(n)}$. So let P_3 be the point

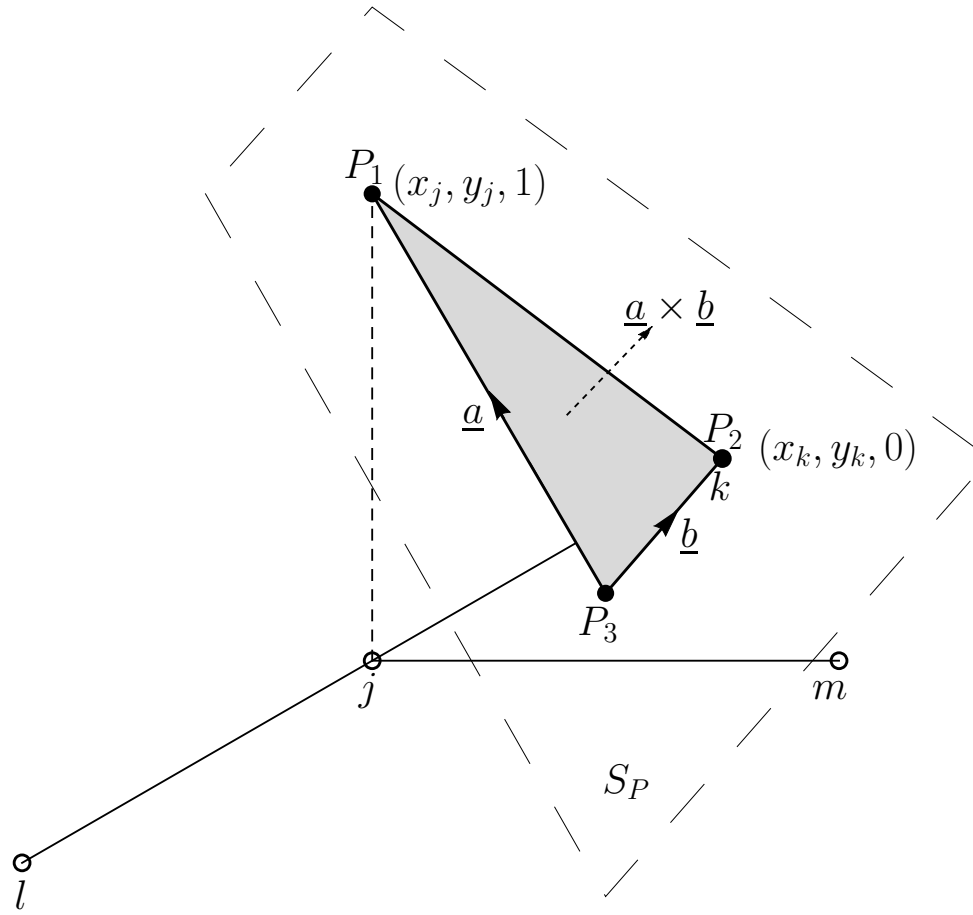


Figure 4.6: Basis function at vertex j with adjacent vertices l, m and k in the $\overline{\text{SG}}(3)$ graph. P_3 is the centroid of the triangle with vertices j, m and k . The plane S_P contains the points P_1, P_2 (vertex k) and P_3 .

$(x_j + x_m + x_l, y_j + y_m + y_l, 0)/3$. The vectors $\underline{a} = \overrightarrow{OP_1} - \overrightarrow{OP_3}$ and $\underline{b} = \overrightarrow{OP_2} - \overrightarrow{OP_3}$ lie in this plane and so the equation of the plane is $(\underline{a} \times \underline{b}) \cdot \underline{x} = (\underline{a} \times \underline{b}) \cdot P_1$. Rearranging this equation for the third component of \underline{x} gives this formula for the basis function. The gradient then follows. \square

The resulting basis functions for fractal generation levels $n = 1$ and $n = 2$ are shown in Figures 4.7 and 4.8. For each generation level of the $\overline{\text{SG}}(3)$ graph the coordinates of the vertices are known (see Appendix A.3 for a detailed description for $n = 1$ and $n = 2$). For a particular element lying between vertex j and vertex

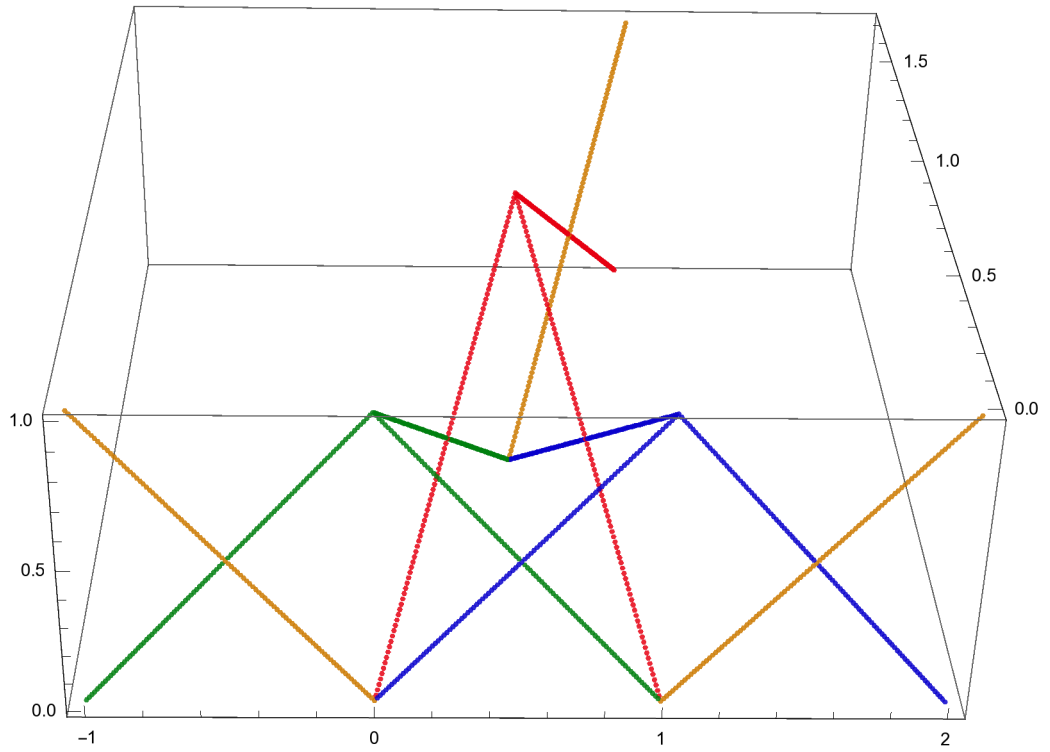


Figure 4.7: The basis functions ϕ_j where $j \in J$ and I at fractal generation level $n = 1$.

i the isoparametric representation, given by

$$(x(s), y(s)) = ((x_j - x_i)s + x_i, (y_j - y_i)s + y_i) \quad (4.2.13)$$

is employed (see Figure 4.9), where $s_1 = 0$ and $s_2 = 1$ and $d\underline{x} = h^{(p)} ds$. Note that the superscript (p) has been used here since there will be a range of edge lengths $h^{(p)}$, $p = 1, \dots, n$ in the generation level n $\overline{\text{SG}}(3)$ graph.

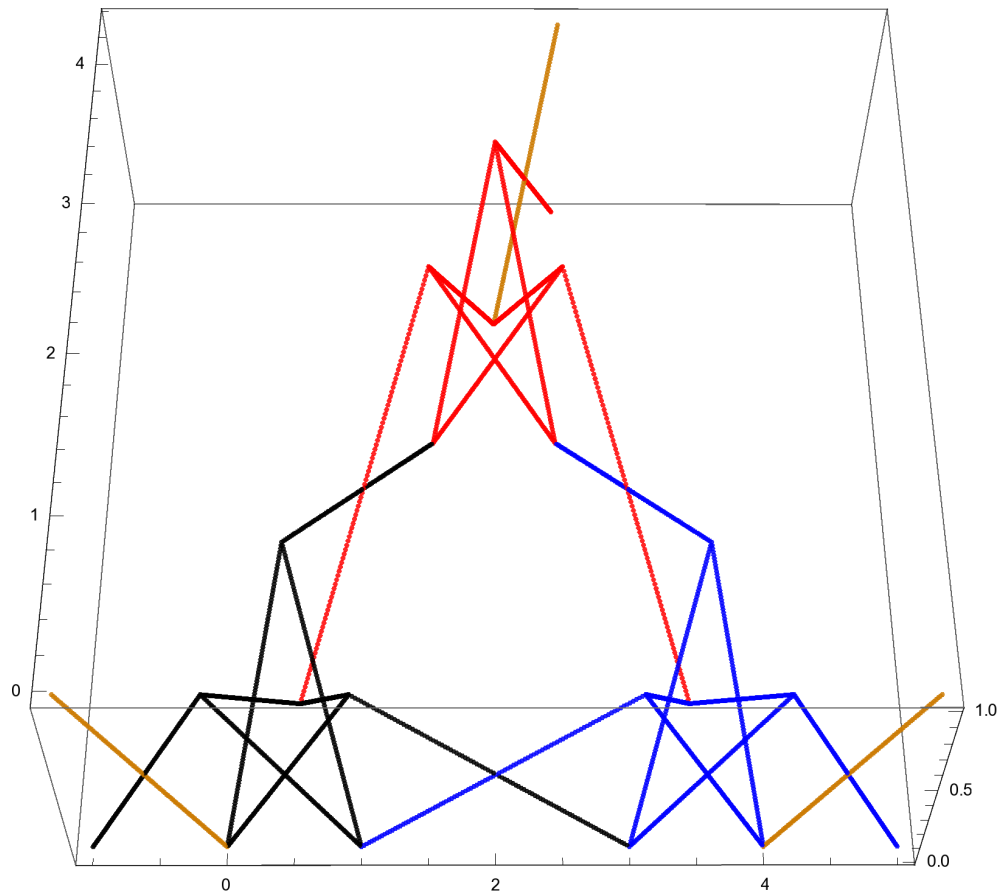


Figure 4.8: The basis functions ϕ_j where $j \in J$ and I at fractal generation level $n = 2$.

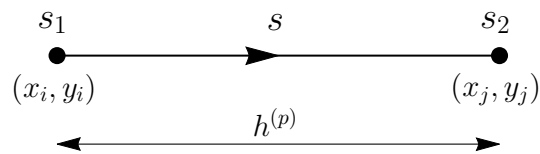


Figure 4.9: An isoparametric element (edge) between vertex (x_i, y_i) and vertex (x_j, y_j) at generation level p .

4.3 Derivation of the matrix recursions

Using the basis function derived in Lemma 4.2.1 it can be shown that the matrix H at fractal generation level n can be related to its counterpart at level $n - 1$.

Lemma 4.3.1.

$$\hat{H}_{ji}^{(n)} = \bar{H}_{ji}^{(n-1)} + \Upsilon^{(n)} W_{ji}^{(n)} + \vartheta^{(n)} P_{ji}^{(n)}, \quad j, i \in V_{\Omega_n^c} \quad (4.3.1)$$

where $\bar{H}_{ji}^{(n-1)}$ is a block diagonal matrix consisting of three blocks of matrix $H_{ji}^{(n-1)}$ for $n \geq 2$, $\bar{H}_{ji}^{(n-1)} = \bar{H}_{ji}^{(n-1)}/h^{(n)}$, $\hat{H}_{ji}^{(n)} = H_{ji}^{(n)}/h^{(n)}$, $\Upsilon^{(n)} = (2^{n-1} - 1)/3$, $\vartheta^{(n)} = 2^{n-1}/6$, $W_{ji}^{(n)} = \mathbb{1}_{V_{\Omega_n^{(1)}}}(j) \mathbb{1}_{\{0\}}(i - j)$ (where $\mathbb{1}_{\{A\}}(a)$ is the indicator function which equals 1 if $a \in A$, and 0 otherwise) and $P_{ji}^{(n)} = \mathbb{1}_{E_{\Omega_n^{(1)}}}(ji)$.

Proof. By using equations (4.2.9) and (4.2.13) for edge jk of length $h^{(p)}$ then,

$${}^{jk}H_{cd}^{(n,p)} = \int_{jk \in E_{\Omega_n}} \phi_c \phi_d d\mathbf{x} = 2^{n-p} h^{(n)} \int_0^1 \phi_c(x(s), y(s)) \phi_d(x(s), y(s)) ds. \quad (4.3.2)$$

From equation (4.2.11), the basis function at vertex j (which has coordinates (a, b)) along a typical edge $jk \in E_{\Omega_n}^{(p)}$ where $p < n$ is

$$\phi_j(x, y) = \frac{1}{h^{(n)}} \left((a - x) (3 + 2^{(1+p-n)}) - (b - y) \sqrt{3} + h^{(n)} \right) \quad (4.3.3)$$

and at vertex k (which has coordinates $(a + 2^{(n-p-1)}h^{(n)}, b + 2^{(n-p-1)}\sqrt{3}h^{(n)})$) is

$$\phi_k(x, y) = \frac{1}{h^{(n)}} \left((a - x) (3 + 2^{p-n}) - \sqrt{3}(b - y) (1 + 2^{p-n}) \right). \quad (4.3.4)$$

Substituting equation (4.2.13) into equations (4.3.3) and (4.3.4) gives

$$\phi_j(x(s), y(s)) = 1 - s$$

and

$$\phi_k(x(s), y(s)) = s.$$

Now if $(c = d = j)$ or $(c = d = k)$ in equation (4.3.2) then

$${}^{jk}H_{jj}^{(n,p)} = 2^{n-p}h^{(n)} \int_0^1 (1-s)^2 ds = \frac{2^{n-p}}{3}h^{(n)} = {}^{jk}H_{kk}^{(n,p)}$$

and if $(c = j \text{ and } d = k)$ or $(c = k \text{ and } d = j)$ in equation (4.3.2) then

$${}^{jk}H_{jk}^{(n,p)} = 2^{n-p}h^{(n)} \int_0^1 (1-s)s ds = \frac{2^{n-p}}{6}h^{(n)} = {}^{jk}H_{kj}^{(n,p)}.$$

A similar calculation can be conducted for the case $p = n$ albeit the basis functions calculation is slightly different and follows the prescription in the proof of Lemma

2. So equation (4.3.2) becomes, for $jk \in E_{\Omega_n}^{(p)}$, $n \geq 1$ and $p \leq n$

$${}^{jk}H_{cd}^{(n,p)} = 2^{n-p}h^{(n)} \begin{cases} \frac{1}{3} & \text{if } (c = d = j) \text{ or } (c = d = k) \\ \frac{1}{6} & \text{if } (c = j \text{ and } d = k) \text{ or } (c = k \text{ and } d = j), j \neq k \\ 0 & \text{otherwise.} \end{cases} \quad (4.3.5)$$

We now consider the basis functions at input/output vertices $V_{\partial\Omega_n^o}$ and the integration of equation (4.3.2) in the boundary edges $jk \in E_{\partial\Omega_n}$. Equation (4.3.2) becomes

$${}^{jk}H_{cd}^{(n,n)} = h^{(n)} \begin{cases} \frac{1}{3} & \text{if } (c = d = j \in V_{\partial\Omega_n^o}) \\ 0 & \text{otherwise.} \end{cases} \quad (4.3.6)$$

The matrix $H_{cd}^{(n)}$ is assembled element by element (edge by edge) as follows

$$H_{cd}^{(n)} = \sum_{p=1}^n \sum_{jk \in E_{\Omega_n}^{(p)}} {}^{jk}H_{cd}^{(n,p)} = \sum_{p=2}^n \sum_{jk \in E_{\Omega_n}^{(p)}} {}^{jk}H_{cd}^{(n,p)} + \sum_{jk \in E_{\Omega_n}^{(1)}} {}^{jk}H_{cd}^{(n,1)}. \quad (4.3.7)$$

The first term on the right hand side of this equation can be written

$$\begin{aligned} \sum_{p=2}^n \sum_{jk \in E_{\Omega_n}^{(p)}} jk H_{cd}^{(n,p)} &= \sum_{p=2}^{n-1} \sum_{jk \in E_{\Omega_n}^{(p)}} jk H_{cd}^{(n,p)} + \sum_{jk \in E_{\Omega_n}^{(n)}} jk H_{cd}^{(n,n)} \\ &= \sum_{p'=1}^{n-2} \sum_{jk \in E_{\Omega_n}^{(p'+1)}} jk H_{cd}^{(n,p'+1)} + \sum_{jk \in E_{\Omega_n}^{(n)}} jk H_{cd}^{(n,n)}. \end{aligned}$$

Since $E_{\Omega_n}^{(p)} = \bar{E}_{\Omega_{n-1}^o}^{(p-1)}$, $E_{\Omega_n}^{(p)} = \bar{E}_{\Omega_{n-1}}^{(p-1)}$, and $E_{\partial\Omega_n} \subseteq \bar{E}_{\partial\Omega_{n-1}} \subseteq \bar{E}_{\Omega_{n-1}}^{(n-1)}$ for $1 < p < n$, then, $E_{\Omega_n}^{(n)} = E_{\Omega_n}^{(n)} \cup E_{\partial\Omega_n} = \bar{E}_{\Omega_{n-1}^o}^{(n-1)} \cup E_{\partial\Omega_n} = \left(\bar{E}_{\Omega_{n-1}}^{(n-1)} \setminus \bar{E}_{\partial\Omega_{n-1}} \right) \cup E_{\partial\Omega_n} = \bar{E}_{\Omega_{n-1}}^{(n-1)} \setminus \left(\bar{E}_{\partial\Omega_{n-1}} \setminus E_{\partial\Omega_n} \right)$. Hence,

$$\begin{aligned} \sum_{p=2}^n \sum_{jk \in E_{\Omega_n}^{(p)}} jk H_{cd}^{(n,p)} &= \sum_{p'=1}^{n-2} \sum_{jk \in \bar{E}_{\Omega_{n-1}}^{(p')}} jk H_{cd}^{(n,p'+1)} + \sum_{jk \in \bar{E}_{\Omega_{n-1}}^{(n-1)}} jk H_{cd}^{(n,n)} \\ &\quad - \sum_{jk \in \bar{E}_{\partial\Omega_{n-1}} \setminus E_{\partial\Omega_n}} jk H_{cd}^{(n,n)} \\ &= \sum_{p'=1}^{n-1} \sum_{jk \in \bar{E}_{\Omega_{n-1}}^{(p')}} jk H_{cd}^{(n,p'+1)} - \sum_{jk \in \bar{E}_{\partial\Omega_{n-1}} \setminus E_{\partial\Omega_n}} jk H_{cd}^{(n,n)}. \end{aligned}$$

It can be shown that $jk H_{cd}^{(n,p'+1)} = jk H_{cd}^{(n-1,p')}$, and then from equation (4.3.6),

$$\sum_{p=2}^n \sum_{jk \in E_{\Omega_n}^{(p)}} jk H_{cd}^{(n,p)} = \bar{H}_{cd}^{(n-1)} - \frac{h^{(n)}}{3} W_{cd}^{(n)} \quad (4.3.8)$$

since in $\bar{E}_{\partial\Omega_{n-1}} \setminus E_{\partial\Omega_n}$ we have $c = d$ in equation (4.3.5), and $\bar{H}_{cd}^{(n-1)}$ is a block diagonal matrix of dimension $N_n \times N_n$ consisting of three blocks given by $H_{cd}^{(n-1)}$ of dimension $N_{n-1} \times N_{n-1}$. Now the second term on the right hand side of equation

(4.3.7) can be written

$$\sum_{jk \in E_{\Omega_n}^{(1)}} {}^{jk}H_{cd}^{(n,1)} = 2^{n-1}h^{(n)} \left(\frac{1}{6}P_{cd}^{(n)} + \frac{1}{3}W_{cd}^{(n)} \right).$$

Combining this with equation (4.3.8) then equation (4.3.7) becomes

$$\hat{H}_{ji}^{(n)} = \bar{\hat{H}}_{ji}^{(n-1)} + \frac{1}{3}(2^{n-1} - 1)W_{ji}^{(n)} + \frac{2^{n-1}}{6}P_{ji}^{(n)}$$

where $\bar{\hat{H}}_{ji}^{(n-1)} = \bar{H}_{ji}^{(n-1)}/h^{(n)}$ and $\hat{H}_{ji}^{(n)} = H_{ji}^{(n)}/h^{(n)}$. □

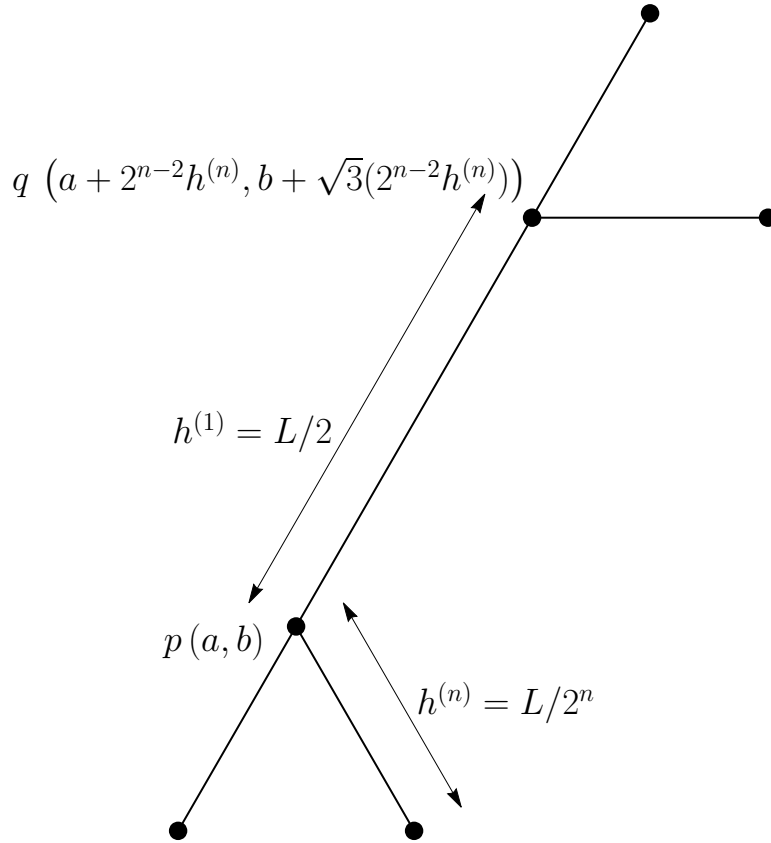


Figure 4.10: The element (edge) between vertices p and q with the longest length $h^{(1)}$ in $\overline{\text{SG}}(3)$. Here $h^{(n)}$ denotes the length of the smallest edge in $\overline{\text{SG}}^{(n)}(3)$ where $h^{(n)} = L/2^n$.

A similar approach can be used to derive the matrix $K_{ji}^{(n)}$.

Lemma 4.3.2.

$$\hat{K}_{ji}^{(n)} = \bar{K}_{ji}^{(n-1)} + \epsilon^{(n)} W_{ji}^{(n)} + \chi^{(n)} P_{ji}^{(n)}, \quad j, i \in V_{\Omega_n^o} \quad (4.3.9)$$

where $\bar{K}_{ji}^{(n-1)}$ is a block diagonal matrix consisting of three blocks of matrix $K_{ji}^{(n-1)}$ for $n \geq 2$, $\bar{K}_{ji}^{(n-1)} = h^{(n)} \bar{K}_{ji}^{(n-1)}$, $\hat{K}_{ji}^{(n)} = h^{(n)} K_{ji}^{(n)}$, $\epsilon^{(n)} = 2^{n-1} (12 + 2^{4-2n} + 3(2^{3-n})) - 28$ and $\chi^{(n)} = 2^{n-1} (12 + 2^{3-2n} + 3(2^{3-n}))$.

Proof. By using equations (4.2.10) and (4.2.13) for edge jk of length $h^{(p)}$ then,

$${}^{jk}K_{cd}^{(n,p)} = \int_{jk \in E_{\Omega_n}} \nabla \phi_c \cdot \nabla \phi_d d\underline{x} = 2^{n-p} h^{(n)} \int_0^1 \nabla \phi_c(x(s), y(s)) \cdot \nabla \phi_d(x(s), y(s)) ds. \quad (4.3.10)$$

Equations (4.3.3) and (4.3.4), give for $jk \in E_{\Omega_n}^{(p)}$ where $p < n$

$$\nabla \phi_j(x, y) = \frac{1}{h^{(n)}} \left(- (3 + 2^{(1-n+p)}), \sqrt{3} \right)$$

and

$$\nabla \phi_k(x, y) = \frac{1}{h^{(n)}} \left(- (3 + 2^{p-n}), \sqrt{3} (1 + 2^{p-n}) \right).$$

Now if $(c = d = j)$ or $(c = d = k)$ in equation (4.3.10) then

$$\begin{aligned} {}^{jk}K_{jj}^{(n,p)} &= 2^{n-p} h^{(n)} \int_0^1 \frac{1}{h^{(n)}} \left(- (3 + 2^{(1-n+p)}), \sqrt{3} \right) \cdot \frac{1}{h^{(n)}} \left(- (3 + 2^{(1-n+p)}), \sqrt{3} \right) ds \\ &= \frac{2^{n-p}}{h^{(n)}} (12 + 2^{(2-2n+2p)} + 3(2^{(2-n+p)})) = {}^{jk}K_{kk}^{(n,p)} \end{aligned}$$

and if $(c = j \text{ and } d = k)$ or $(c = k \text{ and } d = j)$ in equation (4.3.10) then

$$\begin{aligned} {}^{jk}K_{jk}^{(n,p)} &= \frac{2^{n-p}}{h^{(n)}} \int_0^1 \left(- (3 + 2^{(1-n+p)}), \sqrt{3} \right) \cdot \left(- (3 + 2^{p-n}), \sqrt{3} (1 + 2^{p-n}) \right) ds \\ &= \frac{2^{n-p}}{h^{(n)}} (12 + 2^{(1-2n+2p)} + 3 (2^{(2-n+p)})) = {}^{jk}K_{kj}^{(n,p)}. \end{aligned}$$

Hence, for $jk \in E_{\Omega_n}^{(p)}$, $n \geq 2$ and $p < n$

$${}^{jk}K_{cd}^{(n,p)} = \frac{2^{n-p}}{h^{(n)}} \begin{cases} 12 + 2^{(2-2n+2p)} + 3 (2^{(2-n+p)}) & \text{if } (c = d = j) \text{ or } (c = d = k) \\ 12 + 2^{(1-2n+2p)} + 3 (2^{(2-n+p)}) & \text{if } (c = j \text{ and } d = k) \text{ or } (c = k \text{ and } d = j) \\ 0 & \text{otherwise.} \end{cases} \quad (4.3.11)$$

A similar calculation can be undertaken for the case when $jk \in E_{\Omega_n}^{(n)}$ and $p = n$.

It transpires that

$${}^{jk}K_{cd}^{(n,n)} = \frac{1}{h^{(n)}} \begin{cases} 4 & \text{if } (c = d = j) \text{ or } (c = d = k) \\ 2 & \text{if } (c = j \text{ and } d = k) \text{ or } (c = k \text{ and } d = j) \\ 0 & \text{otherwise.} \end{cases} \quad (4.3.12)$$

Similarly, for the boundary edges $jk \in E_{\partial\Omega_n}$, equation (4.3.10) becomes

$${}^{jk}K_{cd}^{(n,n)} = \frac{1}{h^{(n)}} \begin{cases} 28 & \text{if } (c = d = j \in V_{\partial\Omega_n}) \\ 0 & \text{otherwise.} \end{cases} \quad (4.3.13)$$

As before the matrix $K_{cd}^{(n)}$ is assembled in an element by element (edge by edge) manner via

$$K_{cd}^{(n)} = \sum_{p=1}^n \sum_{jk \in E_{\Omega_n}^{(p)}} {}^{jk}K_{cd}^{(n,p)} = \sum_{p=2}^n \sum_{jk \in E_{\Omega_n}^{(p)}} {}^{jk}K_{cd}^{(n,p)} + \sum_{jk \in E_{\Omega_n}^{(1)}} {}^{jk}K_{cd}^{(n,1)}. \quad (4.3.14)$$

The first term on the right hand side of this equation can be written

$$\begin{aligned} \sum_{p=2}^n \sum_{jk \in E_{\Omega_n}^{(p)}} jk K_{cd}^{(n,p)} &= \sum_{p=2}^{n-1} \sum_{jk \in E_{\Omega_n}^{(p)}} jk K_{cd}^{(n,p)} + \sum_{jk \in E_{\Omega_n}^{(n)}} jk K_{cd}^{(n,n)} \\ &= \sum_{p'=1}^{n-2} \sum_{jk \in E_{\Omega_n}^{(p'+1)}} jk K_{cd}^{(n,p'+1)} + \sum_{jk \in E_{\Omega_n}^{(n)}} jk K_{cd}^{(n,n)}. \end{aligned}$$

Since $E_{\Omega_n}^{(p)} = \bar{E}_{\Omega_{n-1}}^{(p-1)}$ for $1 < p < n$, and $E_{\Omega_n}^{(n)} = E_{\Omega_n}^{(n)} \cup E_{\partial\Omega_n} = \bar{E}_{\Omega_{n-1}}^{(n-1)} \cup E_{\partial\Omega_n} = (\bar{E}_{\Omega_{n-1}}^{(n-1)} \setminus \bar{E}_{\partial\Omega_{n-1}}) \cup E_{\partial\Omega_n} = \bar{E}_{\Omega_{n-1}}^{(n-1)} \setminus (\bar{E}_{\partial\Omega_{n-1}} \setminus E_{\partial\Omega_n})$. Hence,

$$\begin{aligned} \sum_{p=2}^n \sum_{jk \in E_{\Omega_n}^{(p)}} jk K_{cd}^{(n,p)} &= \sum_{p'=1}^{n-2} \sum_{jk \in \bar{E}_{\Omega_{n-1}}^{(p')}} jk K_{cd}^{(n,p'+1)} + \sum_{jk \in \bar{E}_{\Omega_{n-1}}^{(n-1)}} jk K_{cd}^{(n,n)} \\ &\quad - \sum_{jk \in \bar{E}_{\partial\Omega_{n-1}} \setminus E_{\partial\Omega_n}} jk K_{cd}^{(n,n)} \\ &= \sum_{p'=1}^{n-1} \sum_{jk \in \bar{E}_{\Omega_{n-1}}^{(p')}} jk K_{cd}^{(n,p'+1)} - \sum_{jk \in \bar{E}_{\partial\Omega_{n-1}} \setminus E_{\partial\Omega_n}} jk K_{cd}^{(n,n)}. \end{aligned}$$

It can be shown that $jk K_{cd}^{(n,p'+1)} = jk K_{cd}^{(n-1,p')}$, and then from equation (4.3.13),

$$\sum_{p=2}^n \sum_{jk \in E_{\Omega_n}^{(p)}} jk K_{cd}^{(n,p)} = \bar{K}_{cd}^{(n-1)} - \frac{28}{h^{(n)}} W_{cd}^{(n)} \quad (4.3.15)$$

by a similar argument to that in Lemma 4.3.1. Examining the second term on the right hand side of equation (4.3.14), and using equation (4.3.11) with $p = 1$, gives

$$\begin{aligned} \sum_{jk \in E_{\Omega_n}^{(1)}} jk K_{cd}^{(n,1)} &= \frac{2^{n-1}}{h^{(n)}} (12 + 2^{3-2n} + 3(2^{3-n})) P_{cd}^{(n)} \\ &\quad + \frac{2^{n-1}}{h^{(n)}} (12 + 2^{4-2n} + 3(2^{3-n})) W_{cd}^{(n)}. \end{aligned}$$

Combining this with equation (4.3.15) then equation (4.3.14) becomes

$$\hat{K}_{ji}^{(n)} = \bar{K}_{ji}^{(n-1)} + \epsilon^{(n)} W_{ji}^{(n)} + \chi^{(n)} P_{ji}^{(n)}$$

where $\bar{K}_{ji}^{(n-1)} = h^{(n)} \bar{K}_{ji}^{(n-1)}$, $\hat{K}_{ji}^{(n)} = h^{(n)} K_{ji}^{(n)}$, $\epsilon^{(n)} = 2^{n-1} (12 + 2^{4-2n} + 3(2^{3-n})) - 28$ and $\chi^{(n)} = 2^{n-1} (12 + 2^{3-2n} + 3(2^{3-n}))$. \square

Theorem 4.3.3.

$$\hat{A}_{ji}^{(n)} = \bar{A}_{ji}^{(n-1)} + \alpha^{(n)} W_{ji}^{(n)} + \beta^{(n)} P_{ji}^{(n)}, \quad (4.3.16)$$

where $\bar{A}_{ji}^{(n-1)}$ is a block diagonal matrix consisting of three blocks of matrix $A_{ji}^{(n-1)}$ for $n \geq 2$, $\bar{A}_{ji}^{(n-1)} = \bar{A}_{ji}^{(n-1)}/h^{(n)}$, $\alpha^{(n)} = q^2 \Upsilon^{(n)} + \epsilon^{(n)}$ and $\beta^{(n)} = q^2 \vartheta^{(n)} + \chi^{(n)}$.

Proof. Combining equations (4.3.1) and (4.3.9) gives equation (4.2.8) as

$$\begin{aligned} \hat{A}_{ji}^{(n)} &= q^2 \left(\bar{H}_{ji}^{(n-1)} + \Upsilon^{(n)} W_{ji}^{(n)} + \vartheta^{(n)} P_{ji}^{(n)} \right) + \left(\bar{K}_{ji}^{(n-1)} + \epsilon^{(n)} W_{ji}^{(n)} + \chi^{(n)} P_{ji}^{(n)} \right) \\ &= q^2 \bar{H}_{ji}^{(n-1)} + \bar{K}_{ji}^{(n-1)} + \alpha^{(n)} W_{ji}^{(n)} + \beta^{(n)} P_{ji}^{(n)}. \end{aligned}$$

As discussed in [9] when redimensionalising we need to rescale the frequency by $(c_T/h^{(n)})^{-1}$. Hence,

$$\hat{A}_{ji}^{(n)} = \bar{A}_{ji}^{(n-1)} + \alpha^{(n)} W_{ji}^{(n)} + \beta^{(n)} P_{ji}^{(n)},$$

where $\bar{A}_{ji}^{(n-1)} = q^2 \bar{H}_{ji}^{(n-1)} + \bar{K}_{ji}^{(n-1)}$. \square

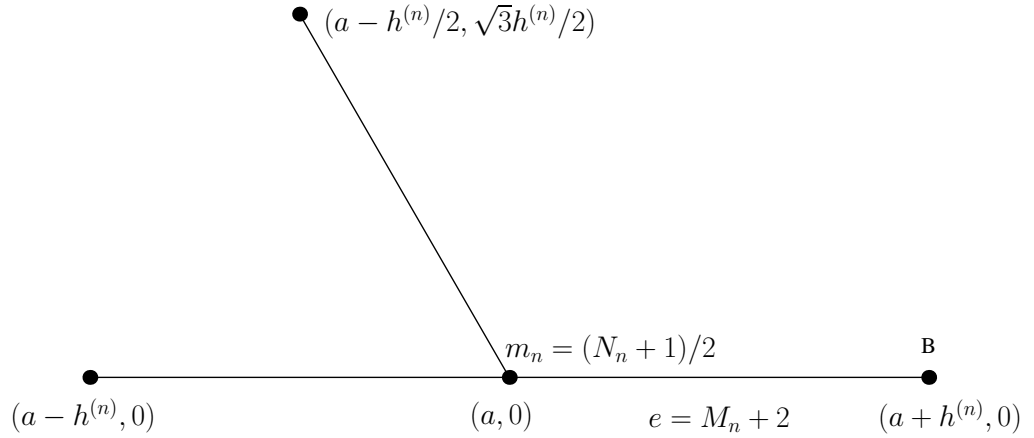


Figure 4.11: The boundary element for $e = M_n + 2$

A similar treatment can be given to equation (4.2.7)

Lemma 4.3.4.

$$b_j^{(n)} = h^{(n)} \eta U_i \mathbb{1}_{E_{\partial\Omega_n}}(ji), \quad j \in V_{\partial\Omega_n^o}, i \in V_{\partial\Omega_n} \quad (4.3.17)$$

where $\eta = 4 - q^2/6$.

Proof. By using equations (4.2.7) and (4.2.13) for edge ji then,

$$\begin{aligned} b_j^{(n)} &= - \sum_{i \in V_{\partial\Omega_n}} \left(\int_{ji \in E_{\partial\Omega_n}} \left(q^2 \phi_j \phi_i + (h^{(n)})^2 \nabla \phi_j \cdot \nabla \phi_i \right) d\underline{x} \right) U_{B_i} \\ &= -h^{(n)} \sum_{i \in V_{\partial\Omega_n}} \left(\int_0^1 \left(q^2 \phi_j(x(s), y(s)) \phi_i(x(s), y(s)) \right. \right. \\ &\quad \left. \left. + (h^{(n)})^2 \nabla \phi_j(x(s), y(s)) \cdot \nabla \phi_i(x(s), y(s)) \right) ds \right) U_{B_i} \end{aligned} \quad (4.3.18)$$

where $j \in V_{\partial\Omega_n^o}$. From equation (4.2.11), the basis function at vertex $j \in V_{\partial\Omega_n^o}$ (without loss of generality we will examine the vertex with coordinates $(a, 0)$) along

a typical edge $ji \in E_{\partial\Omega_n}$ is

$$\phi_j(x, y) = \frac{1}{h^{(n)}} \left(a + h^{(n)} - x - 3\sqrt{3}y \right) \quad (4.3.19)$$

and at vertex $i \in V_{\partial\Omega_n}$ (which has coordinates $(a + h^{(n)}, 0)$) is

$$\phi_i(x, y) = \frac{1}{h^{(n)}} \left(-a + x + \frac{y}{\sqrt{3}} \right). \quad (4.3.20)$$

Substituting equation (4.2.13) into equations (4.3.19) and (4.3.20) gives

$$\phi_j(x(s), y(s)) = 1 - s \quad (4.3.21)$$

and

$$\phi_i(x(s), y(s)) = s. \quad (4.3.22)$$

In addition equations (4.3.19) and (4.3.20), give

$$\nabla\phi_j(x(s), y(s)) = \frac{1}{h^{(n)}} \left(-1, -3\sqrt{3} \right) \quad (4.3.23)$$

and

$$\nabla\phi_i(x(s), y(s)) = \frac{1}{h^{(n)}} \left(1, +\frac{1}{\sqrt{3}} \right). \quad (4.3.24)$$

Substituting equations (4.3.21) to (4.3.24) into equation (4.3.18) gives

$$b_j^{(n)} = h^{(n)} \left(4 - \frac{q^2}{6} \right) U_i \quad j \in V_{\partial\Omega_n^o}, i \in V_{\partial\Omega_n} \text{ and } ji \in E_{\partial\Omega_n}.$$

□

4.3.1 Application of the mechanical boundary conditions

Appropriate electrical and mechanical boundary conditions can be applied in a similar fashion to those in Sections 2.3.1 and 3.4 leading to the following theorem. In this chapter, the cross-sectional area (A_r) of each edge of the fractal graph is $A_r = \xi L/2^n = \xi h^{(n)}$ and the length of the shortest edge decreases as the generation level increases and so, by fixing ξ , the cross-sectional area will also decrease as the fractal generation level increases.

Theorem 4.3.5.

$$U_i = G_{ji}^{(n)} \bar{\delta}_j, \quad (4.3.25)$$

where

$$G_{ji}^{(n)} = \left(\hat{A}_{ji}^{(n)} - \hat{B}_{ji}^{(n)} \right)^{-1} \quad (4.3.26)$$

represents the Green's transfer matrix, $\hat{B}_{ji}^{(n)} = \text{diag}\{\bar{\gamma}_1, \dots, \bar{\gamma}_{m_n}, \dots, \bar{\gamma}_{N_n}\}$, $\bar{\gamma}_j = \eta\gamma_j$, $\bar{\delta}_j = \eta\delta_j$,

$$\gamma_j = \begin{cases} (1 - qZ_B/Z_T)^{-1}, & j = 1 \\ (1 - qZ_L/Z_T)^{-1}, & j = m_n \text{ or } N_n \\ 0 & \text{otherwise,} \end{cases} \quad (4.3.27)$$

$$\delta_j = \begin{cases} -\gamma_1 \zeta Q / (\mu_T \xi), & j = 1 \\ \gamma_{m_n} (\zeta Q / (\mu_T \xi) - 2A_L q Z_L / Z_T), & j = m_n \text{ or } N_n \\ 0 & \text{otherwise,} \end{cases} \quad (4.3.28)$$

Z_B is the mechanical impedance of the backing material, $Z_L = \mu_L A_r / c_L$ is the mechanical impedance of the load, $Z_T = \mu_T A_r / c_T$, $\zeta = e_{24} / \varepsilon_{11}^T$, Q is the electrical charge, $\xi = A_r / h^{(n)}$, A_r is the cross-sectional area of the electrode, A_L is the amplitude of the incoming wave that is received by the transducer (in transmission mode A_L is zero), μ_L is the shear modulus of the load material and c_L is its wave

speed.

Proof. From equation (2.3.57), $U_i = \gamma_j U_j + \delta_j$, $i \in V_{\partial\Omega_n}$, $j \in V_{\partial\Omega_n^o}$, $ji \in E_{\partial\Omega_n}$ and hence, equation (4.3.17) becomes

$$b_j^{(n)} = h^{(n)} \bar{\gamma}_j U_j + h^{(n)} \bar{\delta}_j, \quad j \in V_{\partial\Omega_n^o}. \quad (4.3.29)$$

Putting this equation into equation (4.2.5) gives

$$\hat{A}_{ji}^{(n)} U_i = \bar{\gamma}_j U_j + \bar{\delta}_j.$$

Hence,

$$\left(\hat{A}_{ji}^{(n)} - \hat{B}_{ji}^{(n)} \right) U_i = \bar{\delta}_j.$$

□

4.4 Renormalisation

This section follows a similar derivation as that in Section 2.4 to derive a renormalisation recursion relationship. An iterative procedure can be developed from equation (4.3.16) which can be written as

$$\hat{A}^{(n+1)} = \bar{\hat{A}}^{(n)} + \alpha^{(n+1)} W^{(n+1)} + \beta^{(n+1)} P^{(n+1)}, \quad n \geq 1.$$

Using Theorem 4.3.5 a recursion relationship can be derived that relates the pivotal elements of the matrix $G_{ji}^{(n+1)}$ to those in $G_{ji}^{(n)}$ in a similar fashion to the derivation of equation (2.4.6).

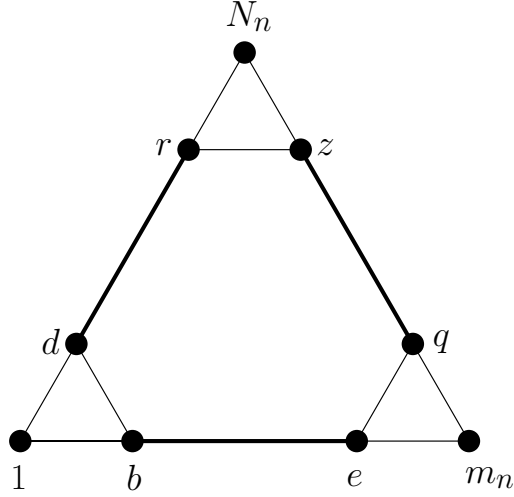


Figure 4.12: Three weighted Sierpinski Gasket graphs of generation level $n - 1$ ($\overline{\text{SG}}^{(n-1)}(3)$) are connected by the edges in bold $((d, r), (b, e)$ and $(q, z))$ to create the weighted Sierpinski Gasket graph at generation level n ($\overline{\text{SG}}^{(n)}(3)$).

Lemma 4.4.1.

$$\hat{G}^{(n+1)} = \bar{G}^{(n)} - \bar{G}^{(n)} (\alpha^{(n+1)} W^{(n+1)} + \beta^{(n+1)} P^{(n+1)}) \hat{G}^{(n+1)} \quad (4.4.1)$$

where $\hat{G}^{(n)} = (\hat{A}^{(n)})^{-1}$ and $\bar{G}^{(n)}$ is a block diagonal matrix consisting of three blocks of matrix $\hat{G}^{(n)}$.

Proof. From equations (4.3.25) and (4.3.27) it is clear that we only need to know the elements of $G_{ji}^{(n)}$ in columns $1, m_n$ and N_n . In addition we will only require elements U_j , $j \in V_{\partial\Omega_n^o}$ and so we only need to be able to calculate the pivotal Green's functions $G_{ji}^{(n)}$, $j, i \in V_{\partial\Omega_n^o}$. If we temporarily ignore matrix \hat{B} in equation (4.3.26) (associated with the application of the boundary conditions) then, due to the symmetries of the weighted $\overline{\text{SG}}$ graph, we have

$$\left(\hat{G}^{(n+1)}\right)^{-1} = \left(\bar{G}^{(n)}\right)^{-1} + \alpha^{(n+1)} W^{(n+1)} + \beta^{(n+1)} P^{(n+1)}.$$

That is

$$\left(\bar{\hat{G}}^{(n)}\right)^{-1} = \left(\hat{G}^{(n+1)}\right)^{-1} - \left(\alpha^{(n+1)}W^{(n+1)} + \beta^{(n+1)}P^{(n+1)}\right).$$

Hence, using the $N_{n \times 1} \times N_{n \times 1}$ identity matrix denoted by I_{n+1} ,

$$\begin{aligned} I_{n+1} &= \bar{\hat{G}}^{(n)} \left(\left(\hat{G}^{(n+1)}\right)^{-1} - \left(\alpha^{(n+1)}W^{(n+1)} + \beta^{(n+1)}P^{(n+1)}\right) \right) \\ &= \bar{\hat{G}}^{(n)} \left(\left(\hat{G}^{(n+1)}\right)^{-1} - \left(\alpha^{(n+1)}W^{(n+1)} + \beta^{(n+1)}P^{(n+1)}\right) \hat{G}^{(n+1)} \left(\hat{G}^{(n+1)}\right)^{-1} \right) \\ &= \bar{\hat{G}}^{(n)} \left(I_{n+1} - \left(\alpha^{(n+1)}W^{(n+1)} + \beta^{(n+1)}P^{(n+1)}\right) \hat{G}^{(n+1)} \right) \left(\hat{G}^{(n+1)}\right)^{-1}. \end{aligned}$$

Hence,

$$\hat{G}^{(n+1)} = \bar{\hat{G}}^{(n)} - \bar{\hat{G}}^{(n)} \left(\alpha^{(n+1)}W^{(n+1)} + \beta^{(n+1)}P^{(n+1)}\right) \hat{G}^{(n+1)}.$$

□

To calculate $G_{ji}^{(n)}$ the boundary conditions must be reintroduced and in fact this is given by equation (2.4.7), which is reproduced here for convenience,

$$G^{(n)} = \hat{G}^{(n)} + \hat{G}^{(n)} \hat{B}^{(n)} G^{(n)}. \quad (4.4.2)$$

4.4.1 Derivation of the pivotal recursion relationships

The renormalisation recursion relationships for the pivotal Green's functions arise from the system of linear equations in $\hat{G}_{ji}^{(n+1)}$. The three subgraphs of Figure 4.12 have a single connection point to one another at the corners and, due to the symmetries of the $\overline{\text{SG}}$ graph, the recursions in equation (4.4.1) give rise to only two pivotal Green's functions, known as, corner-to-same corner ($\hat{G}_{ii}^{(n)} = \hat{x}$, say, where $i \in V_{\partial\Omega_n^2}$) and corner-to-other-corner ($\hat{G}_{jk}^{(n)} = \hat{y}$, say, where $j, k \in V_{\partial\Omega_n^2}$, $j \neq k$); the so called input/output vertices. For ease of notation let, $\hat{X} = \hat{G}_{ii}^{(n+1)}$ and

$\hat{Y} = \hat{G}_{ji}^{(n+1)}$ where $j, i \in V_{\partial\Omega_n^o}$, $i \neq j$. The matrix is symmetrical and consequently, $\hat{G}_{ij}^{(n)} = \hat{G}_{ji}^{(n)}$.

Lemma 4.4.2. *The renormalisation recursion relations for the pivotal Green's functions (ignoring temporarily the boundary conditions) are given by*

$$\hat{X} = \frac{3(\hat{x} - \hat{y})(\hat{x} + 2\hat{y}) + \Delta_1 + \Delta_2}{3(\hat{x} + \hat{y})} \quad (4.4.3)$$

and

$$\hat{Y} = \frac{-\beta^{(n+1)}\hat{y}^2(1 + (\hat{x} - \hat{y})(\alpha^{(n+1)} + \beta^{(n+1)}))}{\delta_1\delta_2} \quad (4.4.4)$$

where $\Delta_1 = 2\hat{y}^2/\delta_1$, $\Delta_2 = 2\hat{y}^2(2 + (\hat{x} - \hat{y})(2\alpha^{(n+1)} + \beta^{(n+1)}))/\delta_2$, $\delta_1 = 1 + (\hat{x} + \hat{y})(\alpha^{(n+1)} + \beta^{(n+1)})$ and $\delta_2 = 1 + 2\hat{x}\alpha^{(n+1)} - \hat{y}\beta^{(n+1)} + (\hat{x}^2 - \hat{y}^2)((\alpha^{(n+1)})^2 - (\beta^{(n+1)})^2)$.

Proof. The $(i, j)^{th}$ element of the matrix equation (4.4.1) can be written as,

$$\hat{G}_{ji}^{(n+1)} = \bar{G}_{ji}^{(n)} - \sum_{h,k} \bar{G}_{jh}^{(n)} \left(\alpha^{(n+1)} W_{hk}^{(n+1)} + \beta^{(n+1)} P_{hk}^{(n+1)} \right) \hat{G}_{ki}^{(n+1)}. \quad (4.4.5)$$

From the definitions of $W_{ji}^{(n)}$ and $P_{ji}^{(n)}$ (see Lemma 4.3.1) since the block diagonal structure implies $\bar{G}_{1h}^{(n)} = 0$ if $h > N_n$, we get

$$\begin{aligned} \hat{G}_{11}^{(n+1)} &= \bar{G}_{11}^{(n)} - \sum_{h,k} \bar{G}_{1h}^{(n)} \left(\alpha^{(n+1)} W_{hk}^{(n+1)} + \beta^{(n+1)} P_{hk}^{(n+1)} \right) \hat{G}_{k1}^{(n+1)} \\ &= \bar{G}_{11}^{(n)} - \left(\bar{G}_{1b}^{(n)} \left(\alpha^{(n+1)} W_{bb}^{(n+1)} \hat{G}_{b1}^{(n+1)} + \beta^{(n+1)} P_{be}^{(n+1)} \hat{G}_{e1}^{(n+1)} \right) \right. \\ &\quad \left. + \bar{G}_{1d}^{(n)} \left(\alpha^{(n+1)} W_{dd}^{(n+1)} \hat{G}_{d1}^{(n+1)} + \beta^{(n+1)} P_{dr}^{(n+1)} \hat{G}_{r1}^{(n+1)} \right) \right) \\ &= \hat{G}_{11}^{(n)} - \left(\hat{G}_{1b}^{(n)} \left(\alpha^{(n+1)} \hat{G}_{b1}^{(n+1)} + \beta^{(n+1)} \hat{G}_{e1}^{(n+1)} \right) \right. \\ &\quad \left. + \hat{G}_{1N}^{(n)} \left(\alpha^{(n+1)} \hat{G}_{b1}^{(n+1)} + \beta^{(n+1)} \hat{G}_{e1}^{(n+1)} \right) \right) \end{aligned}$$

where $be, dr \in E_{\Omega_n}^{(1)}$ and in particular $b = (N_n + 1) / 2 = m_n$, $d = N_n$, $e = N_n + 1$ and $r = 2N_n + 1$. From symmetry ($\hat{G}_{b1}^{(n+1)} = \hat{G}_{d1}^{(n+1)}$, $\hat{G}_{e1}^{(n+1)} = \hat{G}_{r1}^{(n+1)}$), then

$$\hat{X} = \hat{x} - 2\hat{y} \left(\alpha^{(n+1)} \hat{G}_{b1}^{(n+1)} + \beta^{(n+1)} \hat{G}_{e1}^{(n+1)} \right). \quad (4.4.6)$$

Similarly,

$$\begin{aligned} \hat{G}_{b1}^{(n+1)} &= \bar{\bar{G}}_{b1}^{(n)} - \sum_{h,k} \bar{\bar{G}}_{bh}^{(n)} \left(\alpha^{(n+1)} W_{hk}^{(n+1)} + \beta^{(n+1)} P_{hk}^{(n+1)} \right) \hat{G}_{k1}^{(n+1)} \\ &= \bar{\bar{G}}_{b1}^{(n)} - \left(\bar{\bar{G}}_{bb}^{(n)} \left(\alpha^{(n+1)} W_{bb}^{(n+1)} \hat{G}_{b1}^{(n+1)} + \beta^{(n+1)} P_{be}^{(n+1)} \hat{G}_{e1}^{(n+1)} \right) \right. \\ &\quad \left. + \bar{\bar{G}}_{bd}^{(n)} \left(\alpha^{(n+1)} W_{dd}^{(n+1)} \hat{G}_{d1}^{(n+1)} + \beta^{(n+1)} P_{dr}^{(n+1)} \hat{G}_{r1}^{(n+1)} \right) \right) \\ &= \hat{G}_{m_n 1}^{(n)} - \left(\hat{G}_{m_n m_n}^{(n)} \left(\alpha^{(n+1)} \hat{G}_{b1}^{(n+1)} + \beta^{(n+1)} \hat{G}_{e1}^{(n+1)} \right) \right. \\ &\quad \left. + \hat{G}_{m_n N_n}^{(n)} \left(\alpha^{(n+1)} \hat{G}_{b1}^{(n+1)} + \beta^{(n+1)} \hat{G}_{e1}^{(n+1)} \right) \right). \end{aligned}$$

That is

$$\hat{G}_{b1}^{(n+1)} = \hat{y} - \left(\alpha^{(n+1)} \hat{G}_{b1}^{(n+1)} + \beta^{(n+1)} \hat{G}_{e1}^{(n+1)} \right) (\hat{x} + \hat{y}).$$

Hence,

$$\hat{G}_{b1}^{(n+1)} = \frac{\hat{y} - \beta^{(n+1)} \hat{G}_{e1}^{(n+1)} (\hat{x} + \hat{y})}{1 + \alpha^{(n+1)} (\hat{x} + \hat{y})}. \quad (4.4.7)$$

Also

$$\begin{aligned}
\hat{G}_{e1}^{(n+1)} &= \bar{G}_{e1}^{(n)} - \sum_{h,k} \bar{G}_{eh}^{(n)} \left(\alpha^{(n+1)} W_{hk}^{(n+1)} + \beta^{(n+1)} P_{hk}^{(n+1)} \right) \hat{G}_{k1}^{(n+1)} \\
&= -\bar{G}_{ee}^{(n)} \left(\alpha^{(n+1)} W_{ee}^{(n+1)} \hat{G}_{e1}^{(n+1)} + \beta^{(n+1)} P_{eb}^{(n+1)} \hat{G}_{b1}^{(n+1)} \right) \\
&\quad -\bar{G}_{eq}^{(n)} \left(\alpha^{(n+1)} W_{qq}^{(n+1)} \hat{G}_{q1}^{(n+1)} + \beta^{(n+1)} P_{qz}^{(n+1)} \hat{G}_{z1}^{(n+1)} \right) \\
&= -\hat{G}_{11}^{(n)} \left(\alpha^{(n+1)} \hat{G}_{e1}^{(n+1)} + \beta^{(n+1)} \hat{G}_{b1}^{(n+1)} \right) \\
&\quad -\hat{G}_{1N}^{(n)} \left(\alpha^{(n+1)} \hat{G}_{q1}^{(n+1)} + \beta^{(n+1)} \hat{G}_{z1}^{(n+1)} \right)
\end{aligned}$$

where $q = 2N_n$ and $Z = 2N_n + m_n$. Since $\hat{G}_{q1}^{(n+1)} = \hat{G}_{z1}^{(n+1)}$

$$\hat{G}_{e1}^{(n+1)} = -\hat{x}\alpha^{(n+1)}\hat{G}_{e1}^{(n+1)} - \hat{x}\beta^{(n+1)}\hat{G}_{b1}^{(n+1)} - \hat{y}(\alpha^{(n+1)} + \beta^{(n+1)})\hat{G}_{q1}^{(n+1)}.$$

Hence,

$$\hat{G}_{e1}^{(n+1)} = \frac{-\hat{x}\beta^{(n+1)}\hat{G}_{b1}^{(n+1)} - \hat{y}(\alpha^{(n+1)} + \beta^{(n+1)})\hat{G}_{q1}^{(n+1)}}{1 + \hat{x}\alpha^{(n+1)}}. \quad (4.4.8)$$

Finally,

$$\begin{aligned}
\hat{G}_{q1}^{(n+1)} &= \bar{G}_{q1}^{(n)} - \sum_{h,k} \bar{G}_{qh}^{(n)} \left(\alpha^{(n+1)} W_{hk}^{(n+1)} + \beta^{(n+1)} P_{hk}^{(n+1)} \right) \hat{G}_{k1}^{(n+1)} \\
&= -\bar{G}_{qe}^{(n)} \left(\alpha^{(n+1)} W_{ee}^{(n+1)} \hat{G}_{e1}^{(n+1)} + \beta^{(n+1)} P_{eb}^{(n+1)} \hat{G}_{b1}^{(n+1)} \right) \\
&\quad -\bar{G}_{qq}^{(n)} \left(\alpha^{(n+1)} W_{qq}^{(n+1)} \hat{G}_{q1}^{(n+1)} + \beta^{(n+1)} P_{qz}^{(n+1)} \hat{G}_{z1}^{(n+1)} \right) \\
&= -\hat{G}_{N_n 1}^{(n)} \left(\alpha^{(n+1)} \hat{G}_{e1}^{(n+1)} + \beta^{(n+1)} \hat{G}_{b1}^{(n+1)} \right) \\
&\quad -\hat{G}_{N_n N_n}^{(n)} \left(\alpha^{(n+1)} \hat{G}_{q1}^{(n+1)} + \beta^{(n+1)} \hat{G}_{z1}^{(n+1)} \right).
\end{aligned}$$

That is

$$\hat{G}_{q1}^{(n+1)} = -\hat{y} \left(\alpha^{(n+1)} \hat{G}_{e1}^{(n+1)} + \beta^{(n+1)} \hat{G}_{b1}^{(n+1)} \right) - \hat{x} (\alpha^{(n+1)} + \beta^{(n+1)}) \hat{G}_{q1}^{(n+1)}.$$

Hence,

$$\hat{G}_{q1}^{(n+1)} = \frac{-\hat{y} \left(\alpha^{(n+1)} \hat{G}_{e1}^{(n+1)} + \beta^{(n+1)} \hat{G}_{b1}^{(n+1)} \right)}{1 + \hat{x} (\alpha^{(n+1)} + \beta^{(n+1)})}. \quad (4.4.9)$$

Equations (4.4.6), (4.4.7), (4.4.8) and (4.4.9) provide four equations in the four unknowns \hat{X} , $\hat{G}_{b1}^{(n+1)}$, $\hat{G}_{e1}^{(n+1)}$ and $\hat{G}_{q1}^{(n+1)}$. Rearranging these equations gives (using Mathematica [150])

$$\hat{X} = \frac{3(\hat{x} - \hat{y})(\hat{x} + 2\hat{y}) + \Delta_1 + \Delta_2}{3(\hat{x} + \hat{y})}.$$

Also

$$\hat{G}_{b1}^{(n+1)} = \frac{\hat{y} \left(1 + \alpha^{(n+1)} (\hat{x}^2 - \hat{y}^2) (\alpha^{(n+1)} + \beta^{(n+1)}) + \hat{x} (2\alpha^{(n+1)} + \beta^{(n+1)}) \right)}{\delta_1 \delta_2}, \quad (4.4.10)$$

$$\hat{G}_{e1}^{(n+1)} = \frac{-\hat{y} \beta^{(n+1)} (\hat{x} + (\hat{x}^2 - \hat{y}^2) (\alpha^{(n+1)} + \beta^{(n+1)}))}{\delta_1 \delta_2}, \quad (4.4.11)$$

and

$$\hat{G}_{q1}^{(n+1)} = \frac{-\hat{y}^2 \beta^{(n+1)}}{\delta_1 \delta_2}. \quad (4.4.12)$$

Now, for $\hat{Y} = \hat{G}_{s1}^{(n+1)}$, where $s = m_{n+1}$, equation (4.4.5) gives

$$\begin{aligned} \hat{G}_{s1}^{(n+1)} &= \bar{\bar{G}}_{s1}^{(n)} - \sum_{h,k} \bar{\bar{G}}_{sh}^{(n)} \left(\alpha^{(n+1)} W_{hk}^{(n+1)} + \beta^{(n+1)} P_{hk}^{(n+1)} \right) \hat{G}_{k1}^{(n+1)} \\ &= -\bar{\bar{G}}_{se}^{(n)} \left(\alpha^{(n+1)} W_{ee}^{(n+1)} \hat{G}_{e1}^{(n+1)} + \beta^{(n+1)} P_{eb}^{(n+1)} \hat{G}_{b1}^{(n+1)} \right) \\ &\quad - \bar{\bar{G}}_{sq}^{(n)} \left(\alpha^{(n+1)} W_{qq}^{(n+1)} \hat{G}_{q1}^{(n+1)} + \beta^{(n+1)} P_{qz}^{(n+1)} \hat{G}_{z1}^{(n+1)} \right) \\ &= -\bar{\bar{G}}_{m_n 1}^{(n)} \left(\alpha^{(n+1)} \hat{G}_{e1}^{(n+1)} + \beta^{(n+1)} \hat{G}_{b1}^{(n+1)} \right) \\ &\quad - \bar{\bar{G}}_{m_n N_n}^{(n)} \left(\alpha^{(n+1)} \hat{G}_{q1}^{(n+1)} + \beta^{(n+1)} \hat{G}_{q1}^{(n+1)} \right) \end{aligned}$$

since $\hat{G}_{z1}^{(n+1)} = \hat{G}_{q1}^{(n+1)}$, $\hat{G}_{se}^{(n)} = \hat{G}_{m1}^{(n)}$ and $\hat{G}_{sq}^{(n)} = \hat{G}_{m_n N_n}^{(n)}$. Hence,

$$\hat{Y} = -\hat{y} \left(\alpha^{(n+1)} \hat{G}_{e1}^{(n+1)} + \beta^{(n+1)} \hat{G}_{b1}^{(n+1)} \right) - \hat{y} \left(\alpha^{(n+1)} + \beta^{(n+1)} \right) \hat{G}_{q1}^{(n+1)}. \quad (4.4.13)$$

Putting equations (4.4.10), (4.4.11) and (4.4.12) into this equation gives

$$\hat{Y} = \frac{-\beta^{(n+1)} \hat{y}^2 \left(1 + (\hat{x} - \hat{y}) \left(\alpha^{(n+1)} + \beta^{(n+1)} \right) \right)}{\delta_1 \delta_2}.$$

□

The boundary conditions can now be considered and in fact we recover equations (2.4.23) to (2.4.26). The recursion relationships (4.4.3) and (4.4.4) require initial values for \hat{x} and \hat{y} . To obtain these the matrix $\hat{A}^{(1)}$ is formed from equation (4.2.8) where $H^{(1)}$ is given by inserting $n = 1$ into equations (4.3.5), (4.3.6) and (4.3.7), and $K^{(1)}$ from equations (4.3.12), (4.3.13) and (4.3.14). It transpires that $\hat{A}_{ii}^{(1)} = 36 + q^2$ where $i = 1, 2, 3$ and $\hat{A}_{ji}^{(1)} = 2 + (q^2/6)$ where $j, i = 1, 2, 3$ and $j \neq i$. Hence $\hat{x} = \hat{G}_{11}^{(1)} = ((\hat{A}^{(1)})^{-1})_{11}$ and $\hat{y} = \hat{G}_{12}^{(1)} = ((\hat{A}^{(1)})^{-1})_{12}$.

4.5 Electrical impedance and transmission and reception sensitivities

The derivation of the operating characteristics of the device follows similar lines as presented in Sections 2.5 and 2.6. In this chapter, note that we have one η represented in equation (4.3.17), so this can be related with Chapter 2 as $\eta_1^{(n)} = \eta_m^{(n)} = \eta$. Hence, the non-dimensionalised electrical impedance (\hat{Z}_E) is given by

$$\hat{Z}_E(f; n) = \frac{Z_E}{Z_0} = \frac{Z_T}{C_0 q \mu_T \xi Z_0} \left(1 + \frac{\zeta^2 C_0 \eta}{\mu_T \xi} (\sigma_1 + \sigma_2) \right) \quad (4.5.1)$$

where

$$\sigma_1 = \gamma_1 \left(G_{N_n 1}^{(n)} - G_{11}^{(n)} \right) \quad \text{and} \quad \sigma_2 = \gamma_{m_n} \left(-G_{N_n m_n}^{(n)} - G_{N_n N_n}^{(n)} + 2G_{1m_n}^{(n)} \right).$$

The non-dimensionalised transmission sensitivity ψ_F is given by

$$\psi_F(f; n) = \frac{F_F}{V} \left(\frac{1}{\zeta C_0} \right) = \frac{aZ_L}{(Z_E + b)\mu_T \xi C_0} K^{(n)}, \quad (4.5.2)$$

where

$$K^{(n)} = \gamma_{m_n} \left(-\eta \left(\gamma_1 G_{m_n 1}^{(n)} - \gamma_{m_n} \left(G_{m_n m_n}^{(n)} + G_{m_n N_n}^{(n)} \right) \right) + 1 \right).$$

The non-dimensionalised reception sensitivity ϕ_F is given by

$$\begin{aligned} \phi_F(f; n) &= \frac{V_F}{F} (e_{24} L) \\ &= \frac{2\zeta e_{24} L \eta \sigma_2}{\xi \mu_T} \left(1 - \frac{aZ_T \zeta^2 \eta (\sigma_1 + \sigma_2)}{(Z_E + b) q \mu_T^2 \xi^2} - \frac{aZ_T}{(Z_E + b) q \mu_T \xi C_0} \right)^{-1} \end{aligned} \quad (4.5.3)$$

These expressions can be compared with the non-dimensionalised form for the electrical impedance ($\bar{Z}_E(f)$), transmission (ψ_E) and reception (ψ_E) sensitivities of the standard (Euclidean) transducer that are given by equations (2.5.8), (2.5.15) and (2.6.4), respectively.

4.6 Results

As in Sections 2.8 and 3.7 we can compare the fractal design with a conventional standard (Euclidean) design in terms of the key operating characteristics. As before, the presence of higher amplitudes, multiple resonances, and improved bandwidth are the key performance indicators of interest in this section. A careful examination of the transmission and reception sensitivities of the fractal device as

the fractal generation level is increased has been performed. However, to keep the presentation here succinct and to produce results that are pertinent to devices that can be physically produced, we will focus on fractal generation level $n = 3$. From a practical perspective, these fractal transducers will only be able to be manufactured at low fractal generation levels. To perform a fair comparison, the volume of piezoelectric material in the standard (Euclidean) design (vol_E) and fractal design (vol_F) are kept consistent. The volume of the piezoelectric material in the standard (Euclidean) design is $vol_E = L^2 d_E = LA_E$, where L is the length of the front face (see Figure 4.13), d_E is the thickness and A_E is the area occupied by the electrode. The volume of the piezoelectric material in the fractal design is $vol_F = S_n d_F$, where S_n is the area of the front face of the fractal piezoelectric design at generation level n (the black area in Figure 4.14) and d_F is the thickness. The area of each level n triangle is $\sqrt{3}L^2/4^{n+1}$ and there are 3^{n-1} of them. Therefore the area S_n is then given by $S_n = \sqrt{3}L^2(1 - (3/4)^{n+1})/4$ and equating vol_E and vol_F gives $d_F = L^2 d_E / S_n$. The fractal transducer has one electrode of area $A'_F = d_F h^{(n)}$ at one face and two electrodes of area A'_F each on the opposite face (see Figure 4.14). As the device operates essentially as a capacitor in this circuit, and since the total capacitance of two capacitors in parallel is just the sum of those two capacitances, then we take the total area to be $A_F = 2A'_F$. Hence, $A_F = 2d_F h^{(n)} = 2d_F L / 2^n$, and we define the design ratio to be $\xi = 2d_F$. So by choosing a particular value for the design ratio ξ , the fractal generation level n , the thickness d_E and the length L , this sets d_F , which in turn sets A_E , A_F and the volume of piezoelectric material. As the sensitivity of a device is very much dictated by the volume of piezoelectric material then this is why we have chosen to keep this identical in both the fractal and Euclidean designs. In the results shown here we have chosen to keep the sidelengths of the two transducers equal and this results in the surface area of the

fractal device being smaller than that of the Euclidean device and the thickness of the fractal device being larger than the Euclidean device. There is an alternative design route whereby we could adjust the sidelengths of the fractal device to be larger than the Euclidean device in such a way that the volumes, surface areas, and thicknesses are equal for both devices. When one examines this second scenario one finds that the sensitivity plots are very similar. A typical profile of the

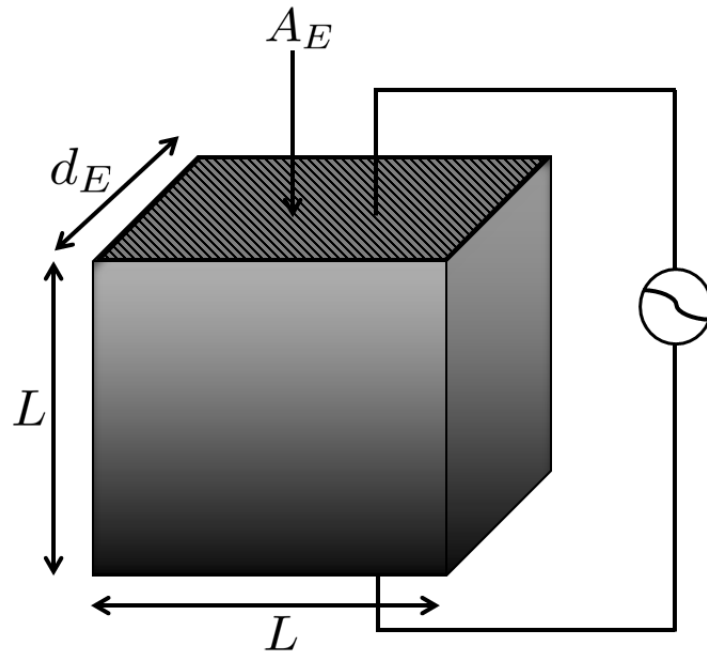


Figure 4.13: Volume of the standard (Euclidean) transducer (vol_E).

electrical impedance spectrum (magnitude) given by equation (4.5.1) is shown in Figure 4.15 ($n = 3$) (dashed line); it is compared to the equivalent profile given by a model of the standard (Euclidean) design given by equation (2.5.8) (full line). The overall trend of the curve is that of a capacitor ($1/(C_0 f)$ profile where C_0 is the transducer capacitance and f is the frequency) with prominent resonances. From the above analysis $A_E = \sqrt{3}(1 - (3/4)^{n+1})2^{n-3}A_F$ and the coefficient of A_F is monotonically increasing as a function of the fractal generation level n and is greater than one for all $n \geq 3$. Hence, reasonable values of n , $A_E \gg A_F$. Since

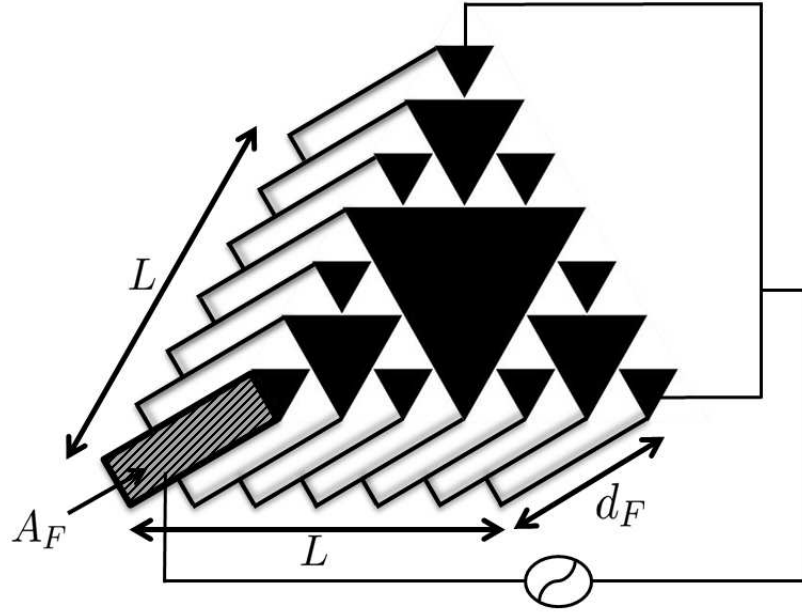


Figure 4.14: A three-dimensional schematic of the Sierpinski Gasket ultrasonic transducer at fractal generation level $n = 2$. The black triangles are the front faces of the piezoelectric material. The device is connected to an electrical circuit as shown where each electrode has surface area A_F .

$C_0 = A_{E/F} \varepsilon_{11}^T / L$ then $C_{0E} \gg C_{0F}$ (where $C_{0E/F}$ is the transducer capacitance in the E -standard (Euclidean) / F -fractal design) and so $1/(C_{0E}f) \ll 1/(C_{0F}f)$. Since the standard (Euclidean) design has a larger capacitance then this explains why its electrical impedance is in general lower (see the discussion in Section 2.8.1). It can be seen in Figure 4.15, for the standard (Euclidean) design (full line), the mechanical resonance $f_r = 0.9$ MHz and the electrical resonance $f_a = 1.2$ MHz. These frequencies correspond of course to the first maximum in the transmission sensitivity plot (Figure 4.16, full line) and the reception sensitivity plot (Figure 4.17, full line). As in Section 2.8.1 $f_a = c_T/(2L) = 1.2$ MHz which agrees with the reception sensitivity maximum for the homogenised estimate for f_a (the full line in Figure 4.15). For the fractal design the electrical impedance resonance frequencies are much higher ($f_r^{(3)} = 4.2$ MHz and $f_a^{(3)} = 4.3$ MHz) as the edge

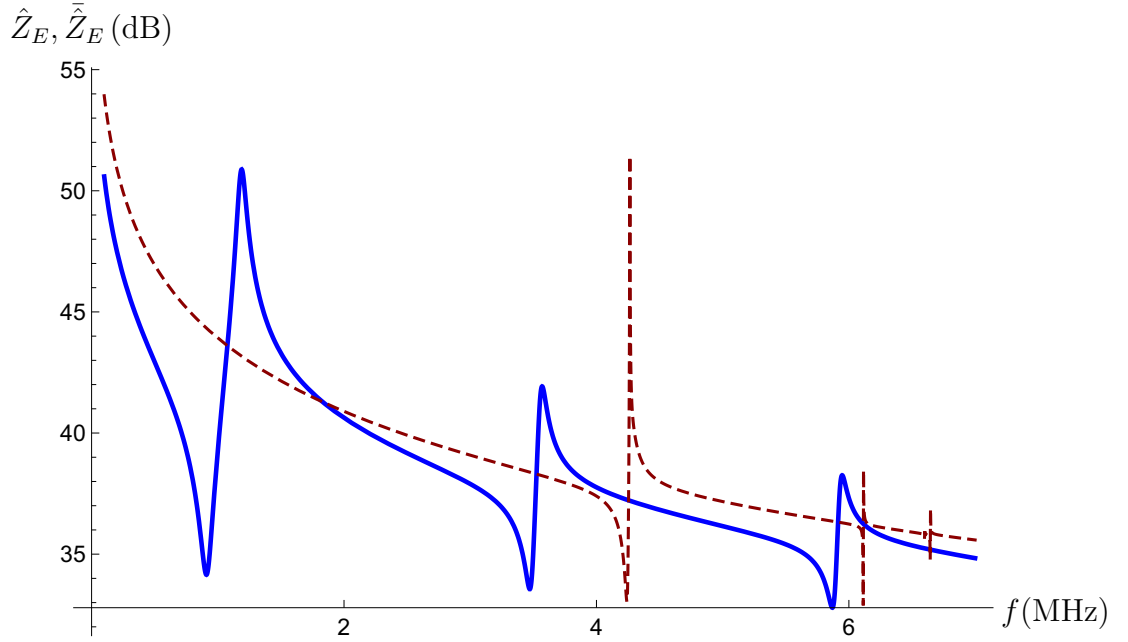


Figure 4.15: Non-dimensionalised electrical impedance (equation (4.5.1)) versus frequency for the $\overline{\text{SG}}(3)$ transducer (\hat{Z}_E) at fractal generation level $n = 3$ (dashed line). The non-dimensionalised electrical impedance of the standard (Euclidean) transducer (\tilde{Z}_E) (equation (2.5.8)) is plotted for comparison (full line). Parameter values are given in Appendix A.5.

lengths in the graph are shorter in the dual graph. Importantly, the magnitude of the electrical impedance at the electrical resonance frequency is lower than the standard (Euclidean) design; there is about a 2 dB drop. As there is no damping mechanism in the model, and no backing or matching layers, the values of the electrical impedance at the resonances do, to some extent, depend on the spatial resolution used when plotting. Figure 4.16 shows that the transmission sensitivity of the fractal design has a maximum amplitude (gain) that is higher than the Euclidean case (standard design) at its lower operating frequency (37 dB at 4.2 MHz compared to 32 dB at 3.5 MHz for the Euclidean case). If we take the noise floor to be 3 dB below the peak gain of the standard (Euclidean) design (that is the 29 dB level in this plot) then the operational bandwidth of the standard (Euclidean) design is 0.2 MHz whereas the fractal design has an operational bandwidth of around

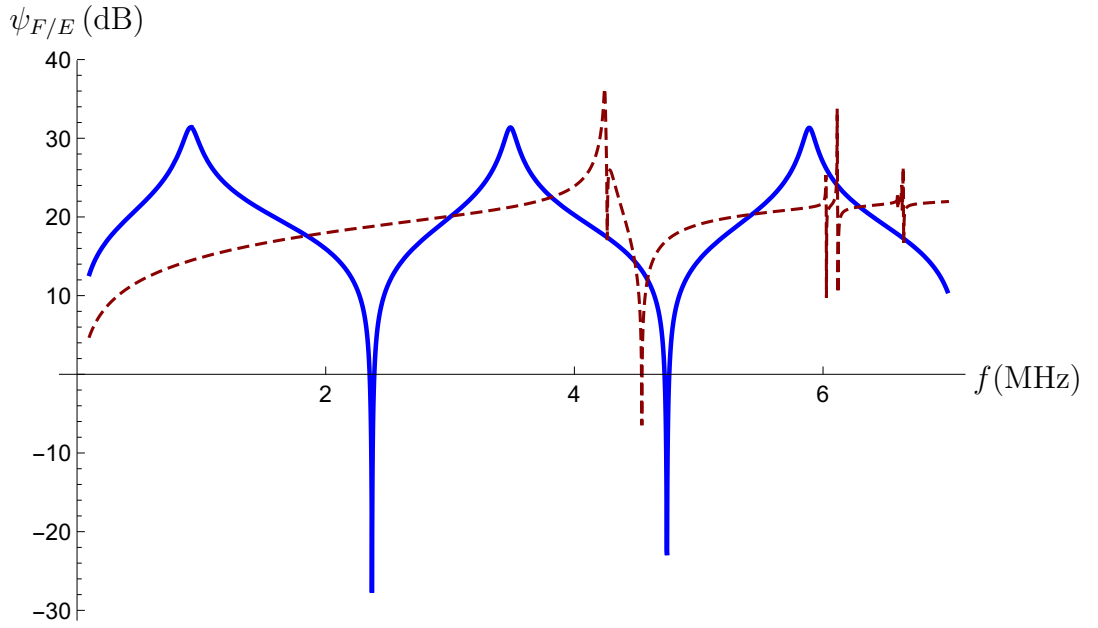


Figure 4.16: Non-dimensionalised transmission sensitivity (equation (4.5.2)) versus frequency for the $\overline{\text{SG}}(3)$ transducer (ψ_F) at fractal generation level $n = 3$ (dashed line). The non-dimensionalised transmission sensitivity of the standard (Euclidean) transducer (ψ_E) (equation (2.5.15)) is plotted for comparison (full line). Parameter values are given in Appendix A.5.

0.1 MHz. Figure 4.17 shows that the reception sensitivity spectrum has a much larger gain; there is a 18 dB improvement in the reception sensitivity gain from the standard (Euclidean) design to the fractal design. This peak in the reception sensitivity also results in an enhanced bandwidth; if we take the noise floor to be 3 dB below the peak gain of the standard (Euclidean) design (that is the 14 dB level in this plot) then the operational bandwidth of the standard (Euclidean) design is 0.2 MHz whereas the fractal design has an operational bandwidth of around 3.2 MHz.

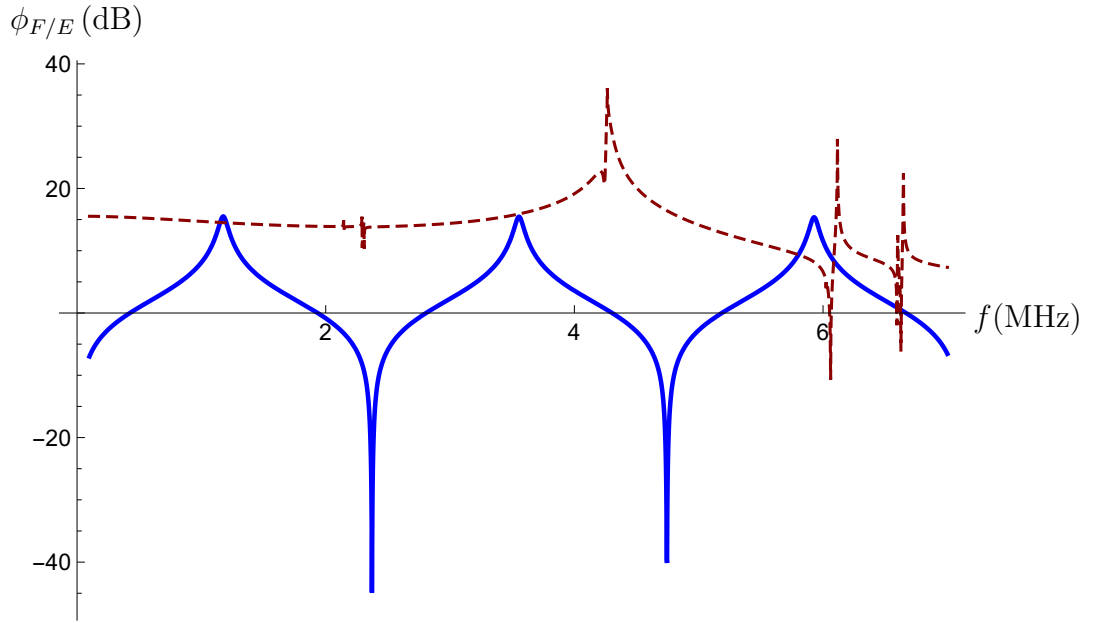


Figure 4.17: Non-dimensionalised reception sensitivity (equation (4.5.3)) versus frequency for the $\overline{\text{SG}}(3)$ transducer (ϕ_F) at fractal generation level $n = 3$ (dashed line). The non-dimensionalised reception sensitivity of the standard (Euclidean) transducer (ϕ_E) (equation (2.6.4)) is plotted for comparison (full line). Parameter values are given in Appendix A.5.

Design	f_r (MHz)	f_a (MHz)	ψ_{max} (dB)	ϕ_{max} (dB)	BW_T (MHz)	BW_R (MHz)
Fractal (F)	4.2	4.3	37.0	35.0	0.1	3.2
Standard (E)	0.9	1.2	32.0	17.0	0.2	0.2

Table 4.1: A comparison between the operating characteristics of a fractal transducer and an equivalent standard design at fractal generation level $n = 3$. The mechanical resonance frequency is denoted by f_r (MHz), the electrical resonance frequency is denoted by f_a (MHz), the transmission sensitivity gain is denoted by ψ_{max} (dB), the reception sensitivity gain is denoted by ϕ_{max} (dB), the transmission sensitivity bandwidth is denoted by BW_T (MHz) and the reception sensitivity bandwidth is denoted by BW_R (MHz).

4.6.1 Convergence

A careful study of the non-dimensionalised electrical impedance, transmission sensitivity and reception sensitivity spectra show that more resonances appear as

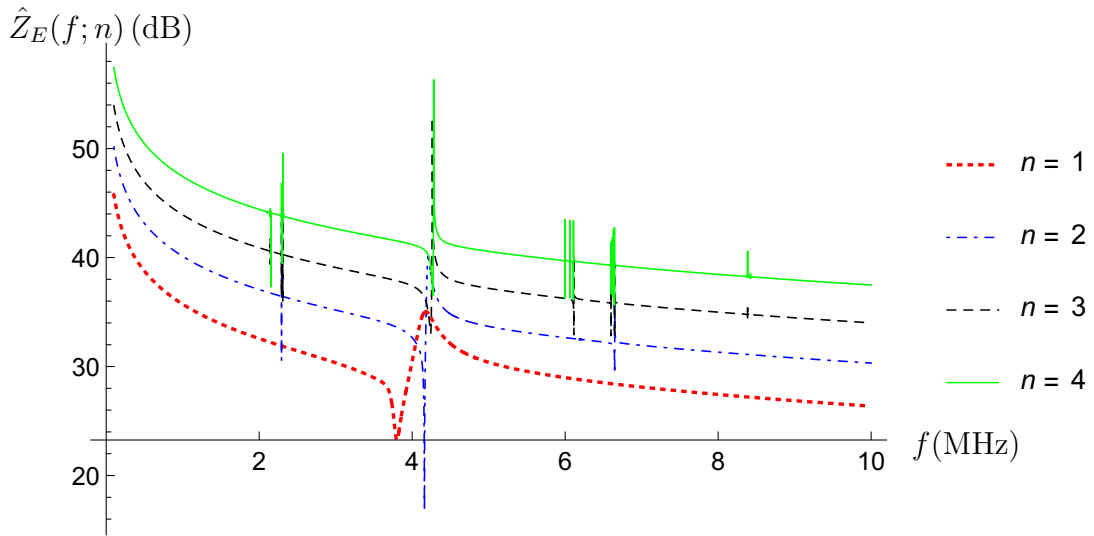


Figure 4.18: The convergence of the non-dimensionalised electrical impedance (equation (4.5.1)) versus frequency for the $\overline{SG}(3)$ graph transducer for fractal generation level $n = 1, 2, 3$ and 4.

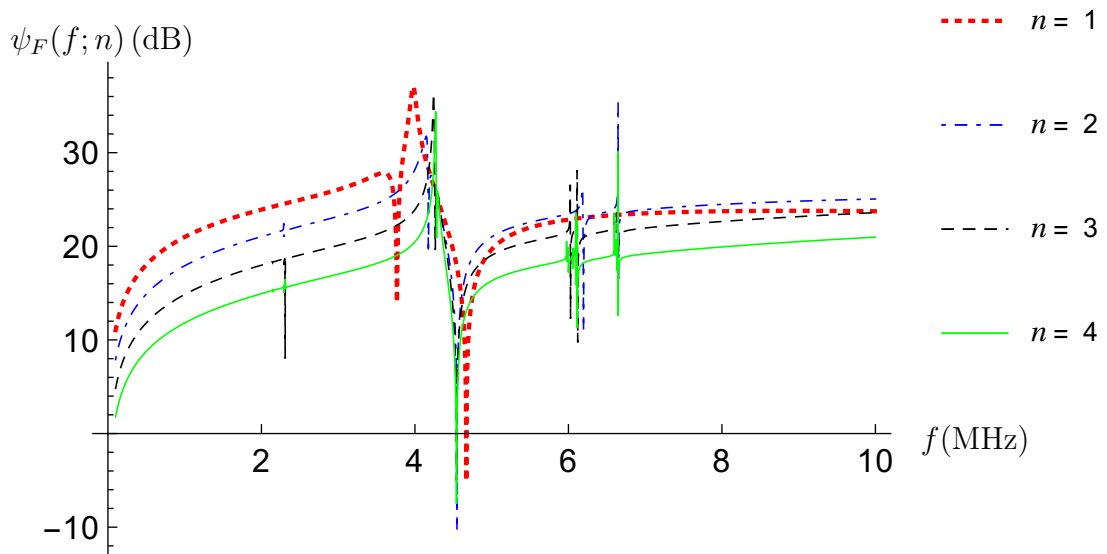


Figure 4.19: The convergence of the non-dimensionalised transmission sensitivity (equation (4.5.2)) versus frequency for the $\overline{SG}(3)$ graph transducer for fractal generation level $n = 1, 2, 3$ and 4.

the fractal generation level increases (see Figures 4.18, 4.19 and 4.20). So far we have examined the performance of the pre-fractal transducer since such a design could be manufactured. From a mathematical perspective it would be of interest

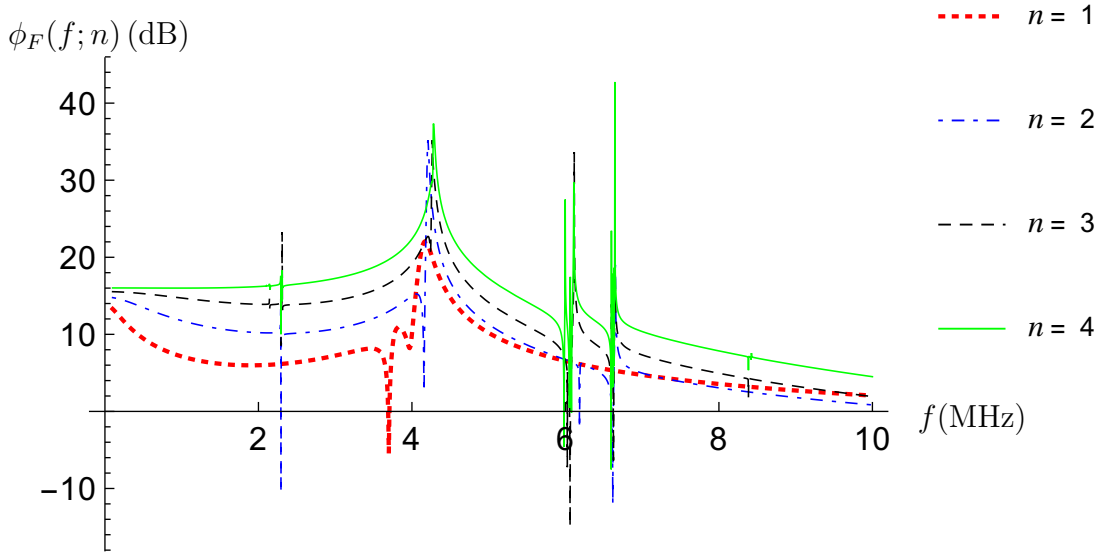


Figure 4.20: The convergence of the non-dimensionalised reception sensitivity (equation (4.5.3)) versus frequency for the $\overline{SG}(3)$ graph transducer for fractal generation level $n = 1, 2, 3$ and 4.

to examine the fractal design whereby the number of generation levels tends to infinity. Such an investigation would of course rely on the renormalisation recursion relationships given by equations (4.4.3) and (4.4.4) having steady state solutions. To empirically assess whether or not such solutions exist one can plot the output from the model as a function of the fractal generation level. Similar to Section 2.8.2, the norm of the difference between the energy in the power spectrum at successive generation levels, integrated with respect to frequency, can be calculated for the transmission/reception sensitivities. Figure 4.21 shows the dependence of these norms on the generation level. Scrutiny of the underlying spectra shows that the transmission sensitivity accrues more and more resonances as the fractal generation n increases. As the length scale of the smallest edge is decreasing with n then resonances at higher frequencies appear; note that the lack of damping in the model permits these resonances to have amplitudes which would not be present in an experimental setting. As n is increased further, then the various

peaks become quite dense and a very flat response emerges which does not change over the frequency range of interest (up to 10MHz). Hence, the successive spectra start to reach a steady state and this accounts for the steady state that is reached after $n = 6$. A similar story holds for the reception sensitivity.

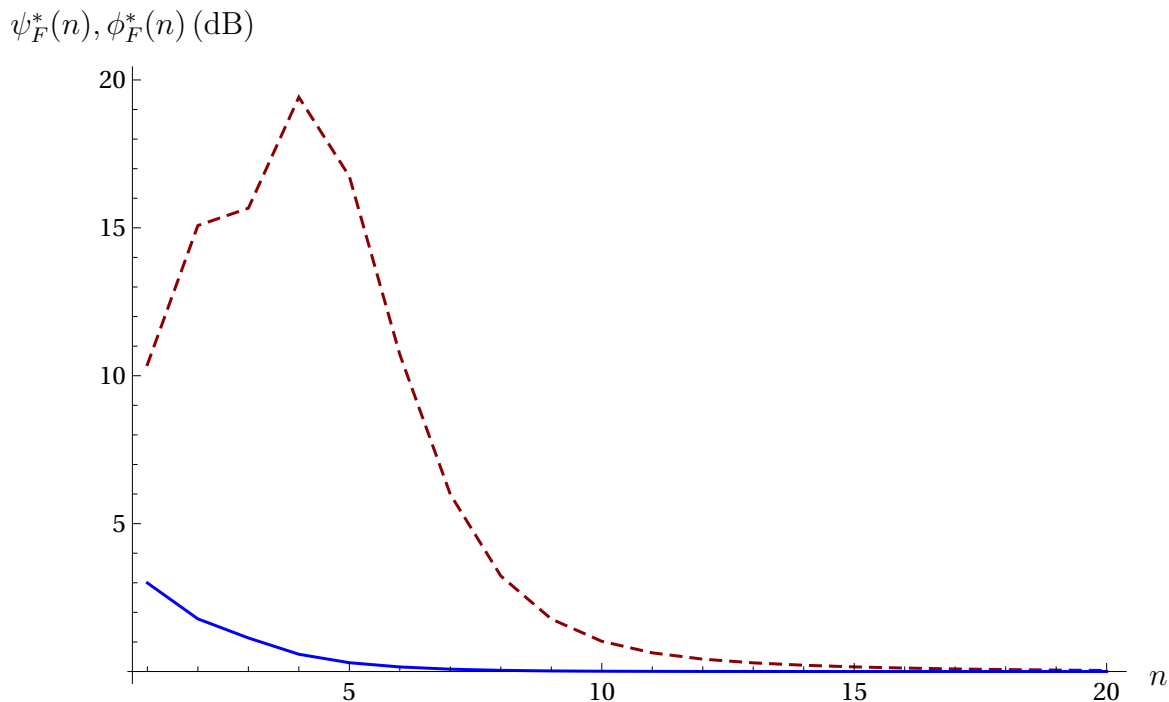


Figure 4.21: The convergence of the transmission and reception sensitivities is examined by plotting the differences in the energies in successive spectra as the fractal generation level increases. Non-dimensionalised transmission sensitivity ($\psi_F^*(n)$) (equation (2.8.1)) (full line) and non-dimensionalised reception sensitivity ($\phi_F^*(n)$) (equation (2.8.2)) (dashed line) versus the fractal generation level. The transmission sensitivity converges by generation level $n = 6$ and the reception sensitivity by generation level $n = 15$, over this frequency range where $f_i \in [0.1, 10]$ MHz.

4.7 Conclusions

The fractal that was used to simulate the self-similar transducer in this chapter was the Sierpinski gasket (or rather its complement) [144]. The weighted graph counterpart of this fractal (denoted $\overline{\text{SG}}(3)$) [145] was used to express the electrical and mechanical fields in terms of a finite element methodology [7]. The finite ele-

ment analysis required yet another set of new basis functions. The fractal design has multiple length scales (the standard (Euclidean) design typically has a single length scale) and, since these are resonating devices, this resulted in a rich set of resonating frequencies. The finite element formulation yielded again to a renormalisation approach and two coupled recursion relationships for the pivotal Green's functions drove the calculation of the transmission and reception sensitivities of the device. The results showed that this pre-fractal transducer resonates at more frequencies than the standard (Euclidean) transducer. Importantly, the fractal transducer gave rise to significantly higher amplitude transmission and reception sensitivities than the standard (Euclidean) design, a 5 dB increase in transmission mode and a 18 dB increase in reception mode. The reception sensitivity also resulted in a wider bandwidth than the standard (Euclidean) design; a 3 MHz increase. The convergence of the fractal device's performance as the fractal generation level increases was also considered. It was seen that, in both transmission and reception modes, the outputs converge by generation level $n = 6$ and $n = 15$ respectively.

Chapter 5

Conclusion

5.1 Aim

The aim of this PhD thesis was to investigate the benefits of fractal geometry in ultrasound transducer design. Three designs for a fractal ultrasound transducer were constructed and compared to a standard design. The two fractals that were used in these self-similar transducers were the Sierpinski gasket and its complement.

5.2 Motivation

The graph counterpart of the Sierpinski gasket was used to express the electrical and mechanical fields in terms of a finite element methodology. This is the first time that ultrasound wave propagation in a fractal structure has been modelled using a finite element analysis and so this required new basis functions. The standard design has a single length scale whereas the fractal design has multiple length scales, and since these are resonating devices, this resulted in a rich set of resonating frequencies. Indeed the broadband resonators found in nature and in musical instruments depend on this principle. The finite element formulation

resulted in a matrix equation whose solution yielded to a renormalisation approach. This is turn led to a small set of recursion relationships for the pivotal Green's functions that drive the calculation of the transmission and reception sensitivities of the devices. The focus was on low fractal generation levels as these are most relevant to manufacturing constraints.

5.3 Results

In Chapter 2, we compared the operational qualities of a fractal transducer with that of a standard transducer, and showed that the fractal transducer resonates at many more frequencies than the standard transducer. Importantly, at certain generation levels the fractal transducer gave rise to a significantly higher amplitude transmission and reception sensitivity than the standard design. At fractal generation level $n = 3$, the transmission sensitivity spectrum had a 15 dB gain improvement; from 28 dB in the standard transducer to around 43 dB in the fractal transducer. However the bandwidth around this peak sensitivity was smaller than that of the standard (Euclidean) case. The fractal device's performance converged in both transmission and reception modes as the fractal generation level increased to around $n = 10$ and $n = 16$ respectively. Note that it was not possible to compare the results here to the previously conducted finite difference modelling [19] as this studied the in-plane vibrations of the device rather than the out-of-plane (thickness direction) vibrations studied here.

In Chapter 3, we had a more realistic fractal transducer design that used a combination of ceramic and polymer elements. At fractal generation level $n = 6$, we showed that a significantly higher amplitude reception sensitivity was produced by

the fractal transducer when compared to the standard design; note however that a lower transmission sensitivity amplitude resulted. The reception sensitivity also resulted in a wider bandwidth than the standard design. The fractal device's performance converged again in both transmission and reception modes as the fractal generation level increased to around $n = 10$ and $n = 5$ respectively.

In Chapter 4, a comparison between the operating characteristics of the complement of the Sierpinski gasket fractal transducer and an equivalent standard transducer, showed that as before, the model predicts that the fractal transducer has more resonance frequencies. Indeed, this appears to be the first investigation of this particular fractal. Furthermore, the fractal transducer also resulted in a higher amplitude (or gain) in transmission and reception sensitivities than the standard design; a 5 dB increase in transmission mode and around a 18 dB increase in reception mode. The reception sensitivity also produced a wider bandwidth than the standard design; a 3 MHz increase. However, the standard design produced a wider bandwidth than the fractal design. The fractal device's performance converged once again in the transmission and reception modes as the fractal generation level increased.

Fractal Device	f_r (MHz)	f_a (MHz)	ψ_{max} (dB)	ϕ_{max} (dB)	BW_T (MHz)	BW_R (MHz)
SG(3) at $n = 3$	2.2	2.3	43.0	25.0	0.07	0.11
SG(3,4) at $n = 6$	1.2	2.0	26.0	14.0	0.5	3.0
$\overline{SG}(3)$ at $n = 3$	4.2	4.3	37.0	35.0	0.1	3.2

Table 5.1: A comparison between the operating characteristics of the different fractal transducers, which are a fractal ultrasonic transducer based on the Sierpinski gasket SG(3) at fractal generation level $n = 3$ (Chapter 2), a fractal ultrasonic transducer based on the Sierpinski gasket with both piezoelectric and polymer phases SG(3,4) at fractal generation level $n = 6$ (Chapter 3) and a fractal ultrasonic transducer based on the complement of the Sierpinski gasket $\overline{SG}(3)$ at fractal generation level $n = 3$ (Chapter 4). The mechanical resonance frequency is denoted by f_r (MHz), the electrical resonance frequency is denoted by f_a (MHz), the transmission sensitivity gain is denoted by ψ_{max} (dB), the reception sensitivity gain is denoted by ϕ_{max} (dB), the transmission sensitivity bandwidth is denoted by BW_T (MHz) and the reception sensitivity bandwidth is denoted by BW_R (MHz).

A comparison between the different transducer designs in this thesis can be performed. The fractal generation level of each transducer has been chosen to produce the best results for that design. As shown in the Table 5.1 the SG(3) transducer produces the highest peak transmission sensitivity (43 dB). The $\overline{SG}(3)$ fractal transducer produced the highest amplitude (35 dB) in reception sensitivity and the widest bandwidth (3.2 MHz). The SG(3,4) fractal transducer also generated the broadest bandwidth (0.5 MHz) in transmission mode.

5.4 Further work

The positive results in this theoretical work have subsequently led to engineers manufacturing these fractal devices [154]. One area of future work could involve a comparison between the theoretical results presented here and these experimental findings. These encouraging results suggest that it will be worthwhile studying other fractal designs. Some work in this direction has been recently undertaken by other authors [155].

Appendix A

Appendix

A.1 Geometrical and basis function details for fractal generation levels of the SG(3) graph

j	(x_j, y_j)	Adjacent vertices to (x_j, y_j)		
		(x_{j+1}, y_{j+1})	(x_{j+2}, y_{j+2})	(x_{j+3}, y_{j+3})
1	$(0, 0)$	A	2	3
2	$(h, 0)$	1	3	B
3	$(\frac{h}{2}, \frac{\sqrt{3}}{2}h)$	1	2	C
A	$(-h, 0)$	1		
B	$(2h, 0)$	2		
C	$(h, \sqrt{3}h)$	3		

Table A.1: Coordinates of the vertices and a list of the adjacent vertices to vertex (x_j, y_j) for fractal generation level $n = 1$ of the SG(3) graph. The vertex labelling is given in Figure 2.4.

j	(x_j, y_j)	Adjacent vertices to (x_j, y_j)		
		(x_{j+1}, y_{j+1})	(x_{j+2}, y_{j+2})	(x_{j+3}, y_{j+3})
1	$(0, 0)$	A	2	3
2	$(h, 0)$	1	3	4
3	$(\frac{h}{2}, \frac{\sqrt{3}}{2}h)$	1	2	7
4	$(2h, 0)$	2	5	6
5	$(3h, 0)$	4	6	B
6	$(\frac{5h}{2}, \frac{\sqrt{3}}{2}h)$	4	5	8
7	$(h, \sqrt{3}h)$	3	8	9
8	$(2h, \sqrt{3}h)$	6	7	9
9	$(\frac{3h}{2}, \frac{3\sqrt{3}}{2}h)$	7	8	C
A	$(-h, 0)$	1		
B	$(4h, 0)$	5		
C	$(2h, 2\sqrt{3}h)$	9		

Table A.2: Coordinates of the vertices and a list of the adjacent vertices to vertex (x_j, y_j) for fractal generation level $n = 2$ of the SG(3) graph. The vertex labelling is given in Figure 2.5.

j	a	b	c	d
1	1	0	0	$-\frac{1}{h^2}$
2	0	$\frac{2}{h}$	0	$-\frac{1}{h^2}$
3	0	$\frac{1}{h}$	$\frac{\sqrt{3}}{h}$	$-\frac{1}{h^2}$
A	0			$\frac{1}{h^2}$
B	$-\frac{1}{3}$			$\frac{1}{3h^2}$
C	$-\frac{1}{3}$			$\frac{1}{3h^2}$

Table A.3: Coefficients of the basis functions ϕ_j for fractal generation level $n = 1$ of the SG(3) graph.

j	a	b	c	d
1	1	0	0	$-\frac{1}{h^2}$
2	0	$\frac{2}{h}$	0	$-\frac{1}{h^2}$
3	0	$\frac{1}{h}$	$\frac{\sqrt{3}}{h}$	$-\frac{1}{h^2}$
4	-3	$\frac{4}{h}$	0	$-\frac{1}{h^2}$
5	-8	$\frac{6}{h}$	0	$-\frac{1}{h^2}$
6	-6	$\frac{5}{h}$	$\frac{\sqrt{3}}{h}$	$-\frac{1}{h^2}$
7	-3	$\frac{2}{h}$	$\frac{2\sqrt{3}}{h}$	$-\frac{1}{h^2}$
8	-6	$\frac{4}{h}$	$\frac{2\sqrt{3}}{h}$	$-\frac{1}{h^2}$
9	-8	$\frac{3}{h}$	$\frac{3\sqrt{3}}{h}$	$-\frac{1}{h^2}$
A	0			$\frac{1}{h^2}$
B	$-\frac{9}{7}$			$\frac{1}{7h^2}$
C	$-\frac{9}{7}$			$\frac{1}{7h^2}$

Table A.4: Coefficients of the basis functions ϕ_j for fractal generation level $n = 2$ of the SG(3) graph.

A.2 Geometrical and basis function details for fractal generation levels of the SG(3,4) graph

j	(x_j, y_j)	Adjacent vertices to (x_j, y_j)			
		(x_{j+1}, y_{j+1})	(x_{j+2}, y_{j+2})	(x_{j+3}, y_{j+3})	(x_{j+4}, y_{j+4})
1	$(0, 0)$	A	2	3	4
2	$(h, 0)$	1	3	B	4
3	$(\frac{h}{2}, \frac{\sqrt{3}h}{2})$	1	2	C	4
4	$(\frac{h}{2}, \frac{h}{2\sqrt{3}})$	1	2	3	
A	$(-h, 0)$	1			
B	$(2h, 0)$	2			
C	$(h, \sqrt{3}h)$	3			

Table A.5: Coordinates of the vertices and a list of the adjacent vertices to vertex (x_j, y_j) for fractal generation level $n = 1$ of the SG(3,4) graph. The vertex labelling is given in Figure 3.3.

j	(x_j, y_j)	Adjacent vertices to (x_j, y_j)			
		(x_{j+1}, y_{j+1})	(x_{j+2}, y_{j+2})	(x_{j+3}, y_{j+3})	(x_{j+4}, y_{j+4})
1	$(0, 0)$	A	2	3	4
2	$(h, 0)$	1	3	5	4
3	$(\frac{h}{2}, \frac{\sqrt{3}h}{2})$	1	2	9	4
4	$(\frac{h}{2}, \frac{h}{2\sqrt{3}})$	1	2	3	
5	$(2h, 0)$	2	6	7	8
6	$(3h, 0)$	5	7	B	8
7	$(\frac{5h}{2}, \frac{\sqrt{3}h}{2})$	5	6	10	8
8	$(\frac{5h}{2}, \frac{h}{2\sqrt{3}})$	5	6	7	
9	$(h, \sqrt{3}h)$	3	10	11	12
10	$(2h, \sqrt{3}h)$	7	9	11	12
11	$(\frac{3h}{2}, \frac{3\sqrt{3}h}{2})$	9	10	C	12
12	$(\frac{3h}{2}, \frac{7h}{2\sqrt{3}})$	9	10	11	
A	$(-h, 0)$	1			
B	$(4h, 0)$	6			
C	$(2h, 2\sqrt{3}h)$	11			

Table A.6: Coordinates of the vertices and a list of the adjacent vertices to vertex (x_j, y_j) for fractal generation level $n = 2$ of the SG(3,4) graph. The vertex labelling is given in Figure 3.4.

j	a	b	c	d	f	g
1	1	0	0	$-\frac{1}{h^2}$	$\frac{3}{h^2}$	$-\frac{4\sqrt{3}}{h^2}$
2	0	$\frac{2}{h}$	$-\frac{4\sqrt{3}}{h}$	$-\frac{1}{h^2}$	$\frac{3}{h^2}$	$\frac{4\sqrt{3}}{h^2}$
3	0	$-\frac{5}{h}$	$\frac{3\sqrt{3}}{h}$	$\frac{5}{h^2}$	$-\frac{3}{h^2}$	0
4	0	$\frac{3}{h}$	$\frac{\sqrt{3}}{h}$	$-\frac{3}{h^2}$		
5	0	$-\frac{2}{h}$	0	$-\frac{1}{h^2}$		
6	-3	$\frac{4}{h}$	0	$-\frac{1}{h^2}$		
7	-3	$\frac{2}{h}$	$\frac{2\sqrt{3}}{h}$	$-\frac{1}{h^2}$		

Table A.7: Coefficients of the basis functions ϕ_j , $j = 1, \dots, 4$ (see equations (3.2.26), (3.2.27), (3.2.28) and (3.2.35)) and ψ_j , $j = 5, 6, 7$ (see equations (3.2.29), (3.2.30), (3.2.31) and (3.2.36)) for fractal generation level $n = 1$ of the SG(3,4) graph.

j	a	b	c	d	f	g
1	1	0	0	$-\frac{1}{h^2}$	$\frac{3}{h^2}$	$-\frac{4\sqrt{3}}{h^2}$
2	0	$\frac{2}{h}$	$-\frac{4\sqrt{3}}{h}$	$-\frac{1}{h^2}$	$\frac{3}{h^2}$	$\frac{4\sqrt{3}}{h^2}$
3	0	$-\frac{5}{h}$	$\frac{3\sqrt{3}}{h}$	$\frac{5}{h^2}$	$-\frac{3}{h^2}$	0
4	0	$\frac{3}{h}$	$\frac{\sqrt{3}}{h}$	$-\frac{3}{h^2}$		
5	-3	$\frac{4}{h}$	$\frac{8\sqrt{3}}{h}$	$-\frac{1}{h^2}$	$\frac{3}{h^2}$	$-\frac{4\sqrt{3}}{h^2}$
6	-8	$\frac{6}{h}$	$-\frac{12\sqrt{3}}{h}$	$-\frac{1}{h^2}$	$\frac{3}{h^2}$	$\frac{4\sqrt{3}}{h^2}$
7	30	$-\frac{25}{h}$	$\frac{3\sqrt{3}}{h}$	$\frac{5}{h^2}$	$-\frac{3}{h^2}$	0
8	-18	$\frac{15}{h}$	$\frac{\sqrt{3}}{h}$	$-\frac{3}{h^2}$		
9	-3	$\frac{14}{h}$	$-\frac{2\sqrt{3}}{h}$	$-\frac{1}{h^2}$	$\frac{3}{h^2}$	$-\frac{4\sqrt{3}}{h^2}$
10	30	$-\frac{8}{h}$	$-\frac{14\sqrt{3}}{h}$	$-\frac{1}{h^2}$	$\frac{3}{h^2}$	$\frac{4\sqrt{3}}{h^2}$
11	-8	$-\frac{15}{h}$	$\frac{9\sqrt{3}}{h}$	$\frac{5}{h^2}$	$-\frac{3}{h^2}$	0
12	-18	$\frac{9}{h}$	$\frac{7\sqrt{3}}{h}$	$-\frac{3}{h^2}$		
13	0	$-\frac{2}{h}$	0	$-\frac{1}{h^2}$		
14	-15	$\frac{8}{h}$	0	$-\frac{1}{h^2}$		
15	-15	$\frac{4}{h}$	$\frac{4\sqrt{3}}{h}$	$-\frac{1}{h^2}$		

Table A.8: Coefficients of the basis functions ϕ_j , $j = 1, \dots, 12$ (see equations (3.2.32), (3.2.33), (3.2.34) and (3.2.35)) and ψ_j , $j = 13, 14, 15$ for fractal generation level $n = 2$ of the SG(3,4) graph.

A.3 Geometrical and basis function details for fractal generation levels of the $\overline{\text{SG}}(3)$ graph

j	(x_j, y_j)	Adjacent vertices to (x_j, y_j)		
		(x_{j+1}, y_{j+1})	(x_{j+2}, y_{j+2})	(x_{j+3}, y_{j+3})
1	$(0, 0)$	A	2	3
2	$(h^{(1)}, 0)$	1	3	B
3	$(h^{(1)}/2, \sqrt{3}h^{(1)}/2)$	1	2	C
A	$(-h^{(1)}, 0)$	1		
B	$(2h^{(1)}, 0)$	2		
C	$(h^{(1)}, \sqrt{3}h^{(1)})$	3		

Table A.9: Coordinates of the vertices and a list of the adjacent vertices to vertex (x_j, y_j) for fractal generation level $n = 1$ of the $\overline{\text{SG}}(3)$ graph. The vertex labelling is given in Figure 4.3.

j	(x_j, y_j)	Adjacent vertices to (x_j, y_j)		
		(x_{j+1}, y_{j+1})	(x_{j+2}, y_{j+2})	(x_{j+3}, y_{j+3})
1	$(0, 0)$	A	2	3
2	$(h^{(2)}, 0)$	1	3	4
3	$(h^{(2)}/2, \sqrt{3}h^{(2)}/2)$	1	2	7
4	$(3h^{(2)}, 0)$	2	5	6
5	$(4h^{(2)}, 0)$	4	6	B
6	$(7h^{(2)}/2, \sqrt{3}h^{(2)}/2)$	4	5	8
7	$(3h^{(2)}/2, 3\sqrt{3}h^{(2)}/2)$	3	8	9
8	$(5h^{(2)}/2, 3\sqrt{3}h^{(2)}/2)$	6	7	9
9	$(2h^{(2)}, 2\sqrt{3}h^{(2)})$	7	8	C
A	$(-h^{(2)}, 0)$	1		
B	$(5h^{(2)}, 0)$	5		
C	$(5h^{(2)}/2, 5\sqrt{3}h^{(2)}/2)$	9		

Table A.10: Coordinates of the vertices and a list of the adjacent vertices to vertex (x_j, y_j) for fractal generation level $n = 2$ of the $\overline{\text{SG}}(3)$ graph. The vertex labelling is given in Figure 4.4.

A.4 The material properties of PZT-5H and polymer HY1300/CY1301 hardset

The material properties of PZT-5H [2,3,8,156]

$$c_{pq}^T = \begin{bmatrix} 12.6 & 7.95 & 8.41 & 0 & 0 & 0 \\ 7.95 & 12.6 & 8.41 & 0 & 0 & 0 \\ 8.41 & 8.41 & 11.7 & 0 & 0 & 0 \\ 0 & 0 & 0 & 2.3 & 0 & 0 \\ 0 & 0 & 0 & 0 & 2.3 & 0 \\ 0 & 0 & 0 & 0 & 0 & 2.325 \end{bmatrix} \times 10^{10} N/m^2,$$

$$e_{ip} = \begin{bmatrix} 0 & 0 & 0 & 0 & 17 & 0 \\ 0 & 0 & 0 & 17 & 0 & 0 \\ -6.5 & -6.5 & 23.3 & 0 & 0 & 0 \end{bmatrix} C/m^2,$$

$$\varepsilon_{ij}^T = \begin{bmatrix} 1700\varepsilon_0 & 0 & 0 \\ 0 & 1700\varepsilon_0 & 0 \\ 0 & 0 & 1470\varepsilon_0 \end{bmatrix} C/(Vm),$$

where $\varepsilon_0 = 8.854 \times 10^{-12} C/(Vm)$. The density is $\rho_T = 7500 kgm^{-3}$.

The material properties of polymer HY1300/CY1301 hard-set [146,157]

$$c_{pq}^P = \begin{bmatrix} 0.71976 & 0.404985 & 0.404981 & 0 & 0 & 0 \\ 0.40498 & 0.71976 & 0.40498 & 0 & 0 & 0 \\ 0.40498 & 0.40498 & 0.71976 & 0 & 0 & 0 \\ 0 & 0 & 0 & 0.15739 & 0 & 0 \\ 0 & 0 & 0 & 0 & 0.15739 & 0 \\ 0 & 0 & 0 & 0 & 0 & 0.15739 \end{bmatrix} \times 10^{10} N/m^2,$$

and

$$\varepsilon_{ij}^P = \begin{bmatrix} 4\varepsilon_0 & 0 & 0 \\ 0 & 4\varepsilon_0 & 0 \\ 0 & 0 & 4\varepsilon_0 \end{bmatrix} C/(Vm),$$

where The density is $\rho_P = 1150 \text{ kgm}^{-3}$.

A.5 Parameter values for the front and back mechanical loads and the electrical load

Design Parameter	Symbol	Magnitude	Dimensions
Parallel electrical impedance load	Z_P	1000	Ohms
Series electrical impedance load	Z_0	50	Ohms
Length of SG	L	1	mm
Mechanical impedance of the front load	Z_L	1.5	MRayls
Mechanical impedance of the backing layer	Z_B	2	MRayls
Wave speed in the front load	c_L	1500	ms^{-1}
Wave speed in the backing layer	c_B	1666	ms^{-1}
Density of the front load	ρ_L	1000	kgm^{-3}
Density of the backing layer	ρ_B	1200	kgm^{-3}
Shear modulus of the front load	μ_L	2.25×10^9	Nm^{-2}
Shear modulus of the backing layer	Y_B	2.78×10^9	Nm^{-2}
Thickness of the piezoelectric material in the standard (Euclidean) design	d_E	10	mm

Table A.11: Parameter values for the front and back mechanical loads and the electrical load [19,157].

A.6 Nomenclature

The tables below provide a full nomenclature of terms used within the thesis. It is worth noting that, as far as notation concerned, the literature is not consistent and care should be taken when comparing with other work.

Notation	Description
A, B, C	The boundary vertices in the fractal graph
$A_{ji}^{(n)}$	One of the matrices used to construct $G_{ji}^{(n)}$ (see equation (4.2.8))
$\hat{A}_{ji}^{(n)}$	$A_{ji}^{(n)} / h^{(n)}$
$\hat{A}^{(n)}$	The block diagonal matrix consisting of 3 copies of $\hat{A}_{ji}^{(n)}$
A_r	The cross-sectional area of each edge of the fractal graph $A_r = \xi L / 2^n$
A_L	Amplitude of pressure wave incident on the transducer during reception mode
A_B	The amplitude of the wave transmitted into the backing material
A_E	The area occupied by the electrode in the standard design
A_F	$2A'_F$, the total area of two capacitors in the fractal design
A'_F	$d_F h^{(n)}$, the area of one electrode in the fractal design
A_T	$2Z_L / (Z_L + Z_T)$, dimensionless constant (see equation 2.5.15)
a	$Z_P / (Z_0 + Z_P)$
\underline{a}	$\overrightarrow{OP_1} - \overrightarrow{OP_3}$ (vector)
B_L	The amplitude of the transmitted wave (transmission mode) or reflected wave (in reception mode)
B_B	The amplitude of the incoming wave into the backing material
$\hat{B}_{ji}^{(n)}$	One of the matrices used to create $G_{ji}^{(n)}$ (see equation (4.3.26))
b	$Z_0 Z_P / (Z_0 + Z_P)$
$b_j^{(n)}$	A vector arising from the boundary conditions (see equation (4.2.7))
\underline{b}	$\overrightarrow{OP_2} - \overrightarrow{OP_3}$ (vector)
$C^{(n)}$	The set of vertices that are incident to the longest edge (see equation (4.3.5))
C_0	The capacitance of the transducer
C_{0E}	The capacitance of the standard design
C_{0F}	The capacitance of the fractal design
c_{ijkl}	The stiffness tensor of the piezoelectric material
c_T	The (piezoelectrically stiffened) shear wave velocity in the fractal graph
c_P	The polymer shear wave velocity in the fractal graph
c_L	Wave speed in the front load
c_B	Wave speed in the backing layer

Notation	Description
D_i	The electrical displacement tensor
$D^{(n)}$	The set consist of pairs of vertices that are incident to a common longest edge (see equation (4.3.5))
d_E	The thickness of piezoelectric material in the standard design
d_F	The thickness of piezoelectric material in the fractal design
E_i	The electric field vector
e_{kij}	The piezoelectric tensor of the piezoelectric material
e	An element (edge) in fractal graph
F	The force in the transducer
F_E	The force produced at the front face of the standard transducer
F_F	The force produced at the front face of the fractal transducer
F_L	The force in the mechanical load
$F_{ji}^{(n)}$	$(G_{ji}^{(n)})^{-1} = \hat{A}_{ji}^{(n)} - \hat{B}_{ji}^{(n)}$ (see equation (4.3.26))
$\hat{f}^{(n)}$	The non-dimensionalised natural frequency
$f^{(n)}$	The dimensionalised equivalent of $\hat{f}^{(n)}$
f_a	The electrical resonant frequency
f_r	The mechanical resonant frequency
$G_{ji}^{(n)}$	The Green's transfer matrix
$\hat{G}^{(n)}$	$\hat{G}^{(n)} = (\hat{A}^{(n)})^{-1}$ (see equation (2.4.4))
$\bar{\hat{G}}^{(n)}$	The block diagonal matrix consisting of 3 copies of $\hat{G}^{(n)}$
$h^{(n)}$	The edge length of the fractal graph $L/2^n$
$h^{(p)}$	The range of edge lengths $p = 1, \dots, n$ in the generation level n $\overline{\text{SG}}(3)$ graph
$H^1(\Omega)$	Sobolev space of order 1 in domain Ω
$H^1(\partial\Omega)$	Sobolev space of order 1 at the boundary $\partial\Omega$
$H_B^1(\Omega)$	Sobolev space of order 1 in domain Ω where the functions are zero on the boundary
$H_{ji}^{(n)}$	A matrix used to construct $A_{ji}^{(n)}$ (see equation (4.2.9))
$\hat{H}_{ji}^{(n)}$	$H_{ji}^{(n)}/h^{(n)}$
$\bar{\hat{H}}_{ji}^{(n-1)}$	The block diagonal matrix consisting of 3 copies of $\hat{H}_{ji}^{(n-1)}$
I	The set of fictitious vertices of fractal graph
I_T	The current across the transducer (see equations (2.5.2) and (2.5.9))
J	The set of interior vertices of fractal graph
j, k, l, m	Vertices in the $\overline{\text{SG}}(3)$ graphs (see Figure 4.6)
$K_{ji}^{(n)}$	A matrix used to construct $A_{ji}^{(n)}$ (see equation (4.2.10))
$\hat{K}_{ji}^{(n)}$	$h^{(n)}K_{ji}^{(n)}$
$\bar{\hat{K}}_{ji}^{(n-1)}$	The block diagonal matrix consisting of 3 copies of $\hat{K}_{ji}^{(n-1)}$
K_F, K_B	The non-dimensional coefficients (see equation (2.5.8))
$K^{(n)}$	see equation 4.5.2

Notation	Description
L	Length of transducer
$L_{SG}^{(n)}$	$nL/2$, the overall length of the graph $\overline{SG}^{(n)}(3)$ graph
M	The total number of edges in the fractal graph
M_J	The set of the interior elements of fractal graph
M_I	The set of the exterior elements of fractal graph
m	The vertex labelled $(N + 1)/2$
N	3^n , the total number of vertices in the fractal graph
n	The fractal generation level
\underline{n}	The outward pointing unit normal from the edge element dr
P_1, P_2, P_3	The points in the plane S_P (see Figure 4.6)
p, q	The adjacent vertices of the longest elements in the fractal graph (see Figure 4.10)
Q	The electrical charge applied to the boundary of the transducer
q	Laplace variable
$\overline{SG}^{(n)}(3)$	The complement of the Sierpinski gasket graph of degree 3
S_{kl}	The strain tensor
S_S	The finite dimensional subspace correspondury to $H^1(\Omega)$
S_P	The plane contains the points P_1, P_2 and P_3 (see Figure 4.6)
S_B	The finite dimensional subspace correspondury to $H_B^1(\Omega)$
S_n	The area of the main face of the fractal piezoelectric design at generation level n
s	The parameter used in the isoparametric description of each element
s_1, s_2	The adjacent vertices of element s (see Figure 4.9)
T_{ij}	The stress tensor
T_F, T_B	The non-dimensional transmission coefficients (see equation (2.5.8))
t	Time
U	The approxmate displacement in region Ω (see equation (4.2.3))
\bar{U}	The discretised displacement
U_B	The function that approximates the displacement at the boundary
U_{B_i}	The displacement at the boundary vertex B_i
U_A, U_B, U_C	The displacement of the boundary vertices $\{A, B, C\}$
$u_{i,j}$	The displacement gradients
u_i	The component of displacement in the direction of the i^{th} basis vector
\underline{u}	The vector of u_i
\dot{u}_3	The initial condition
$u_{\partial\Omega}$	The displacement in the boundary of fractal graph
$\bar{u}_{\partial\Omega}$	The laplace displacement in the boundary of fractal graph
u_L	The displacement of the load material
\bar{u}	The laplace transform displacement
$\bar{u}_B(0)$	The laplace transform displacemen of the backing material
$\bar{u}_L(0)$	The laplace transform displacemen of the load material

Notation	Description
$P_{ji}^{(n)}$	The adjacency matrix for the subgraph of $\overline{\text{SG}}^{(n)}(3)$ consisting of the edges that connect each of the three $\overline{\text{SG}}^{(n-1)}(3)$ graphs
$V_{ji}^{(n)}$	$1_{D^{(n)}}(j, i)$ (see equation (4.3.1))
V	The voltage applied to the transducer
V_E	The voltage produced by the standard transducer
V_F	The voltage produced by the fractal transducer
vol_E	The volume of piezoelectric material in the standard design
vol_F	The volume of piezoelectric material in the fractal design
W	The test function in the finite dimensional space S_B , $W = \phi_j$
$W_{ji}^{(n)}$	$1_{C^{(n)}}(j, i)$ (see equation (4.3.1))
w	The test function in the infinite dimensional weak formulation
R_F, R_B	The non-dimensionalised reflection coefficients
r	$r = G_{mN}^{(n)}$
\hat{X}	$\hat{X} = \hat{G}_{ii}^{(n+1)}$ where $i \in V_{\partial\Omega_n^o}$
\underline{x}	The spatial coordinates (cartesian)
\underline{x}_j	The spatial location of vertex j in the fractal graph
x	$x = G_{11}^{(n)}$
\hat{x}	$\hat{x} = \hat{G}_{ii}^{(n)} = \hat{G}_{jj}^{(n)}$ where $i, j \in V_{\partial\Omega_n^o}$
x_L	The local coordinate in the mechanical load
x_B	The local coordinate in the backing material
\hat{Y}	$\hat{Y} = \hat{G}_{ji}^{(n+1)}$ where $j, i \in V_{\partial\Omega_n^o}$, $i \neq j$
y	$y = G_{1m}^{(n)} = G_{1N}^{(n)}$
\hat{y}	$\hat{y} = \hat{G}_{ik}^{(n)} = \hat{G}_{hk}^{(n)}$ where $j, k, h \in V_{\partial\Omega_n^o}$, $j \neq k \neq h$
Z_B	Mechanical impedance of backing layer
Z_L	Mechanical impedance of the front load
Z_T	Mechanical impedance of the transducer
Z_P	Parallel electrical impedance load
Z_0	Series electrical impedance load
$Z_E(f; n)$	The dimensionalised electrical impedance of the fractal graph
$\hat{Z}_E(f; n)$	The non-dimensionalised electrical impedance of the fractal graph
$\hat{\hat{Z}}_E(f)$	The non-dimensionalised electrical impedance of the standard transducer
z	$z = G_{mm}^{(n)} = G_{NN}^{(n)}$

Notation	Description
α	Non-dimensionalised parameter given by equation (4.3.16)
β	Non-dimensionalised parameter given by equation (4.3.16)
γ_j	Non-dimensionalised parameter given by equation (4.3.27)
$\bar{\gamma}_j$	$\eta\gamma_j$
Δ_1, Δ_2	see equation (4.4.3)
δ_1, δ_2	see equation (4.4.3)
$\bar{\delta}_j$	Non-dimensionalised parameter given by equation (4.3.28)
δ_j	$\eta\delta_j$
\mathcal{L}	Laplace transform: $\theta \rightarrow q$
ε_{ik}	The permittivity tensor
$\epsilon^{(n)}$	Non-dimensionalised parameter given by equation (4.3.9)
$\chi^{(n)}$	Non-dimensionalised parameter given by equation (4.3.9)
$\Upsilon^{(n)}$	Non-dimensionalised parameter given by equation (4.3.1)
$\vartheta^{(n)}$	Non-dimensionalised parameter given by equation (4.3.1)
τ	The wave transit time across the device
$\hat{\lambda}$	$C_0/(1 + qC_0b)$ dimensionless constant (see equation 2.5.15)
$\hat{\lambda}_*$	$qC_0b/(1 + qC_0b)$ (see equation (2.6.4))
ζ	$e_{24}/\varepsilon_{11}^T$
η	Non-dimensionalised parameter given by equation (4.3.17)
θ	The non-dimensionalised temporal variable
μ_L	The shear modulus of the load material
μ_T	The piezoelectrically stiffened shear modulus
ξ	$A_r/h^{(n)}$
σ_1, σ_2	see equation (4.5.1)
ρ_L	Density of the front load
ρ_T	The density of the piezoelectric material
$\phi_{,i}$	The electric potential
ϕ_j	The localised basis function at vertex j
${}^e\phi_j^{(n)}$	The basis function for vertex j in the element e
$\phi_F(f; n)$	The non-dimensionalised reception sensitivity of the fractal transducer
$\phi_E(f)$	The non-dimensionalised reception sensitivity of the standard transducer
$\phi_F^*(n)$	The reception sensitivity of the fractal transducer integrated over all frequencies
$\psi_F(f; n)$	The non-dimensionalised transmission sensitivity of the fractal transducer
$\psi_E(f)$	The non-dimensionalised transmission sensitivity of the standard transducer
$\psi_F^*(n)$	The transmission sensitivity of the fractal transducer integrated over all frequencies
Ω	The set of points lying on the edges and vertices of fractal graph
$\partial\Omega$	The region's boundary
$\hat{\omega}^{(n)}$	The nondimensionalised angular frequency
$\omega^{(n)}$	The dimensionalised equivalent of $\hat{\omega}^{(n)}$

Bibliography

- [1] R. T. Beyer and S. V. Letcher. *Physical Ultrasonics*. Academic Press, New York, (1969).
- [2] J. Yang. *Analysis of Piezoelectric Devices*. World Scientific, Singapore, (2006).
- [3] J. Yang. *The Mechanics of Piezoelectric Structures*. World Scientific, Singapore, (2006).
- [4] E. A. Algehyne and A. J. Mulholland. Sensor Mimics Nature to Detect Dangerous Structural Cracks. *Homeland Defense and Security Information Analysis Center (HDIAC), Spotlight website*, (August 31, 2015).
<https://www.hdiac.org/node/2163>.
- [5] A. Alippi, A. Bettucci, F. Craciun, F. Farrelly, E. Molinari, and A. Petri. Acoustic modes in 2-dimensional self-similar composite plates. *IEEE Ultrasonics Symposium (IUS)*, Baltimore, MA, USA, 1:533–536, (1993).
- [6] G. Hayward. A systems feedback representation of piezoelectric transducer operational impedance. *Ultrasonics*, 22(4):153–162, (1984).

- [7] A. J. Mulholland. Bounds on the Hausdorff dimension of a renormalisation map arising from an excitable reaction-diffusion system on a fractal lattice. *Chaos, Solitons and Fractals*, 35(2):274–284, (2008).
- [8] L. A. Orr, A. J. Mulholland, R. L. O’Leary, A. Parr, R. Pethrick, and G. Hayward. Theoretical Modelling of Frequency Dependent Elastic Loss in Composite Piezoelectric Transducers. *Ultrasonics*, 47(1):130–137, (2007).
- [9] E. A. Algehyne and A. J. Mulholland. A finite element approach to modelling fractal ultrasonic transducers. *IMA Journal of Applied Mathematics*, 80(6):1684–1702, (2015).
- [10] E. Barlow, E. A. Algehyne, and A. J. Mulholland. Investigating the performance of a fractal ultrasonic transducer under varying system conditions. *Symmetry*, 8(6):43–72, (2016).
- [11] A. M. Chiselev, L. Moraru, and A. Gogu. Localization of an object using a bat model inspired from biology. *J. Biophys*, 19(4):251–258, (2009).
- [12] F. M. de Espinosa, O. Martinez, L. E. Segura, and L. Gomez-Ullate. Double frequency piezoelectric transducer design for harmonic imaging purposes in NDT. *IEEE. TUFFC*, 52(6):980–986, (2005).
- [13] D. F. Eberl, R. W. Hardy, and M. J. Kernan. Genetically similar transduction mechanisms for touch and hearing in *Drosophila*. *J. Neurosci*, 20(16):5981–5988, (2000).
- [14] R. N. Miles and R. R. Hoy. The development of a biologically-inspired directional microphone for hearing aids. *Audiol Neurootol*, 11(2):86–94, (2006).
- [15] R. Müller. A numerical study of the role of the tragus in the big brown bat. *JASA*, 116(6):3701–3712, (2004).

- [16] R. Müller, H. Lu, S. Zhang, and H. Peremans. A helical biosonar scanning pattern in the chinese noctule *Nycatalus plancyi*. *JASA*, 119(6):4083–4092, (2006).
- [17] B. Nadrowski, J. T. Albert, and M. C. Göpfert. Transducer-Based Force Generation Explains Active Process in *Drosophila* Hearing. *Current Biology*, 18(18):1365–1372, (2008).
- [18] D. Robert and M. C. Göpfert. Novel schemes for hearing and orientation in insects. *Current Opinion in Neurobiology*, 12(6):715–720, (2002).
- [19] A. J. Mulholland and A. J. Walker. Piezoelectric Ultrasonic Transducers with Fractal Geometry. *Fractals*, 19(4):469–479, (2011).
- [20] A. J. Mulholland, A. J. Walker, J. W. Mackersie, R. L. O’Leary, A. Gachagan, and N. Ramadas. The use of fractal geometry in the design of piezoelectric ultrasonic transducers. In *Ultrasonics Symposium (IUS), 2011 IEEE International*, pages 1559–1562. IEEE, (2011).
- [21] L. A. Orr, A. J. Mulholland, R. L. O’Leary, and G. Hayward. Analysis of Ultrasonic Transducers with Fractal Architecture. *Fractals*, 16(4):333–349, (2008).
- [22] J. Abdalbake, A. J. Mulholland, and J. Gomatam. A renormalization approach to reaction-diffusion processes on fractals. *Fractals*, 11(4):315–330, (2003).
- [23] J. Abdalbake, A. J. Mulholland, and J. Gomatam. Existence and Stability of Reaction-Diffusion Waves on a Fractal Lattice. *Chaos, Solitons and Fractals*, 20(4):799–814, (2004).

- [24] M. T. Barlow. Diffusions on fractals. In P. Bernard, editor, *Lectures on Probability Theory and Statistics*, volume 1690 of Lecture Notes in Math, pages 1–121. Springer, Verlag, (1998).
- [25] G. Derfel, P. J. Grabner, and F. Vogl. Laplace operators on fractals and related functional equations. *Journal of Physics A: Mathematical and Theoretical*, 45(46):463001, (2012).
- [26] K. J. Falconer and J. Hu. Nonlinear Diffusion Equations on Unbounded Fractal Domains. *Journal of mathematical analysis and applications*, 256(2):606–624, (2001).
- [27] M. Giona, W. A. Schwalm, M. K. Schwalm, and A. Adrover. Exact solution of linear transport equations in fractal media - I. Renormalization analysis and general theory. *Chem. Eng. Sci*, 51(20):4717–4729, (1996).
- [28] J. Kigami. *Analysis on Fractals*, volume 143. Cambridge University Press, Cambridge, UK, 2001.
- [29] M. Giona. Transport Phenomena in Fractal and Heterogeneous Media: Input/Output Renormalization and Exact Results. *Chaos, Solitons and Fractals*, 7(9):1371–1396, (1996).
- [30] R. S. Strichartz. Analysis on Fractals. *Notices AMS*, 46(10):1199–1208, (1999).
- [31] R. S. Strichartz. *Differential equations on fractals: a tutorial*. Princeton University Press, (2006).
- [32] C. M. Rumack and D. Levine. *Diagnostic Ultrasound E-Book*. Elsevier Health Sciences, (2017).

- [33] T. G. Leighton. What is ultrasound? *Progress in biophysics and molecular biology*, 93(1-3):3–83, 2007.
- [34] P. S. Sheeran, Y. Daghighi, K. Yoo, R. Williams, E. Cherin, F. S. Foster, and P. N. Burns. Image-guided ultrasound characterization of volatile sub-micron phase-shift droplets in the 20–40 MHz frequency range. *Ultrasound in Medicine and Biology*, 42(3):795–807, (2016).
- [35] François Le Chevalier. *Principles of radar and sonar signal processing*. Artech House, (2002).
- [36] A. Elfes. Sonar-based real-world mapping and navigation. *IEEE Journal on Robotics and Automation*, 3(3):249–265, (1987).
- [37] S. M. Murphy, J. G. Scrutton, and P. C. Hines. Experimental implementation of an echo repeater for continuous active sonar. *IEEE Journal of Oceanic Engineering*, 42(2):289–297, (2017).
- [38] G. E. Santagati and T. Melodia. Sonar inside your body: Prototyping ultrasonic intra-body sensor networks. In *INFOCOM, 2014 Proceedings IEEE*, pages 2679–2687. IEEE, (2014).
- [39] L. Kleeman and R. Kuc. Sonar Sensing. In B. Siciliano and O. Khatib, editors, *Springer Handbook of Robotics*, pages 753–782. Springer, Cham, (2016).
- [40] A. A. Winder. Ii. sonar system technology. *IEEE Transactions on Sonics and Ultrasonics*, 22(5):291–332, (1975).
- [41] J. M. Preston, A. C. Christney, S. F. Bloomer, and I. L. Beaudet. Seabed classification of multibeam sonar images. In *Oceans, 2001. MTS/IEEE Conference and Exhibition*, volume 4, pages 2616–2623. IEEE, (2001).

- [42] K. M. M. Tant, A. J. Mulholland, M. Langer, and A. Gachagan. A fractional Fourier transform analysis of the scattering of ultrasonic waves. *Proc. R. Soc. A*, 471 (2176), 20140958, DOI: 10.1098/rspa.2014.0958, (2015).
- [43] J. Dobson, A. Tweedie, G. Harvey, R. O’Leary, A. Mulholland, K. Tant, and A. Gachagan. Finite element analysis simulations for ultrasonic array NDE inspections. *American Institute of Physics (AIP) Conference Proceedings*, 1706, DOI: 10.1063/1.4940499:040005–1–040005–14, (2016).
- [44] J. D. N. Cheeke. *Fundamentals and applications of ultrasonic waves*. CRC press, (2017).
- [45] M. Bonnet, F. Collino, E. Demaldent, A. Imperiale, and L. Pesudo. A hybrid method combining the surface integral equation method and ray tracing for the numerical simulation of high frequency diffraction involved in ultrasonic ndt. In *Journal of Physics: Conference Series*, volume 1017, page 012007. IOP Publishing, (2018).
- [46] J. Chandrapala. Low intensity ultrasound applications on food systems. *International Food Research Journal*, 22(3):888–895, (2015).
- [47] D. Knorr, M. Zenker, V. Heinz, and D. U. Lee. Applications and potential of ultrasonics in food processing. *Trend Food Sci. Technol*, 15:261–266, (2004).
- [48] F. Chemat, Z. Huma, and M. K. Khan. Applications of ultrasound in food technology: processing, preservation and extraction. *Ultrasonics Sonochemistry*, 18:813–835, (2011).
- [49] A. Shanmugam and M. Ashokkumar. Ultrasonic Preparation of Food Emulsions. *Ultrasound in Food Processing: Recent Advances*, pages 287–310, (2017).

- [50] T. J. Mason, F. Chemat, and M. Ashokkumar. 27-power ultrasonics for food processing. In J. A. Gallego-Jurez and K. F. Graff, editors, *Power Ultrasonics*. Woodhead Publishing, Oxford.
- [51] S. K. Khanal, D. Grewell, S. Sung, and J. Van Leeuwen. Ultrasound applications in wastewater sludge pretreatment: A review. *Crit. Rev. Environ. Sci. Technol*, 37:277–313, (2007).
- [52] S. Pilli, P. Bhunia, S. Yan, R. J. LeBlanc, R. D. Tyagi, and R. Y. Surampalli. Ultrasonic pretreatment of sludge: A review. *Ultrason. Sonochem*, 18(1):1–18, (2011).
- [53] T. J. Mason. Therapeutic ultrasound an overview. *Ultrasonics Sonochemistry*, 18(4):847–852, (2011).
- [54] J. Mostafa, Y. Ali, R. Zohre, and R. Samaneh. Electromagnetic fields and ultrasound waves in wound treatment: A comparative review of therapeutic outcomes. *Biosci Biotechnol Res Asia*, 12(1):185–195, (2015).
- [55] D. L. Miller, N. B. Smith, M. R. Bailey, G. J. Czarnota, K. Hynynen, and I. R. S. Makin. Overview of Therapeutic Ultrasound Applications and Safety Considerations. *Ultrasound in Medicine*, 31(4):623–634, (2012).
- [56] T. Yu, Z. Wang, and T. J. Mason. A review of research into the uses of low level ultrasound in cancer therapy. *Ultrasonics sonochemistry*, 11(2):95–103, (2004).
- [57] D. S. Downing and A. Weinstein. Ultrasound Therapy of Subacromial Bursitis: A Double Blind Trial. *Physical Therapy*, 66(2):194–199, (1986).

- [58] B. Chen, L. Rispoli, T. Stitik, and M. Leong. Successful Treatment of Gluteal Pain from Obturator Internus Tendinitis and Bursitis with Ultrasound-Guided Injection. *American journal of physical medicine & rehabilitation*, 96(10):e181–e184, (2017).
- [59] S. Ruta, C. Quiroz, J. Marin, E. Catay, J. Rosa, R. García-Monaco, and E. R. Soriano. Ultrasound evaluation of the greater trochanter pain syndrome: bursitis or tendinopathy? *JCR: Journal of Clinical Rheumatology*, 21(2):99–101, (2015).
- [60] G. Haupt and A. Haupt. In vitro comparison of 4 ultrasound lithotripsy devices. *The Journal of urology*, 170(5):1731–1733, (2003).
- [61] A. Mink, I. Gti, and J. Szkely. Nasolith removal with ultrasound lithotripsy. *HNO*, 39(3):116–117, (1991).
- [62] T. Ikeda, S. Yoshizawa, N. Koizumi, M. Mitsuishi, and Y. Matsumoto. *Focused Ultrasound and Lithotripsy*, volume 880, pages 113–129. *Advances in Experimental Medicine and Biology*. Springer, Cham, (2016).
- [63] J. P. Shock. Method of ultrasonic cryogenic cataract removal, (1976). US Patent 3,942,519.
- [64] A. C. Day, D. M. Gore, C. Bunce, and J. R. Evans. Laser-assisted cataract surgery versus standard ultrasound phacoemulsification cataract surgery. *The Cochrane Library*, (2016).
- [65] C. C. Ronquillo, B. Zaugg, B. Stagg, K. R. Kirk, I. Gupta, W. R. Barlow, J. H. Pettey, and R. J. Olson. Determining optimal torsional ultrasound power for cataract surgery with automatic longitudinal pulses at maximum

- vacuum ex vivo. *American journal of ophthalmology*, 158(6):1262–1266, (2014).
- [66] J. J. Vaitekunas, L. F. Cosentino, and R. VanZandt. Ultrasonic hemostatic and cutting instrument, (1999). US Patent 6,004,335.
- [67] N. Kharin. Ultrasound device for precise tissue sealing and blade-less cutting, (2015). US Patent 8,968,283.
- [68] N. Heybeli, A. Yeşildağ, O. Oyar, U. K. Gülsoy, M. A. Tekinsoy, and E. F. Mumcu. Diagnostic ultrasound treatment increases the bone fracture–healing rate in an internally fixed rat femoral osteotomy model. *Journal of ultrasound in medicine*, 21(12):1357–1363, (2002).
- [69] M. Hadjiargyrou, K. McLeod, J. P. Ryaby, and C. Rubin. Enhancement of fracture healing by low intensity ultrasound. *Clinical orthopaedics and related research*, 355:S216–S229, (1998).
- [70] J. Chapelon, O. Rouvière, S. Crouzet, and A. Gelet. Prostate Focused Ultrasound Therapy. In J. M. Escoffre and A. Bouakaz, editors, *Therapeutic Ultrasound*, volume 880, pages 21–41. Advances in Experimental Medicine and Biology. Springer, Cham, (2016).
- [71] C. P. Filson, S. Natarajan, D. J. Margolis, J. Huang, P. Lieu, F. J. Dorey, R. E. Reiter, and L. S. Marks. Prostate cancer detection with magnetic resonance-ultrasound fusion biopsy: The role of systematic and targeted biopsies. *Cancer*, 122(6):884–892, (2016).
- [72] M. Whitworth, L. Bricker, and C. Mullan. Ultrasound for fetal assessment in early pregnancy. *The Cochrane Library*, (2015).

- [73] S. Kumari, J. Roychowdhury, and S. Biswas. Prediction of early pregnancy failure by use of first trimester ultrasound screening. *International Journal of Reproduction, Contraception, Obstetrics and Gynecology*, 5(7):2135–2140, (2017).
- [74] M. Whitworth, L. Bricker, and C. Mullan. Ultrasound for fetal assessment in early pregnancy. *The Cochrane Library*, (2015).
- [75] I. Casikar, S. Reid, and G. Condous. Ectopic pregnancy: Ultrasound diagnosis in modern management. *Clinical obstetrics and gynecology*, 55(2):402–409, (2012).
- [76] H. K. Blaas. Detection of structural abnormalities in the first trimester using ultrasound. *Best Practice & Research Clinical Obstetrics & Gynaecology*, 28(3):341–353, (2014).
- [77] G. T. Haar. Therapeutic applications of ultrasound. *Progress in biophysics and molecular biology*, 93(1-3):111–129, (2007).
- [78] Shahram Vaezy and Vesna Zderic. Hemorrhage control using high intensity focused ultrasound. *International Journal of Hyperthermia*, 23(2):203–211, (2007).
- [79] V. Zderic, A. Keshavarzi, M. L. Noble, M. Paun, S. R. Sharar, L. A. Crum, R. W. Martin, and S. Vaezy. Hemorrhage control in arteries using high-intensity focused ultrasound: A survival study. *Ultrasonics*, 44(1):46–53, 2006.
- [80] E. S. C. Koh and E. G. McNally. Ultrasound of skeletal muscle injury. *Seminars in Musculoskeletal Radiology*. 11(02):162–173, (2007).

- [81] P. H. Lento and S. Primack. Advances and utility of diagnostic ultrasound in musculoskeletal medicine. *Current reviews in musculoskeletal medicine*, 1(1):24–31, (2008).
- [82] R. Bubnov, V. Yevseenko, and I. Semeniv. Ultrasound guided injections of platelets rich plasma for muscle injury in professional athletes. Comparative study. *Medical ultrasonography*, 15(2):101, (2013).
- [83] D. Hayashi, B. Hamilton, A. Guerhazi, R. de Villiers, M. D. Crema, and F. W. Roemer. Traumatic injuries of thigh and calf muscles in athletes: role and clinical relevance of MR imaging and ultrasound. *Insights into imaging*, 3(6):591–601, (2012).
- [84] J. T. Finnoff, J. Ray, G. Corrado, D. Kerkhof, and J. Hill. Sports Ultrasound: Applications Beyond the Musculoskeletal System. *SAGE*, 8(5):412–417, (2016).
- [85] John C. Hill and Iigo San Milln. Validation of musculoskeletal ultrasound to assess and quantify muscle glycogen content. a novel approach. *The Physician and Sportsmedicine*, 42(3):45–52, (2014).
- [86] D. C. Nieman, R. A. Shanely, K. A. Zwetsloot, M. P. Meaney, and G. E. Farris. Ultrasonic assessment of exercise-induced change in skeletal muscle glycogen content. *BMC sports science, medicine and rehabilitation*, 7(1):9, (2015).
- [87] R. J. Verbeek, C. P. Sentner, G. P. A. Smit, N. M. Maurits, T. G. J. Derks, J. H. van der Hoeven, and D. A. Sival. Muscle ultrasound in patients with glycogen storage disease types I and III. *Ultrasound in Medicine and Biology*, 42(1):133–142, (2016).

- [88] G. Bruyn, P. Hanova, A. Iagnocco, M. Agostino, I. Möller, L. Terslev, M. Backhaus, P. Balint, E. Filippucci, P. Baudoin, R. Vugt, C. Pineda, R. Wakefield, J. Garrido, O. Pecha, and E. Naredo. Ultrasound definition of tendon damage in patients with rheumatoid arthritis. Results of a OMER-ACT consensus-based ultrasound score focussing on the diagnostic reliability. *Annals of the Rheumatic Diseases*, 73(11):1929–1934, (2014).
- [89] E. A. Haavardsholm, A. B. Aga, I. C. Olsen, S. Lillegraven, H. B. Hammer, T. Uhlig, H. Fremstad, T. M. Madland, A. S. Lexberg, H. Haukeland, E. Rodevand, C. Hoili, H. Stray, A. Noraas, I. J. W. Hansen, G. Bakland, L. B. Nordberg, D. van der Heijde, and T. K. Kvien. Ultrasound in management of rheumatoid arthritis: ARCTIC randomised controlled strategy trial. *Bmj*, 354:i4205, (2016).
- [90] J. Dale, A. Stirling, R. Zhang, D. Purves, J. Foley, M. Sambrook, P. G. Conaghan, D. van der Heijde, A. McConnachie, I. B. McInnes, and D. Porter. Targeting ultrasound remission in early rheumatoid arthritis: the results of the TaSER study, a randomised clinical trial. *Annals of the Rheumatic Diseases*, pages annrheumdis–2015, (2016).
- [91] I. Lentacker, S. C. De Smedt, and N. N. Sanders. Drug loaded microbubble design for ultrasound triggered delivery. *Soft Matter*, 5:2161–2170, (2009).
- [92] Ching-Hsiang Fan, Chien-Yu Ting, Hao-Li Liu, Chiung-Yin Huang, Han-Yi Hsieh, Tzu-Chen Yen, Kuo-Chen Wei, and Chih-Kuang Yeh. Antiangiogenic-targeting drug-loaded microbubbles combined with focused ultrasound for glioma treatment. *Biomaterials*, 34:2142–2155, (2013).
- [93] H. Dewitte, K. Vanderperren, H. Haers, E. Stock, L. Duchateau, M. Hesta, J. H. Saunders, S. C. De Smedt, and I. Lentacker. Theranostic mRNA-loaded

- microbubbles in the lymphatics of dogs: Implications for drug delivery. *Theranostics*, 5:97–109, (2015).
- [94] M. Cochran, T. Bustamante, J. Eisenbrey, and M. Wheatley. In vitro characterization of docetaxel loaded microbubbles for ultrasound triggered drug delivery. *Pharmaceutical Engineering*, 32:1–10, (2012).
- [95] M. Bazan Peregrino, B. Rifai, R. C. Carlisle, J. Choi, C. D. Arvanitis, L. W. Seymour, and C. C. Coussios. Cavitation-enhanced delivery of a replicating oncolytic adenovirus to tumors using focused ultrasound. *Journal of Controlled Release*, 169:40–47, (2013).
- [96] D. Gourevich, A. Volovick, O. Dogadkin, L. Wang, H. Mulvana, Y. Medan, A. Melzer, and S. Cochran. In vitro investigation of the individual contributions of ultrasound-induced stable and inertial cavitation in targeted drug delivery. *Ultrasound in Medicine & Biology*, 41:1853–1864, (2015).
- [97] F. Yan, L. Li, Z. Deng, Q. Jin, J. Chen, W. Yang, C. K. Yeh, J. Wu, R. Shandas, X. Liu, and H. Zheng. Paclitaxel-liposome-microbubble complexes as ultrasound-triggered therapeutic drug delivery carriers. *Journal of Controlled Release*, 166:246–255, (2013).
- [98] C. Niu, Z. Wang, G. Lu, T. M. Krupka, Y. Sun, Y. You, W. Song, H. Ran, P. Li, and Y. Zheng. Doxorubicin loaded superparamagnetic PLGA-iron oxide multifunctional microbubbles for dual-mode US/MR imaging and therapy of metastasis in lymph nodes. *Biomaterials*, 34:2307–2317, (2013).
- [99] J.M. Escoffre, C. Mannaris, B. Geers, A. Novell, I. Lentacker, M. Averkion, and A. Bouakaz. Doxorubicin liposome-loaded microbubbles for contrast

- imaging and ultrasound triggered drug delivery. *IEEE Transactions on Ultrasonics, Ferroelectrics and Frequency Control*, 60:78–87, (2013).
- [100] S. Mitragotri. Healing sound: the use of ultrasound in drug delivery and other therapeutic applications. *Nature Reviews Drug Discovery*, 4(3):255, (2005).
- [101] Jose-Luis Capelo-Martnez. *Ultrasound in Chemistry: Analytical Application*. WILEY-VCH, (2009).
- [102] A. U. Badnore and A. B. Pandit. Synthesis of nanosized calcium carbonate using reverse miniemulsion technique: Comparison between sonochemical and conventional method. *Chemical Engineering and Processing: Process Intensification*, 98:13–21, (2015).
- [103] V. Jannin, L. Blas, S. Chevrier, C. Miolane, F. Demarne, and D. Spitzer. Evaluation of the digestibility of solid lipid nanoparticles of glyceryl dibehenate produced by two techniques: Ultrasonication and spray-flash evaporation. *European Journal of Pharmaceutical Sciences*, 111:91–95, (2018).
- [104] T. Pham, S. K. Brar, R. Tyagi, and R. Surampalli. Ultrasonication of wastewater sludgeconsequences on biodegradability and flowability. *Journal of hazardous materials*, 163(2-3):891–898, (2009).
- [105] A. Rastegar. Self-similar fractals in arithmetic. *arXiv:math.NT/0404498v2*, (2008).
- [106] A. Rastegar. Self-Similarity in Geometry, Algebra and Arithmetic. *arXiv:math.NT/1211.4968v2*, (2015).
- [107] B. Mandelbrot. *The fractal geometry of nature*. W.H. Freeman, San Francisco, (1977).

- [108] A. Carpinteri and F. Mainardi. *Fractals and fractional calculus in continuum mechanics*. Springer-Verlag Wien, New York, (1977).
- [109] G. A. Edgar. *Measure, Topology, and Fractals Geometry*. Springer-Verlag Wien, New York, (1990).
- [110] J. Feder. *Fractals*. Springer Science & Business Media, New York, (2013).
- [111] P. Webster et al. Fractal Islamic Geometric Patterns Based on Arrangements of $\{n/2\}$ Stars. *Proceedings of Bridges Mathematics, Music, Art, Architecture, Culture, Pittsfield, MA*, 1201, (2013).
- [112] K. M. Iftekharuddin, Wei Jia, and R. Marsh. Fractal analysis of tumor in brain MR images. *Machine Vision and Applications, Springer-Verlag*, 13(5):352–362, (2003).
- [113] K. M. Iftekharuddin, J. Zheng, M. A. Islam, and R. J. Ogg. Fractal-based brain tumor detection in multimodal MRI. *Applied Mathematics and Computation, Elsevier*, 207(1):23–41, (2009).
- [114] J. M. Blackledge, A. K. Evans, and M. J. Turner. *Fractal Geometry: Mathematical Methods, Algorithms, Applications*. Horwood Publishing, Chichester, UK, (2002).
- [115] S. Chen, T. Oviir, C. Lin, L. Leu, B. Cho, and L. Hollender. Digital imaging analysis with mathematical morphology and fractal dimension for evaluation of periapical lesions following endodontic treatment. *Oral Surgery, Oral Medicine, Oral Pathology, Oral Radiology and Endodontics, Elsevier*, 100(4):467–472, (2005).
- [116] Y. Fisher. *Fractal Image Compression: Theory and Application*. Springer-Verlag, Berlin, Germany, (1995).

- [117] A. M. Biswas, S. Karmakar, S. Sharma, and M. K. Kowar. Performance of fractal image compression for medical images: A comprehensive literature review. *International Journal of Applied Information Systems (IJ AIS)*, 8(4):14–24, (2015).
- [118] K. K. Veena and P. Bhuvaneshwari. Various techniques of fractal image compression-A review. *International Journal of Engineering and Computer Science*, 4(3):10984–10987, (2015).
- [119] P. Meakin. The Growth of Fractal Aggregates. In R. Pynn and T. Riste, editors, *Time-Dependent Effects in Disordered Materials*, volume 167, pages 45–70. Springer, Boston, (1987).
- [120] T. Vicsek. *Fractal growth phenomena*. World scientific, Hong Kong, (1992).
- [121] S. Al-Zainaldin, P. W. J. Glover, and P. Lorinczi. Synthetic Fractal Modelling of Heterogeneous and Anisotropic Reservoirs for Use in Simulation Studies: Implications on Their Hydrocarbon Recovery Prediction. *Transport in Porous Media*, 116(1):181–212, (2017).
- [122] F. Family and T. Vicsek. *Dynamics of Fractal Surfaces*. World Scientific, (1991).
- [123] Y. Saito and S. Omura. Domain competition during ballistic deposition: Effect of surface diffusion and surface patterning. *Physical Review E*, 84(2):021601, (2011).
- [124] F. L. Braga, O. A. Mattos, V. S. Amorin, and A. B. Souza. Diffusion limited aggregation of particles with different sizes: Fractal dimension change by anisotropic growth. *Physica A: Statistical Mechanics and its Applications*, 429:28–34, (2015).

- [125] A. Ghosh, R. Batabyal, G. P. Das, and B. N. Dev. An extended fractal growth regime in the diffusion limited aggregation including edge diffusion. *AIP Advances*, 6(1):015301, (2016).
- [126] D. Liu, W. Zhou, Z. Qiu, and X. Song. Fractal Simulation of Flocculation Processes Using a Diffusion-Limited Aggregation Model. *Fractal and Fractional*, 1(1):12, (2017).
- [127] M. Lattuada, H. Wu, and M. Morbidelli. A simple model for the structure of fractal aggregates. *Journal of colloid and interface science*, 268(1):106–120, (2003).
- [128] E. Domany, S. Alexander, D. Bensimon, and L. P. Kadanoff. Solutions to the Schrödinger equation on some fractal lattices. *Physical Review B*, 28(6):3110, (1983).
- [129] J. Hyde, D. J. Kelleher, J. Moeller, L. G. Rogers, and L. Seda. Magnetic Laplacians of locally exact forms on the Sierpinski Gasket. *arXiv preprint arXiv:1604.01340*, (2016).
- [130] E. Domany, S. Alexander, D. Bensimon, and L. P. Kadanoff. Solutions to the Schrödinger equation on some fractal lattices. *Physical Review B*, 28:3110–3123, (1983).
- [131] S. Saremi and T. J. Sejnowski. Correlated percolation, fractal structures, and scale-invariant distribution of clusters in natural images. *IEEE transactions on pattern analysis and machine intelligence*, 38(5):1016–1020, (2016).
- [132] S. Li and S. Boettcher. Renormalization group for a continuous-time quantum search in finite dimensions. *Physical Review A*, 95(3):032301, (2017).

- [133] H. O. Peitgen, H. Jürgens, and D. Saupe. *Chaos and fractals: new frontiers of science*. Springer Science & Business Media, (2006).
- [134] R. Hilfer and A. Blumen. Renormalisation on Sierpinski-type fractals. *Journal of Physics A: Mathematical and General*, 17(10):L537, (1984).
- [135] L. Molent, A. Spagnoli, A. Carpinteri, and R. Jones. Using the lead crack concept and fractal geometry for fatigue lifing of metallic structural components. *International Journal of Fatigue*, 102:214–220, (2017).
- [136] M. Giona. First-order reactiondiffusion kinetics in complex fractal media. *Chemical Engineering Science*, 47(6):1503–1515, (1992).
- [137] B. Yu and J. Li. Some fractal characters of porous media. *Fractals*, 9(03):365–372, (2001).
- [138] V. E. Tarasov. Acoustic waves in fractal media: Non-integer dimensional spaces approach. *Wave Motion*, 63:18–22, (2016).
- [139] P. Adler. *Porous Media: Geometry and Transports*. Elsevier, (2013).
- [140] J. F. Gouyet, M. Rosso, and B. Sapoval. Fractal surfaces and interfaces. In A. Bunde and S. Havlin, editors, *Fractals and Disordered Systems*, pages 263–302. Springer, Berlin, (1996).
- [141] L. M. Sander and S. V. Ghaisas. Fractals and patterns in catalysis. *Physica A: Statistical Mechanics and its Applications*, 233(3):629–639, (1996).
- [142] S. B. Yuste and K. Lindenberg. Subdiffusion-limited $A + A$ reactions. *Phys. Rev. Lett.*, 87:118301, (2001).
- [143] S. Canning, A. J. Walker, and P. A. Roach. The Effectiveness of a Sierpinski Carpet-Inspired Transducer. *Fractals*, 25(05):1750050, (2017).

- [144] K. Falconer. *Fractal Geometry: Mathematical Foundations and Applications*. 2nd ed. John Wiley and Sons, Chichester, West Sussex, UK, (2004).
- [145] W. A. Schwalm and M. K. Schwalm. Extension theory for lattice Green functions. *Phys.Rev.B*, 37(16):9524–9542, (1988).
- [146] R. L. OLeary, G. Smillie, G. Hayward, and A.C.S. Parr. CUE materials database, technical report. *Centre for Ultrasonic Engineering, University of Strathclyde, Glasgow, Scotland*, (2002). www.cue.ac.uk.
- [147] H. F. Tiersten. Thickness vibrations of piezoelectric plates. *JASA*, 35(1):53–58, (1963).
- [148] H. F. Tiersten. *Linear Piezoelectric Plate Vibrations: Elements of the Linear Theory of Piezoelectricity and the Vibrations Piezoelectric Plates*. Springer, New York, (2013).
- [149] G. Hayward, C. J. McLeod, and T. S Duranni. A systems model of the thickness mode piezoelectric transducer. *JASA*, 76(2):369–382, (1984).
- [150] Wolfram Research, Inc. *Mathematica*. Version 10.0. Champaign, Illinois, (2014).
- [151] W. A. Smith and B. A. Auld. Modeling 1-3 Composite Piezoelectric: Thickness-Mode Oscillations. *IEEE*, 38(1):40–47, (1991).
- [152] H. L. W. Chan and J. Unsworth. Simple model for piezoelectric ceramic/polymer 1-3 composites used in ultrasonic transducer applications. *IEEE Transactions on Ultrasonics, Ferroelectrics, and Frequency Control*, 36(4):434–441, (1989).

- [153] Y. Sun, X. Gao, H. Wang, Z. Chen, and Z. Yang. A wideband ultrasonic energy harvester using 1-3 piezoelectric composites with non-uniform thickness. *Applied Physics Letters*, 112(4):043903, (2018).
- [154] H. Fang, Z. Qiu, R. L. O’Leary, A. Gachagan, and A. J. Mulholland. Improving the operational bandwidth of a 1–3 piezoelectric composite transducer using Sierpinski Gasket fractal geometry. In *Ultrasonics Symposium (IUS), 2016 IEEE International*, pages 1–4. IEEE, (2016).
- [155] S. Canning, A. J. Walker, and P. A. Roach. A Mathematical Model of a Novel 3D Fractal-Inspired Piezoelectric Ultrasonic Transducer. *Sensors*, 16(12):2170, (2016).
- [156] B. A. Auld. *Acoustic Fields and Waves in Solids*, 1. John Wiley and Sons, New York, (1973).
- [157] A. J. Mulholland, S. N. Ramadas, R. L. O’Leary, A.C. S. Parr, A. Troge, G. Hayward, and R. A. Pethrick. A theoretical analysis of a piezoelectric ultrasound device with an active matching layer. *Ultrasonics*, 47(1):102–110, (2007).